

ARM LOCKING FOR LASER INTERFEROMETER SPACE ANTENNA

By

YINAN YU

A DISSERTATION PRESENTED TO THE GRADUATE SCHOOL
OF THE UNIVERSITY OF FLORIDA IN PARTIAL FULFILLMENT
OF THE REQUIREMENTS FOR THE DEGREE OF
DOCTOR OF PHILOSOPHY

UNIVERSITY OF FLORIDA

2011

© 2011 Yinan Yu

To my parents who provided me everything in my life without any reservation

ACKNOWLEDGMENTS

This work would not have been possible if were not for the help from many UF graduate students, faculty and staff. Especially I would like to express my deepest gratitude to my PhD degree supervisor, Dr. Guido Mueller who has been everlasting helpful and has offered all kinds of assistance, support and guidance on my research as well as on the writing of this thesis.

I would also like to show my gratitude to my committee members, Dr. Tanner, Dr. Whiting, Dr. Klimenko and Dr. Sarajedini, for taking their precious time to help me fulfill my requirements for the PhD degree. I also wish to give special thanks to my current and former lab colleagues: Vinzenz Wand, Shawn Mitryk, Dylan Sweeney and Joseph 'Pep' Sanjuan, for their supportive assistances and productive discussions.

Finally, I would like to express my love and gratitude to my family for their support and encouragement. Especially, I owe my passionate gratitude and love to my wife, also academic partner, Yiliang Bao, for her heartfelt and considerate assistance to both my life and career.

TABLE OF CONTENTS

	<u>page</u>
ACKNOWLEDGMENTS	4
LIST OF TABLES	8
LIST OF FIGURES	9
ABSTRACT	13
CHAPTER	
1 GRAVITATIONAL WAVE ASTRONOMY	15
1.1 Introduction	15
1.2 Gravitational Radiation in General Relativity	19
1.2.1 Propagation of Gravitational Waves	19
1.2.2 Generation of Gravitational Waves	21
1.2.3 Interaction of Gravitational Waves with Test Masses	24
1.3 Sources of Gravitational Waves	26
1.3.1 High Frequency Range	27
1.3.2 Low Frequency Range	28
1.3.2.1 Galactic binaries	29
1.3.2.2 Coalescence of massive black holes	33
1.3.2.3 Extreme mass ratio inspirals	34
1.3.2.4 Cosmic gravitational background radiation	36
1.4 Detection of Gravitational Waves	37
1.4.1 Detection Methods	38
1.4.2 Interferometric Detectors	41
1.4.2.1 Principle and configuration	42
1.4.2.2 Noise limitations	45
2 LASER INTERFEROMETER SPACE ANTENNA	49
2.1 Overview	49
2.1.1 Sensitivity	50
2.1.2 Disturbance Reduction System	52
2.1.3 Interferometric Measurement System	54
2.2 Noise Cancellation for LISA	59
2.2.1 Time Delay Interferometry	59
2.2.1.1 Michelson X-combination	60
2.2.1.2 Sagnac combination	62
2.2.1.3 TDI Limitations	63
2.2.2 Pre-stabilization	64
2.2.2.1 Pound-Drever-Hall frequency stabilization	65
2.2.2.2 Mach-Zehnder frequency stabilization	67

2.3	Arm Locking	71
2.3.1	Architecture	72
2.3.2	Arm Locking Sensors	74
2.3.2.1	Single arm locking	74
2.3.2.2	Common arm locking	79
2.3.2.3	Dual arm locking	82
2.3.2.4	Sagnac arm locking	86
2.3.3	Frequency Pulling	88
2.3.3.1	Doppler impact on arm locking	88
2.3.3.2	Frequency pulling rate	90
2.3.3.3	Modified dual arm locking	94
2.3.4	Integration with Tunable Pre-stabilization References	99
2.3.4.1	Arm locking with Pound-Drever-Hall stabilization	99
2.3.4.2	Arm locking with Mach-Zehnder stabilization	102
2.3.4.3	Arm locking only	102
2.3.5	Arm Locking Limitations	103
2.3.5.1	Limited controller gain in far-end PLL	103
2.3.5.2	Realistic noise sources in arm locking	107
3	UNIVERSITY OF FLORIDA LISA INTERFEROMETER SIMULATOR	115
3.1	Optical Components	115
3.2	Electronic Components	117
3.2.1	Digital Signal Processing Hardware	117
3.2.2	Phasemeter	118
3.2.2.1	Design	119
3.2.2.2	Performance	121
3.2.3	Electronic Phase Delay	122
4	EXPERIMENTAL VERIFICATION OF SINGLE ARM LOCKING	125
4.1	Motivation	125
4.2	Preliminary Test With Numerical Control Oscillator (NCO) Tracking	127
4.2.1	Experimental Setup	127
4.2.2	Digital Filter Design	130
4.2.3	Measurement Results	132
4.2.4	Noise Analysis	136
4.3	Single Arm Locking Integrated with a Tunable Reference	138
4.3.1	Heterodyne Phase-locked Loop	139
4.3.1.1	Experimental setup	139
4.3.1.2	Closed-loop dynamics	141
4.3.1.3	Results and analysis	143
4.3.2	Piezoelectric Transducer (PZT) Actuated Cavity	146
4.3.2.1	Characterization of the PZT cavity	146
4.3.2.2	Experimental setup	148
4.3.2.3	Results and analysis	150

4.3.3	Electro-optic Modulator (EOM) Sideband Locking	152
5	EXPERIMENTAL VERIFICATION OF DUAL/MODIFIED DUAL ARM LOCKING	154
5.1	Common Arm Locking	154
5.1.1	Common Arm Locking Sensor	154
5.1.2	Preliminary Test with Numerical Control Oscillator (NCO) Tracking	156
5.2	Dual Arm Locking	159
5.2.1	Dual Arm Locking Sensor	159
5.2.2	Preliminary Test with NCO Tracking	161
5.2.3	Integration with Pre-stabilized Laser	166
5.3	Modified Dual Arm Locking	168
5.3.1	Modified Dual Arm Locking Sensor	168
5.3.2	Preliminary Test with NCO Tracking	170
5.3.3	Integration with Pre-stabilized Laser	172
5.4	Arm locking Integrated With Far-end Phase-locking	173
5.4.1	Transponder Noise Floor - Time Domain Simulation	175
5.4.2	Experimental Verification - Simple Model	177
5.4.3	Experimental Verification - Full Model	179
6	DOPPLER FREQUENCY ERROR IN ARM LOCKING	187
6.1	Doppler Frequency Error in LISA	187
6.2	Investigation of Frequency Pulling on UFLIS	189
6.2.1	Generation of Doppler Frequency Errors	190
6.2.2	Frequency Pulling in Single Arm Locking	191
6.2.3	Frequency Pulling in Dual and Modified Dual Arm Locking	193
6.2.3.1	Time-domain simulations with AC-coupled controller	193
6.2.3.2	Experiments with modified dual arm locking sensor	196
7	CONCLUSION AND OUTLOOK	202
7.1	Control System of Arm Locking	202
7.2	Noise Limitations	203
7.3	Doppler-induced Frequency Pulling	204
7.4	Outlook	205
	REFERENCES	207
	BIOGRAPHICAL SKETCH	214

LIST OF TABLES

<u>Table</u>		<u>page</u>
2-1	Parameters of the noise analysis for arm locking	110
5-1	Parameters in time-domain arm locking simulations with transponder noise . .	175
6-1	Parameters in AC-coupled dual arm locking simulations with Doppler errors . .	194
6-2	Parameters of the AC-coupled filter used in simulations	194

LIST OF FIGURES

<u>Figure</u>	<u>page</u>
1-1 Inspiral of a white dwarf binary system	30
1-2 Artist's illustration of an EMRI	35
1-3 Schematic of a basic Michelson interferometer	41
1-4 Strain sensitivities of LIGO S6	47
2-1 Heliocentric orbit of the LISA constellation	50
2-2 LISA sensitivity curve	51
2-3 Interferometric Measurement System of LISA	55
2-4 Interferometers on the optical bench of LISA	56
2-5 Michelson X-combination and Sagnac combination	61
2-6 Pound-Drever-Hall frequency stabilization	65
2-7 Mach-Zehnder frequency stabilization for LISA	68
2-8 Arm locking architecture in the LISA constellation	72
2-9 Magnitude and phase responses of the single arm locking sensor	75
2-10 Instability of single arm locking when using a $1/s$ controller	76
2-11 Typical values of Δ which indicates the noise suppression	78
2-12 Example of the closed-loop transfer function of single arm locking	79
2-13 Time domain simulation to demonstrate initial transients in single arm locking	80
2-14 Transfer function of the common arm locking sensor	81
2-15 Transfer functions of the differential arm and the integrated differential arm	82
2-16 Transfer function of the linear combination $H(s)$	84
2-17 Transfer function of the dual arm locking sensor	85
2-18 Transfer function of the Sagnac-based dual arm locking sensor	87
2-19 Generic single arm locking loop with a Doppler frequency error	90
2-20 Generic dual arm locking loop with Doppler frequency errors	92
2-21 Magnitude and phase responses of the modified dual arm locking sensor	95

2-22	Magnitude and phase responses of the dual and common components	96
2-23	Generic modified dual arm locking loop with Doppler frequency errors	97
2-24	Magnitude responses of $H_+(s)$ and $H_-(s)$ for modified dual arm locking	98
2-25	PZT actuation cavity as a tunable reference for arm locking	100
2-26	Sideband cavity lock as a tunable reference for arm locking	101
2-27	Heterodyne phase-locking as a tunable reference for arm locking	101
2-28	Arm locking with the phase-locked laser at the far spacecraft	103
2-29	Arm locking with various noise sources	108
2-30	Noise floors in common arm locking	111
2-31	Noise floors in dual arm locking	112
2-32	Noise floors in modified dual arm locking	113
3-1	Frequency noise of the cavity stabilized laser	116
3-2	Implementation of the phasemeter on a Pentek board	119
3-3	Phasemeter performance measured with split-and-subtracted VCO signals	121
3-4	Transfer function and noise floor of the EPD unit tested with 1 s delay	124
4-1	Experimental setup of single arm locking using an NCO to track the input noise	128
4-2	Single arm locking with NCO tracking - Laplace domain	129
4-3	Magnitude response of controller for single arm locking	131
4-4	Magnitude response of the $1/\sqrt{s}$ filter	132
4-5	Noise spectra of the single arm locking test at high frequencies	132
4-6	Time series of the single arm locking test at high frequencies	133
4-7	Noise spectra of the single arm locking test at low frequencies	134
4-8	Time series of the single arm locking test at low frequencies	134
4-9	Single arm locking with NCO tracking - Laplace domain with noise sources	135
4-10	Comparison with a 30-bit digitization noise floor	137
4-11	Comparison of frequency drift rate between a 30-bit filter and a 32-bit filter	138
4-12	Experimental setup of single arm locking using a phase-locked laser	140

4-13 Single arm locking with heterodyne PLL - Laplace domain	141
4-14 Noise spectra of single arm locking with heterodyne PLL	144
4-15 Single arm locking with heterodyne PLL - Laplace domain with noise sources	145
4-16 Experimental setup of single arm locking using a PZT actuated cavity	148
4-17 Single arm locking with a PZT cavity - Laplace domain	149
4-18 Noise spectra of single arm locking with a PZT actuated cavity	151
4-19 Single arm locking with a PZT cavity - Laplace domain with noise sources	152
5-1 Design of the common arm locking sensor and the sensor transfer function	155
5-2 Experimental setup of common arm locking using NCO tracking	156
5-3 Noise spectra of common arm locking test with NCO tracking	157
5-4 Common arm locking with NCO tracking in the Laplace domain	158
5-5 Lock acquisition process in common arm locking	159
5-6 Implementation diagram of the dual arm locking sensor	160
5-7 Magnitude responses of the dual arm locking sensor	161
5-8 Preliminary experimental setup of dual arm locking with NCO tracking	162
5-9 Noise spectra of dual arm locking with NCO tracking	163
5-10 Noise spectra of 48-bit dual arm locking with NCO tracking	164
5-11 Lock acquisition process in dual arm locking	165
5-12 Experimental setup of dual arm locking using a phase-locked laser	166
5-13 Noise spectra of dual arm locking with heterodyne PLL	167
5-14 Implementation diagram of the modified dual arm locking sensor	168
5-15 Magnitude responses of the modified dual arm locking sensor	169
5-16 Experimental setup of modified dual arm locking with NCO tracking	170
5-17 Noise spectra of the modified dual arm locking test with NCO tracking	171
5-18 Magnitude responses of $H_+(s)$ and $H_-(s)$ used in the experiment	172
5-19 Experimental setup of modified dual arm locking using a phase-locked laser	173
5-20 Noise spectra of dual arm locking with heterodyne PLL	174

5-21	Time domain simulation of modified dual arm locking with transponder noise	177
5-22	Experimental setup of dual arm locking with FG signal as the transponder noise	178
5-23	Noise spectra of dual arm locking with FG signal as the transponder noise	180
5-24	Experimental setup of modified dual arm locking with far-end PLL	181
5-25	Closed-loop dynamics of modified dual arm locking with far-end PLL	182
5-26	Noise spectra of the transponder noise observed in modified dual arm locking	185
5-27	Noise spectra of the stabilized laser frequency and the transponder noise floor	186
6-1	Experimental setup of AC-coupled single arm locking with Doppler error	192
6-2	Measurement results of AC-coupled single arm locking with Doppler error	192
6-3	Performance of dual arm locking with an AC-coupled controller	195
6-4	Experimental setup of dual/modified dual arm locking with Doppler errors	197
6-5	Frequency pulling of dual/modified dual arm locking with Doppler errors	197
6-6	Performance of modified dual arm locking in the presence of Doppler errors	198
6-7	Linear drift in the laser frequency stabilized by modified dual arm locking	199
6-8	Frequency pulling in lock acquisition due to a step function in Doppler errors	200

Abstract of Dissertation Presented to the Graduate School
of the University of Florida in Partial Fulfillment of the
Requirements for the Degree of Doctor of Philosophy

ARM LOCKING FOR LASER INTERFEROMETER SPACE ANTENNA

By

Yinan Yu

May 2011

Chair: Guido Mueller

Major: Physics

The Laser Interferometer Space Antenna (LISA) is a collaborative National Aeronautics and Space Administration (NASA)/European Space Agency (ESA) space mission to detect gravitational waves in the frequency region of 3×10^{-5} Hz to 1 Hz by means of laser interferometry. It will be the first space-based interferometric gravitational wave detector to be launched in 2020s. LISA will consist of three identical spacecraft arranged in a quasi-equilateral triangular constellation with 5 Gm on each side. Each spacecraft houses two drag-free proof masses that follow the geodesic motion. The Interferometric Measurement System (IMS) of LISA monitors changes in the proper distance between two proof masses on each respective spacecraft.

Laser frequency stabilization is one of the most significant and difficult issues for the IMS of LISA. Arm locking as a proposed frequency stabilization technique, transfers the stability of the long arm lengths to the laser frequency. The arm locking sensor synthesizes an adequately filtered linear combination of the inter-spacecraft phase measurements to estimate the laser frequency noise, which can be used to control the laser frequency. Due to the large propagation delay during the light transmission, the arm locking controller needs to be carefully designed to retain enough phase margin. A potential problem for arm locking is that the Doppler shift of the return beam will cause a constant pulling in the master laser frequency if unaccounted for in the phase measurement. Until now all the benchtop experiments on arm locking verified only the

basic single arm locking configuration with unrealistic short delay time and without any Doppler estimation error at the phasemeter. At the University of Florida we developed the hardware-based University of Florida LISA Interferometer Simulator (UFLIS) to study and verify laser frequency noise reduction and suppression techniques under realistic LISA-like conditions. These conditions include the variable Doppler shifts between the spacecraft, LISA-like signal travel times, far-end heterodyne phase-locking, realistic laser frequency and timing noise. In this dissertation we will systematically introduce the cutting edge of experimental studies of arm locking under these realistic conditions. We have built an analog/digital hybrid system to demonstrate the control system of various arm locking schemes and their incorporation with pre-stabilization subsystems. We measured the noise suppression in our experiments as well as the frequency pulling in the presence of Doppler frequency error. With the achievement of meeting the requirement, our pioneering work have sufficiently demonstrated the validity and feasibility of arm locking under LISA-like conditions.

CHAPTER 1 GRAVITATIONAL WAVE ASTRONOMY

1.1 Introduction

Since the dawn of human civilization, the curiosity to the universe has always been a primary motivation for human to pursue science. Einstein once said, “The most incomprehensible thing about the world is that it is comprehensible.” The observational astronomy is undoubtedly a first step in human’s historical attempts to understand the universe, thanks to electromagnetic waves that allowed Aristotle to observe celestial constellations by naked eyes and allowed Galileo to observe Jupiter and orbiting moons by optical telescopes. Starting from the 19th century, the universe observable to human has been substantially expanded from visible light to currently the full spectrum of electromagnetic waves. A variety of ground-based and space-based observatories, covering from radio to Gamma ray, have been developed to study the evolution of stars and galaxies, as well as the origin of the universe.

In addition to the magnificent achievements electromagnetic observations have already obtained, another different observation method started to gradually grow in the second half of the 20th century. Gravity, as the dominant force in the universe, results in gravitational waves generated from accelerated objects, which is predicted by Einstein’s General Theory of Relativity. In this theory, gravitational waves are oscillations of spacetime geometry propagating with the speed of light [1]. Einstein never thought gravitational waves could possibly be detected due to their extremely weak interactions with matters. Nevertheless, Joseph Weber started to build the very first gravitational wave detectors using resonant masses in 1960s [2]. Also during this period, general relativity began to demonstrate its power in the research of astrophysics and cosmology. Relativistic gravity, as well as gravitational radiations, were found to play an important role in various astronomical systems. The most famous example of gravitational radiations is the 13-year observation to the binary pulsar PSR1913+16

[3, 4], which first indirectly verified the existence of gravitational waves, as well as the validity of general relativity in strong gravitational fields. The success of PSR1913+16 indicates that like electromagnetic waves, gravitational waves can also be used as an observation method to study the universe, which is known as gravitational wave astronomy.

Actually, gravitational wave astronomy will reveal abundant information about astronomical systems that could not be achieved by traditional electromagnetic wave astronomy [5]. For example, the gravitational radiation from black hole coalescence provides the only possible direct observation method to study black hole physics. The electromagnetic radiation from black holes (known as Hawking radiation), if any, would be impossible to detect for current technology. Also due to the weak interaction with matters, gravitational waves are hardly attenuated or scattered ever since they are generated. This indicates that they could carry information about some exotic phenomena that electromagnetic detections cannot reach, such as the interior of supernova explosions or physics of the very early universe.

Although the prospect of gravitational wave astronomy is exciting, the detection of gravitational waves still remains to be a challenge for current technology due to their extremely weak interactions with masses. For example, the typical upper limit of the gravitational wave strain generated by the coalescence of stellar mass black holes is no more than 10^{-23} when arrive at the Earth. The manifestation of gravitational wave strains is an oscillating change in the relative distance between test masses. Based on this principle, laser interferometers can be naturally used to construct gravitational wave detectors via precise interferometry. The ground-based Laser Interferometer Gravitational Wave Observatory (LIGO) is based on an equal-armed Michelson interferometer with arm lengths of 4 km [6]. Nevertheless, the required displacement sensitivity is still on the order of $\sim 10^{-19}$ m Hz^{-1/2}. To reach the required sensitivity,

various techniques have been developed for LIGO and other ground-based detectors to enhance their detection sensitivity and suppress random noises.

LIGO and other ground-based detectors are expected to detect gravitational waves at frequencies higher than ~ 30 Hz. For frequencies below ~ 30 Hz, the seismic noise from ground vibrations starts to dominate the sensitivity curve rapidly and becomes a limitation for current ground-based detectors. The detection of gravitational waves at lower frequencies requires either a completely different detection method or an absolute isolation from seismic noise by placing the detector in space. Laser Interferometer Space Antenna (LISA) is a proposed large-scaled laser interferometer on the heliocentric orbit in order to detect gravitational waves at frequencies from 3×10^{-5} Hz to 1 Hz [7, 8]. LISA consists of three spacecraft forming a near-equilateral triangle with each side length 5×10^9 m. Since the arm length is far longer than all ground-based detectors, the length change due to gravitational wave strains will become more significant, which provides LISA a sensitivity of 10^{-20} Hz $^{-1/2}$ at 3 mHz. With this sensitivity, LISA will be able to detect low-frequency gravitational waves emitted from coalescences of massive black holes (MBH) out to redshift $z \sim 20$ [9, 10]. Other primary gravitational wave sources LISA will detect include extreme mass ratio inspirals (EMRI) where the dynamics of a test mass captured in Kerr geometry can be experimentally studied, resolved and unresolved Galactic compact binaries, even gravitational relics of Big Bang known as the stochastic background and maybe cosmic strings predicted in some versions of the string theory. In summary, LISA will perform a series of new scientific measurements to various gravitational wave sources in the universe with multiple goals, including relevant astrophysical research in such as binaries and galaxies, tests of general relativity in strong gravitational fields, as well as discoveries of new physics and cosmology.

Like the Michelson interferometer used in ground-based detectors, LISA will also measure the change in distance between two free-falling proof masses. However,

the configuration and operation of LISA are quite different from a standard Michelson interferometer in a number of ways. As LISA consists of three spacecraft and each of them orbits the sun independently, the arm length between two proof masses is a time-variable quantity, which cannot be made identical to each other even in principle. Time Delay Interferometry (TDI) as a post-processing technique synthesizes equal arm interferometry to extract gravitational wave signals [11, 12]. Nevertheless, the random fluctuations in the laser frequency cannot be suppressed adequately by TDI with limited precision of the arm length knowledge. To overcome this problem, the pre-stabilization of the laser frequency is essential. In addition to common methods such as Pound-Drever-Hall technique used for the laser stabilization in ground-based detectors, the architecture of LISA inherently provides a unique frequency stabilization technique known as arm locking. Since the LISA arm length is a very stable reference in the LISA frequency band, arm locking takes it as a frequency reference to stabilize the laser frequency via the synthesization of an adequately filtered linear combination of the interferometry signals. The main subject of this dissertation is about arm locking, including the analytical performance [13], numerical simulations in the time domain and especially the experimental verification in laboratory [14, 15].

This dissertation is divided into seven chapters. The remaining part of Chapter 1 introduces the theory of gravitational radiation, gravitational wave sources and detections. In this part I put emphasis on the gravitational wave sources for LISA. Chapter 2 covers the overview of LISA, including the scientific requirements and payload, where the technique of arm locking is the main subject to be focused on. Chapter 3 to Chapter 6 discuss the experimental verifications of arm locking on the hardware simulator of LISA interferometry developed at the University of Florida. The final part, Chapter 7, gives the conclusions and outlook on arm locking and LISA interferometry.

1.2 Gravitational Radiation in General Relativity

1.2.1 Propagation of Gravitational Waves

Gravitational radiation is one of the most fundamental phenomena predicted by Einstein's General Theory of Relativity. The propagation of gravitational waves in spacetime can be described as an approximate solution of linearized Einstein field equations in the presence of a weak gravitational field. ¹

The Einstein field equations can be written as

$$R_{\mu\nu} - \frac{1}{2}g_{\mu\nu}R = \frac{8\pi G}{c^4} T_{\mu\nu}. \quad (1-1)$$

We assume the gravitational field is weak enough such that the metric $g_{\mu\nu}$ can be decomposed into the flat Minkowski metric plus a small linear perturbation, i.e.,

$$g_{\mu\nu} = \eta_{\mu\nu} + h_{\mu\nu}, \quad |h_{\mu\nu}| \ll 1. \quad (1-2)$$

This approximation is known as the theory of linearized gravity where only the first order of the perturbation $h_{\mu\nu}$ is taken into account. In this theory the overall spacetime metric $g_{\mu\nu}$ can be described as a perturbation tensor field $h_{\mu\nu}$ propagating within the flat Minkowski spacetime. This tensor field is symmetric and Lorentz invariant.

To solve the Einstein field equations using this approximation, we calculate the Riemann curvature tensor

$$R_{\mu\nu\rho\sigma} = \frac{1}{2}(\partial_\nu\partial_\rho h_{\mu\sigma} + \partial_\mu\partial_\sigma h_{\nu\rho} - \partial_\mu\partial_\rho h_{\nu\sigma} - \partial_\nu\partial_\sigma h_{\mu\rho}). \quad (1-3)$$

We define the trace of the perturbation as $h = \eta^{\mu\nu} h_{\mu\nu}$ and the trace-reverse metric perturbation as $\bar{h}_{\mu\nu} = h_{\mu\nu} - \frac{1}{2}\eta_{\mu\nu}h$. Based on the Riemann tensor calculated in Eq.1-3,

¹ The theoretical introduction of general relativity and gravitational waves in this chapter is mainly adapted from Ref. [16] by Misner *et al.* and Ref. [17] by Maggiore.

the Einstein field equations can be reduced into the linearized form

$$\square \bar{h}_{\mu\nu} + \eta_{\mu\nu} \partial^\rho \partial^\sigma \bar{h}_{\rho\sigma} - \partial^\rho \partial_\nu \bar{h}_{\nu\rho} - \partial_\rho \partial^\nu \bar{h}_{\nu\rho} = -\frac{16\pi G}{c^4} T_{\mu\nu}. \quad (1-4)$$

Due to the Lorentz invariance of $h_{\mu\nu}$, we could exploit the gauge freedom to choose the Lorenz gauge

$$\partial^\nu \bar{h}_{\mu\nu} = 0. \quad (1-5)$$

In this gauge the last three terms on the left side of Eq. 1-4 vanish. Therefore, we obtain the linearized Einstein field equation

$$\square \bar{h}_{\mu\nu} = -\frac{16\pi G}{c^4} T_{\mu\nu}, \quad (1-6)$$

which is essentially a four-dimension wave equation with six independent components of $h_{\mu\nu}$.

In the region far away from the source, the wave propagation equation is

$$\square \bar{h}_{\mu\nu} = 0. \quad (1-7)$$

The general solution of this equation is given by the linear superposition of the following eigenfunction

$$\bar{h}_{\mu\nu} = A_{\mu\nu} \exp(ik_\mu x^\mu), \quad (1-8)$$

where the four-dimension wave vector k_μ must satisfy the condition $\eta_{\mu\nu} k^\mu k^\nu = 0$. This indicates the gravitational wave travels through a null geodesic with the speed of light.

Since the Lorenz gauge is not unique, it allows us to add more constraints to eliminate additional degrees of freedom by introducing the transverse-traceless gauge (TT gauge). In this gauge the perturbation metric is independent of the time components and is both traceless and transverse. We use the notation of $h_{\mu\nu}^{\text{TT}}$ to represent the metric tensor $\bar{h}_{\mu\nu}$ in the TT gauge, which is given by

$$h_{0\nu}^{\text{TT}} = 0, \quad \eta^{\mu\nu} h_{\mu\nu}^{\text{TT}} = 0, \quad \partial_\mu h_{\text{TT}}^{\mu\nu} = 0. \quad (1-9)$$

Under the constraints of both the Lorenz gauge and the TT gauge, the metric tensor has only two independent components, corresponding to two orthogonal modes of linear polarization of gravitational waves. If we assume the gravitational wave travels in the z direction, the metric tensor can be completely characterized by the form

$$h_{\mu\nu}^{\text{TT}}(t, z) = \begin{pmatrix} h_+ & h_\times & 0 \\ h_\times & -h_+ & 0 \\ 0 & 0 & 0 \end{pmatrix} \cos[\omega(t - z/c)], \quad (1-10)$$

where the notations of h_+ and h_\times are known as the plus and the cross polarizations of gravitational waves, respectively. Eq. 1-10 can also be written in the form of a spacetime interval:

$$ds^2 = -cdt^2 + dz^2 + [1 + h_+ \cos(\omega(t - z/c))]dx^2 + [1 - h_+ \cos(\omega(t - z/c))]dy^2 + 2h_\times \cos(\omega(t - z/c))dxdy. \quad (1-11)$$

1.2.2 Generation of Gravitational Waves

In the region near the radiation source, the energy-momentum tensor $T_{\mu\nu}$ does not vanish. By solving the matter-coupled Einstein equation, we could obtain the relation between the motion of the source and generation of gravitational waves. Generally, an inhomogeneous wave equation such as

$$\square \bar{h}_{\mu\nu} = -\frac{16\pi G}{c^4} T_{\mu\nu} \quad (1-12)$$

can be solved using the retarded Green's function, which is also used for similar problems in electromagnetism. We consider the radiation from a four-dimension point source $\delta^{(4)}(x - x')$ and then the Green's function $G(x - x')$ is the solution for the wave equation: $\square_x G(x - x') = \delta^{(4)}(x - x')$, where \square_x represents the d'Alembertian operator with derivatives respective to the field point x .

The retarded Green's function can be expressed as

$$G(x - x') = -\frac{1}{4\pi|\mathbf{x} - \mathbf{x}'|} \delta(x_{\text{ret}}^0 - x'^0), \quad (1-13)$$

where $x'^0 = ct'$, $x_{\text{ret}}^0 = ct_{\text{ret}}$ and $t_{\text{ret}} \equiv t - \frac{|\mathbf{x} - \mathbf{x}'|}{c}$ is called the retarded time.

Thus the solution for Eq. 1-12 is given by the integration

$$\begin{aligned} \bar{h}_{\mu\nu}(t, \mathbf{x}) &= -\frac{16\pi G}{c^4} \int G(x - x') T_{\mu\nu}(x') d^4x' \\ &= \frac{4G}{c^4} \int \frac{1}{|\mathbf{x} - \mathbf{x}'|} T_{\mu\nu} \left(t - \frac{|\mathbf{x} - \mathbf{x}'|}{c}, \mathbf{x}' \right) d^3x'. \end{aligned} \quad (1-14)$$

If the radiation source $T_{\mu\nu}$ is non-relativistic, which means the typical velocities inside the source are significantly smaller than the speed of light, in the far field approximation we have

$$\bar{h}_{\mu\nu}(t, \mathbf{x}) \approx \frac{4G}{c^4} \frac{1}{r} \int T_{\mu\nu} \left(t - \frac{r}{c}, \mathbf{x}' \right) d^3x', \quad (1-15)$$

where $r = |\mathbf{x} - \mathbf{x}'|$ is the spatial distance.

With the Lorenz gauge condition and the conservation law of the energy-momentum tensor $\partial_\mu T^{\mu\nu} = 0$, the formula can be further reduced into

$$\bar{h}_{\mu\nu}(t, \mathbf{x}) = \frac{2G}{c^4} \frac{1}{r} \frac{d^2 I_{\mu\nu}}{dt^2} \left(t - \frac{r}{c} \right), \quad (1-16)$$

where

$$I_{\mu\nu} = \int x'_\mu x'_\nu T^{00}(t, \mathbf{x}') d^3x' \quad (1-17)$$

is defined as the quadrupole moment tensor of the energy density of the source. If the source is a perfect fluid with a rest frame energy density ρ , the quadrupole moment tensor is simply equivalent to the moment of inertia of the source. Eq. 1-16 is known as the quadrupole formula, which indicates that the gravitational wave strain generated from a non-relativistic source is proportional to the second derivative of the quadrupole moment tensor. In contrast, the leading term in an electromagnetic radiation is a time-changing dipole moment.

It is easy to show that for a binary system that consists of two stars with mass M and orbital radius R , the orbital frequency is given by $f_{\text{orb}} = \frac{1}{2\pi} \sqrt{\frac{GM}{4R^3}}$. From the quadrupole formula, one can deduce that the gravitational wave frequency of this binary system is twice of the orbital frequency, i.e., $f_{\text{GW}} = 2f_{\text{orb}}$.

The luminosity (i.e., the total power) of the gravitational quadrupole radiation is given by

$$\begin{aligned} L_{\text{GW}} &= \frac{G}{5c^5} \left\langle \frac{d^3 t_{\mu\nu}}{dt^3} \frac{d^3 t_{\mu\nu}}{dt^3} \right\rangle \\ &= \frac{G}{5c^5} \left\langle \frac{d^3 I_{\mu\nu}}{dt^3} \frac{d^3 I_{\mu\nu}}{dt^3} - \frac{1}{3} \left(\frac{d^3 I}{dt^3} \right)^2 \right\rangle, \end{aligned} \quad (1-18)$$

where $t_{\mu\nu} = I_{\mu\nu} - \frac{1}{3}\delta_{\mu\nu}I = \int (x'_\mu x'_\nu - \frac{1}{3}\delta_{\mu\nu}r^2) T^{00}(t, \mathbf{x}') d^3x'$ is known as the reduced quadrupole moment, which is the counterpart of the reduced quadrupole moment in electromagnetism. The angle brackets represent an average over several characteristic wavelengths of the source.

Now we will estimate how much the power the gravitational radiation has. First, the third time derivative of the reduced quadrupole moment has the same order of magnitude to the quantity MR^2/T^3 , where M is the accelerated mass, R is the size of the radiation system and T is the time for the mass to move from one side to the other. For a binary system T can be considered as the orbital period. On the other hand, the quantity MR^2/T^3 can be written as

$$\frac{MR^2}{T^3} = \frac{M(R/T)^2}{T} \sim \frac{E_{\text{kinetic}}}{T} \sim L_{\text{internal}}, \quad (1-19)$$

where E_{kinetic} is the translational kinetic energy of the accelerated mass when moving from one side to the other and L_{internal} is the internal luminosity or the power inside the system flowing from one side to the other.

Therefore, a rough estimation of Eq. 1–18 is given by the square of the internal luminosity:

$$L_{\text{GW}} \sim \frac{G}{c^5} L_{\text{internal}}^2. \quad (1-20)$$

From this relation one can further deduce how long the gravitational radiation will need to exhaust the total energy of the system. We will explain the binary system as an example in Section 1.3.2.

1.2.3 Interaction of Gravitational Waves with Test Masses

The motion of a test mass in a curved spacetime is described by the geodesic equation:

$$\frac{d^2 x^\mu}{d\tau^2} + \Gamma_{\nu\rho}^\mu \frac{dx^\nu}{d\tau} \frac{dx^\rho}{d\tau} = 0. \quad (1-21)$$

We consider two nearby geodesics, which are parametrized by $x^\mu(\tau)$ and $x^\mu(\tau) + \xi^\mu(\tau)$ respectively. If we take the difference between their geodesic equations and expand it to the first order since $|\xi^\mu|$ is very small, it yields

$$\frac{d^2 \xi^\mu}{d\tau^2} + 2\Gamma_{\nu\rho}^\mu \frac{dx^\nu}{d\tau} \frac{d\xi^\rho}{d\tau} + \xi^\sigma \partial_\sigma \Gamma_{\nu\rho}^\mu \frac{dx^\nu}{d\tau} \frac{dx^\rho}{d\tau} = 0. \quad (1-22)$$

This equation can be written in a simpler form if we introduce the covariant derivative $\frac{DV^\mu}{D\tau} \equiv \frac{dV^\mu}{d\tau} + \Gamma_{\nu\rho}^\mu V^\nu \frac{dx^\rho}{d\tau}$, which is known as the geodesic deviation equation:

$$\frac{D^2 \xi^\mu}{D\tau^2} = -R_{\nu\rho\sigma}^\mu \xi^\rho \frac{dx^\nu}{d\tau} \frac{dx^\sigma}{d\tau}. \quad (1-23)$$

Therefore, the geodesic deviation equation describes a tidal gravitational force applying on nearby geodesics. To further derive how the test mass behaves in the presence of the tidal force, we will need to choose a reference frame.

In the TT gauge gravitational waves can be represented as simple as in Eq. 1–10. We consider two test masses with a coordinate separation ξ^i and if they are at rest at $\tau = 0$, we have $dx^i/d\tau = 0$ and $dx^0/d\tau = c$. Therefore, Eq. 1–22 is reduced to

$$\frac{d^2 \xi^i}{d\tau^2} = - \left(2c\Gamma_{0\rho}^i \frac{d\xi^\rho}{d\tau} + c^2 \xi^\sigma \partial_\sigma \Gamma_{00}^i \right), \quad (1-24)$$

Moreover, in the TT gauge the Christoffel symbol

$$\Gamma_{00}^i = \frac{1}{2}(2\partial_0 h_{0i} - \partial_i h_{00}) \quad (1-25)$$

also vanishes since h_{00} and h_{0i} equal zero in the TT gauge. The only non-vanishing term is $\Gamma_{0j}^i = \frac{1}{2}\partial_0 h_{ij}$ and then the equation is further simplified into

$$\frac{d^2 \xi^i}{d\tau^2} = -\dot{h}_{ij} \frac{d\xi^j}{d\tau}. \quad (1-26)$$

Therefore, if the two test masses do not have an initial relative velocity $\frac{d\xi^i}{d\tau}$, then we also have $\frac{d^2 \xi^i}{d\tau^2} = 0$ and their coordinate distance always remains the same. In other words, in the TT gauge the position of test masses does not change due to gravitational waves. This conclusion does not imply that the interaction of gravitational waves with test masses is zero; instead, what gravitational waves change is the proper distance between test masses as demonstrated in Eq. 1-11. If we assume that the coordinates of the two test masses are given by $(0, 0, 0, 0)$ and $(0, L, 0, 0)$, from Eq. 1-11 the proper distance is then given by

$$s = L(1 + h_+ \cos(\omega t))^{1/2} \approx L(1 + \frac{1}{2}h_+ \cos(\omega t)). \quad (1-27)$$

Due to the invariance of the TT gauge, gravitational wave detectors require a more convenient reference frame to measure the position change of test masses. Such a reference frame known as the proper detector frame requires the test mass to be drag-free (at least in certain directions) and its relevant coordinates will be changed by gravitational waves. In this frame the geodesic deviation equation yields

$$\ddot{\xi}^i = \frac{1}{2}h_{ij}^{\ddot{T}T}\xi^j. \quad (1-28)$$

where the second order derivative is with respect to the coordinate time rather than the proper time.

Starting from Eq. 1–28, we consider a gravitational wave propagating along the z axis and the test masses are located in the x-y plane. At $z = 0$, the + polarization can be written as

$$h_{ab}^{TT} = h_+ \sin \omega t \begin{pmatrix} 1 & 0 \\ 0 & -1 \end{pmatrix}, \quad a, b = 1, 2. \quad (1-29)$$

Substitute Eq. 1–28 with Eq. 1–29 and we obtain the coordinate changes on x and y directions:

$$\begin{aligned} \delta\ddot{x} &= -\frac{h_+}{2}(x_0 + \delta x)\omega^2 \sin \omega t, \\ \delta\ddot{y} &= \frac{h_+}{2}(y_0 + \delta y)\omega^2 \sin \omega t. \end{aligned} \quad (1-30)$$

Ignore the negligible δx , δy terms on the right side and integrate twice over time:

$$\begin{aligned} \delta x &= \frac{h_+}{2}x_0 \sin \omega t, \\ \delta y &= -\frac{h_+}{2}y_0 \sin \omega t. \end{aligned} \quad (1-31)$$

Similar approach can be performed to evaluate the coordinate changes due to the \times polarization:

$$\begin{aligned} \delta x &= \frac{h_\times}{2}y_0 \sin \omega t, \\ \delta y &= \frac{h_\times}{2}x_0 \sin \omega t. \end{aligned} \quad (1-32)$$

Eq. 1–31 and Eq. 1–32 describes how gravitational waves displace test masses transversely with respect to their propagation direction. This kind of tidal distortions is the measurement principle behind all resonant and interferometric gravitational wave detectors.

1.3 Sources of Gravitational Waves

In this section we have a review on typical astrophysical gravitational wave sources classified by their radiation frequencies. The frequency range for observable

gravitational wave sources starts from ~ 10 kHz and extends downward by roughly 22 orders of magnitude [18].

In Section 1.2.2 we already mentioned that the frequency of gravitational waves emitted from a binary system is twice of the orbital frequency. In general cases, the gravitational wave frequency of a certain source is of the same order to the natural frequency of the system, which is given by

$$f_0 = \sqrt{\frac{\bar{\rho}G}{4\pi}}, \quad (1-33)$$

where $\bar{\rho}$ is the mean density of the mass-energy in the source. It can be simply estimated by $\bar{\rho} = \frac{3M}{4\pi R^3}$, where M is the mass and R is the radius. Therefore, a gravitational wave source with a higher mean density will radiates at a higher frequency. For a neutron star with a $1.4M_\odot$ mass and a 10 km radius, the gravitational wave frequency is close to 2 kHz. For a white dwarf with a $0.5M_\odot$ mass and a 10^4 km radius, the gravitational wave frequency is close to 3 mHz, which is in the LISA science band. For black holes, since the Schwarzschild radius of a black hole is related to the mass: $R = 2GM/c^2$, the natural frequency is inversely proportional to the black hole mass. For a $10M_\odot$ stellar mass black hole the frequency is close to 1 kHz, while for a $2.5 \times 10^6 M_\odot$ massive black hole the frequency is as low as 4 mHz.

1.3.1 High Frequency Range

The gravitational wave sources in this high frequency range will be detected by ground-based interferometric detectors as well as resonant bars. These sources include the coalescence of neutron star and stellar mass black holes, gravitational collapse of supernovae, spinning pulsars and stochastic radiation background from the Big Bang. We will introduce the inspiral binaries and the stochastic background in the next section (Low frequency range) and this section only involves sources that are exclusive to the high frequency range.

One particularly interesting high-frequency source is spinning pulsars. To radiate gravitational waves, the mass-energy distribution of the pulsar must be asymmetric otherwise the quadrupole moment is time-independent. The mechanism to produce this asymmetry could be a “lump”, where the asymmetry is static relative to the neutron star, or a “wave”, where the asymmetry is in motion. The former cases can possibly be seen in spheroid-shaped neutron stars [19], neutron stars with a misalignment of the magnetic field with the rotation axis or neutron stars with accretions. Since the contribution to gravitational radiations is completely from the asymmetric portion, the gravitational wave frequency of a pulsar is also twice of the spinning frequency. Since the spinning frequency of a pulsar is ultra stable, the gravitational wave signal will be seen in a very narrow frequency bin. Unlike inspiral binaries, the gravitational radiation of a pulsar is probably not the primary mechanism to cause it to spin down [18].

In addition, the core collapse of a supernova that forms a new neutron star or black hole is also likely to be an important source in the high frequency range. The rotational core collapse of a supernova is asymmetric, which was already confirmed by observations to the supernova SN 1987A [20]. This asymmetry may be associated with a transient and non-periodic burst signal. However, the waveform and amplitude predictions of burst signals are very difficult to model analytically and so far relies entirely on numerical simulations. It is yet not clear what fraction of the total mass-energy will be released in the form of gravitational radiation. The current best estimation yields an upper limit of 10^{-6} [18], which makes the gravitational bursts in the Virgo cluster undetectable. In comparison, the rate of core collapse supernovae in our Galaxy is estimated to be one per a few decades and the corresponding burst signal should be detectable for current detectors.

1.3.2 Low Frequency Range

In this section we will focus on the gravitational wave sources in the LISA science band, including galactic binaries, coalescence of massive black holes, extreme mass

ratio inspirals and cosmic gravitational radiation background.² The science objective of LISA is to detect and study the gravitational radiations from these unprecedentedly observed sources. Based on the detection results, LISA will comprehensively reveal more astrophysical information on binaries, black holes, galaxy structures, etc. LISA will also precisely test the validity of general relativity in very strong gravitational fields like the vicinity of a Kerr black hole. Finally, LISA will probe new physics and cosmology by tracing gravitational waves from the very early universe.

1.3.2.1 Galactic binaries

The inspiral of compact binary systems is the best understood gravitational wave source and so far the only observationally confirmed source. In Einstein's theory, gravitational radiations damp the energy from the orbital motion and cause the orbit to gradually shrink. This phenomenon has already been confirmed in the observation to the binary pulsar PSR1913+16 by Hulse and Taylor since 1974 [3, 4]. As the two neutron stars inspiral closer, the orbital frequency continues to increase, which generates a chirp signal in the form of gravitational radiations. In PSR1913+16 one member is a radio pulsar, which provides a very accurate clock for orbital period measurements. On the other hand, both the quadrupole amplitude and the orbital decay rate only depend on the masses of the binary system (see below). The orbital decay rate therefore can be directly predicted by general relativity, given that the required parameters are already obtained by other observations. By comparing the theoretical and the measured orbital decay rate, the prediction of general relativity is successfully verified with an observational error less than 1%.

Here we will derive how a binary orbit evolves in the presence of gravitational radiation braking. Suppose we have two stars of masses m_1 and m_2 on an elliptical orbit

² For a comprehensive review of gravitational wave sources in the LISA science band, see Ref. [21].

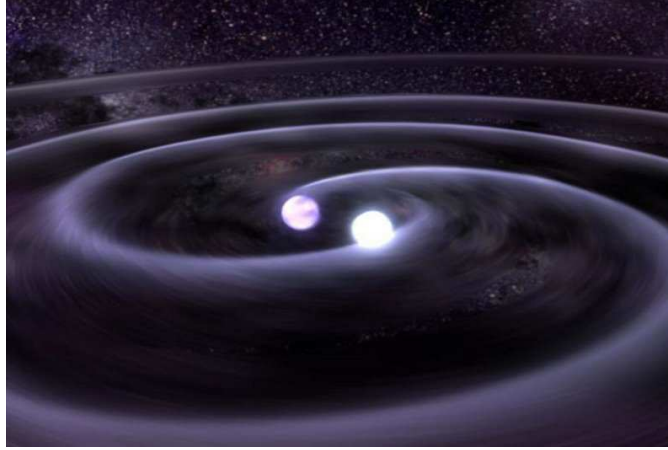


Figure 1-1. Artist's illustration of a white dwarf binary system in the inspiral phase, courtesy of NASA.

with an angular velocity ω and the semi-major axis of the elliptical orbit is a . Then the Kepler's law yields

$$\omega^2 a^3 = (m_1 + m_2)G = MG. \quad (1-34)$$

From the virial theorem, the kinetic energy of the binary system is given by

$$E_{\text{kinetic}} = -\frac{1}{2}E_{\text{potential}} = \frac{G}{2} \frac{m_1 m_2}{a}. \quad (1-35)$$

Based on Eq. 1-20, the luminosity of the gravitational radiation is proportional to the square of the orbiting power, which is given by the product of the kinetic energy and the angular velocity:

$$\begin{aligned} L_{\text{GW}} &\sim \frac{G}{c^5} L_{\text{internal}}^2 \sim \frac{G}{c^5} \left(\omega \frac{G}{2} \frac{m_1 m_2}{a} \right)^2 \\ &\sim \frac{G^4 \mu^2 M^3}{4c^5 a^5}, \end{aligned} \quad (1-36)$$

where $\mu = m_1 m_2 / M$ is the reduced mass.

If we follow an exact calculation, the result is given by

$$L_{\text{GW}} = \frac{32G^4 \mu^2 M^3}{5c^5 a^5} f(e), \quad (1-37)$$

where $f(e)$ is a correction function due to the eccentricity. For a circular orbit with $e = 0$, we have $f(e) = 1$.

For binary systems, the decay rate of the total energy is equal to the gravitational radiation power, i.e.,

$$\frac{dE_{\text{total}}}{dt} = -L_{\text{GW}}, \quad (1-38)$$

where the total energy E_{total} just equals to the negative of the kinetic energy.

We are interested in the decay rate of the orbital period dT/dt . Based on the Kepler's law, the period is associated to the kinetic energy via the relation $T = \text{const} \cdot (-E_{\text{kinetic}})^{-3/2}$. By taking derivatives on each side we have

$$\frac{\dot{T}}{T} = -\frac{3}{2} \frac{\dot{E}_{\text{kinetic}}}{E_{\text{kinetic}}}. \quad (1-39)$$

Substitute with Eq. 1-38 and we have

$$\frac{\dot{T}}{T} = -\frac{96}{5} \frac{G^3 \mu M^2}{c^5 a^4} f(e), \quad (1-40)$$

which can be further written as

$$\frac{\dot{T}}{T} = -\frac{96}{5} \frac{G^{5/3} \mu M^{2/3}}{c^5} \left(\frac{T}{2\pi} \right)^{-8/3} f(e). \quad (1-41)$$

If we assume $f(e) = 1$, the solution of this differential equation is

$$T(t) = \left(T_0^{8/3} - \frac{8}{3} kt \right)^{3/8}, \quad (1-42)$$

where T_0 is the period at $t = 0$ and the constant k is given by

$$k = \frac{96}{5c^5} (2\pi)^{8/3} (G\mu^{3/5} M^{2/5})^{5/3}. \quad (1-43)$$

Eq. 1-42 describes how fast the orbital period of a binary system decreases over time due to gravitational radiations, which completely depends on the constant k .

Eq. 1-43 indicates that the speed of orbit shrinking only depends on the combination $\mu^{3/5} M^{2/5}$ from the binary masses. This combination is known as the chirp mass of the

binary system:

$$\mathcal{M}_{\text{chirp}} = \mu^{3/5} M^{2/5} = (m_1 m_2)^{3/5} (m_1 + m_2)^{-1/5}. \quad (1-44)$$

In other words, the chirp mass of the binary system determines how fast the frequency of the chirp signal sweeps the spectrum. By observing the time-varying frequency of the gravitational radiation, one can directly deduce the chirp mass of the binary system.

Since most stars in the universe have a stellar mass and also are binaries, white dwarf binaries are numerous in the Galaxy, much more than neutron star or black hole binaries. Although the gravitational radiation from white dwarfs is relatively weak, the close distance in our Galaxy ensures a high SNR ~ 100 at relatively high frequencies (> 1 mHz). These two conditions make the white dwarf binaries the guaranteed sources for LISA. LISA should be capable of detecting thousands of them individually and measuring their physical parameters such as distance, orbital period and spatial orientation precisely [22]. In particular, a number of resolved white dwarf binaries with a short orbital period (a few minutes) are expected to be detected soon after LISA is engaged. LISA can use them as instrument verification sources by measuring and comparing their distances and physical parameters [23]. In addition, LISA is also expected to detect neutron star and stellar mass black hole binaries that are at in-band low frequencies [24, 25].

On the other hand, the population of white dwarf binaries in the Galaxy is very large ($\sim 10^7$) at frequencies below a 1 mHz [26]. These galactic binaries form a confusion-dominated foreground, whereas a diffuse background is generated from extragalactic binaries. Consequently, only the brightest and closest sources among the confusion foreground can be particularly resolved by LISA. Nevertheless, this foreground is still of interest for LISA measurements since it represents statistical information such as the total number and geometrical distribution of the galactic binaries in this frequency region.

1.3.2.2 Coalescence of massive black holes

Massive black holes are black holes of mass $10^5 M_\odot$ to $10^9 M_\odot$. Abundant evidences indicate that almost every galaxy has a massive black hole in its center. They are thought to be the “engine” to power up active galactic nuclei (AGN) and quasars [27]. Due to the gigantic mass, the frequency of gravitational radiations from coalescences of massive black holes is much lower yet the amplitude is much more significant than stellar mass black holes. The gravitational radiation from coalescences of massive black holes is the strongest signal that LISA is expected to detect. The detection range can reach as far as $z \sim 20$ and the signal is even well above the noise amplitude with a high SNR of 10^2 to 10^3 . Also compared to stars, the dimension of galaxies is not insignificant relative to the distance between each other, which makes the galaxy merger rate actually rather high. Therefore, LISA should be able to detect the mergers of massive black holes with a decent detection rate, approximately 1 per year at redshift $z < 1$ [28]. This estimation does not take into account the formation of galaxies via mergers of small protogalaxies of mass up to $10^6 M_\odot$. If these protogalaxies also contain a seed black hole of mass $10^4 M_\odot$ in their center, the merger rate for LISA may be as high as one thousand per year.

Same as stellar mass black hole binaries, the coalescence of massive black hole binaries can be divided into three phases: inspiral, merger and ringdown [29, 30]. The inspiral and ringdown phase can be analytically modeled by the post-Newtonian (PN) approximation and the perturbation theory, while a full description of the merger phase requires numerical relativity [31]. During the inspiral phase the two black holes are separated far from each other ($R \gg 4M$) and spiral together with an initial velocity $v/c \sim 0.05$, which can be considered as an adiabatic evolution. Like galactic binaries, LISA will be able to measure the physical parameters during the inspiral phase with very high accuracy. During the emission of gravitational radiations, the two black holes approach each other and the orbit eventually decays to the Innermost Stable Circular

Orbit (ISCO). In Schwarzschild geometry, the ISCO is located at $R_{\text{ISCO}} = 6GM/c^2$, where $M = m_1 + m_2$ is the total mass of the black hole binary.

When their distance becomes shorter than r_{ISCO} , two black holes plunge into each other and their horizons start to merge into one, forming a distorted black hole. During the merger phase the velocity of black holes can reach $v/c \sim 0.5$ and the post-Newtonian approximation breaks down. However, numerical relativity could exploit the precise parameters obtained in the inspiral phase to predict the merger waveform [32]. The merge of two black holes radiates a transient yet extremely energetic burst signal, which features a very high SNR of thousands for mergers of $10^6 M_{\odot}$ at $z = 1$.

At the end of the merger, the merged black hole starts to settle down from an excited state. During this ringdown phase, the excited black hole radiates gravitational waves in a style of damped oscillations. Eventually it will be stabilized into a stable Kerr black hole, which is entirely characterized by the mass and spin angular momentum, as required by the no-hair theorem. This process can be modeled using a linear perturbation theory in Kerr spacetime. The ringdown waveform is given by the superposition of a whole set of quasi-normal modes solved by the perturbation theory [33]. By detecting the damped oscillations from the black hole in the ringdown phase, LISA should be able to confirm if a massive black hole is actually in the galaxy center and identify a Kerr black hole from its mass and spin angular momentum. Also, it is a test of general relativity in a extremely strong gravitational field.

1.3.2.3 Extreme mass ratio inspirals

A particularly interesting class of source for LISA is known as extreme mass ratio inspirals (EMRIs), in which a small compact object is captured by a massive black hole and inspirals into it [34]. The small compact object in a EMRI can be a white dwarf, neutron star or stellar mass black hole, while LISA will probably detect EMRIs with stellar mass black holes mostly. This is mainly because black holes tend to be concentrated to the galactic center due to dynamic mass segregation. Also compared to

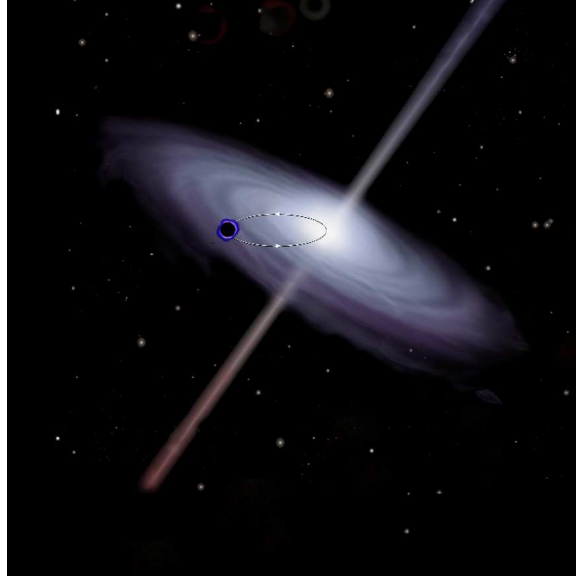


Figure 1-2. Artist's illustration of an EMRI in the center of a galaxy, courtesy of NASA.

EMRIs with white dwarfs or neutron stars, EMRIs with black holes will radiate observable signals with a higher SNR. The formation mechanism of EMRIs is conjectured to be two-body scattering, where a compact object sufficiently close to the galactic center happens to be captured by the massive black hole and subsequently driven onto a highly eccentric orbit (close to 1). As the compact object orbits the massive black hole, gravitational radiation shrinks the orbit and decreases the orbital eccentricity, causing the compact object to spiral in until it is finally disrupted by the tidal force [35].

In the last years of inspiral before plunge, EMRI will be radiating continuously at frequencies to which LISA is sensitive (~ 3 mHz). Due to the extreme mass ratio, the inspiral process is very slow, which makes an individual waveform observable for $\sim 10^5$ cycles/yr [36]. Most abundant EMRIs for LISA detections are believed to consist of a stellar mass black hole of $\sim 10M_{\odot}$ and a massive black hole of $\sim 10^6M_{\odot}$. LISA is capable of detecting such events within $z \sim 1$ and the nearest events in one year may be no further away than $z = 0.1$. Provided the generation mechanism of two-body scattering, the rate of EMRI formations in our Galaxy is approximately one per 4 million years [37]. This generation rate corresponds to a conservative LISA detection rate of 50

per year yet with a large uncertainty due to the weak constraints on stellar populations near galactic nuclei [38].

EMRIs provide an excellent signal to study the Kerr spacetime. Although early EMRI radiations due to highly eccentric orbits are widely discrete in time and thereby unresolvable for LISA, the radiation in the last years of inspiral is believed to faithfully encode the information of the surrounding Kerr spacetime. The motion of the compact object in the Kerr spacetime is geodesic in a short time scale, while for a longer time scale the parameters of the geodesic motion will adiabatically precess due to the orbital circularization. Also, the orbital plane is expected to have Lense-Thirring precession ascribed to the black hole spin. By detecting these intriguing features, LISA should be able to precisely measure the mass and spin angular momentum of the central black hole [39]. If the observed gravitational wave signals are uniquely determined by the measured mass and spin, as required by the no-hair theorem, one can further confirm that the central massive object is a Kerr black hole. If they do not satisfy the no-hair theorem, one can deduce that the central massive object is something else like a boson star [40].

Although the theoretical model of EMRI is seemingly simple due to the extreme mass ratio, the high orbital eccentricity caused by two-body scattering complicates the waveform. So far, the EMRI waveforms still cannot be completely calculated from the perturbation theory. The most common method exploits numerical solutions of Einstein equations in the perturbation theory, known as Teukolsky formalism [41]. In this formalism the field equation describes the perturbative fields in a Kerr metric and a whole set of Teukolsky-based (TB) waveforms have been solved extensively.

1.3.2.4 Cosmic gravitational background radiation

Analogous to the cosmic microwave background (CMB), a stochastic background of gravitational waves with a frequency range of 10^{-18} Hz to high frequencies beyond ~ 10 kHz was produced in the early universe. The primordial gravitational waves

decoupled from matter at the Planck time of $\sim 10^{-43}$ s and traveled through the universe almost without any attenuation or scattering. Therefore, the detection of the cosmic gravitational wave background might be an exclusive way to directly probe the physics in the very early universe. The stochastic background of gravitational waves is usually described in their energy density, which can be expressed as a fraction Ω_{gw} of the critical energy density of the universe. Although the specific value of the energy density is still uncertain, an upper limit has been determined by the constraints from Big Bang nucleosynthesis (BBN), as well as observations to the anisotropy of the CMB and the period of pulsar signals. The observation of COBE to the CMB indicates an upper limit of $\Omega_{\text{gw}} < 10^{-13}$ at 10^{-18} Hz [42].

The stochastic background of gravitational waves may have been generated from the amplification of quantum fluctuations during inflation, which transferred energy into the fluctuations and converted them into gravitational waves. The conventional inflation theory predicts a flat spectrum of Ω_{gw} that is independent of frequencies, which makes the energy density of the inflation-induced background far below the sensitivity of LIGO, LISA ($\sim 10^{-10}$ at 1 mHz) or pulsar timing. However, the actual energy density might still be much higher than the conventional expectation in some variations of the inflation theory [43, 44]. Besides inflation, there are other two mechanisms that may produce stochastic gravitational background: the first-order electroweak phase transition [45, 46] and cosmic strings [47]. Theoretically, these two mechanisms may produce gravitational waves with an observable energy density for LISA in its science band.

1.4 Detection of Gravitational Waves

Theories and observations have indicated that the gravitational wave sources in our universe are numerous and full of information, yet we still lack a reliable tool to measure them. Without direct detections of gravitational radiation from astrophysical systems, gravitational wave astronomy cannot be considered a branch of observational astronomy in the real sense. Starting from 1960s, researchers have been endeavoring in order to

enhance gravitational wave astronomy from “the beginning of knowledge” to “the stage of science”. In this section we will have a review on various detection techniques that have been developed or at least proposed.

1.4.1 Detection Methods

The pioneering detection method, known as the resonant mass detector or the “bar” detector, was proposed and built by Joseph Weber in the early 1960s [2]. A typical bar detector consists of a cylinder made of aluminum with a length of $L \sim 3$ m and a radius of $R \sim 30$ cm. The sensitivity of the bar detector is attributed to the sharp resonance of the cylinder. Bar detectors typically have a resonant frequency of $f_0 \sim 500$ Hz to 1.5 kHz. If the frequency of the gravitational wave is very close (within a few Hz) to the resonant frequency of the bar detector, it will be absorbed and excite mechanical vibrations in the cylinder. In theory, a short gravitational wave burst with a strain h will drive a mechanical vibration with an amplitude $\delta L \sim hL$. For a decent strain amplitude of 10^{-21} , the vibration will have an amplitude of $\sim 10^{-21}$ m. To readout such a tiny oscillation, a series of mechanical oscillation amplifier and resonant transducers are implemented to amplify the oscillation and convert it into a measurable electric signal.

The sensitivity of a well-suspended and isolated bar detector is primarily limited by three intrinsic sources of noise [5, 48]. The first noise source is the thermal noise of the atoms in the cylinder. Compared with Weber’s original design that was operated at room temperature, current detectors are cooled to cryogenic temperatures (~ 100 mK) to reduce the thermal noise. Nevertheless, the thermal noise at this temperature is still too high such that the oscillator is required to have a high mechanical quality factor $Q \sim 10^6$ to further suppress the thermal noise. The second noise source is introduced by the readout chains, such as the electronic noise from the amplifier and transducer, as well as the reverse effect of the transducer that converts the electric signal into an mechanical force applying on the cylinder, known as the back-action noise. The readout noise limits the detector bandwidth within a very narrow range (~ 1 Hz) around

the resonant frequency. The third kind of noise is a quantum effect coming from the zero-point vibrations.

In addition to bar detectors, electromagnetic waves can also be used to precisely measure the change in the coordinate distance between test masses. In an electromagnetic detection the gravitational wave modulates the propagation time of the electromagnetic wave by disturbing the motion of test masses. So far, developed detection methods based on electromagnetic detections fall into three categories:

- Spacecraft ranging
- Pulsar timing
- Interferometry

In the first method, the test masses are Earth and a free-falling spacecraft in geodesic motions. During the detection a communication signal is emitted from the transmitter on Earth and travels to the spacecraft. The spacecraft is usually a scientific probe in a Jupiter or Saturn mission, in order to get a long transmission time ($\sim 2 - 4 \times 10^3$ s). At the spacecraft the signal will be coherently transponded back and returned to Earth. By monitoring the outgoing and returning time of the communication signal, one can deduce the effect of gravitational waves on the signal propagation. Similar measurements under the same principle can be performed by tracking the Doppler shift frequency added onto the communication signal [49], since gravitational waves will induce relative motions between test masses. The fractional change in the communication signal frequency is given by

$$\frac{\Delta\nu}{\nu} = \frac{1}{2} \cos 2\phi [(1 - \cos \theta)h(t) - 2 \cos \theta h(t - l/c - l \cos \theta/c) - (1 + \cos \theta)h(t - 2l/c)], \quad (1-45)$$

where l is the Earth-spacecraft distance at angle θ to the propagation direction on the z-axis. ϕ is the angle between the principle polarization vector of the gravitational wave and the projection of the spacecraft position on the transverse plane. This equation indicates that an impulse in $h(t)$ will appear at three different times in the Doppler shift

frequency, known as the three-pulse response. It should be noted that time delays or Doppler shifts caused by other classical and relativistic effects (e.g., orbital motions, Shapiro time delay, etc.) need to be modeled and subtracted out from the measurement data.

Pulsar timing exploits the extreme regularity of pulsar signals as a timing reference to monitor the time of arrival (TOA) to the Earth. The timing data from pulsars can be analyzed to search for low-frequency gravitational waves [50], especially the upper limit of the energy density of the cosmic stochastic background [51]. The fractional change in the pulse frequency due to gravitational waves is given by

$$\frac{\Delta\nu}{\nu} = \frac{1}{2} \cos 2\phi (1 - \cos \theta) [h(t) - h(t - l/c - l \cos \theta/c)], \quad (1-46)$$

where l is the Earth-pulsar distance at angle θ to the propagation direction on the z-axis. ϕ is the angle between the principle polarization vector of the gravitational wave and the projection of the pulsar position on the transverse plane. In comparison to Eq. 1-45, an impulse in $h(t)$ only appears at two different times in the frequency change, thereby known as the two-pulse response due to the one-way transmission from the pulsar to the Earth.

In data analysis, the actual TOA of radio pulses is compared with a theoretical model based on Eq. 1-46, which yields a timing residual δt . In theory, pulsar timing is capable of detecting gravitational waves on the order of magnitude $h(f) \sim \delta t \cdot f$, where f is the gravitational wave frequency. This gives a strain sensitivity of $10^{-15} - 10^{-16}$ at 10^{-9} Hz. In practical measurements, the data of timing residuals will be correlated between different pulsars with a number of N to enhance the detection sensitivity, which yields $h(f) \sim \delta t \cdot f / \sqrt{N}$. In addition to influences of the intrinsic timing jitter and local instrument noises, the radio pulses also encounter a series of interstellar medium (ISM) effects during the propagation, such as dispersion, scattering, scintillation and refraction, which require additional measurements and analysis to correct them.

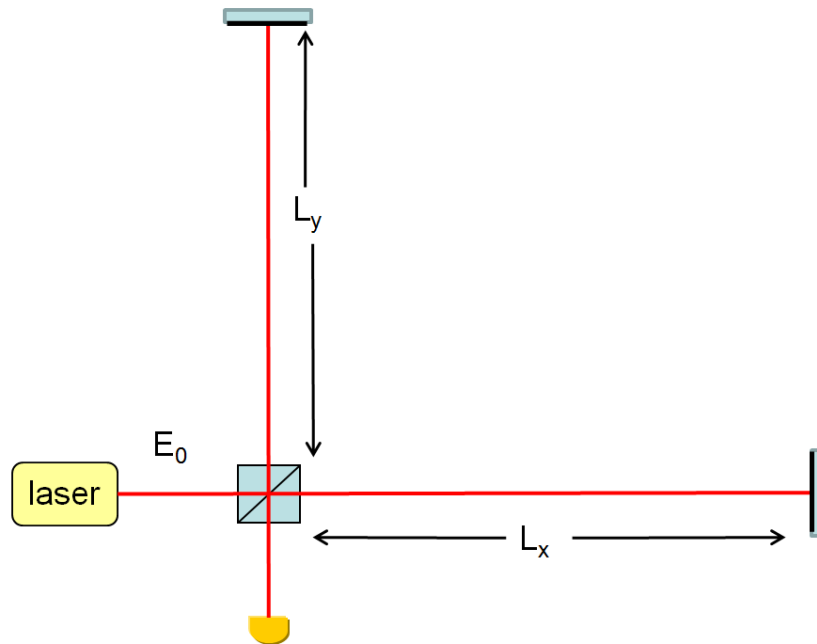


Figure 1-3. Schematic of a basic Michelson interferometer

Under current understanding of gravitational wave detections, the most promising technique is interferometry. Michelson interferometers are inherently ideal gravitational wave detectors ascribed to the application on precise length measurements. Today, a variety of the 1st generation interferometric gravitational wave detectors (LIGO [6], VIRGO [52], GEO [53], TAMA [54]) are in operation and the 2nd generation detectors (Advanced LIGO [6], LCGT [55]) are already in development [56]. Moreover, the space-based interferometric detectors, LISA and conceptualized DECIGO [57], may also be launched in the near future.

1.4.2 Interferometric Detectors

The concept of interferometric detectors is as simple as a Michelson interferometer, as shown in Figure 1-3. A monochromatic laser source emits a beam to the beamsplitter, which separates the beam with equal probability amplitudes. The two interferometer arms have nearly identical lengths and are perpendicular to each other. At the end of each arm, a totally reflective mirror is placed to bounce the beam back. After the round-trip on each arm, the two beams recombine at the beamsplitter and are then

received by the photodetector. The mirrors in a ground-based interferometer are not free-falling due to the suspension to balance the gravity, but they still can be used as test masses since we are only concerned with the horizontal plane. If gravitational waves modulate the arm lengths into L_x and L_y , the laser power received at the photodetector is proportional to

$$|E_{\text{PD}}|^2 = E_0^2 \sin^2[k_L(L_y - L_x)], \quad (1-47)$$

where E_0 is the magnitude of the input electric field and k_L is the wavenumber of the laser. Here we take into account the π phase shift in the reflected beam at the beamsplitter.

1.4.2.1 Principle and configuration

As previously mentioned in Section 1.2.3, the interaction of gravitational waves with interferometric detectors can be evaluated in either the TT frame or the proper detector frame. Here we will briefly review the calculation in the TT frame, where the coordinates of mirrors do not change in the presence of gravitational waves, while the proper distance does. The light round-trip travel time on each arm can be calculated starting from the spacetime interval given by Eq. 1-11 or Eq. 1-27. Here we directly give the result:

$$t_2 - t_0 = \frac{2L_x}{c} + \frac{L_x}{c} h(t_0 + L_x/c) \text{sinc}\left(\frac{\omega L}{c}\right). \quad (1-48)$$

Assuming that the interferometer is on the x-y plane and the gravitational wave $h(t) = h_+ \cos(\omega t)$ only has the plus polarization and is propagating in the z-axis, this equation gives the light round-trip travel time in an arm on the x-axis, where the arm length is L_x . The laser beam is emitted from the beamsplitter at t_0 and returns to the beamsplitter at t_2 . Note that when the frequency of gravitational waves is not too high, i.e., $\omega L/c \rightarrow 0$, the sinc function approaches 1 and the light travel time approaches $(2L_x + L_x h(t))/c$. However, when the frequency of gravitational waves is either too high ($\omega L/c \gg 1$) or at multiples of $\pi c/L$, the sinc function equals to zero and the interferometer is insensitive to such gravitational waves. The multiples

of $\pi c/L$ in the angular frequency are therefore called interferometer nulls. Since the arm length of current ground-based detectors is on the order of \sim km, interferometer nulls have no influence on their detection performance. However, the sensitivity of space-based detectors such as LISA and DECIGO with a much longer arm length might be compromised at these frequencies.

The light round-trip travel time in the other interferometer arm can be obtained in a similar form. From the light travel times we can write down the returning electrical fields at the beamsplitter and then the total electric field received at the photodetector is given by

$$E_{PD}(t) = -iE_0 e^{-i\omega_L(t-2L/c)} \sin[\phi_0 + \Delta\phi(t)], \quad (1-49)$$

where $L \equiv (L_x + L_y)/2$ is defined as the common arm length and $\phi_0 = k_L(L_x - L_y)$ is the intrinsic phase difference due to the arm length mismatch. $\Delta\phi(t)$ comes from the modulations from gravitational waves and is given by

$$\begin{aligned} \Delta\phi(t) &= h_+ k_L L \operatorname{sinc}\left(\frac{\omega L}{c}\right) \cos[\omega(t - L/c)] \\ &\approx h_+ k_L L \cos[\omega(t - L/c)]. \quad (\text{for } \omega L/c \ll 1) \end{aligned} \quad (1-50)$$

From the purpose of detection, $\Delta\phi(t)$ should be as large as possible, which requires the design of interferometers to be optimized. In other words, in the phase shift the factor

$$k_L L \operatorname{sinc}\left(\frac{\omega L}{c}\right) = \frac{k_L}{k} \sin\left(\frac{\omega L}{c}\right) \quad (1-51)$$

should reach the maximum. Therefore, we require $\omega L/c = n\pi/2$, or the arm length needs to be at least $\lambda/4$, where λ is the wavelength of gravitational waves. Unfortunately this is a problem for most gravitational wave sources: For a gravitational wave at \sim 100 Hz, the optimized arm length is \sim 750 km, which is an unrealistic requirement for current ground-based detectors.

The solution for ground-based detectors is an overcoupled Fabry-Perot cavity. A Fabry-Perot cavity that consists of two low-transmissivity mirrors is capable of trapping the photons inside for a certain amount of time and then substantially increases the effective arm length. In theory, the storage time, which is the average time for a photon trapped inside the cavity, is given by

$$\tau_s \approx \frac{L \mathcal{F}}{c \pi}, \quad (1-52)$$

where L is the cavity length and \mathcal{F} is the finesse of the cavity. Compared to a simple Michelson interferometer, the effective arm length is enhanced by a factor of $(2/\pi)\mathcal{F}$. For ground-based detectors the typical finesse is $\sim 10^2$. In the presence of a Fabry-Perot cavity on each arm, the phase shift due to gravitational waves is given by

$$\Delta\phi(f) \approx h_+ \frac{4\mathcal{F}}{\pi} k_L L \frac{1}{\sqrt{1 + (f/f_p)^2}}, \quad (1-53)$$

where $f_p = 1/(4\pi\tau_s)$ is called the pole frequency of the Fabry-Perot cavity.

In practice, an interferometric detector will encounter various realistic issues that need to be addressed. First, laser beams must have spatial profiles that are not ideal plane wavefronts in the transverse direction. The best choice of a profile is a Gaussian beam, which corresponds to the TEM_{00} mode from the spatial Hermite-Gaussian solutions of the paraxial wave equation. The advantage of a Gaussian beam is the spherical wavefront that can be mode-matched to spherical-shaped mirrors. For interferometric detectors, the laser is required to be overwhelmingly operating at the TEM_{00} mode and the other higher modes that cause noises must be minimized. In addition to careful alignments, the laser field is first sent into another Fabry-Perot cavity known as the mode cleaner before enters the beamsplitter, ensuring that only the TEM_{00} mode is on resonance and transmitted to the mirrors. A second mode cleaner is placed between the beamsplitter and the photodetector to further filter out the higher modes. Another important issue is to make sure every Fabry-Perot cavity is operating

on resonance. The solution is known as the Pound-Drever-Hall (PDH) technique which locks the laser to the resonant frequency of the cavity via feedback control. We will see more details of the PDH technique in Section 2.2.2.1.

1.4.2.2 Noise limitations

The main noise sources of an interferometric detector can be classified into two categories: The first class comes from the quantization of light, including the shot noise and the radiation pressure noise. They jointly determine the standard quantum limit (SQL) of interferometric detectors. The second class involves noise sources from internal Brownian motions or other external effects, which manifest themselves as a displacement noise in the measurement.

- Shot noise - The limited number N of photons received per second by a photodiode will cause a standard deviation given by \sqrt{N} in the number of photons. The observed power fluctuation is then given by

$$\delta P_{\text{shot}} = \frac{\sqrt{N}\hbar\omega_L}{T} = \sqrt{\frac{\hbar\omega_L}{T}P}. \quad (1-54)$$

This power fluctuation will couple into the readout of the interferometer output. When represented in the strain sensitivity, it is given by

$$S_{\text{shot}}^{1/2}(f) = \frac{1}{8\mathcal{F}L} \sqrt{\frac{4\pi\hbar\lambda_L c}{\eta P_{\text{bs}}}} \sqrt{1 + (f/f_p)^2}, \quad (1-55)$$

where $P_{\text{bs}} = CP_0$ is the power entering the beamsplitter after power recycling and η is the efficiency of the photodiode. Therefore, in the frequency domain the shot noise floor is flat until $f = f_p$ and then increases with a f slope, dominating the high frequency range above ~ 100 Hz. Also, increasing the laser power to accumulate more photons per second will help to reduce the shot noise.

- Radiation pressure noise - On the other hand, a too large number of photons may also cause a problem. When the photons strike the mirror they will exert a continuous radiation pressure by transferring a momentum $2\hbar\omega_L/c$. The radiation pressure is then given by $F = 2P/c$ which comes with fluctuations due to the variations in the power. From Eq. 1-54, the uncertainty in the radiation pressure is then given by

$$S_{\text{rad}}^{1/2} = 2\sqrt{\frac{2\hbar\omega_L P}{c^2}}. \quad (1-56)$$

This force fluctuation can be converted into a displacement noise in the mirror via the Laplace transform of $F = M\ddot{x}$, where M is the mass of the mirror. When the radiation pressure noise couples into the readout, the strain sensitivity is given by

$$S_{\text{rad}}^{1/2}(f) = \frac{16\sqrt{2}\mathcal{F}}{ML(2\pi f)^2} \sqrt{\frac{\hbar P_{\text{bs}}}{2\pi \lambda_L c}} \frac{1}{\sqrt{1 + (f/f_p)^2}}. \quad (1-57)$$

This equation shows that in addition to square root of the laser power, the radiation pressure noise is also proportional to the finesse of the arm cavity.

- Seismic noise - Ground mechanical vibrations are the limit for ground-based detectors in the frequency range below ~ 10 Hz. The seismic noise represented as a displacement noise is approximately on the order of

$$\delta L_{\text{seismic}} \sim 10^{-7} \left(\frac{1 \text{ Hz}}{f^2} \right) \text{ m Hz}^{-1/2}. \quad (1-58)$$

The mitigation of seismic noise in the mirror is realized by sophisticated isolation and suspension systems. In the suspension system, a set of N pendulums are placed in cascade to filter out the high frequency noise with a transfer function of $(f_0^2/f^2)^N$, where f_0 is the resonance frequency of the pendulum.

- Gravity gradient noise - The local Newtonian gravitational field can vary due to the environment change, such as the time-varying tidal force or fluctuations in the mass density from near sources. Since the gravitational force cannot be screened, the gravity gradient noise cannot be attenuated. However, it decreases rapidly at high frequencies and is not dominant at low frequencies for current ground-based detectors. Gravity gradient noise will be the ultimate sensitivity limit for the next generation ground-based detectors to pursue.
- Thermal noise - Thermal vibrations in the suspended pendulum and the mirror will both couple into the measurements. The dominant noise in the frequency range $\sim 10 - 10^2$ Hz is the Brownian thermal noise of the mirror coating. In addition, the thermal fluctuations in the suspension will induce spurious motions of the mirror in both horizontal and vertical directions. The normal modes of the suspension wire may also be present in the frequency spectrum as very narrow peaks.

As an example, the sensitivity curve of LIGO is illustrated in Figure 1-4. The figure shows that at about 100 Hz the strain sensitivity reaches its maximum of $\sim 3 \times 10^{-23} \text{ Hz}^{-1/2}$. At higher frequencies the sensitivity curve increases moderately with a f slope due to the shot noise limit. For frequencies in the range from ~ 40 Hz to ~ 100 Hz the sensitivity is mainly dominated by the coating thermal noise on the test mass. For frequencies below ~ 40 Hz the most drastic change happens: The seismic

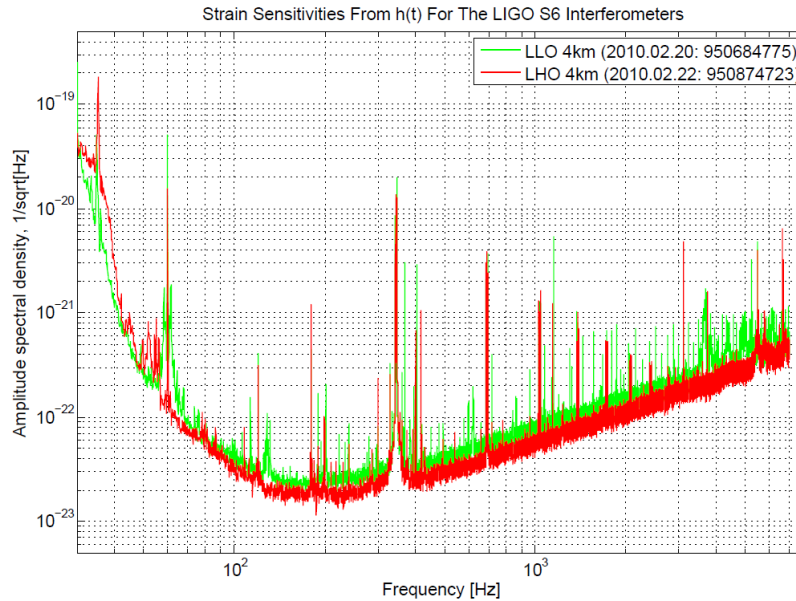


Figure 1-4. Strain sensitivities of LIGO S6, courtesy of LIGO.

noise dominates the low frequency region and sensitivity sharply drops. Advanced LIGO will utilize much better isolation schemes; nevertheless, the corner frequency where the seismic noise starts to dominate will still be around 10 Hz, which makes the detection of low-frequency gravitational waves impossible for ground-based detectors.

For an absolute isolation from seismic noise, the only feasible way is to place the interferometer into space. The first space-based interferometric detector project is Laser Interferometer Space Antenna (LISA) [7, 8], which is aimed to detect gravitational waves between 3×10^{-5} Hz and 1 Hz. Another proposed space-based interferometric detector, Deci-hertz Interferometer Gravitational Wave Observatory (DECIGO) [57], will detect gravitational waves mainly between 0.1 Hz and 10 Hz to bridge the frequency gap between LISA and ground-based detectors. DECIGO will synthesize the constellation design of LISA (See the next chapter for details of LISA), yet with much shorter arm lengths of 1000 km such that LIGO-like Fabry-Perot interferometers can be used as arm cavities. The interferometry used in LISA, on the other hand, is quite different from

standard Michelson interferometry used in ground-based detectors. We will focus on the LISA technology in the next chapter.

CHAPTER 2 LASER INTERFEROMETER SPACE ANTENNA

2.1 Overview

The Laser Interferometer Space Antenna (LISA) is a collaborative NASA/ESA space mission to detect gravitational waves in the frequency range of 3×10^{-5} Hz to 1 Hz [58]. It will be the first space-based interferometric gravitational wave detector to be launched in 2020s. Unlike the equal-arm Michelson interferometer configured in standard ground-based interferometric gravitational wave detectors, LISA consists of three identical spacecraft trailing the earth by about 20° in independent heliocentric orbits, arranged in a quasi-static equilateral triangle, as shown in Figure 2-1. The arm length between each two spacecraft is approximately 5 Gm and varies by up to $\pm 1\%$ over the 10-year lifetime of the mission. This time-dependent variation in arm length is mainly caused by the different gravitational pull of Earth on the individual spacecraft. This motion also Doppler shifts the frequency of the received lasers used to perform the interferometry.

Each spacecraft houses two drag-free proof masses that follow the geodesic motion. A housing around the proof mass functions as a sensor to detect the relative position between the proof mass and the spacecraft. The Disturbance Reduction System (DRS) controls the thrusters on the spacecraft and minimize the acceleration of the proof mass due to undesired external forces. The Interferometric Measurement System (IMS) of LISA monitors changes in the separation between two proof masses on each respective spacecraft. Any modulation on the separation caused by gravitational waves and other spurious accelerations of the proof masses will be measured via interferometry with the desired sensitivity.

LISA will use 1064 nm lasers with an output power of approximately 2 W. The transmitted laser field has a significant diffraction loss due to the long arm length, therefore only a very small portion of light (~ 100 pW) will be received by the photodetector

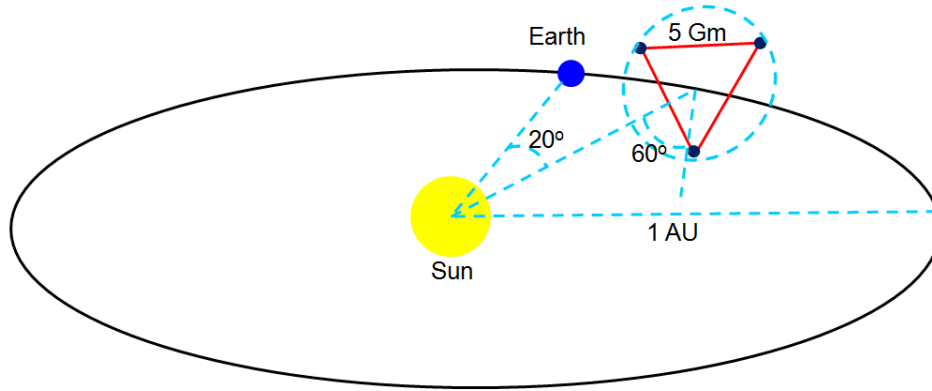


Figure 2-1. The heliocentric orbit of the LISA constellation. The constellation trails the Earth by 20° and the plane of it is inclined with respect of the elliptic by 60° . The arm length between each two spacecraft is generally 5 Gm.

on the far spacecraft. For this reason, the laser field emitted from the far spacecraft transponds the received laser phase through a heterodyne phase-locked loop with an offset frequency in the range of 2 – 20 MHz. When the laser field from the far spacecraft is transmitted back to the local spacecraft it will be superimposed with the local laser field to generate a beat signal. A digital phasemeter will measure the phase of this interferometer output with sufficient precisions ($\sim \mu\text{cycles Hz}^{-1/2}$), in order to extract the gravitational wave signals during the post-processing [59].

2.1.1 Sensitivity

The sensitivity requirement of LISA is usually represented by the linear spectral density (LSD) of the gravitational wave strain amplitude, $\sqrt{S_h(f)}$, which is plotted in Figure 2-2. The strain is proportional to changes in the separation between two proof masses, which is also known as the single link equivalent position uncertainty $\delta L_{\text{single link}}(f)$. Mathematically, the strain sensitivity is given by

$$\sqrt{S_h(f)} = \sqrt{5} \frac{2}{\sqrt{3}} T(f) \frac{\delta L_{\text{single link}}(f)}{L}. \quad (2-1)$$

In Eq. 2-1, $\sqrt{5}$ represents the averaged antenna response over the whole sky. $\frac{2}{\sqrt{3}} = 1/\sin(60^\circ)$ is the projection of the equilateral triangular constellation onto an

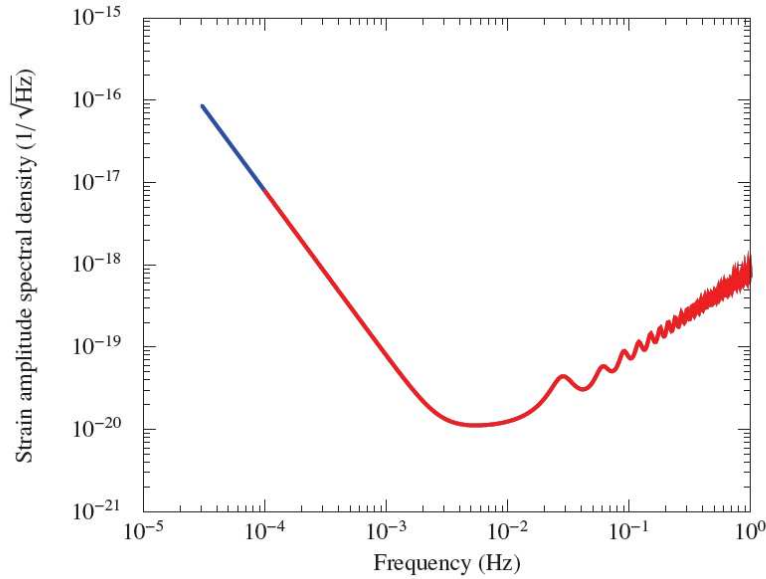


Figure 2-2. The LISA sensitivity curve describes the strain amplitude spectral density versus frequency. The red curve represents the requirement on the strain sensitivity (10⁻⁴ Hz to 1 Hz) and the blue curve is the extended goal (3 × 10⁻⁵ Hz to 1 Hz). Adapted from Ref [60]: *LISA: Unveiling a hidden universe: Assessment study report*.

equivalent L-shaped Michelson interferometer. $T(f)$ is the instrument transfer function, which converts the single link equivalent position uncertainty into the strain response to gravitational waves with different frequencies, assuming that the LISA constellation will form the Michelson X-combination for Time Delay Interferometry (TDI).

Recall the interferometer response of a Michelson interferometer to gravitational waves, as we discussed in Section 1.4.2.1. The instrument transfer function of LISA can be understood in a very similar way: It is basically flat at low frequencies, which indicates the instrument sensitivity is independent of the gravitational wave frequency if it is low enough. At high frequencies $f_{\text{GW}} > \frac{c}{2L}$, the instrument sensitivity gradually decreases with a slope of f as the frequency of the gravitational wave increases. Especially at frequencies where the arm length is exactly multiples of half of the gravitational wave wavelength, the LISA arm has zero response for gravitational waves with normal incidence. At these interferometer nulls the averaged sensitivity further

decreases (by about a factor of 2) but never goes down to zero [61], since gravitational waves with the same frequency while from different sources have different incident directions onto LISA.

Based on the noise budget described in Ref [60], the single link equivalent position uncertainty $\delta L_{\text{single link}}(f)$ is limited at low frequencies by acceleration noise $\delta x_{\text{DRS}}(f)$ caused by spurious residual forces that act on the proof masses. At high frequencies, it is limited by sensing noise and displacement noise $\delta x_{\text{IMS}}(f)$ generated inside the interferometric measurement system. The combined noise limitation is then given by the sum of the power spectral density (PSD) of these two uncertainties, i.e.,

$$\delta L_{\text{single link}}(f) = \sqrt{\delta x_{\text{DRS}}^2(f) + \delta x_{\text{IMS}}^2(f)}. \quad (2-2)$$

The specific expressions of the allocated acceleration noise and the path length noise are

$$\delta x_{\text{DRS}}(f) \approx \frac{3 \text{ fm/s}^2}{(2\pi f)^2 \sqrt{\text{Hz}}} \sqrt{1 + \left(\frac{f}{8 \text{ mHz}}\right)^4} \sqrt{1 + \left(\frac{0.1 \text{ mHz}}{f}\right)^4} \quad (2-3)$$

and

$$\delta x_{\text{IMS}}(f) \approx \frac{18 \text{ pm}}{\sqrt{\text{Hz}}} \sqrt{1 + \left(\frac{2.8 \text{ mHz}}{f}\right)^4}, \quad (2-4)$$

where the magnitudes of $\sim 3 \text{ fm}/(\text{s}^2 \cdot \sqrt{\text{Hz}})$ and $\sim 18 \text{ pm}/\sqrt{\text{Hz}}$ are respectively the total noise budgets of the DRS and the IMS. Both have a 35% margin over the total subsystem allocations. A substantial contribution to the displacement noise in the IMS is attributed to the shot noise at photodiodes. Given a typical 100 pW received power at photodiodes, the shot noise budget is given by

$$\delta x_{\text{shot}} = \frac{\lambda}{2\pi} \sqrt{\frac{h\nu}{P}} \approx \frac{7 \text{ pm}}{\sqrt{\text{Hz}}}. \quad (2-5)$$

2.1.2 Disturbance Reduction System

As a gravity laboratory and interferometric gravitational wave detector, LISA has to contain test masses whose motion is purely determined by the surrounding spacetime

geometry, or at least be free-falling in the directions of interest. The main objective of the Disturbance Reduction System is to provide such a drag-free environment for the proof masses by isolating them from random external forces, as well as maintain the spacecraft centered on the proof masses via micro-Newton thrusters. Possible random external forces that may cause spurious acceleration noise include solar radiation pressure, interplanetary magnetic fields, gravity, electrostatic and magnetic disturbances from the spacecraft, time-variable gas pressure due to temperature fluctuations, etc.

To maintain the proof mass to follow the geodesic motion, each spacecraft is loaded with two Gravitational Reference Sensors (GRS's) [62], each mounted in the line of sight to the telescope. Each GRS provides a housing that contains electrodes to enclose a proof mass and monitor its position individually. The electrodes are arranged in a certain pattern such that all possible relevant displacements and rotations of the proof mass can be read out by measuring the capacitance between the proof mass and the housing, known as capacitive sensing [63, 64]. The measurement sensitivity of capacitive sensing is on the level of $1.8 \text{ nm Hz}^{-1/2}$ for displacements in sensitive directions and $200 \text{ nrad Hz}^{-1/2}$ for rotations. By applying AC voltages on the electrodes, the orientation and position of the proof mass in the non-sensitive directions can be appropriately controlled.

The proof mass of LISA is an alloy cube (73% gold and 27% platinum) with a mass of 1.96 kg and dimension of 46 mm. This mixing ratio was chosen to minimize the magnetic susceptibility of the proof mass to $|\chi| < 2 \times 10^{-5}$ [65, 66]. Nevertheless, the non-zero magnetic susceptibility requires strict magnetic cleanliness of the spacecraft. The surfaces of the proof masses are coated with a golden layer to increase the reflectivity for the short arm interferometry.

As a precursor of the LISA mission, LISA Pathfinder will be launched in the 2010s [67]. The LISA Pathfinder mission will test the technique of drag-free operations, including the identical GRS and similar test mass interferometers (see the next section),

etc. The requirement of the residual acceleration noise of the test masses on LISA Pathfinder is relaxed by about a factor of 10 compared to LISA.

2.1.3 Interferometric Measurement System

The Interferometric Measurement System monitors the fluctuations in the separation between two proof masses on different spacecraft. The IMS is composed of three subsystems: the optical system, the laser system and the phase measurement system. In this section we will focus on the optical system of LISA, also known as an optical assembly housed by each spacecraft. Each optical assembly consists of a pair of units and each unit consists of an optical bench, a telescope and a GRS. The telescopes are pointing to the other two spacecraft individually. The optical bench is parallel to the primary mirror of the telescope such that the optical bench is perpendicular to the plane of the LISA constellation, whereas the GRS is mounted behind the optical bench.

As the main part of the optical system, the optical bench directs the laser beams to the desired spatial positions for interferences. The separation between two proof masses is monitored through the combination of three different interferences generated on the optical bench, which is illustrated in Figure 2-3. All the interferometric measurements in LISA are heterodyne detections, where the two laser beams with close frequencies ($\Delta\nu \sim 2\text{--}20$ MHz) generate a heterodyne beat signal to be measured by a photodetector. The photodetector LISA will use are quadrant photodetectors (QPD's) that can detect the heterodyne phase as well as the angles of the wavefront. This is known as differential phase sensing or wavefront sensing [68]. As shown in Figure 2-4:

- A local laser beam is transmitted from the local laser into the optics through an optical fiber.
- An adjacent laser beam is transmitted from the adjacent bench through another optical fiber known as the back-link fiber.
- A far laser beam is transmitted from the far spacecraft through the telescope.

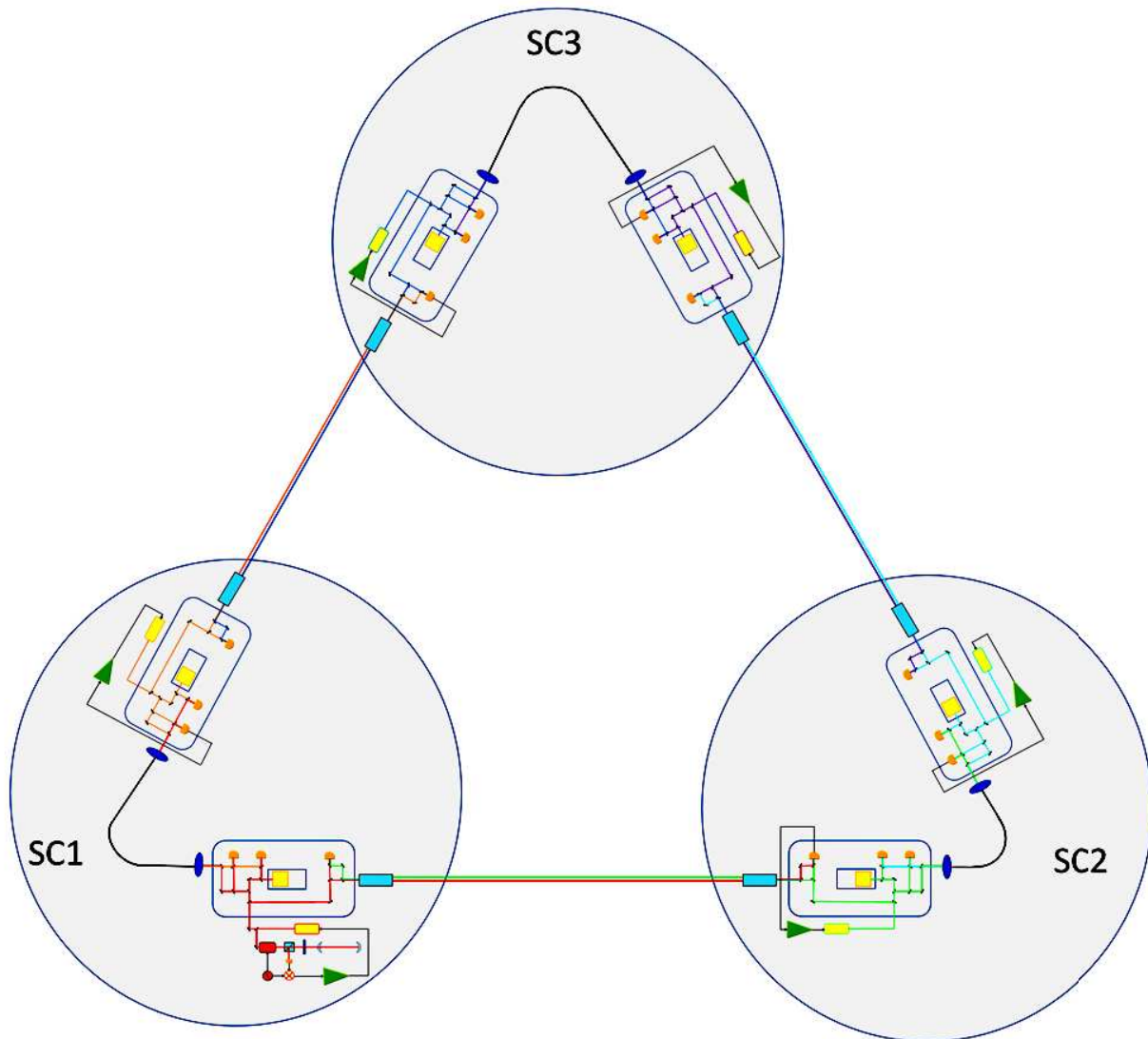


Figure 2-3. The Interferometric Measurement System of LISA. Each spacecraft houses two optical benches, which transmit/receive laser beams to/from the other two spacecraft via telescopes, forming six one-way links. In this diagram one laser (the “red” laser) on SC_1 is used as the master laser, which is pre-stabilized to an optical cavity. The other five lasers are phase-locked either locally to the master laser via the back-link fiber or using the beat signal with the far laser via optical transponders. The distance between two proof masses on each arm is monitored by three distinct measurements: one measurement between optical benches (long arm) and two measurements between each proof mass and its respective optical bench (short arm + reference).

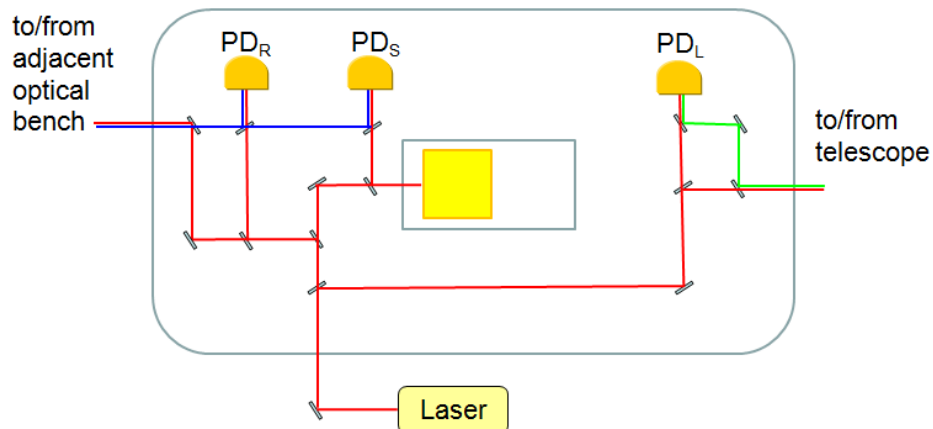


Figure 2-4. Interferometers on the optical bench of LISA. The interferometry used in LISA is heterodyne detections, where two lasers with close frequencies are combined to generate a beat signal with its phase detected at the photodetector. On each optical bench three interferometers are constructed using three photodetectors and their measurements are combined to measure the distance between two proof masses on each arm. Note that this is just an oversimplified diagram to illustrate the interferometers, whereas there are also non-interferometric beams propagating through the optical bench. Also, the GRS and its housed proof mass are actually not in the plane of the optical bench.

Figure 2-3 shows that the adjacent beam and the original local beam generate a heterodyne interference at the photodiode PD_R , which measures the relative phase noise of the two lasers and the additional noise introduced by the back-link fiber. This measurement is known as the reference measurement. The adjacent beam is also superimposed onto the local beam that is reflected off from the proof mass. This interference that occurs at the photodiode PD_S is monitored as the short arm measurement, which contains the fluctuation information of the distance from the proof mass to the optical bench [69]. Therefore, the short arm interferometer of LISA is also called the test mass interferometer, where the readout can be sent to the DRS to actively control the motion of the proof mass in corporation with capacitive sensing. The third kind of interference that occurs between the local beam and the received and delayed far beam is recorded by the photodiode PD_L . This beat note carries the

fluctuation information of the LISA long arm length from a local optical bench to a far optical bench, which is known as the long arm measurement. Since the long arm interferometer is used to detect the length fluctuations due to gravitational waves, it is also referred to as the science interferometer. Therefore, we can write down the photodiode readouts of these three interferences:

- Reference measurement: $\varphi_R(t) = \Phi_l(t) - \Phi_a(t) + N_a(t)$
- Short arm measurement: $\varphi_S(t) = \Phi_l(t) - \Phi_a(t) + \frac{2\pi}{\lambda} \Delta L_{pm}(t) + N_a(t)$
- Long arm measurement: $\varphi_L(t) = \Phi_l(t) - \Phi_f(t - \tau_{ji}(t)) + N_{Trans}(t - \tau_{ji}(t)) + h_{ji}(t)$.

In the above expressions other uncorrelated noise such as shot noise introduced at the photodiode and the technical noise introduced at the phasemeter ADCs are ignored. $\Phi_l(t)$, $\Phi_a(t)$ and $\Phi_f(t)$ are the phases of the local beam, the adjacent beam and the far beam, respectively. $N_a(t)$ contains the noise in the back-link fiber. $\Delta L_{pm}(t)$ is the relative position between the proof mass and the optical bench. The light travel time from SC_j to SC_i $\tau_{ji}(t)$ is a function of time ascribed to the relative motion between spacecraft. The transponder noise, $N_{Trans}(t)$, primarily includes the phase-locked loop noise from far spacecraft. $h_{ji}(t)$ is the phase fluctuation due to the incident gravitational wave strain applied on the LISA long arm length (optical bench to optical bench).

Although the laser phase noise dominates in all three measured phases, the linear combination of the reference measurement and the short arm measurement, $\varphi_S(t) - \varphi_R(t)$, eliminates the laser phase noise in $\Phi_l(t)$ and $\Phi_a(t)$, as well as the additional noise $N_a(t)$. Thus the only remaining term $\frac{2\pi}{\lambda} \Delta L_{pm}(t)$ represents the relative position of the proof mass.

However, a more complicated version of this noise cancellation scheme is used for the case of long arm interferometry, where the existence of delay time prevents the laser phase noise from being automatically eliminated. Due to the significant inequality between arm length which varies over time, the laser phase noise on two long arms becomes uncorrelated and no longer cancels out in a standard Michelson

combination, not to mention that the transponder noises on two long arms are intrinsically uncorrelated. The technique to solve this problem is known as Time Delay Interferometry [70, 71]. As a post-processing algorithm, TDI synthesizes equal-armed Michelson interferometry by time-shifting the interferometry signal data properly such that the laser phase noise, clock transfer noise, bench motion, etc., are canceled out in certain linear combinations. More details of TDI will be seen in the next section.

In addition to the three basic interferometers described above, the optical bench also includes the point-ahead angle mechanism (PAAM). The PAAM ensures that in the long arm interferometry the direction of the transmitted beam is not changed when received by the far photodetector due to the transverse relative motion of the spacecraft. The transverse component of the velocity is time-dependent; therefore, the PAAM is required to be an on-board technique to correct the time-varying deviation angle. It is estimated that this time-varying angle will accurately track the orbital motion of the constellation. Consequently, the correction mechanism can be implemented before launch and a feedback control loop is not necessary.

The telescope is another crucial component of the optical assembly that is used to transmit laser fields in the long arm interferometry. The telescope for LISA will use an off-axis Cassegrain reflector design with a magnification of 80 \times . Each telescope is pointing to the corresponding far spacecraft to gather the incoming beam (~ 100 pW) as well as to expand and collimate the outgoing beam (~ 1 W). The laser beam from the local optical bench will be focused onto the secondary mirror, where it is magnified and reflected to the primary mirror. From the primary mirror the collimated beam will be sent to the far optical bench, where a reverse process will be performed. The design of the telescope determines the power of the received beam and thereby the shot noise limit for the IMS. The mechanical stability of the pathlength between the primary and the secondary mirror is critical as the pathlength noise will directly enter the readout of the

long arm interferometer. Given the total IMS noise budget of $18 \text{ pm Hz}^{-1/2}$, the required pathlength stability for the telescope is no more than $1 \text{ pm Hz}^{-1/2}$.

2.2 Noise Cancellation for LISA

LISA will use lasers with a wavelength of probably around $1 \text{ }\mu\text{m}$. The laser will have to have frequency actuation capabilities sufficient to meet the LISA frequency noise requirements. For quite a long time, the laser frequency control has been a significant and complicated topic in studies on the long arm interferometry. In a laser interferometric measurement, the laser frequency noise is required to cause an equivalent noise no higher than the quantity to be measured. In the IMS noise budget, the allocated pathlength noise for the laser frequency is $2 \text{ pm Hz}^{-1/2}$, corresponding to a laser phase noise below $1.2 \times 10^{-5} \text{ cycles Hz}^{-1/2}$ or a laser frequency noise below $5.6 \times 10^{-6} \text{ Hz Hz}^{-1/2}$. Since the arm lengths of the LISA constellation are inherently unequal to each other and also time-varying, the laser frequency noise does not cancel out in a standard Michelson-like way. In comparison, the typical frequency noise of a free-running laser is on the level of $10 \text{ kHz}/f \text{ Hz Hz}^{-1/2}$, which requires the laser frequency noise to be reduced by more than 12 orders of magnitude at 3 mHz.

Current understanding of the laser frequency control gives a three-level approach to mitigate the frequency noise [72]. The first two steps are active stabilization techniques and the third step is a post-processing technique. The laser frequency will first be actively stabilized to a local reference on spacecraft (pre-stabilization), then stabilized to the LISA arm (arm locking) and finally get canceled out to the requirement in the post-processing (TDI).

2.2.1 Time Delay Interferometry

The concept of Time Delay Interferometry (TDI) is to synthesize interferometry (TDI observables) by linearly combining phase measurements of single links and appropriately time-shifting the measurement data during post-processing [11, 73]. As an algorithm in the time domain, TDI is capable of eliminating the laser phase

noise, differential clock noise and spacecraft motions in the long arm interferometry while maintaining the phase fluctuations due to gravitational wave strains. The noise suppression performance of TDI is primarily limited by the arm length knowledge, which determines the light travel time used for accurately time-shifting and fractional delaying the measurement data.

The TDI algorithm that assumes fixed arm length between spacecraft, also known as the first generation TDI or “TDI 1.0”, only exploits the phase measurements delayed by the respective propagation distance to form TDI observables. The second generation TDI or “TDI 2.0” takes the time-varying arm length caused by spacecraft relative motions into account by time-shifting the phase measurements by multiples of the propagation distance [70, 74]. A “TDI 3.0” algorithm which includes the relative accelerations between spacecraft has also been conceptualized, but is unnecessary to meet the LISA noise budget. The individual phase measurement can be linearly combined to form various TDI observables, such as an unequal-armed Michelson interferometer (X combination) or a Sagnac interferometer (ζ combination). In this section we will introduce the basic Michelson X-combination with fixed arm length to explain the noise cancellation in TDI.

2.2.1.1 Michelson X-combination

The Michelson X-combination exploits the phase measurements on four links to form an equal-armed Michelson interferometer. It should be noted that the phase-locking on the far spacecraft (or correlation between lasers) is not necessary for any kind of TDI combinations; however, using optical transponders could simplify the Michelson X-combination such that only the two phase readouts on SC_1 are required. As shown in Figure 2-5 (left), SC_1 is used as the local spacecraft located at the vertex. Since the two lasers on SC_1 are phase-locked to each other via the back-link fiber, the local spacecraft can be considered as the beamsplitter that generates two in-phase coherent beams in a standard Michelson interferometer. The laser field $\Phi_1(t)$ emitted from SC_1 propagates

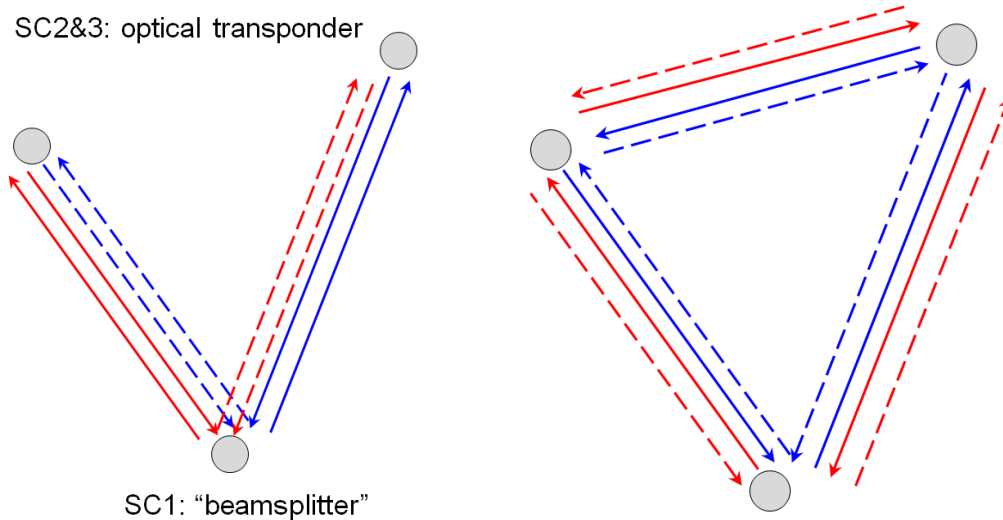


Figure 2-5. (Left) The Michelson X-combination in static TDI, where SC_1 is used as a beamsplitter to generate two coherent beams and the laser beams transmitted from SC_2 and SC_3 resemble the coherent light back reflected from mirrors in a Michelson interferometer. In post-processing the beat signals are delayed by a virtual round-trip travel time on the other arm, which is illustrated as the dashed line. (Right) The Sagnac combination in static TDI, where two coherent beams are transmitted from SC_1 following a clockwise and counterclockwise closed trajectory. Due to the rotation of the constellation, a travel time difference of $\sim 47 \mu\text{s}$ is generated. Similar post-processing will be used to cancel out the laser frequency noise, clock noise, etc.

through the long arm 1-2 and 1-3 individually and phase-locks the far laser on SC_2 and SC_3 . Therefore, the laser field transmitted from SC_2 and SC_3 resembles the coherent light back reflected from mirrors in a Michelson interferometer. If we assume that the far-end PLL yields a phase noise $\varphi_{\text{PLL}i}(t)$, $i = 2, 3$, the phase measurement of the heterodyne interferometry on SC_1 is given by

$$S_i(t) = \Phi_1(t) - \Phi_1(t - \tau_{1i} - \tau_{i1}) + \varphi_{\text{PLL}i}(t - \tau_{i1}) + h_{1i}(t - \tau_{i1}) + h_{i1}(t), \quad (2-6)$$

where τ_{ij} is the one-way light travel time from SC_i to SC_j , $h_{1i}(t)$ and $h_{i1}(t)$ are phase perturbations from gravitational waves. The linear combination of Michelson X is given by

$$X(t) = S_2(t) - S_3(t) - S_2(t - \tau_{13} - \tau_{31}) + S_3(t - \tau_{12} - \tau_{21}). \quad (2-7)$$

The additional terms can be interpreted as the beat signal $S_i(t)$ on SC_1 delayed by a virtual round-trip travel time on the other arm, which is illustrated as the dashed line in Figure 2-5 (left). If we substitute Eq.2-7 with Eq.2-6, all phase noise terms are canceled out. In principle, this algorithm reconstructs an equal-armed Michelson interferometer and extract the common phase noise out of seemingly uncorrelated phase measurements. The residual transponder noise from the far-end PLL will also be measured on the far spacecraft. It is then appropriately time-shifted and subtracted from the X-combination. Similar procedures will also be made for the removal of clock noise, bench motion, back-link fiber noise, etc. On the other hand, the phase perturbations from gravitational waves will be maintained in the post-processed signal, yielding

$$\begin{aligned}
X(t) = & h_{12}(t - \tau_{21}) + h_{21}(t) - h_{13}(t - \tau_{31}) - h_{31}(t) \\
& - h_{12}(t - \tau_{21} - \tau_{13} - \tau_{31}) - h_{21}(t - \tau_{13} - \tau_{31}) \\
& + h_{13}(t - \tau_{31} - \tau_{12} - \tau_{21}) + h_{31}(t - \tau_{12} - \tau_{21}). \tag{2-8}
\end{aligned}$$

Briefly speaking, the deduction from Eq. 2-6 to Eq. 2-8 demonstrates the basic post-processing technique to extract gravitational waves from LISA readouts.

2.2.1.2 Sagnac combination

Another notable TDI observable is the Sagnac combination, which uses the LISA signals to form a Sagnac interferometer [75]. A standard Sagnac interferometer consists of a beamsplitter to generate two coherent beams, which propagate around a closed loop in opposite directions and then are recombined at the beamsplitter. In LISA, six links from three spacecraft are used to construct a Sagnac combination. As shown in Figure 2-5 (right), the two coherent beams are transmitted from SC_1 following a clockwise and counterclockwise trajectory, respectively. Since the LISA constellation is not static due to the rotation, a light path difference ΔL between the two propagations in

opposite directions is generated. This is known as the Sagnac effect:

$$\Delta L = L_{12} + L_{23} + L_{31} - (L_{13} + L_{32} + L_{21}) = \frac{4\boldsymbol{\Omega} \cdot \mathbf{A}}{c}. \quad (2-9)$$

In this equation $\boldsymbol{\Omega}$ is the angular velocity of the rotation and \mathbf{A} is the area enclosed by the lightpath. The angular velocity of the LISA constellation is given by 1 cycle/year, corresponding to 2×10^{-7} rad/s. Given that the constellation is inclined by 60° with respect to the ecliptic, the parallel component of the angular velocity is only half of the magnitude. Therefore, the lightpath difference is approximately $\Delta L \approx 14.4$ km, which is equivalent to a propagation time difference of approximately $47 \mu\text{s}$.

If we assume the phase noise from all phase-locked loops in the constellation is zero, in the clockwise trajectory the phase measurements are given by

$$\begin{aligned} \phi_{23}(t) &= \phi_{12}(t - \tau_{12}) - h_{12}(t), \\ \phi_{31}(t) &= \phi_{23}(t - \tau_{23}) - h_{23}(t), \\ S_{13}(t) &= \phi_{13}(t) - \phi_{31}(t - \tau_{31}) + h_{31}(t). \end{aligned} \quad (2-10)$$

Thus we obtain

$$S_{13}(t) = \phi_{13}(t) - \phi_{12}(t - \tau_{12} - \tau_{23} - \tau_{31}) + h_{12}(t - \tau_{23} - \tau_{31}) + h_{23}(t - \tau_{31}) + h_{31}(t). \quad (2-11)$$

By following the same procedure, the other phase measurement on SC_1 is given by

$$S_{12}(t) = \phi_{12}(t) - \phi_{13}(t - \tau_{13} - \tau_{32} - \tau_{21}) + h_{13}(t - \tau_{32} - \tau_{21}) + h_{32}(t - \tau_{21}) + h_{21}(t). \quad (2-12)$$

Since the difference between the clockwise propagation time $\tau_{CW} = \tau_{12} + \tau_{23} + \tau_{31}$ and the counterclockwise propagation time $\tau_{CCW} = \tau_{13} + \tau_{32} + \tau_{21}$ is $\sim 47 \mu\text{s}$, we still need time-shifting to cancel out the arm length difference.

2.2.1.3 TDI Limitations

The TDI capability of noise suppression is limited by several realistic effects, primarily the arm length knowledge which directly depends on the ranging accuracy.

In addition to the ranging accuracy, limiting effects include the velocity correction error, analog chain error ¹, phasemeter noise and scattered light, etc.

The ranging system LISA will use is pseudo-random noise (PRN) ranging, which phase modulates the carrier of the far laser with a PRN code stream. The travel time then can be measured via the correlation between the local and received PRN code. Current estimation of the PRN ranging error is $\delta L \approx 1 \text{ m}$ ($\sim 1 \text{ ns}$ in terms of timing error).

Allocated by the IMS noise budget, the residual laser frequency noise at the TDI output is required to be below $2 \text{ pmHz}^{-1/2} \times \sqrt{1 + (2.8 \text{ mHz}/f)^4}$. With a 1 m ranging accuracy, the required laser frequency noise at the TDI input is given by

$$\delta\nu_{\text{pre-TDI}}(f) < 282 \times \sqrt{1 + \left(\frac{2.8 \text{ mHz}}{f}\right)^4} \text{ Hz Hz}^{-1/2}. \quad (2-13)$$

In comparison to the noise suppression limited by ranging, other limiting effects yield more relaxed requirements for $\delta\nu_{\text{pre-TDI}}$, which indicates the ranging accuracy on LISA arm length is the dominant limitation for TDI. Due to the limited ranging accuracy, TDI would not meet the 2 pm requirement on residual laser frequency noise by itself, since a free-running laser typically carries frequency noise on the level of $10 \text{ kHz}/f \text{ Hz Hz}^{-1/2}$. This frequency noise is several orders of magnitude beyond the stability specified in Eq. 2-13; therefore, the laser frequency must be actively pre-stabilized to achieve the requirement.

2.2.2 Pre-stabilization

The frequency stabilization plan is to lock the laser frequency to a stable reference. On the local spacecraft, such a stable reference can be either a high-finesse Fabry-Perot cavity made of ultra-low expansion glass or an atomic or molecular spectral line [76]. The modulation-demodulation method uses an optical cavity known as Pound-Drever-Hall

¹ The analog chain consists of a photoreceiver, a pre-amplifier and an anti-aliasing filter successively placed before the ADCs.

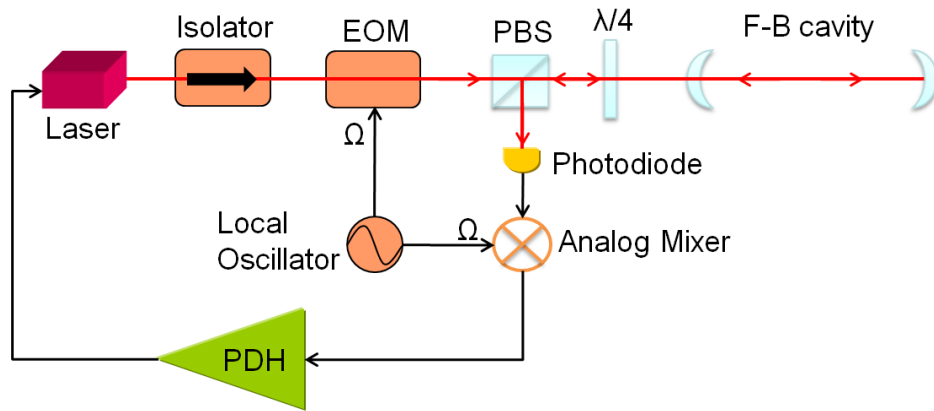


Figure 2-6. The experimental setup of Pound-Drever-Hall stabilization.

(PDH) technique [77]. It has been well studied in laboratory, giving a frequency noise suppression performance of $\sim 30 \text{ Hz}/\sqrt{\text{Hz}}$ at 3 mHz [78]. Besides the widely favored PDH technique, another pre-stabilization method is based on a heterodyne Mach-Zehnder interferometer, which exploits the pathlength mismatch between two different lasers as the frequency reference. This method has been used in the LISA Technology Package (LTP) for LISA Pathfinder [79]. Note that in all six lasers only one master laser is needed to be pre-stabilized using one of the methods described above, and the other five lasers are stabilized using phase-locking either locally to the master laser via the back-link fiber or using the beat signal with the far laser via optical transponders.

2.2.2.1 Pound-Drever-Hall frequency stabilization

The Pound-Drever-Hall technique is the most used frequency stabilization method in optical experiments [80]. The optical cavity used in laboratory is normally a high-finesse ($\sim 10^4$) Fabry-Perot cavity, which consists of two low-loss mirrors bonded to a rigid spacer made of low-expansion material such as Zerodur or ULE. As shown in Figure 2-6, the laser beam with a nominal frequency ω is transmitted through an electro-optical modulator (EOM) driven by a local oscillator with a nominal frequency Ω (typically $> 5 \text{ MHz}$, well larger than the FWHM of the cavity), producing two sidebands $\omega \pm \Omega$.

After the polarizing beam splitter and the quarter-wave plate, the beam is reflected from the optical cavity. We use the reflected beam to feedback control the laser frequency. The reflectivity T_r of an optical cavity is a function of the laser frequency ω :

$$T_r(\omega) \equiv \frac{E_r(\omega)}{E_i(\omega)} = \frac{r_1 - r_2 e^{i\varphi}}{1 - r_1 r_2 e^{i\varphi}}, \quad (2-14)$$

where $\varphi = 2\omega L/c$ is the phase shift due to a round-trip inside the cavity. r_1 , r_2 , t_1 and t_2 are the reflection coefficients and transmission coefficients of mirror 1 and 2 and we assume a lossless cavity with $r_1^2 + t_1^2 = 1$.

If the carrier frequency of the beam exactly matches up the resonant frequency of the cavity $\omega_L = 2\pi nc/L$, the reflected carrier will have zero phase shift. Also, as long as Ω is large enough such that the sidebands are far away from the resonant frequency, their phase shift will be negligible. Therefore, the reflected carrier will generate two heterodyne beat signals with each sideband. Since they are 180° out of phase, the superposition of them on the photodiode would be zero.

If the carrier frequency is slightly off the resonant frequency, a phase shift will be generated in the reflected carrier. When the offset $\delta\omega$ to the resonant frequency is small, the reflectivity transfer function approximates to the first linear order by taking Taylor expansion:

$$\begin{aligned} T_r(\delta\omega) &= \frac{r_1 - r_2}{1 - r_1 r_2} + 2i \frac{r_1^2 r_2 - r_2}{(1 - r_1 r_2)^2} \frac{\delta\omega L}{c} \\ &= \frac{r_1 - r_2}{1 - r_1 r_2} - 2i \mathcal{F} \frac{\delta\nu}{\text{FSR}} \\ &= \frac{r_1 - r_2}{1 - r_1 r_2} - i \frac{\delta\nu}{\text{HWHM}}. \end{aligned} \quad (2-15)$$

In other words, the cavity is able to detect whether the carrier frequency is above or below the resonant frequency since the sign of the phase shift depends on the sign of the frequency offset. Also due to the phase shift, the heterodyne beat signals will no longer cancel out each other. If we demodulate the reflected beam with the same

oscillator Ω and low-pass filter the high frequency component, a zero-crossing DC signal that is linear with respect to the frequency offset can be generated to feedback control the laser frequency.

In the LISA band especially below 1 mHz, the frequency stability of the PDH technique is mainly limited by the temperature fluctuations that causes spurious noises in the cavity length. The relative stability $\Delta L/L$ of the referencing cavity length in our experiments is as low as 10^{-13} , resulting in a frequency noise of about $30 \text{ Hz Hz}^{-1/2}$.

2.2.2.2 Mach-Zehnder frequency stabilization

Mach-Zehnder frequency stabilization requires a dedicated heterodyne interferometer with unequal arm, which is used as the frequency reference. In the LTP baseline design the unequal-armed Mach-Zehnder interferometer is configured using a beam splitter and two acousto-optic modulators (AOM) to generate heterodyne interferometry signals at 1 – 2 kHz [81, 82]. On the LISA optical bench, the integration of such a heterodyne interferometer becomes easier as the interferometry signal between two adjacent lasers is already incorporated into the phase readout. Compared with stabilization to a Fabry-Perot cavity, Mach-Zehnder stabilization simplifies the optical bench setup, where neither an optical cavity nor an EOM is not necessary to be implemented. Also, this pre-stabilization method allows to tune the laser frequency over a wide range without the necessity of changing the pathlength mismatch.

The proposed interferometer setup is illustrated by Figure 2-7. Between the two adjacent lasers on the same spacecraft, one laser marked as the slave laser is phase-locked to the master laser with a frequency offset (2 – 20 MHz) driven by the local oscillator. As we already know, the heterodyne interferometry signal between them is measured at the photodiode PD_R and the phase readout is given by

$$\varphi_R = \Phi_S - \Phi_M. \quad (2-16)$$

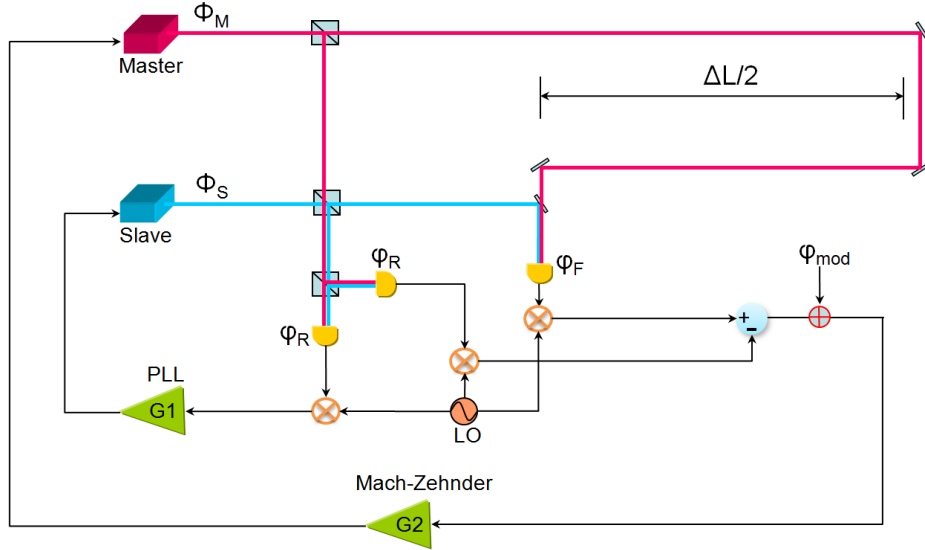


Figure 2-7. The interferometer setup for Mach-Zehnder frequency stabilization. In this setup the slave laser is heterodyne phase-locked to the master laser. Their heterodyne signal φ_R is measured at the reference photodiode. The other arm of the Mach-Zehnder interferometer has an additional pathlength L , which generates a propagation delay in the heterodyne signal φ_F . The error signal of Mach-Zehnder stabilization is given by $\varphi_F - \varphi_R$, which exploits the pathlength mismatch as a reference to stabilize the master laser. Note that the mixers in this diagram may represent phasemeters, each driven by a common local oscillator. The phasemeters demodulate the heterodyne signals with the same offset frequency and measure the phase noise in each of them.

Based on the dynamics of the PLL, in the Laplace domain the phase noise Φ_S of the phase-locked slave laser is given by

$$\Phi_S = \frac{1}{1 + G_1} \Phi_S^0 + \frac{G_1}{1 + G_1} \Phi_M. \quad (2-17)$$

The first term represents the noise suppression of the free-running slave laser and the second terms indicates that the phase noise of the slave laser tracks the phase noise of the referenced master laser. Therefore, the phase measurement at PD_R can be written as

$$\varphi_R = \frac{1}{1 + G_1} \Phi_S^0 - \frac{1}{1 + G_1} \Phi_M. \quad (2-18)$$

We place an additional unequal-armed interferometer φ_F on the optical bench, which together with φ_R constitutes an unequal-armed Mach-Zehnder interferometer. The phase measurement at PD_F is given by

$$\varphi_F = \Phi_S - \Phi_M e^{-s\tau}, \quad (2-19)$$

where $\tau = \Delta L/c$ and ΔL is the arm length mismatch of this interferometer. Substitute Eq. 2-17 into this equation and we have

$$\varphi_F = \frac{1}{1 + G_1} \Phi_S^0 + \left(\frac{G_1}{1 + G_1} - e^{-s\tau} \right) \Phi_M. \quad (2-20)$$

Eq. 2-20 cannot be directly used as an error signal to control the master laser frequency since it depends on the phase noise of the free-running slave laser and the transfer function of the PLL controller. However, if we combine the phase measurements on both two photodiodes by subtracting them, we get

$$\varphi_F - \varphi_R = (1 - e^{-s\tau}) \Phi_M, \quad (2-21)$$

which can be used to detect the phase fluctuations of the master laser. This sensor transfer function only depends on the arm length mismatch. With a high-gain feedback controller G_2 , the phase noise of the master laser can be stabilized to

$$\Phi_{M-\text{lock}} = \frac{1}{1 + (1 - e^{-s\tau})G_2} \Phi_M. \quad (2-22)$$

In Section 2.3.2.1 we will learn that Mach-Zehnder stabilization is essentially a benchtop “mini” version of single arm locking, which exploits the LISA arm as a reference to stabilize the laser frequency.

If we apply a phase modulation φ_{mod} at the subtractor of the sensor, this phase modulation will be coupled into the phase noise of the stabilized master laser as a reference:

$$\Phi_{M-\text{lock}} = \frac{1}{1 + (1 - e^{-s\tau})G_2} \Phi_M + \frac{G_2}{1 + (1 - e^{-s\tau})G_2} \varphi_{\text{mod}}. \quad (2-23)$$

Thus we have

$$\frac{\partial \Phi_{\text{M-lock}}}{\partial \varphi_{\text{mod}}} = \frac{G_2}{1 + (1 - e^{-s\tau}) G_2}. \quad (2-24)$$

It is easy to demonstrate that in the high gain limit ($G_2 \gg 1$), Eq. 2-24 approximates to

$$\frac{\partial \Phi_{\text{M-lock}}}{\partial \varphi_{\text{mod}}} \approx \frac{1}{s\tau}. \quad (2-25)$$

The above relation holds for frequencies much lower than $1/\tau$, which is always valid in the locking bandwidth (~ 20 Hz). In terms of frequency, it can be represented as

$$\frac{\partial \nu_{\text{M-lock}}}{\partial \varphi_{\text{mod}}} \approx \frac{1}{\tau}, \quad (2-26)$$

which indicates the frequency of the master laser can be continuously tuned by introducing a phase offset φ_{mod} at the sensor. The actuation factor from the phase modulation to the frequency tuning is given by $1/\tau$.

The noise performance of Mach-Zehnder stabilization is limited by the pathlength stability of the interferometer, as well as sensing noise sources introduced by the photodiodes and phasemeters (shot noise, digitization noise, etc.) If we assume the sensing noise is equivalent to $1 \text{ pm}/\sqrt{\text{Hz}}$, for a 0.5 m pathlength mismatch the expected stabilized frequency noise is approximately given by

$$\delta \nu_{\text{MZ}} = 800 \times \sqrt{1 + \left(\frac{2.8 \text{ mHz}}{f}\right)^4} \text{ Hz Hz}^{-1/2}. \quad (2-27)$$

Although this expected performance is inferior to the fixed cavity and does not meet the requirement for pre-stabilization, Mach-Zehnder stabilization provides an intrinsic frequency tunability that the PDH stabilization does not have, which makes the incorporation of Mach-Zehnder stabilization with arm locking much easier. The incorporation can be achieved by adjusting the phase of the local oscillator that is used to demodulate the Mach-Zehnder heterodyne signal through arm locking. More details of the integration of Mach-Zehnder stabilization and arm locking will be seen in Section

2.3.4.2. In addition, a variation of Mach-Zehnder stabilization that uses a Fabry-Perot cavity to achieve the arm length mismatch has also been developed. Due to the better stability of the cavity length, the stabilization performance is expected to be superior to the standard Mach-Zehnder method, which has been demonstrated in relevant benchtop experiments [83].

2.3 Arm Locking

In comparison to Mach-Zehnder stabilization that exploits the path length to the adjacent optical bench as a reference, the LISA long arm (from optical bench to optical bench) is another path length reference which provides an even better stability ($\delta L/L \sim 10^{-21} \text{ Hz}^{-1/2}$) in the LISA band. Techniques that transfer the stability of the long arm lengths to the laser frequency are generally known as arm locking. Unlike Mach-Zehnder stabilization that requires an extra interference path in the setup, the arm locking architecture is intrinsically embedded in the LISA constellation: Arm locking synthesizes the error signal from the inter-spacecraft phase measurements, which are already available at the photodetectors. This feature allows that the control system of arm locking can be fully implemented in on-board data processing and no additional resource is needed. With constellation phase locking on far spacecraft, the local laser beam has an interference with its replica delayed by the light round-trip travel time $\tau \approx 33 \text{ s}$. Such a long time delay is very uncommon in ordinary sensors, as it may cause excessive phase shift at interferometer null frequencies and then limit the control bandwidth. However, the pioneering work done by Sheard *et al* has demonstrated that the bandwidth of arm locking is not necessarily limited by the long time delay and a high gain controller design is achievable if the phase margin is carefully retained [84]. More studies on arm locking have analytically demonstrated that the instantaneous phase information can be recovered via an adequate linear combination of phase measurements.

noise of the pre-stabilized laser on SC_1 is $\Phi_{L1}^0(s)$ in the Laplace domain, then the phase of the laser from $SC_{2,3}$ received by the photodetector on SC_1 will be given by

$$\Phi_{Li}(s) = \frac{1}{1 + G_i(s)} \Phi_{Li}^0(s) e^{-s\tau_{i1}} + \frac{G_i(s)}{1 + G_i(s)} \Phi_{L1}^0(s) e^{-s(\tau_{i1} + \tau_{i1})} + \phi_{N(i)}(s), \quad (2-28)$$

where $i = 2, 3$ and $\Phi_{Li}^0(s)$ is the initial phase noise of the free-running laser. $\phi_{N(i)}(s)$ includes all other kinds of noise in the phase-locked loop, including shot noise, clock noise and spacecraft jitter. We ignore this term as it is much lower than the laser phase noise, although it will ultimately limit the performance of arm locking (See Section 2.3.5).

The beat signals between the laser fields from $SC_{2,3}$ with the master laser on SC_1 will be measured by the phasemeter on SC_1 :

$$\begin{aligned} \phi_{1i}(s) &= \Phi_{L1}^0(s) - \Phi_{Li}(s) \\ &= \Phi_{L1}^0(s) \left(1 - \frac{G_i(s)}{1 + G_i(s)} e^{-s\tau_i} \right) - \frac{1}{1 + G_i(s)} \Phi_{Li}^0(s) e^{-s\tau_{i1}}, \end{aligned} \quad (2-29)$$

where $\tau_2 = \tau_{12} + \tau_{21}$ and $\tau_3 = \tau_{13} + \tau_{31}$ are the round-trip light travel times on both arms, respectively. Since in LISA the phase-locked loop controller yields the high gain limit, Eq. 2-29 can be simplified by approximations $\frac{G_i(s)}{1+G_i(s)} \approx 1$ and $\frac{1}{1+G_i(s)} \approx 0$. From Eq. 2-29 we can derive the transfer function of the two arms:

$$P_{1i}(s) = \frac{\phi_{1i}(s)}{\Phi_{L1}^0(s)} \approx 1 - e^{-s\tau_i}, \quad i = 2, 3. \quad (2-30)$$

The two phasemeter outputs $\phi_{12}(s)$ and $\phi_{13}(s)$ are manipulated to construct an arm locking sensor signal. Following the notation used in Ref [13, 85], this manipulation can be described by a 1×2 mapping vector \mathbf{S}_k . If we write down the two interferometer outputs as a 2×1 phase vector $\boldsymbol{\varphi}_1$, the sensor signal is then simply given by

$$\phi_{\text{err}}(s) = \mathbf{S}_k(s) \cdot \boldsymbol{\Phi}_1(s), \quad (2-31)$$

where $\boldsymbol{\Phi}_1(s) = \begin{bmatrix} \phi_{12}(s) \\ \phi_{13}(s) \end{bmatrix}$.

When the arm locking loop is closed, the phase noise at the local laser output is given by

$$\begin{aligned}\Phi_{L1}(s) &= \Phi_{L1}^0(s) - \frac{G_1(s)}{1 + G_1(s)H(s)} \mathbf{S}_k \cdot \Phi_1(s) \\ &= \frac{\Phi_{L1}^0(s)}{1 + G_1(s)H(s)},\end{aligned}\quad (2-32)$$

where $G_1(s)$ is the arm locking controller and

$$H(s) = \mathbf{S}_k(s) \cdot \begin{bmatrix} P_{12}(s) \\ P_{13}(s) \end{bmatrix}\quad (2-33)$$

is the arm locking sensor. Compared with the initial phase noise of the pre-stabilized laser, the stabilized phase noise is suppressed by the open-loop gain $G_1(s)H(s)$.

2.3.2 Arm Locking Sensors

2.3.2.1 Single arm locking

Single arm locking is the original idea of arm locking proposed by Sheard *et al.*. In the single arm locking configuration only the interferometer output on one arm will be used and consequently we have $H_S(s) = P_{12}(s) = 1 - e^{-s\tau_2}$. As shown in Figure 2-9, the sensor transfer function has zero magnitude response at DC as well as at frequencies n/τ_2 known as nulls. The phase response starts from a 90° phase advance at DC and has discontinuities at these nulls where the phase jumps from -90° to 90° . The transfer function also have multiple unity gain frequencies, on both sides near each null.

These unity gain frequencies place additional stability constraints on the controller design. In practice an integrator with a single pole at DC is widely used in feedback controllers as it provides a high gain at DC and the gain declines with a $1/s$ slope at high frequencies, which is required by the limited bandwidth. However, this kind of controller essentially does not work for single arm locking because the $1/s$ slope would bring in an additional 90° phase shift. As the loop gain increases, the phase margin will be further decreased, which will destroy the system stability. This problem is illustrated by Figure

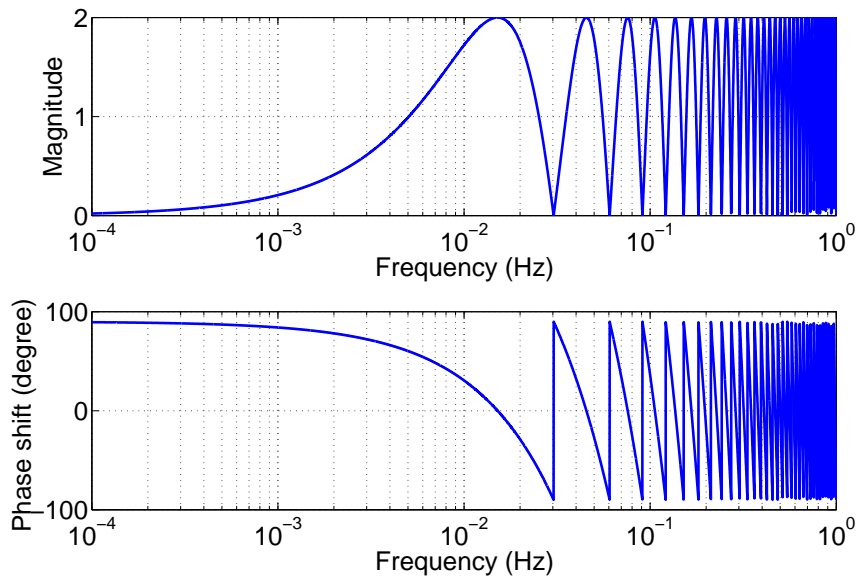


Figure 2-9. The magnitude and phase response of the single arm locking sensor. Note that for the magnitude response we are not using the logarithmic scale in the y axis (as we do in most cases) just to show the situation near interferometer nulls more clearly. In the logarithmic scale the magnitude response versus the Fourier frequency actually approximates to an f slope at low frequencies.

2-10, where the open-loop transfer function is given by the single arm locking sensor multiplied by a $1/s$ slope. With a gain factor of 10, at the unity gain frequencies the phase shift is already very close to 180° .

To avoid losing excessive phase in bandwidth, the proposed design of the controller has to have a slope less steep than $1/s$ to compensate the phase loss at zero crossings. For instance, a $1/s^{1/2}$ or $1/s^{2/3}$ slope will only bring in a 45° or 60° phase shift, respectively. We assume a generic arm locking controller filter with the transfer function $G(f) = kf^{-\alpha}e^{i\varphi}$, where $0 < \alpha < 1$, k is a real gain factor and φ is the phase shift introduced by the filter. As we know, the closed-loop transfer function of a feedback control loop is defined as

$$TF_{CL}(f) \equiv \frac{\widetilde{\phi_{out}}(f)}{\widetilde{\phi_{in}}(f)} \equiv \frac{1}{1 + TF_{OL}(f)}. \quad (2-34)$$

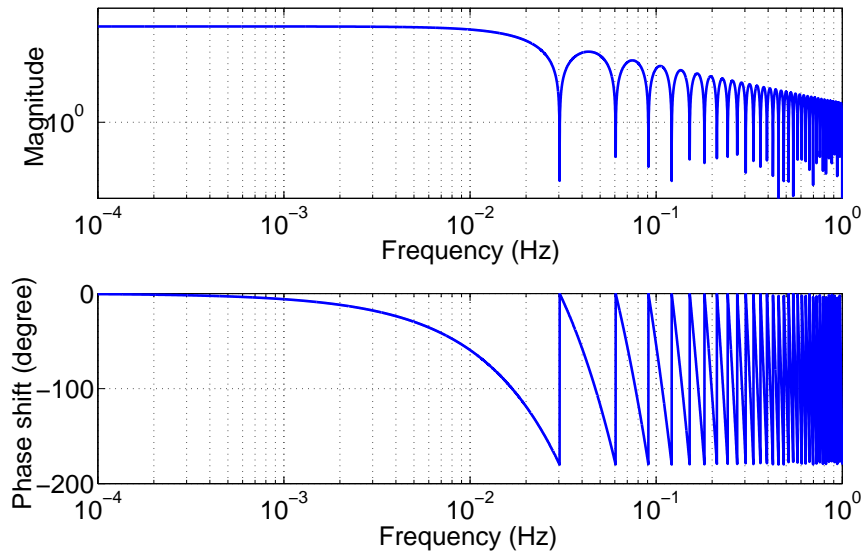


Figure 2-10. An ordinary integrator with a transfer function of $1/s$ is not suitable to be a single arm locking controller due to the excessive phase shift placed by the sensor nulls. With a gain factor of 10 the system has already become unstable since at the unity gain frequencies the phase shift is very close to 180° .

With the controller filter described above, the open-loop transfer function of the single arm locking loop is given by

$$TF_{OL}(f) = \frac{G_0(1 - e^{-i2\pi f\tau})e^{i\varphi}}{kf^\alpha}, \quad (2-35)$$

where G_0 is the open-loop gain and $\tau = \tau_2 \approx 33$ s is the round-trip light travel time.

The noise suppression performance of an arm locking loop is determined by the magnitude of the closed-loop transfer function $|TF_{CL}(f)|$. When $|TF_{CL}(f)| < 1$ we have noise suppressions, otherwise we have noise amplifications.

If we substitute Eq. 2–35 into Eq. 2–34 and evaluate the magnitude of the closed-loop transfer function $|TF_{CL}(f)|$, it yields

$$\begin{aligned}
 |TF_{CL}(f)| &= \left| \frac{kf^\alpha e^{i\varphi}}{kf^\alpha e^{i\varphi} + G_0(1 - e^{-i2\pi f\tau})} \right| \\
 &= \sqrt{\frac{k^2 f^{2\alpha}}{k^2 f^{2\alpha} + 2G_0^2(1 - \cos 2\pi f\tau) - 2kG_0 f^\alpha (\cos(\varphi + 2\pi f\tau) - \cos \varphi)}} \\
 &= \sqrt{\frac{k^2 f^{2\alpha}}{k^2 f^{2\alpha} + \Delta}}. \tag{2-36}
 \end{aligned}$$

From the result of Eq. 2–36, the noise suppression performance depends on the value of

$$\Delta = 2G_0^2(1 - \cos 2\pi f\tau) - 2kG_0 f^\alpha (\cos(\varphi + 2\pi f\tau) - \cos \varphi), \tag{2-37}$$

i.e., $\Delta > 0$, $\Delta = 0$, $\Delta < 0$ corresponds to the case of noise suppression, no suppression and noise amplification, respectively. ²

A specific model to numerically evaluate Δ is shown in Figure 2-11. In this system model we assume the loop gain $G_0 = 10$ and the filter has a magnitude response $|G(f)| = 1/f^{1/2}$ with a 45° phase shift. The plot shows that in the frequency region $f \ll 1/\tau$, we have $\Delta \approx 0$, which means a simple $1/f^\alpha$ slope does not provide any noise suppression at DC. This can also be seen from the transfer function of the single arm locking sensor, which has a f slope starting from DC. To overcome this f slope in the sensor and obtain some noise suppression at DC, the controller must have at least a $1/f$ slope in the frequency region $f \ll 1/\tau$.

In the frequency region where f is comparable to n/τ , Δ is generally larger than zero but with a few exceptions. At some certain frequencies which are very close to

² From the point of view of mathematics, the value of Δ is obviously required to have a lower limit: $\Delta > -k^2 f^{2\alpha}$, otherwise the expression of the magnitude response would not be meaningful. In practice, the value of Δ generally meets this requirement in the LISA band since the Fourier frequency is low.

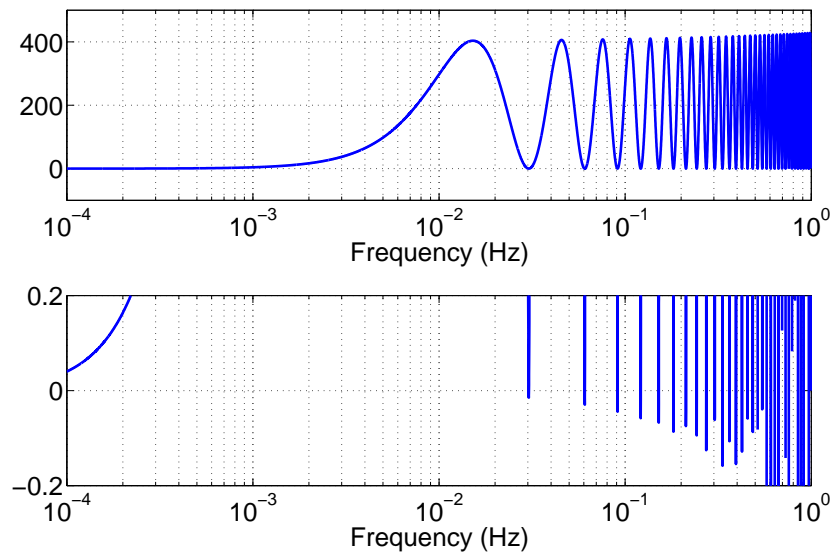


Figure 2-11. An example of the value of Δ that indicates the noise suppression, which is given by Eq. 2-37. Larger value of Δ indicates more noise suppressions. Note that in this model we did not include integrators at low frequencies; therefore we do not have any suppression at DC. The value of Δ can be negative at certain frequencies near each null, corresponding to noise amplifications due to the excessive phase loss.

each null n/τ , numerical calculation shows that Δ can be less than zero, causing noise amplifications at these frequencies. These noise amplifications correspond to multiple peaks with finite heights in the closed-loop transfer function as shown in Figure 2-12. It is worth noting that noise amplifications do not occur exactly at sensor nulls n/τ . Actually when $f = n/\tau$, $\Delta = 0$ and the control loop has no noise suppressions or amplifications.

As shown in Figure 2-12, an ideal single arm-locking controller would be designed in the following manner: starting from DC the filter has a steep slope of at least $1/f$ to suppress the low frequency noise and stops right before the first null $1/\tau$; starting from the first null the filter transfer function has a $1/f^{1/2}$ or $1/f^{2/3}$ slope in bandwidth and starts to flatten out beyond the bandwidth.

Although the idea of single arm locking has been theoretically and experimentally validated by multiple researchers, the shortcomings of single arm locking make it

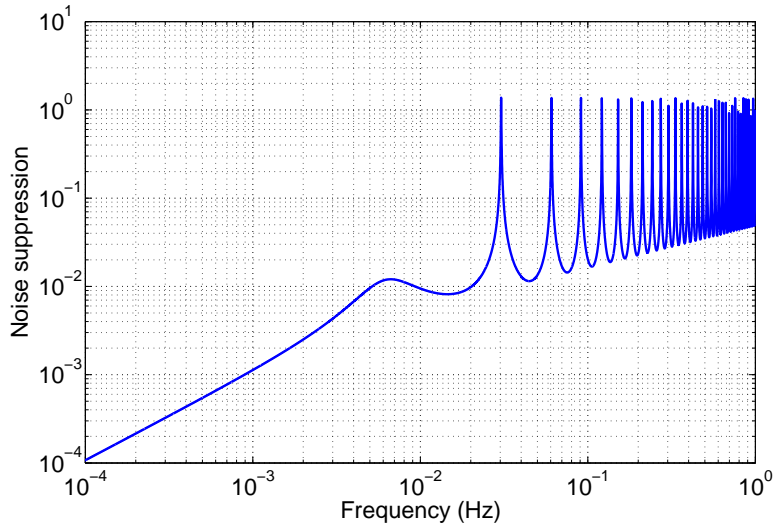


Figure 2-12. An example of the closed-loop transfer function of single arm locking, where the light travel time is 33 s. The controller consists of a filter with a $1/f^{1/2}$ slope and two-stage integrators.

ultimately inappropriate for realistic LISA. It is very noticeable that the first null shows up right inside the LISA band, which in any case is not an ideal noise suppression performance due to the noise amplifications near the nulls. Moreover, since the first null is in the LISA band, the gain around that region must be high enough to provide a decent noise suppression. Considering the controller will have a slope less steep than $1/f$, an extremely large bandwidth would be needed in single arm locking.

The third disadvantage of single arm locking is the start-up transients caused by the non-zero initial error signal, which creates the repeating 33 seconds noise with damped oscillations [86, 87].

2.3.2.2 Common arm locking

Under most circumstances, the lengths of two LISA arms are different by a relatively small amount except for some certain short periods. For this reason, common arm locking, as the simplest arm locking configuration that utilizes the interferometer outputs on both two arms, exploits the arm length mismatch to push the first null of the sensor to higher frequencies beyond the LISA band. As Markus Herz pointed out using the

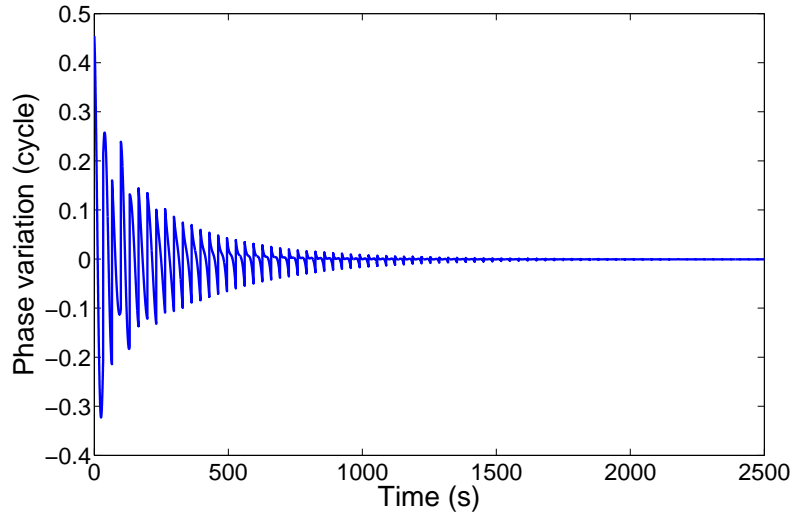


Figure 2-13. The time domain simulation to demonstrate the initial transients in single arm locking. The quasiperiodic transient is “frozen” inside the output signal with a 33 s oscillation and decays with a time constant of approximately ~ 500 s for this specific model.

second arm allows to reduce the start-up transients[88]. The mapping vector $\mathbf{S}_k(s)$ of common arm locking configuration is $[1, 1]$, as it simply combines the two interferometer outputs by adding them. Thus the sensor transfer function of common arm locking is given by

$$\begin{aligned}
 H_C(s) = P_+(s) &= [1, 1] \cdot \begin{bmatrix} P_{12}(s) \\ P_{13}(s) \end{bmatrix} \\
 &= P_{12}(s) + P_{13}(s) \\
 &= 2 - e^{-s\tau_2} - e^{-s\tau_3}.
 \end{aligned} \tag{2-38}$$

If we define $\bar{\tau} \equiv (\tau_2 + \tau_3)/2$ and $\Delta\tau \equiv (\tau_2 - \tau_3)/2 > 0$, the transfer function can also be represented in the angular frequency by taking the transformation $s = i\omega$:

$$P_+(\omega) = 2[1 - \cos(\Delta\tau\omega)e^{-i\bar{\tau}\omega}]. \tag{2-39}$$

This sensor transfer function resembles that of single arm locking $H_S(\omega) = 1 - e^{-i\tau\omega}$. The difference is that the round-trip time on one arm is replaced by the averaged

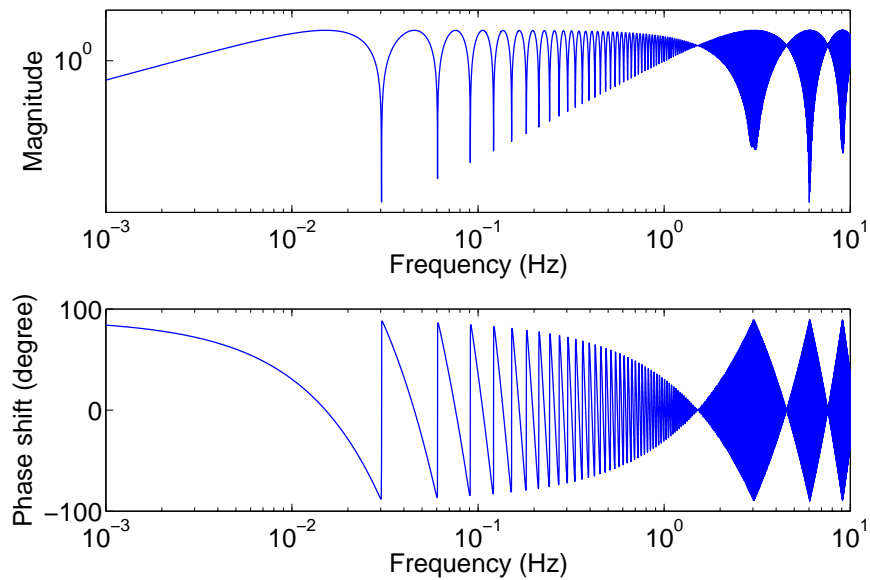


Figure 2-14. The magnitude and phase response of the common arm locking sensor. The averaged light travel time is 33 s and the arm length mismatch is $\sim 1\%$. Note that the first sensor null is located at $1/\Delta\tau \approx 6$ Hz and the magnitude at $1/\bar{\tau} = 30$ mHz is not zero as $\cos(2\pi(\Delta\tau/\bar{\tau}))$ is not equal to 1. Therefore, frequencies at the multiples of $1/\bar{\tau}$ (but not at the multiples of $1/\Delta\tau$) are referred to as “local minima” rather than sensor nulls in this dissertation. Nevertheless, local minima still correspond to large phase shift and thereby may cause noise amplifications in the closed-loop.

round-trip time on both arms. Also, the term that represents the delayed phase is multiplied with a coefficient $\cos(\Delta\tau\omega)$. Due to this coefficient, the magnitude of the transfer function does not decrease to zero when $\omega = 2n\pi/\bar{\tau}$ unless ω is also integer multiples of $2\pi/\Delta\tau$. The magnitude response and phase shift of the common arm locking sensor is shown in Figure 2-14, which describes the situation of $\bar{\tau} = 33$ s and $\Delta\tau = 0.16$ s ($\sim 1\%$ arm length mismatch).

Figure 2-14 also shows that the phase shift at $1/\bar{\tau} \approx 30$ mHz is still close to 90° , which means that the controller is still required to maintain a relatively low gain to compensate the excessive phase loss. Similar to single arm locking, noise amplifications will also occur near the frequencies with large phase shift in common arm locking. This characteristic indicates that despite of the introduction of a second arm, common arm

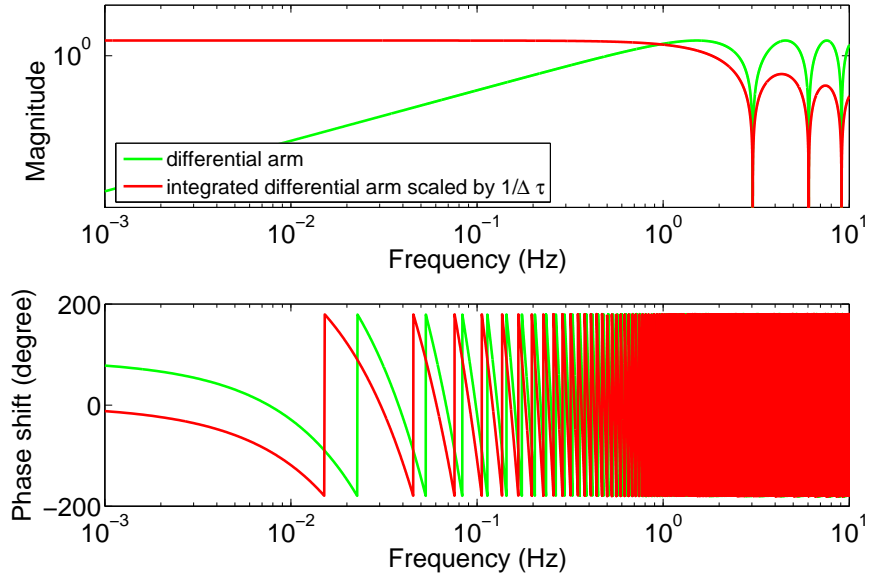


Figure 2-15. The magnitude and phase response of the differential arm (green) and the integrated differential arm scaled by $1/\Delta\tau$ (red). The averaged light travel time is 33 s and the arm length mismatch is $\sim 1\%$. They only contain the information of the delayed phase, therefore the maximum of their phase shift is 180° and they cannot be solely used as an arm locking sensor.

locking is essentially not a significant improvement of single arm locking in terms of the gain advantage and system stability.

2.3.2.3 Dual arm locking

Dual arm locking, also known as direct arm locking, combines the phase measurements on two different arms and then directly provide a feedback signal by estimating the instantaneous phase information. The original idea of dual arm locking is from Andrew Sutton and Daniel Shaddock [85]. Compared with single arm locking and common arm locking, dual arm locking exhibits several remarkable improvements such as no noise amplification in the LISA band and significantly better noise suppression performance.

In addition to the common arm sensor described in Eq.(2-15), we can also define the differential arm sensor:

$$P_-(s) = P_{12}(s) - P_{13}(s) = e^{-s\tau_3} - e^{-s\tau_2}. \quad (2-40)$$

Again, when represented in the angular frequency domain, the differential arm sensor is given by

$$P_\omega = 2i \sin(\Delta\tau\omega) e^{-i\bar{\tau}\omega}, \quad (2-41)$$

where the definitions of $\bar{\tau}$ and $\Delta\tau$ are the same as in the common arm sensor. We plot the magnitude response and phase shift of the differential arm sensor in Figure 2-15.

The differential arm sensor only contains information of the purely delayed phase, therefore it cannot be solely used for feedback control. However, the differential arm signal can be linearly combined with the common arm signal in a certain way such that the delayed term in the common arm sensor will be eliminated. In the Laplace domain, such a linear combination is given by

$$H(s) = P_+(s) + \frac{1}{s\Delta\tau} P_-(s). \quad (2-42)$$

Switched back to the angular frequency, the linear combination yields

$$\begin{aligned} H(\omega) &= 2 - 2 \cos(\Delta\tau\omega) e^{-i\bar{\tau}\omega} + \frac{1}{\Delta\tau} \frac{2i \sin(\Delta\tau\omega) e^{-i\bar{\tau}\omega}}{i\omega} \\ &= 2 \left[1 - (\cos(\Delta\tau\omega) - \text{sinc}(\Delta\tau\omega)) e^{-i\bar{\tau}\omega} \right]. \end{aligned} \quad (2-43)$$

At low frequencies ($\omega \ll \frac{1}{\Delta\tau}$), both $\cos(\Delta\tau\omega)$ and $\text{sinc}(\Delta\tau\omega)$ are approximately equal to 1. Therefore, the transfer function of this combination is approximately given by $H(\omega) \approx 2$, i.e., the magnitude response retains almost flatness with a factor of 2 and the phase shift is also almost entirely zero in the LISA band. In other words, this linear combination extracts the instantaneous input phase from the interferometer outputs. Due to the integration of the differential arm path, the differential arm sensor dominates at low frequencies and the integrated differential arm retains the zero phase shift in this region. The flat magnitude response and zero phase shift at low frequencies allow a more flexible controller design, compared with the nulls at high frequencies that limit the controller slope and therefore the achievable gain.

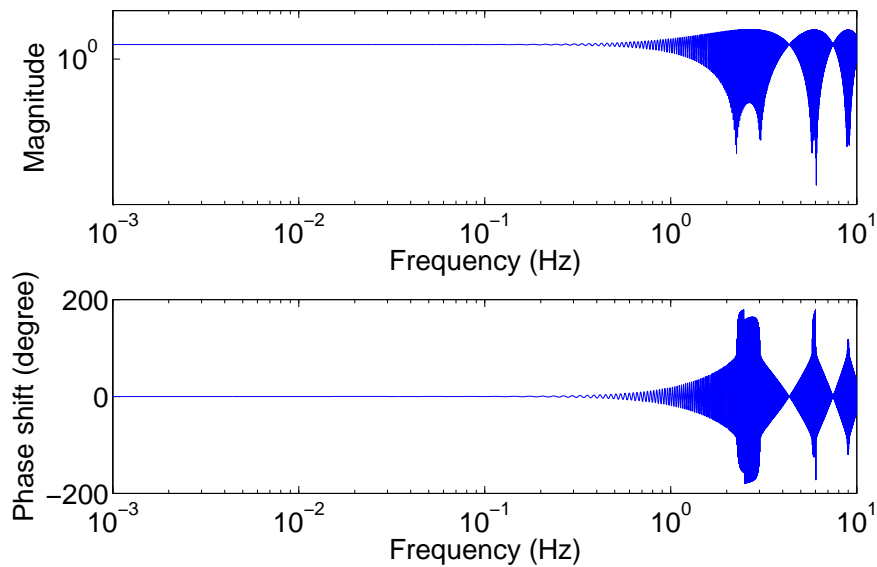


Figure 2-16. The magnitude and phase response of the linear combination $H(s)$. The averaged light travel time is 33 s and the arm length mismatch is $\sim 1\%$. For frequencies far below $1/\Delta\tau$ the frequency response is almost flat, since the information of the instantaneous phase in this frequency region is recovered through the linear combination. However, at high frequencies the phase shift can be as large as 180° at frequencies of $1/(2\Delta\tau)$, due to the excessive phase loss from the integrated differential arm.

Figure 2-16 illustrates the magnitude response and the phase shift of this linear combination, where we have $\bar{\tau} = 33$ s and $\Delta\tau = 0.16$ s. It clearly shows that at high frequencies the shape of the transfer function has a drastic change compared with the low frequency case. The first null shows up at the frequency $1/\Delta\tau = 6.1$ Hz and the maximum phase shift can reach almost 180° at frequencies slightly less than 3 Hz, due to the excessive phase loss from the integrated differential arm. Therefore, such a sensor would easily produce some system instability in the presence of a moderately high loop gain.

A method proposed by Sutton *et al.* to solve this stability problem is to add a second-order elliptical low-pass filter $E(s)$ in the differential arm path. More generally, any low-pass filter that has a unity gain at DC and a pole near the frequency of $1/4\Delta\tau$ is capable of attenuating and phase-shifting the differential arm within the instability region.

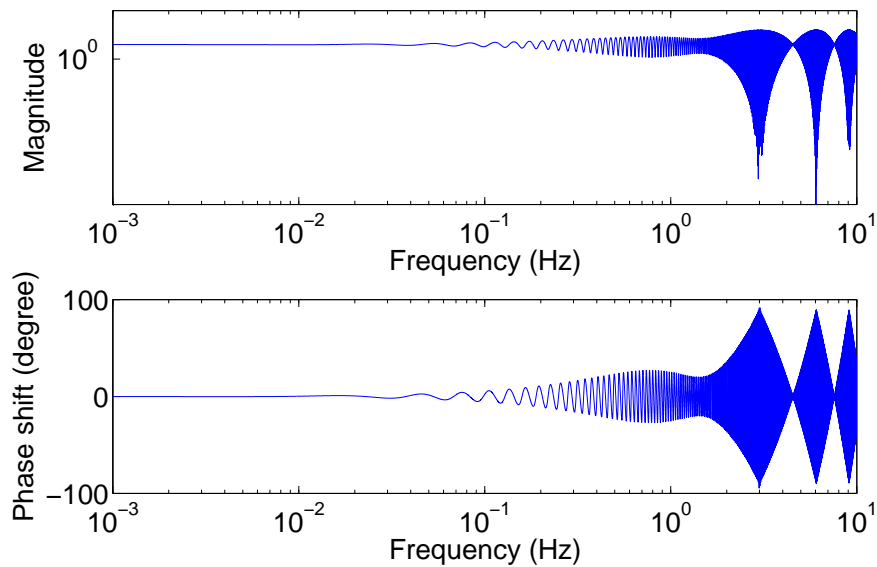


Figure 2-17. The magnitude and phase response of the dual arm locking sensor. The averaged light travel time is 33 s and the arm length mismatch is $\sim 1\%$. In this design a low-pass filter is added into the differential path to attenuate the phase shift. The low-pass filter ensures that the common arm dominates at all frequencies above $1/\Delta\tau$ such that the phase loss at sensor nulls is alleviated back to 90° . The controller is then only required to maintain enough phase margin at $1/(2\Delta\tau)$, which is well above the LISA band.

Without affecting the overall magnitude response, this filter ensures that the common arm dominates at all frequencies above $1/\Delta\tau$ such that the phase loss at sensor nulls is alleviated back to 90° . The magnitude and phase responses of this linear combination with the filtered differential arm are shown in Figure 2-17, where the low-pass filter has a single pole at 1 Hz. The first impulse null of this dual arm locking sensor is at $1/\Delta\tau$, while at $n/2\Delta\tau$ the magnitude response has a local minimum. The phase response shows that either at sensor nulls or at local minima, the sensor transfer function has a phase shift of approximately 90° . Since the dual arm locking sensor does not have any local minimum in the LISA band and at high frequencies both sensor nulls and local minima correspond to a $\sim 90^\circ$ phase shift, in this dissertation we do not distinguish the

sensor nulls and local minima for dual arm locking. In the following chapters the sensor nulls of dual arm locking are defined at frequencies of $n/(2\Delta\tau)$.

Taken together, the mapping vector of dual arm locking can be written as $\mathbf{S}_k(s) = [1 + \frac{E(s)}{s\Delta\tau}, 1 - \frac{E(s)}{s\Delta\tau}]$ and the dual arm locking sensor is given by

$$H_D(s) = P_+(s) + \frac{E(s)}{s\Delta\tau} P_-(s) \quad (2-44)$$

or represented in the angular frequency:

$$H_D(\omega) = 2 [1 - (\cos(\Delta\tau\omega) - E(i\omega)\text{sinc}(\Delta\tau\omega)) e^{-i\bar{\tau}\omega}]. \quad (2-45)$$

Another significant improvement compared to single arm locking is the fast decaying initial transients. Similar to single arm locking, the initial transients in dual arm locking are also 33 s quasi-periodic oscillations, but with a much shorter time constant.

In realistic LISA, the realization of dual arm locking requires the knowledge of the time-variable arm length mismatch. If the $\Delta\tau$ used in the dual arm locking configuration does not exactly match up the real-time arm length mismatch, the sensor transfer function will be slightly distorted with increased ripples at multiples of $1/\bar{\tau}$. The current knowledge is that even without on-board ranging the LISA arm length will be known to the accuracy of ~ 10 km, corresponding to an error in $\delta\tau \sim 30 \mu\text{s}$. This tiny error will only cause a negligible effect on the dual arm locking sensor and consequently the arm locking performance.

2.3.2.4 Sagnac arm locking

Sagnac arm locking, which resembles the configuration of the Sagnac combination for TDI, utilizes the entire LISA constellation to obtain the two interferometer outputs. Sagnac arm locking exploits the length mismatch in the perimeter of the constellation loop instead of two LISA arms. On the master spacecraft, the outgoing signal from the pre-stabilized laser is transmitted around the constellation loop counter-clockwise and then interfered with itself, while another outgoing signal from the other laser, which

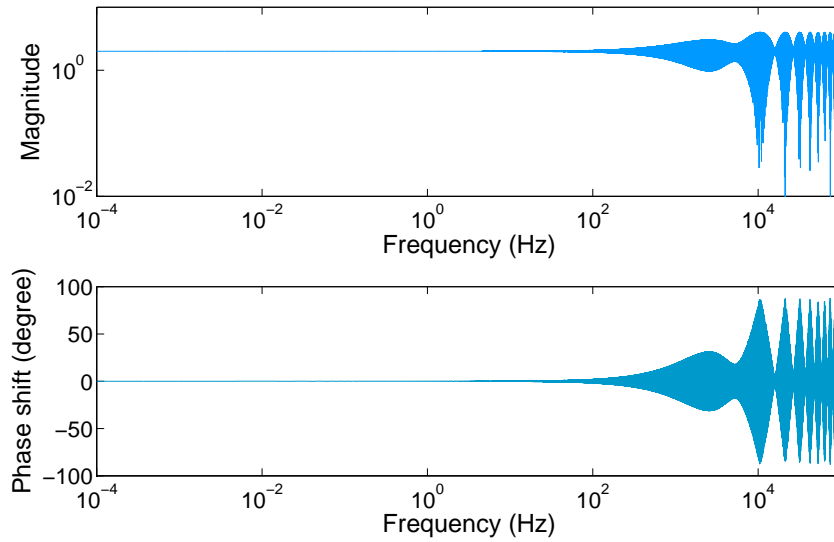


Figure 2-18. The magnitude and phase response of the Sagnac-based dual arm locking sensor. The averaged light travel time is 50 s and differential delay time is 47 μ s. The Sagnac arm locking sensor provides a very nice performance in terms of the bandwidth as both the magnitude and phase shift are entirely flat up to 100 Hz.

is phase-locked to the master laser via the backlink fiber, is transmitted around the loop clockwise and then also interfered with itself. When the phase-locked loop noise on all spacecraft is ignored, the two interferometer outputs in the Sagnac arm locking configuration are given by

$$\begin{aligned}\phi_{CCW}(t) &= \phi_0(t) - \phi_0(t - \tau_{12}) - \phi_0(t - \tau_{23}) - \phi_0(t - \tau_{31}) \\ \phi_{CW}(t) &= \phi_0(t) - \phi_0(t - \tau_{13}) - \phi_0(t - \tau_{32}) - \phi_0(t - \tau_{21})\end{aligned}\quad (2-46)$$

Therefore, the equivalent averaged delay time of these two phase measurements is approximately $\bar{\tau} \approx 50$ s and the equivalent differential delay time is approximately $\Delta\tau \approx 47$ μ s. Compared with the variable differential delay time in dual arm locking, these two values are very constant since the rotation of the constellation is continuous and always in one direction. By taking the two phase measurements, a Sagnac-based dual arm locking sensor can be configured with the transfer function shown in Figure 2-18.

The first null, according to the different light travel time $47 \mu s$, comes at 21 kHz, which allows an extremely high gain performance.

Despite the evident advantages described above, Sagnac arm locking has not been considered seriously by researchers. The main drawback is its complexity, which requires all six links to be operational simultaneously to construct the sensor signal. Also, the noise limitations and the Doppler impact of Sagnac-based dual arm locking are more significant than any other arm locking configurations. We will see more details of this in the following sections.

2.3.3 Frequency Pulling

So far, the discussions above on arm locking are limited to the sensor configuration, suppression gain and system stability under very idealized circumstances. In reality, the simple architecture of arm locking make it encounter several realistic issues. These known issues include the frequency pulling on the stabilized laser frequency due to the Doppler estimation error and various noise limitations such as clock noise, spacecraft jitter and shot noise that restrict the noise suppression performance.

2.3.3.1 Doppler impact on arm locking

Before the discussion on the issue of frequency pulling, we first look at a very brief introduction on how the phasemeter measures the phase of interferometry signals. More details on the principle of the phasemeter will be seen in Section 3.2.2. To measure the phase noise $\phi(t)$ of an input beat signal $S(t) = A(t) \sin(2\pi\nu_L t + \phi(t))$, the phasemeter needs to provide an internal oscillation $S'(t) = \sin(2\pi\nu' t + \phi'(t))$ which then tracks the input signal via phase-locking. Therefore, the preset frequency of the local oscillation ν' needs to be close enough to the nominal frequency of the beat signal ν_L . The feedback signal of this phase-locked loop, when represented as a frequency, is given by

$$f_{\text{feedback}}(t) \approx \nu_L - \nu' + \frac{d\phi(t)}{dt}, \quad (2-47)$$

where $\frac{d\phi(t)}{dt}$ is essentially the frequency noise of the input signal. This frequency will be fed back to the internal oscillation for phase-locking; also it can be integrated to generate the phase fluctuations. Thus, if $\nu_L \neq \nu'$, a linear drift caused by the frequency offset will be seen in the measured phase noise.

This frequency offset also exists in the long arm measurement in LISA: During the transmission of the laser field, the heterodyne frequency of the measurement is modulated by the Doppler shift due to the relative spacecraft motion. The time-variable relative velocities in each arm will be up to 18 m/s, corresponding to a time-variable Doppler shift of up to 17 MHz. Consequently, the frequency ν_L of the laser beat signal depends on the known offset ν_0 used at the far-end phase-locked loop and the not so well known Doppler shift $\nu_D(t)$. Thus the phase of the heterodyne beat signal received by the phasemeter is given by

$$\phi_L(t) = 2\pi(\nu_0 + \nu_D(t))t + \Phi_I(t) - \Phi_I(t - \tau(t)). \quad (2-48)$$

Ideally, the phasemeter would be required to demodulate the beat signal with the difference frequency of the two lasers ($\nu_0 + \nu_D(t)$). Consequently, the preset frequency at the phasemeter would be required to be updated in real-time due to the time-variable Doppler shift $\nu_D(t)$, which is unfortunately difficult to estimate at a very accurate level. Actually, LISA will not estimate the Doppler frequency in real-time when arm locking is in the steady state and a time-variable Doppler frequency error $\Delta\nu_D$ is therefore unavoidable. It appears to be possible to limit the Doppler frequency error to ~ 20 Hz per 200 s averaging time by introducing additional functionality in on-board data processing. A more detailed description of Doppler frequency errors in LISA will be seen in Section 6.1.

The Doppler frequency error will manifest itself as the remaining frequency offset in the phase measurement and then will be integrated up in the arm locking controller, which causes a frequency pulling in the stabilized laser frequency. Generally a linear

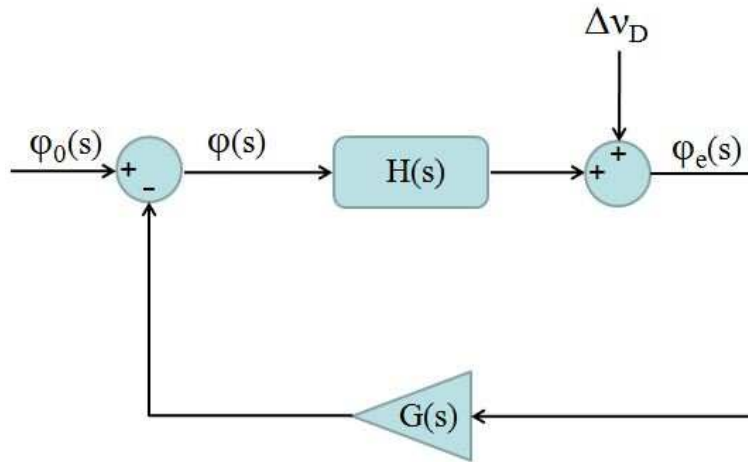


Figure 2-19. A generic single arm locking loop with a Doppler frequency error in the Laplace domain. The Doppler frequency error $\Delta\nu_D$ is added to the error signal $\varphi_e(s)$ during the demodulation of the phasemeter. This Doppler error will be seen by the controller $G(s)$ and may cause a frequency drift in the stabilized phase $\varphi(s)$.

drift in frequency is mostly harmless in the data post-processing. However, a large frequency drift introduces additional requirements on the tunability of the arm locked laser and consequently on that of all six lasers in the LISA constellation. In the following section we will quantify the frequency pulling induced by Doppler errors by investigating the frequency response of a generic arm locking loop.

2.3.3.2 Frequency pulling rate

Figure 2-19 shows a generic single arm locking loop with a Doppler frequency error input in the Laplace domain. The transfer functions of the single arm locking sensor and controller are $H(s)$ and $G(s)$, respectively. For single arm locking, the Doppler error is introduced in the demodulation at the phasemeter right before the controller. In this diagram, the closed-loop transfer function from the Doppler error input to the stabilized laser noise output is given by

$$TF_D(s) = \frac{G(s)}{1 + H(s)G(s)}. \quad (2-49)$$

In a standard control loop when the controller yields the high gain limit $G(s) \rightarrow \infty$, the transfer function is reduced to

$$TF_D(s) \approx \frac{1}{H_1(s)} \approx \frac{1}{\tau s} \quad (\text{at very low frequencies}). \quad (2-50)$$

This indicates for the Doppler error input, the frequency response of a DC-coupled single arm locking loop is equivalent to an integrator, which accumulates the Doppler error over time and causes a drift in the output frequency. In the time domain, the instantaneous output frequency is given by the convolution between the instantaneous Doppler error input and the transfer function described above. Over short time intervals the Doppler error is constant and the laser frequency changes by

$$\begin{aligned} \Delta\nu_L(t) &= \frac{1}{\tau} \int \Delta\nu_D dt \\ &= \frac{\Delta\nu_D}{\tau} t. \end{aligned} \quad (2-51)$$

One potential solution is to reduce the controller gain gradually below the lower limit (3×10^{-5} Hz) of the LISA band, which is known as AC-coupling. This is because the Doppler shift frequency caused by spacecraft motions is a very slow oscillation at $\sim 10^{-8}$ Hz and the same case is for Doppler frequency errors.³ With such an AC-coupled controller the Doppler frequency error will not couple into the arm locking loop. However, the trade-off is that the impulse response of the AC-coupled controller to a Doppler error will show up in the lock acquisition and become a part of initial transients. Relevant experimental and numerical demonstrations will be seen in Chapter 6 and here we only evaluate the frequency pulling rate in the steady state. In the low

³ Strictly speaking, the Doppler frequency error oscillates at the same frequency as the Doppler shift frequency only in the steady state of arm locking but not during the lock acquisition. See Chapter 6 for more details.

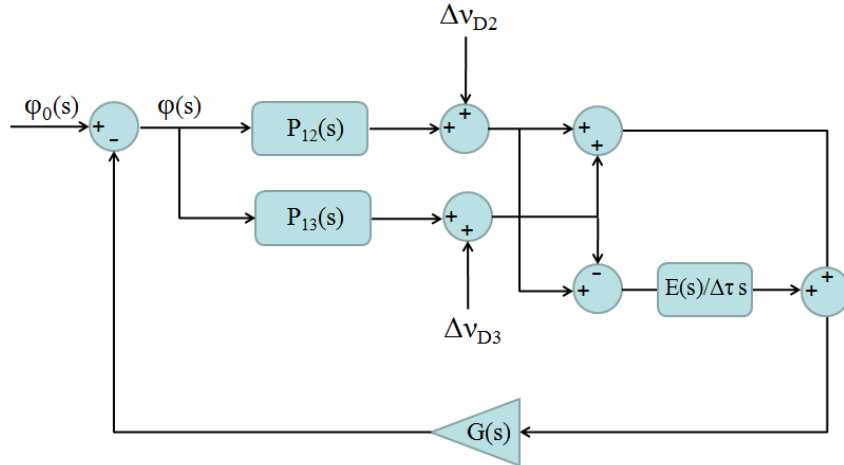


Figure 2-20. A generic dual arm locking loop with Doppler frequency errors in the Laplace domain. Two independent Doppler frequency errors are generated at two phasemeters on the local spacecraft. When the two phase measurements are added and subtracted in the dual arm locking sensor, the Doppler frequency errors are also added and subtracted. The differential Doppler error will be accumulated by the integrator in the differential path.

gain limit ($H(s)G(s) \rightarrow 0$ at very low frequencies), we have

$$TF_D(s) \approx G(s) \quad (\text{at very low frequencies}). \quad (2-52)$$

This means in the low gain limit, the effect on output frequency noise is simply the input Doppler error multiplied with the controller gain in the low frequency range. Thus, in the presence of an AC-coupled controller the Doppler error will not be accumulated by the controller and consequently the residual effect is no more than an insignificant offset added to the output laser frequency ⁴.

Figure 2-20 shows that in dual arm locking the two arms generate two independent Doppler errors $\Delta\nu_{D2}$ and $\Delta\nu_{D3}$, which can be combined to construct a common and a

⁴ The residual effect depends on the specific magnitude response of $G(s)$ at very low frequencies. Here for simplicity we assume that $G(s)$ provides a constantly low gain down to DC.

differential Doppler error. We define

$$\begin{aligned}\Delta\nu_{D+} &= \Delta\nu_{D2} + \Delta\nu_{D3}, \\ \Delta\nu_{D-} &= \Delta\nu_{D2} - \Delta\nu_{D3}.\end{aligned}\tag{2-53}$$

They will show up in the common and differential arm sensors independently and will be amplified by the closed-loop gain in each path:

$$TF_{D+}(s) = \frac{G(s)}{1 + H_D(s)G(s)},\tag{2-54}$$

$$TF_{D-}(s) = \frac{G(s)E(s)}{\Delta\tau s[1 + H_D(s)G(s)]}.\tag{2-55}$$

In the common arm, $TF_{D+}(s)$ is approximately equal to $1/H_D(s)$ in the high gain limit. Since the magnitude of the dual arm locking sensor is flat at low frequencies, a common Doppler error will only cause a frequency offset in dual arm locking. This characteristics is to be distinguished from the frequency response of a common arm locking loop to a common Doppler error. In that case the arm locking sensor is replaced with $H_+(s) = P_+(s)$. Consequently, in the high gain limit a common Doppler error $\Delta\nu_{D+} = \Delta\nu_{D2} + \Delta\nu_{D3}$ will cause the frequency pulling with a drift rate of $\Delta\nu_{D+}/2\bar{\tau}$.

In the differential arm, we have $E(s) \approx 1$ and $H_D(s) \approx 2$ at low frequencies and in the high gain limit the equation approaches $1/2\Delta\tau s$. This frequency response corresponds to a frequency drift rate given by

$$\left(\frac{d\nu_L}{dt}\right)_D = \frac{\Delta\nu_{D-}}{2\Delta\tau}.\tag{2-56}$$

Since this drift rate is inversely proportional to the differential delay time, it becomes undesirable when the arm length mismatch is very small, which is one of the main disadvantages of dual arm locking. To reduce this frequency pulling, several modifications to the controller have been proposed, including adding high-pass filters to suppress the controller gain below the LISA band.

2.3.3.3 Modified dual arm locking

Modified dual arm locking was proposed by our group and, independently, by Kirk McKenzie to solve the Doppler-induced frequency pulling problem as well as to enhance the noise suppression performance [13]. The concept of modified dual arm locking is to maintain the gain advantages of dual arm locking and recover the frequency pulling characteristics of common arm locking by amplifying the common arm sensor below $1/\bar{\tau}$ and keeping the dual arm sensor above $1/\bar{\tau}$. This combination retains the overall flat transfer function of the dual arm locking sensor below $1/2\Delta\tau$ and significantly reduces the frequency pulling due to a Doppler error.

The modified dual arm locking sensor is constructed based on a linear combination of common arm locking sensor and dual arm locking sensor:

$$H_{MD}(s) = F_C(s)P_+(s) + F_D(s)H_D(s), \quad (2-57)$$

where $F_C(s)$ and $F_D(s)$ are two filters designed in a manner that the common arm sensor dominates at frequencies below $1/\Delta\tau$ and the dual arm locking sensor gradually dominates above it. Although the design of $F_C(s)$ and $F_D(s)$ is not unique, $F_C(s)$ is essentially a low-pass filter with one pole at DC and $F_D(s)$ is a high-pass filter with a corner frequency around $\bar{\tau}$. Both filters require an appropriate gain to smooth the crossover between the two sensors. An example of the specific design of $F_C(s)$ and $F_D(s)$ is provided by Kirk McKenzie. The low-pass filter $F_C(s)$ has a pole at DC and a lead compensator with a zero at $5/13\bar{\tau}$ and a pole at $5/2\bar{\tau}$. The high-pass filter $F_D(s)$ has four zeroes at DC, two poles at $7/10\pi\bar{\tau}$, $11/20\pi\bar{\tau}$ and two poles at $1/90\pi\bar{\tau}$. Here we provide another relatively simpler design for our hardware simulations (See Section 5.3 for more details). The transfer function of our modified dual arm locking sensor is illustrated in Figure 2-21, where both the magnitude response and the phase shift are maintained in the LISA band. We also plot the magnitude and phase response of the dual and common components that constitute the modified dual arm locking sensor in

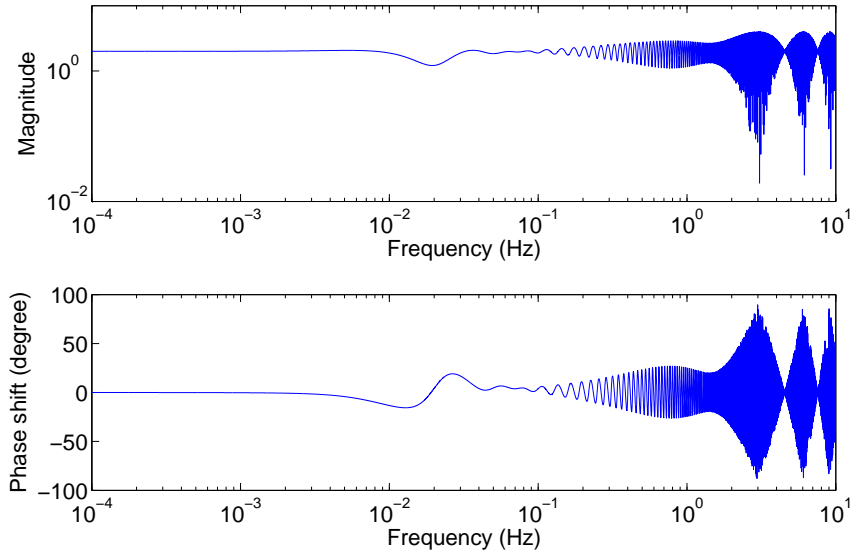


Figure 2-21. The magnitude and phase response of the modified dual arm locking sensor. The averaged light travel time is 33 s and the arm length mismatch is $\sim 1\%$. The modified dual arm locking sensor retains the flatness of the dual arm locking sensor transfer function. At frequencies near $1/\bar{\tau} = 30$ mHz the transfer function has some distortions coming from the crossover between the common and dual arm components. (See Figure 2-22)

Figure 2-22. The figure shows that the common arm component dominates frequencies below $1/\bar{\tau}$ while the dual arm component dominates frequencies above it.

Eq. 2-57 can also be written as a linear combination of common arm sensor and differential arm sensor:

$$\begin{aligned}
 H_{MD}(s) &= F_C(s)P_+(s) + F_D(s)\left[P_+(s) + \frac{E(s)}{s\Delta\tau}P_-(s)\right] \\
 &= [F_C(s) + F_D(s)]P_+(s) + \frac{E(s)F_D(s)}{s\Delta\tau}P_-(s) \\
 &= H_+(s)P_+(s) + H_-(s)P_-(s).
 \end{aligned} \tag{2-58}$$

It is easy to verify that the mapping vector of the modified dual arm locking sensor is given by $\mathbf{S}_k(s) = [H_+ + H_-, H_+ - H_-]$, where $H_+(s) = F_C(s) + F_D(s)$ and $H_-(s) = \frac{E(s)F_D(s)}{s\Delta\tau}$. Actually this general formalism can also be adapted to the common arm locking and

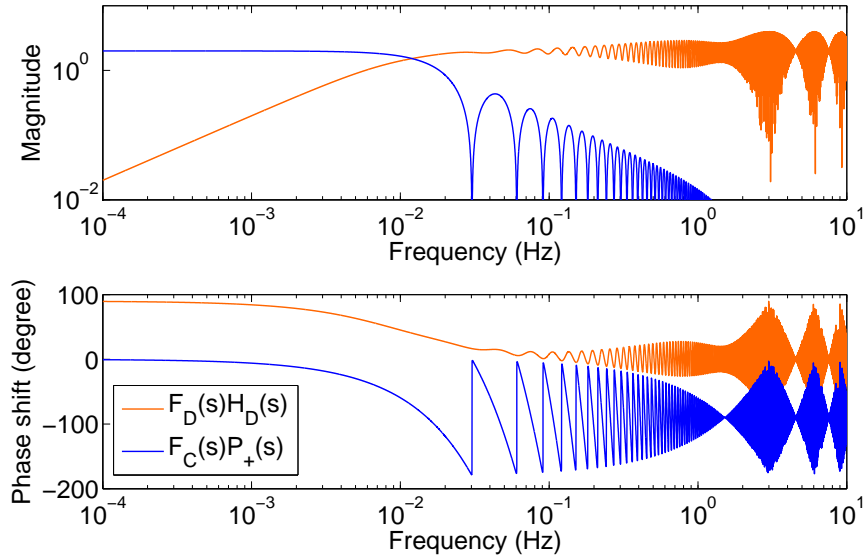


Figure 2-22. The magnitude and phase response of the dual and common arm components that constitute the modified dual arm locking sensor in Figure 2-21. The dual arm component is high-pass filtered and the common arm component is low-pass filtered. Therefore, the common arm component will dominate the frequencies below $1/\bar{\tau}$ and the dual arm component will dominate the frequencies above it. The phase shift of the common arm component in the low frequency region needs to be attenuate to zero to maintain the overall transfer function.

dual arm locking sensor, with $H_+(s) = 1$, $H_-(s) = 0$ (common) and $H_+(s) = 1$, $H_-(s) = \frac{E(s)}{s\Delta\tau}$ (dual).

Figure 2-23 shows the Doppler frequency errors enter the control system of modified dual arm locking. Following the the procedure in the previous section, in the high gain limit the closed-loop transfer functions to the common and differential Doppler error are given by

$$\begin{aligned}
 TF_{D+}(s) &= \frac{G(s)H_+(s)}{1 + H_{MD}(s)G(s)} \approx \frac{1}{2}H_+(s), \\
 TF_{D-}(s) &= \frac{G(s)H_-(s)}{1 + H_{MD}(s)G(s)} \approx \frac{1}{2}H_-(s).
 \end{aligned} \tag{2-59}$$

Since the specific expressions of H_+ and H_- depend on the customized design of filters $F_C(s)$ and $F_D(s)$, the frequency responses to the Doppler errors could be

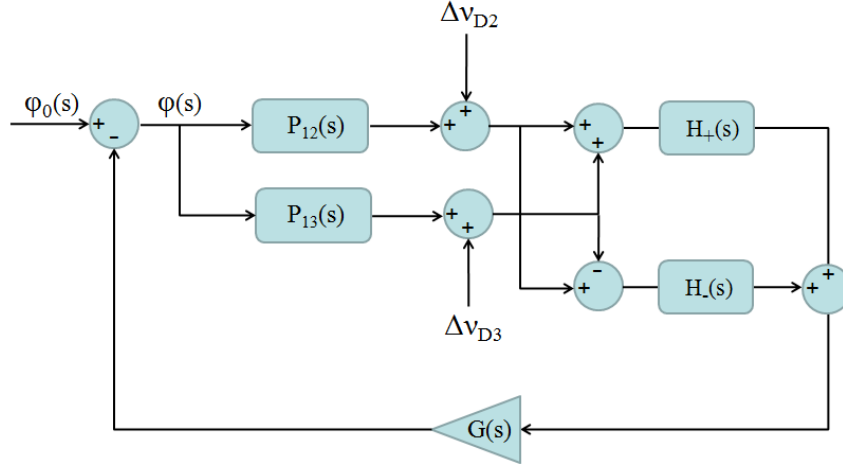


Figure 2-23. A generic modified dual arm locking loop with Doppler frequency errors in the Laplace domain. Compared with Figure 2-20, two filters are placed in the common and differential path individually. The high-pass filter in the differential arm path eliminates the frequency pulling due to the differential Doppler error, while the low-pass filter design in the common arm path allows the frequency pulling due to the common Doppler error. Note that it is also possible to high-pass filter the common arm path to eliminate the frequency pulling completely, which is essentially equivalent to an AC-coupled controller.

complicated to calculate. However, as we know that essentially $F_C(s)$ is a low-pass filter with one pole at DC and $F_D(s)$ is a high-pass filter with a corner frequency around $1/\bar{\tau}$, the noise limitation can be roughly estimated using a simplified design of $F_C = \frac{1}{s\bar{\tau}}$ and $F_D = \frac{s}{s+2\pi/\bar{\tau}}$. Thus we have

$$\begin{aligned}
 H_+(s) &= \frac{1}{\bar{\tau}s} + \frac{s}{s+2\pi/\bar{\tau}}, \\
 H_-(s) &= \frac{1}{s\Delta\tau} \frac{s}{s+2\pi/\bar{\tau}} = \frac{1}{\Delta\tau} \frac{1}{s+2\pi/\bar{\tau}}.
 \end{aligned} \tag{2-60}$$

We plot the magnitude responses of $H_+(s)$ and $H_-(s)$ with $\bar{\tau} = 33 \text{ s}$ and $\Delta\tau = 0.16 \text{ s}$ in Figure 2-24. The magnitude responses of $H_+(s)$ and $H_-(s)$ feature a slope of $1/s\bar{\tau}$ and $1/s\Delta\tau$, respectively. At low frequencies $f \ll 1/\bar{\tau}$, $H_-(s)$ flattens out and approaches a constant value of $\bar{\tau}/(2\pi\Delta\tau)$. At high frequencies $f \gg 1/\bar{\tau}$, $H_+(s)$ flattens out and approaches 1.

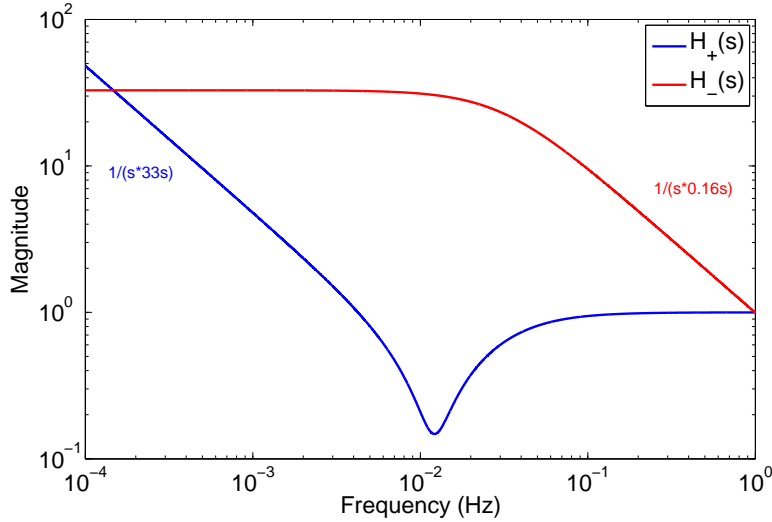


Figure 2-24. The magnitude response of $H_+(s)$ and $H_-(s)$ with $\bar{\tau} = 33$ s and $\Delta\tau = 0.16$ s for modified dual arm locking. In this design the $F_D(s)$ only has a single zero at DC, which makes the magnitude response of $H_-(s)$ flat at low frequencies. A more careful design of $F_D(s)$ should provide a steeper slope to sufficiently suppress the $H_-(s)$ at low frequencies.

If we only consider the steady state, the Doppler frequency error is an oscillation at frequencies below the LISA band, where the the magnitude responses of $H_+(s)$ and $H_-(s)$ approximate to $1/s\bar{\tau}$ and $\bar{\tau}/(2\pi\Delta\tau)$. Consequently, the differential Doppler error $\Delta\nu_{D-}$ will not cause any frequency pulling but an insignificant frequency offset. The dominant frequency pulling rate, which is now completely attributed to the common Doppler error $\Delta\nu_{D+}$, is given by

$$\left(\frac{d\nu_L}{dt}\right)_{MD} = \frac{\Delta\nu_{D+}}{2\bar{\tau}}. \quad (2-61)$$

Compared with dual arm locking, this frequency pulling rate is inversely proportional to the average delay time, which is obviously a substantial improvement when the arm length mismatch is small. However, it should be noted that the common Doppler error $\Delta\nu_{D+}$ may also be much larger than the differential Doppler error $\Delta\nu_{D-}$ by two orders of magnitude, especially during the initial estimations of Doppler errors. This fact indicates that modified dual arm locking is not always superior to dual arm locking in terms of

frequency pulling. In realistic LISA, it should be allowed to switch to the proper arm locking configuration between them according to the real-time arm length mismatch.

2.3.4 Integration with Tunable Pre-stabilization References

Before the frequency pulling caused by Doppler errors in arm locking was realized, the integration of arm locking with pre-stabilization subsystems was already considered because this combination would provide more noise suppressions to relax the burden on TDI. The incorporation of arm locking with a pre-stabilization subsystem requires the reference to be tunable because the lock points for the local reference and the arm locking reference are not generally the same. For instance, a standard Pound-Drever-Hall setup does not provide tunability between two resonant frequencies of the reference cavity; therefore, some modification to the PDH setup must be present to make the resonant frequency adjustable. Now the discovery of frequency pulling increases the required tuning range for the local reference. A reasonable tuning range of the reference should be well larger than the expected frequency pulling range of the laser to avoid possible pre-stabilization issues. Given a cavity pre-stabilized laser and 200 s averaging estimation time, the frequency pulling on the stabilized laser is on the level of a few MHz, which means the tuning range of the tunable reference should be at least at tens of MHz.

Several tunability options with a sufficient tuning range have been suggested for arm locking with different pre-stabilization schemes. Here we will discuss three feasible options: Arm locking with Pound-Drever-Hall stabilization, arm locking with Mach-Zehnder stabilization and arm locking without any pre-stabilization.

2.3.4.1 Arm locking with Pound-Drever-Hall stabilization

For Pound-Drever-Hall stabilization a simple approach is to replace the fixed optical cavity with a PZT tunable cavity, which is actuated by the arm locking feedback signal. As shown in Figure 2-25, by tuning the length of the cavity the central frequency of the stabilized laser can be tuned and further stabilized by the arm locking controller.

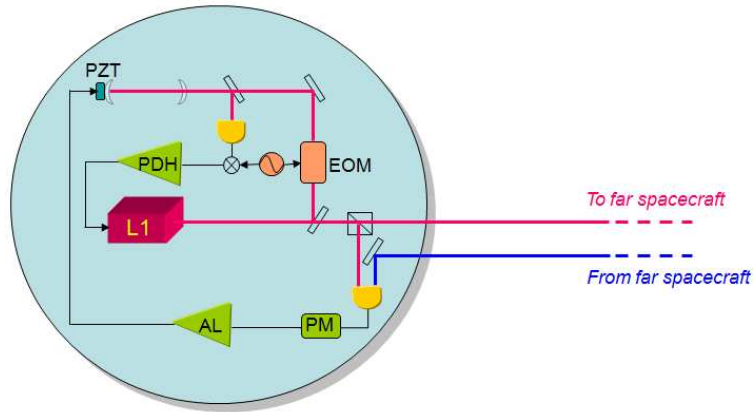


Figure 2-25. The integration of arm locking and Pound-Drever-Hall technique using a PZT actuated cavity as a tunable reference. In this setup the laser is locked to the PZT actuated cavity via the PDH method. The arm locking feedback signal is used to drive the PZT to control the cavity length and thereby the resonant frequency.

The advantage of using a PZT cavity is that the implementation is simple such that the change to the pre-stabilization subsystem is minimized. A benchtop verification of this method is described in Section 4.3.2, where more details will be explained.

A second approach is known as sideband locking, which is illustrated in Figure 2-26. In this approach the RF sideband generated by the EOM is locked to a fixed optical cavity via standard Pound-Drever-Hall technique and the local oscillator driving the EOM is tuned by the arm locking feedback signal. Therefore the tuning of the modulation/demodulation RF signal allows the tuning of the central frequency of the stabilized laser. This method requires a high band phase modulator/demodulator to replace the original local oscillator, but no modification is needed for the resonant cavity. Relevant experiments are described in Section 4.3.3.

As shown in Figure 2-27, it is also possible to keep the Pound-Drever-Hall stabilization completely untouched by introducing an auxiliary laser that is phase-locked to the cavity stabilized laser with an frequency offset. Similar to the sideband locking, the tunability is accomplished via the arm locking feedback signal tuning the heterodyne frequency of the phase-locked loop. This configuration is easy to demonstrate on a

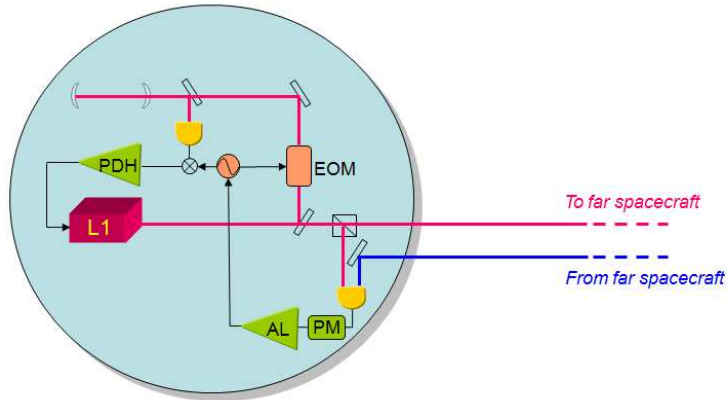


Figure 2-26. The integration of arm locking and Pound-Drever-Hall technique using a fixed cavity locked to the sideband. In this setup the sideband frequency of the laser is locked to the fixed cavity via the PDH method. The arm locking feedback signal is used to adjust the modulation/demodulation RF signal that drives the EOM.

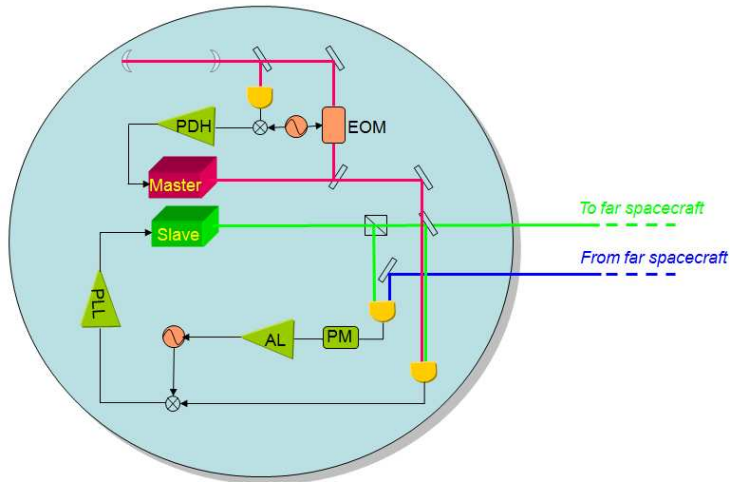


Figure 2-27. The integration of arm locking and Pound-Drever-Hall technique using an auxiliary phase-locked laser. In this setup an auxiliary laser is heterodyne phase-locked to the cavity stabilized laser. The arm locking feedback signal is used to adjust the local oscillator that drives the PLL.

benchtop but would require an additional laser in realistic LISA. The experimental demonstration is described in Section 4.3.1.

It is also worth noting that in all these setups, the arm locking feedback signal is not necessarily used to only adjust the actuators in the pre-stabilization setup; instead, it can also be directly added to the feedback signal from the PDH controller to correct the laser

frequency. In practice, the arm locking feedback signal will be electronically split up and enters the pre-stabilization loop at the two points described above; the laser frequency therefore will be stabilized by their combination. The advantage of this configuration is that the performance of the arm locking system is not limited by the bandwidth of the pre-stabilization loop.

2.3.4.2 Arm locking with Mach-Zehnder stabilization

In addition to the standard Pound-Drever-Hall stabilization, the integration of arm locking and other kinds of pre-stabilization subsystem has also been considered. In particular we already mentioned the integration of arm locking with Mach-Zehnder stabilization in Section 2.2.2.2. Unlike the widely discrete lock-points in the PDH stabilization, Mach-Zehnder stabilization provides an inherent frequency tunability described in Eq. 2–26, which makes the integration much simpler. In the integration the arm locking feedback signal is not only used to adjust the phase of the local oscillator that demodulates the heterodyne beat signal, but it is also directly added to the feedback signal in the Mach-Zehnder stabilization. The second adjustment ensures that the high-bandwidth arm locking performance can be retained and not affected by the low bandwidth of the Mach-Zehnder setup. With the controller designed in Ref. [13], the expected performance meets the TDI capability requirement with a margin greater than 50 at 1 Hz and 800 at 3 Hz.

2.3.4.3 Arm locking only

It is also possible to have arm locking take over the entire stabilization of the laser frequency without any tunable pre-stabilization reference. In such an option the arm locking feedback signal is directly sent back to the frequency actuator of the laser controller; therefore the optical bench subsystem is totally untouched. Analytical studies indicate that even without any pre-stabilization schemes, the dual/modified dual arm locking will provide sufficient noise suppressions and meet the TDI capability requirement across the entire LISA band in most time of a year [13]. The only period

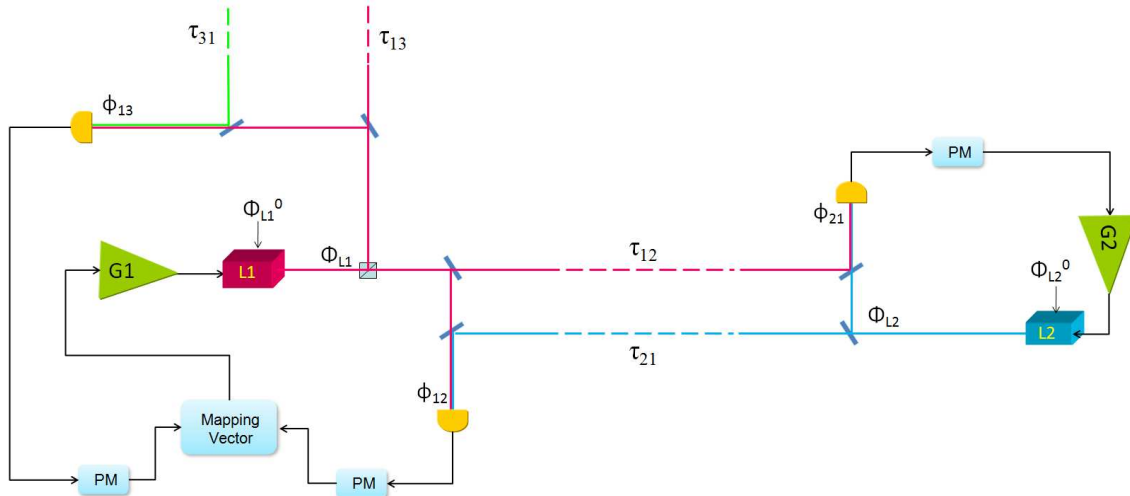


Figure 2-28. Michelson-typed arm locking configuration with the phase-locked laser at the far spacecraft.

when the arm locking performance is insufficient only lasts for 30 min, twice a year. This happens when the arm length mismatch is less than 12 km. In the next section we will analyze the noise limitations in arm locking and identify when they will become a problem.

2.3.5 Arm Locking Limitations

In this section we consider the realistic limitations to the noise suppression performance of arm locking. In reality, the stabilized laser frequency noise is dominated by several expected noise sources. One of the nominal noise sources is the transponder noise which comes from the phase-locking of the far laser. The transponder noise is adequately removed in TDI algorithms; however, arm locking does not have any similar mechanism to take care of it. We will analytically investigate how the transponder noise will affect the arm locking performance. Also, the effects of other significant noise sources, including noise of ultra-stable oscillators (USO's), random spacecraft motion, shot noise and technical noise will be discussed.

2.3.5.1 Limited controller gain in far-end PLL

Figure 2-28 illustrates the generic arm locking configuration with the incorporation of the phase-locked laser at the far spacecraft, where the limited controller gain introduces

a transponder noise. In the analysis we first assume the far-end PLLs are closed while the arm locking loop is still open. Based on Eq. 2–29, in the presence of a gain limited far-end PLL, the phase measurement of the long arm interferometry at the local spacecraft SC_1 is given by

$$\phi_{1i}(s) = \Phi_{L1}^0 \left(1 - \frac{G_i}{1 + G_i} e^{-s\tau_i} \right) - \frac{1}{1 + G_i} \Phi_{Li}^0 e^{-s\tau_{i1}}. \quad (2-62)$$

The first term is directly related to the initial phase noise Φ_{L1}^0 of the pre-stabilized local laser. The second term is an additional random noise source (the residual noise unsuppressed by the far-end PLL) since Φ_{L1}^0 and Φ_{Li}^0 are uncorrelated. Therefore, we can still define the LISA arm transfer function, which yields the first term divided by the the initial phase noise Φ_{L1}^0 :

$$P_{1i}(s) = 1 - \frac{G_i}{1 + G_i} e^{-s\tau_i}, \quad (2-63)$$

which would be reduced to Eq. 2–30 when $G_i \gg 1$. The definition of the arm locking sensor $H(s)$ remains the same as Eq. 2–33, but now it involves the PLL controller gain G_i , $i = 2, 3$.

When the arm locking loop is closed, the stabilized phase noise of the local laser is given by

$$\Phi_{L1}(s) = \Phi_{L1}^0 - \frac{G_1}{1 + G_1 H} \mathbf{S}_k \cdot \boldsymbol{\Phi}_1, \quad (2-64)$$

where \mathbf{S}_k is the mapping vector and $\boldsymbol{\Phi}_1$ is a 2×1 phase vector describing the two interferometer outputs. (See Section 2.3.1)

Now we calculate the stabilized phase noise depending on specific mapping vectors individually. For single arm locking $\mathbf{S}_k = [1, 0]$, Eq 2–64 yields

$$\begin{aligned} \Phi_{L1}(s) &= \Phi_{L1}^0 - \frac{G_1}{1 + G_1 H} \left(\Phi_{L1}^0 \left(1 - \frac{G_2}{1 + G_2} e^{-s\tau_2} \right) - \frac{1}{1 + G_2} \Phi_{L2}^0 e^{-s\tau_{21}} \right) \\ &= \frac{1}{1 + G_1 H} \Phi_{L1}^0 + \frac{G_1}{1 + G_1 H} \frac{1}{1 + G_2} \Phi_{L2}^0 e^{-s\tau_{21}}. \end{aligned} \quad (2-65)$$

The first term of Eq. 2–65 demonstrates that the initial phase noise Φ_{L1}^0 is suppressed by the open-loop gain G_1H . The second term reflects the closed-loop response of single arm locking to the transponder noise $\frac{1}{1+G_2}\Phi_{L2}^0$. Essentially it is equivalent to a Doppler frequency error introduced during the light travel as they both correspond to a closed-loop response of $\frac{G_1}{1+G_1H}$ except for a trivial phase delay $e^{-s\tau_{21}}$. In the high gain limit of the arm locking controller, the closed-loop response approximates to $1/H \approx 1/\tau_S$, which increases the level of $\Phi_{L1}(s)$ by the amount of the accumulated transponder noise.

In the case of dual arm locking $\mathbf{S}_k = [1 + \frac{E(s)}{\Delta\tau_S}, 1 - \frac{E(s)}{\Delta\tau_S}]$, if we use $E(s) \approx 1$ in the LISA frequency band, Eq 2–64 yields

$$\begin{aligned}\Phi_{L1}(s) &= \Phi_{L1}^0 - \frac{G_1}{1+G_1H} \left[1 + \frac{1}{\Delta\tau_S}, 1 - \frac{1}{\Delta\tau_S}\right] \cdot \begin{bmatrix} \Phi_{L1}^0 \left(1 - \frac{G_2}{1+G_2} e^{-s\tau_2}\right) - \frac{1}{1+G_2} \Phi_{L2}^0 e^{-s\tau_{21}} \\ \Phi_{L1}^0 \left(1 - \frac{G_3}{1+G_3} e^{-s\tau_3}\right) - \frac{1}{1+G_3} \Phi_{L3}^0 e^{-s\tau_{31}} \end{bmatrix} \\ &= \frac{1}{1+G_1H} \Phi_{L1}^0 - \frac{1}{1+G_2} \Phi_{L2}^0 e^{-s\tau_{21}} \left(1 + \frac{1}{\Delta\tau_S}\right) - \frac{1}{1+G_3} \Phi_{L3}^0 e^{-s\tau_{31}} \left(1 + \frac{1}{\Delta\tau_S}\right).\end{aligned}\tag{2-66}$$

The first term represents the idealized noise suppression. The additional effects of the transponder noise, which are described by the other two terms, can be written as

$$\delta\varphi_{L1}(s) = \frac{1}{\Delta\tau_S} \left(\frac{1}{1+G_3} \Phi_{L3}^0 e^{-s\tau_{31}} - \frac{1}{1+G_2} \Phi_{L2}^0 e^{-s\tau_{21}} \right) - \left(\frac{1}{1+G_3} \Phi_{L3}^0 e^{-s\tau_{31}} + \frac{1}{1+G_2} \Phi_{L2}^0 e^{-s\tau_{21}} \right).\tag{2-67}$$

The first term in Eq. 2–67 indicates that in the differential arm path the difference between the transponder noises on two arms will be accumulated and scaled with $1/\Delta\tau$. The second term indicates that in the common arm path the sum of the transponder noises will be directly subtracted, which is negligible in comparison to the differential arm path.

In the presence of a modified dual arm locking sensor $\mathbf{S}_k = [H_+ + H_-, H_+ - H_-]$, $H_+(s) = F_C(s) + F_D(s)$, $H_-(s) = \frac{E(s)F_D(s)}{s\Delta\tau}$, the stabilized phase noise is given by

$$\Phi_{L1}(s) = \Phi_{L1}^0 - \frac{G_1}{1 + G_1 H} [H_+ + H_-, H_+ - H_-] \cdot \begin{bmatrix} \Phi_{L1}^0 P_{12} + \delta\varphi_{L2} \\ \Phi_{L1}^0 P_{13} + \delta\varphi_{L3} \end{bmatrix}, \quad (2-68)$$

where $P_{1i} = 1 - \frac{G_i}{1+G_i} e^{-s\tau_i}$ is the arm transfer function and $\delta\varphi_{Li} = \frac{1}{1+G_i} \Phi_{Li}^0 e^{-s\tau_i}$ is the transponder noise delayed by the returning travel time.

Eq. 2-68 yields

$$\begin{aligned} \Phi_{L1}(s) &= \Phi_{L1}^0 - \frac{G_1}{1 + G_1 H} (H_+ P_+ + H_- P_-) \Phi_{L1}^0 + \frac{G_1}{1 + G_1 H} [H_+(\delta\varphi_{L2} + \delta\varphi_{L3}) + H_-(\delta\varphi_{L2} - \delta\varphi_{L3})] \\ &\approx \frac{1}{1 + G_1 H} \Phi_{L1}^0 + \frac{H_+}{H} (\delta\varphi_{L2} + \delta\varphi_{L3}) + \frac{H_-}{H} (\delta\varphi_{L2} - \delta\varphi_{L3}). \end{aligned} \quad (2-69)$$

This indicates the sum of the transponder noises on two arms will be multiplied with $\frac{H_+}{H}$ while the difference between them will be multiplied with $\frac{H_-}{H}$, which is again equivalent to the frequency response to the Doppler errors given by Eq. 2-59. Here we still use the transfer functions of $H_+(s)$ and $H_-(s)$ determined by Eq. 2-60 to analyze the transponder noise floor.

Since the transponder noises $\delta\varphi_{L2}$ and $\delta\varphi_{L3}$ are uncorrelated, in terms of the noise amplitude we have $\delta\varphi_{L2} + \delta\varphi_{L3} \sim \delta\varphi_{L2} - \delta\varphi_{L3}$. Therefore, as shown in Figure 2-24 the differential noise from the differential arm path will dominate most of the LISA band until the crossing of H_+ and H_- at about 0.2 mHz. For frequencies below the crossing the common noise will dominate. Compared with dual arm locking, the noise limitation below $1/\bar{\tau}$ has been decreased from $1/s\Delta\tau$ to the dominant term between $\bar{\tau}/(2\pi\Delta\tau)$ and $1/s\bar{\tau}$. In realistic LISA, the filter F_D can be designed to have a slope steeper than s such that the magnitude of H_- will roll off faster at low frequencies and the common noise will start to dominate at a higher frequency.

In this section we have demonstrated the analytical transponder noise limitation solely caused by the finite gain of the PLL controller. In reality, the transponder noise

of the far-end PLL is primarily contributed other realistic noise sources, such as the frequency noise that enters the ultra-stable oscillator driving the heterodyne PLL. The frequency noise of the USO, or more frequently called clock noise, will also become a part of the transponder noise and may further compromise the arm locking performance. More details will be discussed in the next section.

2.3.5.2 Realistic noise sources in arm locking

The limitation of arm locking performance depends on several realistic noise sources, as well as certain arm locking configurations that determine how the noise sources will contribute to the stabilized laser frequency. Basically, the formalism used to evaluate the effect of the transponder noise can be directly adapted to quantify the arm locking limitation caused by these noise sources, only with different error points. So far, significant noise sources that may be present in arm locking include:

- Clock noise - The phase of a beat signal is measured by comparing it to a timing reference (the local ultra-stable oscillator). Therefore, the acquired phase value is always relative to the phase noise of the referencing clock. The clock noise is proportional to the nominal frequency Ω of the measured beat signal, i.e.,

$$\delta\nu_{\text{clock}}(f) = \Omega \cdot \delta\nu_{\text{clock}}^0(f), \quad (2-70)$$

where $\delta\nu_{\text{clock}}^0(f)$ are the fractional frequency fluctuations, corresponding to the normalized clock frequency noise at 1 Hz clock frequency. The fractional frequency fluctuation is estimated to be approximately $2.4 \times 10^{-12}/\sqrt{f}$ Hz^{-1/2}. The clock noises from phasemeters on the same spacecraft are correlated, while they are uncorrelated on different spacecraft.

- Spacecraft motion - LISA arm length (benchtap to benchtap) is an excellent reference to stabilize the laser frequency. However, the stability of this length reference is still limited by the DRS that drags the spacecraft to track the geodesic motion of the proof mass. The consequent length uncertainty is approximately given by

$$\delta L_{\text{SC}}(f) = 2.5 \times 10^{-9} \sqrt{1 + (f/0.3 \text{ Hz})^4} \text{ m Hz}^{-1/2}. \quad (2-71)$$

The length uncertainty of one arm includes the spacecraft motions of two spacecraft at each end. This limited stability in the length reference will cause a phase noise in the phase measurement.

- Shot noise - Limited number N of photons received per second by photodiodes. From Eq. 2-5, with 100pW light received at the photodiode the shot noise is given

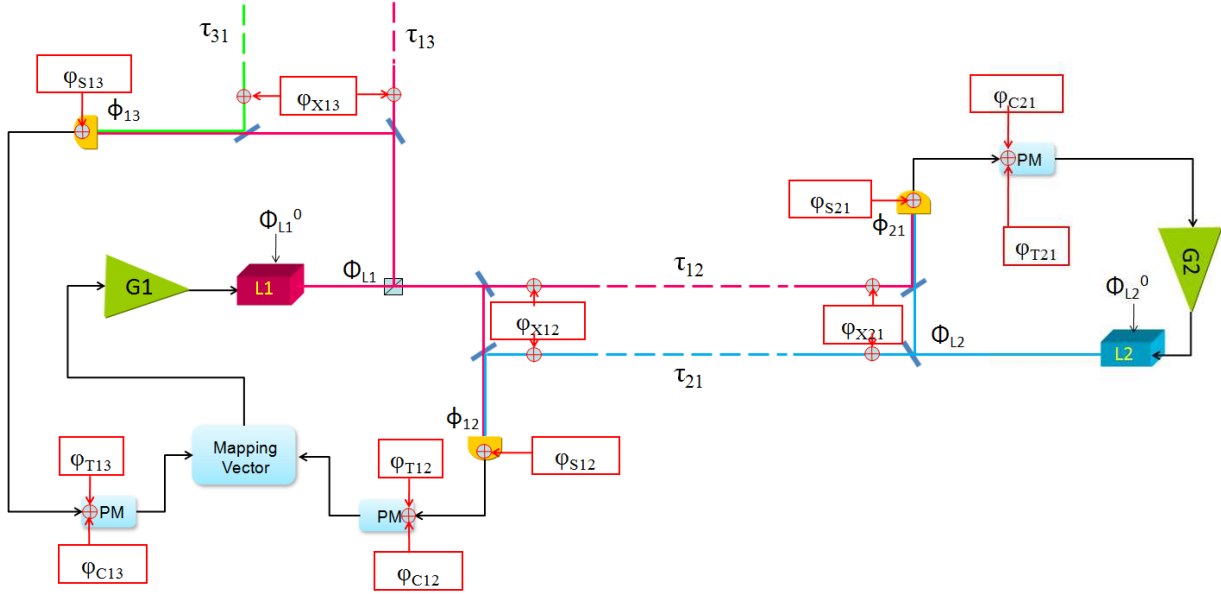


Figure 2-29. The control system of arm locking with various noise sources entering the loop. In the diagram φ_{C21} represents the clock noise introduced in the phase measurement of the beat signal $\phi_{21}(t) = \Phi_2(t) - \Phi_1(t - \tau_{12})$. The same notation is used for the shot noise φ_S and the phasemeter technical noise φ_T . φ_{X21} represents the spacecraft motion of SC_2 applied onto the instantaneous phase $\Phi_2(t)$ and the delayed phase $\Phi_1(t - \tau_{12})$.

by

$$\delta\varphi_{\text{shot}} = \frac{1}{2\pi\sqrt{N}} = \sqrt{\frac{\hbar c}{2\pi} \frac{1}{\lambda P}} = 6.9 \times 10^{-6} \text{ cycles Hz}^{-1/2}. \quad (2-72)$$

- Technical noise - Including the ADC noise in the A/D conversion of the beat signal, as well as the finite precision of integer arithmetic, known as the digitization noise in the phasemeters, arm locking sensor and controller. A digital signal with a sampling frequency of f_s and a precision of N-bit generally carries the digitization noise

$$\delta\nu_{\text{dig}} = \frac{f_{\text{clock}} \cdot 2^{-N}}{\sqrt{6} \cdot f_s}. \quad (2-73)$$

In the presence of a 50 MHz clock frequency and a 100 kHz data rate in a 48-bit phasemeter, the arm locking sensor will sense the digitization noise given by $2.3 \times 10^{-10} \text{ Hz Hz}^{-1/2}$.

Figure 2-29 illustrates the arm locking schematic including the realistic noise sources described above. First we assume the far-end phase-locked loops are in operation while the arm locking loop is not closed yet. Thus the laser phase noise

Φ_{Li} , $i = 2, 3$ from the far spacecraft is given by

$$\Phi_{Li}(s) = \frac{1}{1+G_i} \Phi_{Li}^0 + \frac{G_i}{1+G_i} (\Phi_{L1}^0 e^{-s\tau_{1i}} + \varphi_{X1i} e^{-s\tau_{1i}} + \varphi_{X1i} - \varphi_{S1i} - \varphi_{C1i} - \varphi_{T1i}). \quad (2-74)$$

In this analysis we ignore the transponder noise $\frac{1}{1+G_i} \Phi_{Li}^0$ and assume the high gain limit $\frac{G_i}{1+G_i} \approx 1$. Therefore, the phase noise of the long arm interferometry signal on the local spacecraft is given by

$$\begin{aligned} \phi_{1i}(s) &= \Phi_{L1}^0(s) - (\Phi_{Li}(s) + \varphi_{X1i}) e^{-s\tau_{1i}} - \varphi_{X1i} + \varphi_{S1i} + \varphi_{C1i} + \varphi_{T1i} \\ &\approx \Phi_{L1}^0(s) P_{1i} - \varphi_{X1i} (1 + e^{-s\tau_{1i}}) - 2\varphi_{X1i} e^{-s\tau_{1i}} \\ &\quad + \varphi_{S1i} e^{-s\tau_{1i}} + \varphi_{S1i} + \varphi_{C1i} e^{-s\tau_{1i}} + \varphi_{C1i} + \varphi_{T1i} e^{-s\tau_{1i}} + \varphi_{T1i}. \end{aligned} \quad (2-75)$$

Following the notation used in Eq. 2-31, the phase noises of the two interferometer outputs can be written together as a 2×1 phase vector

$$\begin{aligned} \Phi_1(s) &= \begin{bmatrix} \phi_{12}(s) \\ \phi_{13}(s) \end{bmatrix} \\ &= [\mathbf{N}_L + \mathbf{N}_C + \mathbf{N}_X + \mathbf{N}_S + \mathbf{N}_T], \end{aligned} \quad (2-76)$$

where each vector is given by

$$\begin{aligned} \mathbf{N}_L &= \begin{bmatrix} \Phi_{L1}^0(s) P_{12} \\ \Phi_{L1}^0(s) P_{13} \end{bmatrix}, \quad \mathbf{N}_C = \begin{bmatrix} \varphi_{C12} + \varphi_{C21} e^{-s\tau_{21}} \\ \varphi_{C13} + \varphi_{C31} e^{-s\tau_{31}} \end{bmatrix}, \quad \mathbf{N}_T = \begin{bmatrix} \varphi_{T12} + \varphi_{T2} e^{-s\tau_{21}} \\ \varphi_{T13} + \varphi_{T3} e^{-s\tau_{31}} \end{bmatrix} \\ \mathbf{N}_X &= \begin{bmatrix} -\varphi_{X12} (1 + e^{-s\tau_2}) - 2\varphi_{X21} e^{-s\tau_{21}} \\ -\varphi_{X13} (1 + e^{-s\tau_3}) - 2\varphi_{X31} e^{-s\tau_{31}} \end{bmatrix}, \quad \mathbf{N}_S = \begin{bmatrix} \varphi_{S12} + \varphi_{S21} e^{-s\tau_{21}} \\ \varphi_{S13} + \varphi_{S31} e^{-s\tau_{31}} \end{bmatrix}. \end{aligned} \quad (2-77)$$

Note that for \mathbf{N}_C , \mathbf{N}_X , \mathbf{N}_S and \mathbf{N}_T , each vector element consists of two noise terms (e.g., φ_{C12} and φ_{C21}) that come from two uncorrelated sources. The combined noise amplitude is given by the quadrature sum of the two terms.

Table 2-1. Parameters of the noise analysis for arm locking

Parameter	Symbol	Value	Units
Average delay time	$\bar{\tau}$	33	s
Differential delay time	$\Delta\tau$	0.016	s
Nominal frequency on arm 1-2	Ω_{12}	15	MHz
Nominal frequency on arm 1-3	Ω_{13}	-14	MHz
Fractional frequency fluctuation	$\delta\nu_{\text{clock}}^0$	$2.4 \times 10^{-12}/\sqrt{f}$	$\text{Hz}^{-1/2}$
Arm length stability (SC to SC)	δL_{SC}	$2.5 \times \sqrt{1 + (f/0.3 \text{ Hz})^4}$	$\text{nm Hz}^{-1/2}$
Received power at photodiodes	P	100	pW
TDI capability	$\delta\nu_{\text{TDI}}$	$282 \times \sqrt{1 + (2.8 \text{ mHz}/f)^4}$	$\text{Hz Hz}^{-1/2}$
Arm locking requirement [60]	$\delta\nu_{\text{AL}}$	$0.3 \times \sqrt{1 + (2.8 \text{ mHz}/f)^4}$	$\text{Hz Hz}^{-1/2}$

When the arm locking loop is closed, we evaluate Eq. 2-64

$$\begin{aligned}\Phi_{L1}(s) &= \Phi_{L1}^0 - \frac{G_1}{1 + G_1 H} \mathbf{S}_k \cdot \Phi_1 \\ &= \frac{1}{1 + G_1 H} \Phi_{L1}^0 - \frac{G_1}{1 + G_1 H} \mathbf{S}_k \cdot [\mathbf{N}_C + \mathbf{N}_X + \mathbf{N}_S + \mathbf{N}_T].\end{aligned}\quad (2-78)$$

The second term represents the noise limitations. Here we consider the arm locking performance limited by various noise sources by assuming an infinite controller gain. The analysis is based on the LISA parameters listed in Table 2-1 under different arm locking configurations, where we neglect the technical noise as it should be small compared to the other three. The arm length mismatch is assumed to be as short as 0.1%, corresponding to a 0.016 s differential time delay, in order to demonstrate a critical scenario.

For common arm locking, the arm locking performance is independent of the arm length mismatch. The noise limitations are plotted in Figure 2-30, which shows that for frequencies above 20 mHz and below 0.7 mHz the common arm locking performance is limited by spurious spacecraft motions and for frequencies in the middle range it is dominated by the clock noise. At frequencies $n/\bar{\tau}$ the spacecraft motion cause noise peaks that may fail to meet the arm locking requirement.

For the dual arm locking configuration, the noise limitations are plotted in Figure 2-31. The dominant clock noise and spacecraft motion floor prevent arm locking from

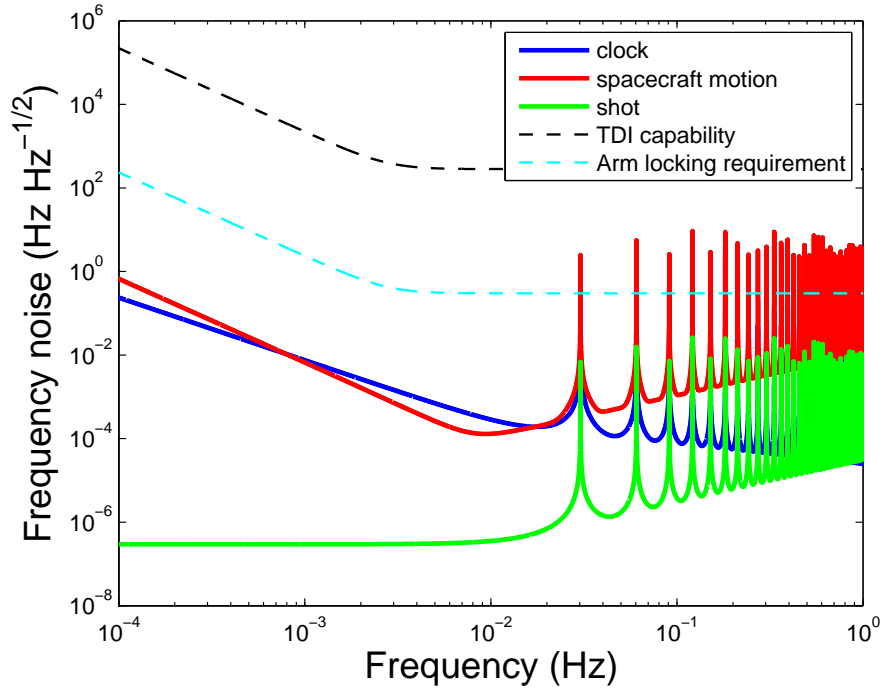


Figure 2-30. The noise floors in common arm locking are independent of the arm length mismatch. At high frequencies the dominant noise is spacecraft motions and at low frequencies the dominant noise is the clock noise.

meeting the requirement for frequencies below about 10 mHz. Analytically, the clock noise floor is given by

$$\begin{aligned} \delta\nu_{\text{clock}}(s) &= \frac{1}{H} \left[1 + \frac{1}{s\Delta\tau}, 1 - \frac{1}{s\Delta\tau} \right] \cdot \begin{bmatrix} \varphi_{C12} + \varphi_{C21}e^{-s\tau_{21}} \\ \varphi_{C13} + \varphi_{C31}e^{-s\tau_{31}} \end{bmatrix} \\ &= \frac{1}{H} \left[\varphi_{C12} + \varphi_{C21}e^{-s\tau_{21}} + \varphi_{C13} + \varphi_{C31}e^{-s\tau_{31}} + \frac{1}{s\Delta\tau} (\varphi_{C12} + \varphi_{C21}e^{-s\tau_{21}} - \varphi_{C13} - \varphi_{C31}e^{-s\tau_{31}}) \right]. \end{aligned} \quad (2-79)$$

Note that the operation of “addition” or “subtraction” between the clock noises contributed by different arms should still be taken as a quadrature sum. This result indicates that the dominant term is the differential arm path, which integrates the differential clock noise between two arms. Due to the structural similarity, the other kinds of noise sources will be coupled into the stabilized frequency noise in the same manner. Therefore, the noise floor in dual arm locking is primarily composed of the integration of

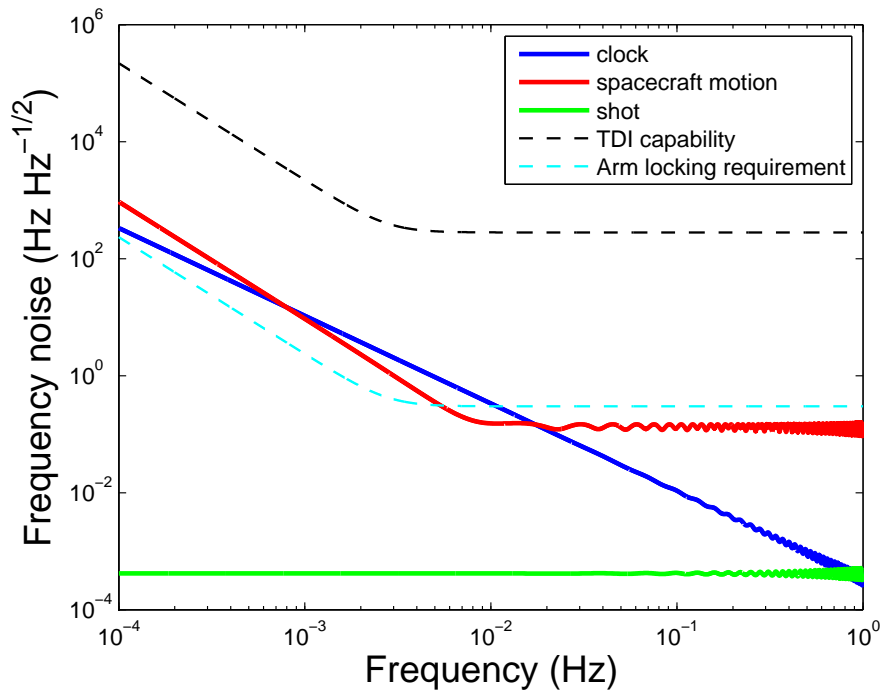


Figure 2-31. The noise floors in dual arm locking are sensitive to the arm length mismatch. Here we assume a relatively short arm length mismatch of 0.1% and the noise floors are significantly higher than the common arm locking situation. As the noise floor in dual arm locking is inversely proportional to the arm length mismatch, the performance of dual arm locking is insufficient to meet the TDI capability when the arm length mismatch is less than about 60 km.

the differential noises and inversely proportional to the arm length mismatch. A shorter arm length mismatch corresponds to a worse noise suppression performance and our analysis indicates that for the differential delay time less than 0.2 ms ($\Delta L < 60$ km) the dual arm locking performance would even be insufficient to meet the requirement for TDI.

A similar approach can be used to evaluate the noise floor in the Sagnac-based dual arm locking configuration. Since in the Sagnac constellation the relay beams will pick up all the clock noises, spacecraft motions, etc. that enter the arm locking control system both clockwise and counter-clockwise, the quadrature sum of these noises will be integrated and multiplied with $1/\Delta\tau$, where the equivalent differential delay time is

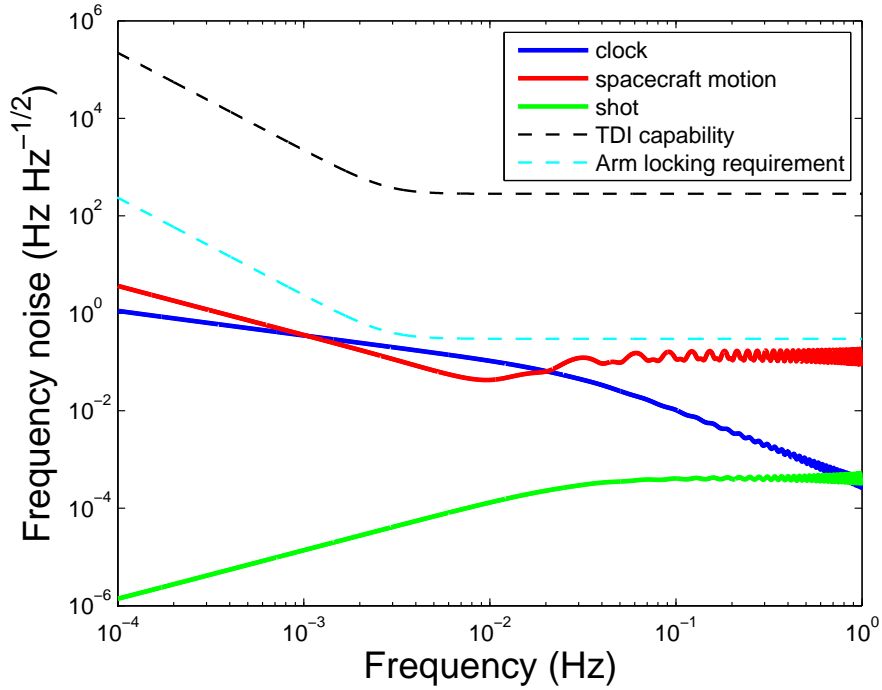


Figure 2-32. The noise floors in modified dual arm locking are less dependent on the arm length mismatch due to the low-frequency filtering scheme. The noise floors are effectively suppressed by the high-pass filter at frequencies below $1/\bar{\tau}$. With a more carefully designed high-pass filter, the noise floors will be further reduced and asymptotically approach the noise floors determined in the common arm locking configuration.

$\approx 47 \mu\text{s}$. Since every noise source will contribute to the overall noise floor twice and scale with a very short differential delay, the noise limitation in Sagnac-based dual arm locking is much higher than any other arm locking configuration.

The analysis for modified dual arm locking can be adapted from Eq. 2-69. For the modified dual arm locking sensor $[H_+ + H_-, H_+ - H_-]$, the clock noise floor is given by

$$\delta\nu_{\text{clock}}(s) = \frac{H_+}{H}(\varphi_{C12} + \varphi_{C21}e^{-s\tau_{21}} + \varphi_{C13} + \varphi_{C31}e^{-s\tau_{31}}) + \frac{H_-}{H}(\varphi_{C12} + \varphi_{C21}e^{-s\tau_{21}} - \varphi_{C13} - \varphi_{C31}e^{-s\tau_{31}}). \quad (2-80)$$

As a simple demonstration, we still take $H_+(s)$ and $H_-(s)$ given by Eq. 2-60 as an example. The noise limitations are plotted in Figure 2-32. Compared with the noise limitation in dual arm locking, the noise level has been decreased below the arm locking

requirement for the entire LISA band, which is well below the TDI capability. Note that due to the simplified design of $F_D(s)$, which exhibits an unoptimized s slope, the noise floors at low frequencies are not maximally suppressed. In realistic LISA a better noise suppression performance should be expected with a more carefully designed $F_D(s)$ if modified dual arm locking will be used. If the magnitude of the $F_D(s)$ filter rolls off faster at low frequencies, the noise floors will become less dependent on the arm length mismatch and asymptotically approach the floor determined by $1/\bar{\tau}$.

At the end of this chapter let us have a brief estimation regarding the LISA arm length mismatch. Now that we know a short arm length mismatch is critical for Doppler-induced frequency pulling and the arm locking performance, we are interested in how long a critical scenario, say $|\Delta L/L| < 0.1\%$, will last in the orbital period of one year. As we know, the arm length mismatch is roughly a sinusoid function with a period of one year and the maximum mismatch is about 1%, i.e.,

$$\Delta L = 0.01 \times L \cdot \sin \Omega t, \quad (2-81)$$

where $\Omega = 2\pi/1 \text{ yr} \approx 2 \times 10^{-7} \text{ Hz}$.

Therefore, the arm length mismatch is

$$\Delta L \approx 5 \times 10^7 \text{ m} \cdot \sin(2 \times 10^{-7} \text{ Hz} \cdot t) \approx 10 \text{ m s}^{-1} \cdot t. \quad (2-82)$$

Thus we obtain the change rate of arm length mismatch of approximately 10 m s^{-1} . For the arm length mismatch below $\pm 0.1\%$, the duration is approximately $2 \times 5 \times 10^6 \text{ m}/10 \text{ m s}^{-1} \approx 10^6 \text{ s}$, which is less than 12 days, twice per year. Note that this is just a quick and rough estimation and a more deliberate calculation depends on the exact LISA orbits. Nevertheless, it still gives us the information that the performance of arm locking will not be substantially degraded by the arm length variations and the scenario will only become critical during a short amount of time every year.

CHAPTER 3 UNIVERSITY OF FLORIDA LISA INTERFEROMETER SIMULATOR

The LISA group at the University of Florida has developed a hardware in the loop simulator for LISA's long arm interferometry which is similar to LISA as possible. So far, a synthesized hardware LISA interferometry and measurement system, the University of Florida LISA Interferometer Simulator (UFLIS), which consists of a variety of LISA component models, has been developed with continuous modification and enhancement. These component models include LISA-like cavity pre-stabilization, digital integrated-circuit board based science phasemeters, LISA-like inter-SC ranging and laser communications, LISA-like variable light travel time and variable Doppler shifts, analog/digital hybrid realistic arm locking, synthesized realistic TDI with fractional delay filtering, generation of gravitational-wave-like signals, etc.

UFLIS is currently the only existing hardware system that can realistically simulate long arm interferometry by providing LISA-like light travel time as well as variable Doppler shifts. Since the three interferometers are independent to each other in the IMS, the absence of the other two interferometer will not degrade the validity of our experiments but will also reduce the complexity. A long-term goal of UFLIS is to inject the generated gravitational-wave-like signals into the simulator and mock the LISA data within the required noise level, and to successfully extract the gravitational-wave-like signals by developing proper LISA data analysis methods. In this chapter we will introduce the current research on the optical/electronic components related to the hardware simulation of arm locking, which are accomplished by our group at the University of Florida.

3.1 Optical Components

In the current optical layout of LISA interferometry benchtop, three 1064 nm Nd:YAG lasers are referred to as L_i , $i = 1, 2, 3$, respectively. Another independent Nd:YAG laser RL is a reference laser which functions as an optical clock to generate beat signals

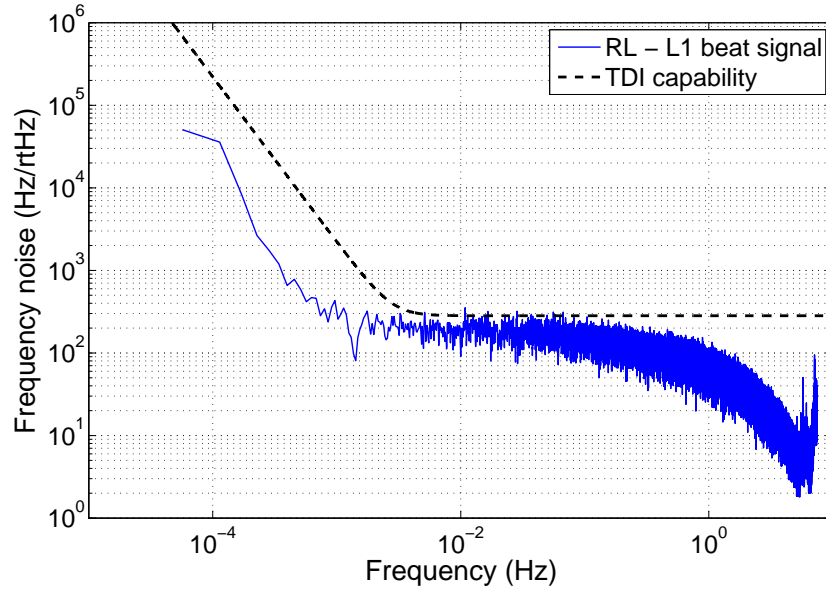


Figure 3-1. Frequency noise of the beat signal between two cavity stabilized laser RL and L_1 .

with frequencies below 20 MHz with each of the other three lasers. The reason we use beat signal rather than the direct laser frequency is that a single laser frequency is in the range of 300 THz which is not possible to be measured by a normal commercial photodiode.

The lasers RL and L_1 are separately locked to their own reference high finesse optical cavity using Pound-Drever-Hall technique for pre-stabilization. Each cavity consists of a Zerodur spacer. Therefore, the beat signal between RL and L_1 provides the input phase noise on the master spacecraft in TDI and arm locking setup. The beat signals between RL and L_2 or L_3 can be used as returning beams from far spacecraft with L_2 or L_3 phase-locked to the master laser L_1 .

Figure 3-1 shows the frequency noise spectrum of the beat signal between RL and L_1 at a nominal frequency of approximately 13 MHz. In the frequency range from 1 mHz to 1 Hz, the frequency noise stays at a level of approximately $100 \sim 200 \text{ Hz}/\sqrt{\text{Hz}}$, which is already below the $282 \text{ Hz Hz}^{-1/2}$ pre-TDI frequency noise requirement. Also, the beat frequency exhibits a long term linear drift by up to $\pm 1 \text{ MHz}$, with a typical drift

rate of 1 Hz/s. This moderate frequency drift can be taken out in the data processing and essentially has no significant influence on laser measurements.

3.2 Electronic Components

To reproduce the measurement environment in LISA's long arm interferometry, we selected a high-speed digital signal processing system (referred to as the "Pentek board") manufactured by the Pentek Corporation. Phasemeters, as well as most important electronic components of UFLIS, are all implemented on this system.

3.2.1 Digital Signal Processing Hardware

The Pentek board consists of three individual electronic boards: Model 4205 motherboard, Model 6256 A/D daughterboard and Model 6228 D/A daughterboard.

Model 4205 contains the following primary elements:

- A 32-bit central microprocessor (CPU) with a 1 GHz clock frequency: Like all CPUs, it carries out each instruction of the program in sequence and performs the basic arithmetical, logical, and input/output operations of the system.
- A 1 GB synchronous dynamic random access memory (SDRAM): It is used to store data while synchronized with the system's PCI bus (meaning it waits for a clock signal before responding to control inputs).
- Four 32-bit velocity interface modules (VIMs): VIM is an interface for the data transfer and communications between the motherboard and the daughterboards. Each two VIMs are connected to one daughterboard, with one data interface and one control/status interface.
- Four bi-directional first-in first-out buffers (BIFOs): After/Before the data is transferred through the VIM, the data will first be written into the BIFO before memory access. Each BIFO is connected to one VIM. Data transfer can also be realized directly between different VIMs without the process of writing/reading into the memory.
- Four direct memory access (DMA) controllers: DMA is capable of reading/writing data from/into the BIFO while directly accessing the memory for reading and writing independently of the intervention from the CPU.
- One serial and one Ethernet port: These ports are for the communication between Model 4205 and computers to upload/download commands and files.

The Model 6256 A/D daughterboard and the Model 6228 D/A daughterboard are connected to the Model 4205 motherboard via VIMs. The primary elements on Model 6256 include:

- Four 14-bit analog-digital converters (ADCs): These ADCs can be clocked at up to 105 MHz. Since the connectors of these ADCs are AC-coupled with a high-pass filter, the ADCs can only digitize an RF signal with the carrier frequency higher than 400 kHz, which is ideal for LISA-like heterodyne beat signals. The full scale of the ADC input amplitude is 4 dBm.
- Two Xilinx Virtex-2 field programmable gate arrays (FPGAs): The digital signal from the ADCs will be sent to the FPGAs, where the logical functions and operations in digital signal processing can be implemented. FPGA contains programmable logic components known as logic blocks, and a hierarchy of reconfigurable interconnects that allow the blocks to be wired together, which allows us to easily configure the FPGA according to the required design. The digital signal on the FPGA yields fixed-point arithmetic, which limits the data precision while improves the calculation efficiency.

The primary elements on Model 6228 include:

- Four 16-bit digital-analog converters (DACs): These DACs can be clocked at up to 500 MHz. Similar to the ADCs, the DACs are also AC-coupled such that they can only generate RF signals with the carrier frequency higher than 400 kHz. The full scale of the DAC output amplitude is -2 dBm.
- A Xilinx Virtex-2 field programmable gate array (FPGA): Model 6228 also provides a similar FPGA that can be programmed for signal processing. The FPGA can be directly connected to the inputs of the DACs.

With these three models, the Pentek board can realize a variety of functions such as the data acquisition, signal measurement and digital filtering. In the following sections we will discuss two basic applications of the Pentek board, which have been widely used in UFLIS.

3.2.2 Phasemeter

Phasemeter is the most fundamental instrument in LISA's measurement system. It is essential for the precise measurement of heterodyne interferometry phases at photodiodes, which is the primary quantities to be measured in IMS. Moreover, phasemeters play an important role in digital control loops in which the sensor detects

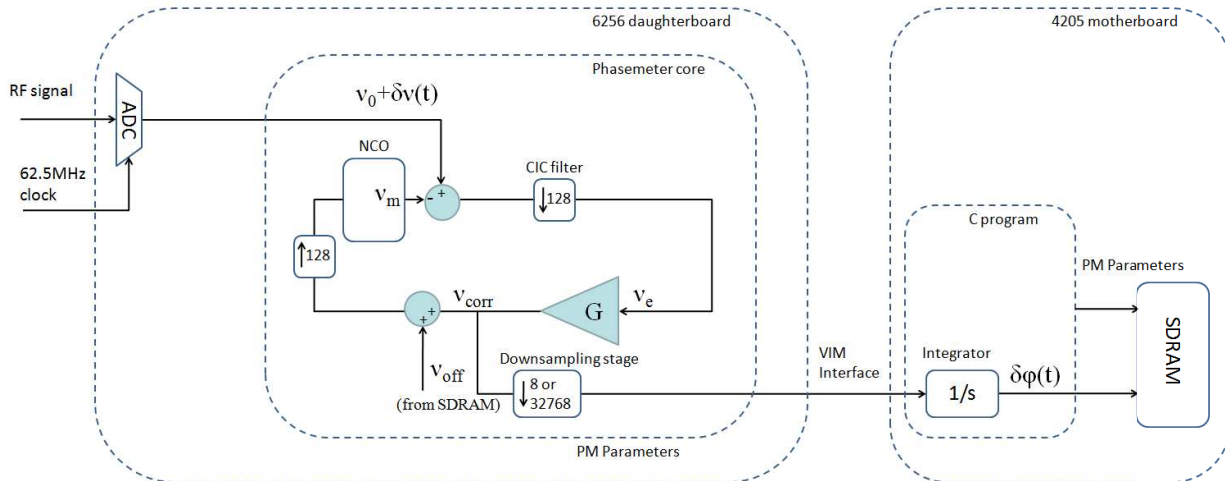


Figure 3-2. The implementation of the phasemeter on a Pentek board. The phasemeter is essentially a “frequency meter” that tracks the frequency fluctuations of the input signal.

the phase, e.g., phase-locking and arm-locking. Therefore, phasemeters can be classified into two types based on the different functions. The former type focuses on the phase measurement in the LISA band, requiring high precisions with a low data rate (~ 3 Hz). The latter type focuses on the phase detection in digital controls where a high bandwidth and consequently fast data rate (~ 100 kHz) will be needed.

As discussed in Section 2.3.5, the phase is measured with respect to a clock reference such that the acquired phase value is always relative to the phase noise of the referencing clock. Therefore, all phase measurements inevitably carry the clock noise.

3.2.2.1 Design

Given that the desired sensitivity of IMS is approximately $18 \text{ pm}/\sqrt{\text{Hz}}$, the science phasemeter needs to be able to measure the arm length change with a precision of $\sim 1 \text{ pm}/\sqrt{\text{Hz}}$. Therefore, the phase measurement with 1064 nm wavelength is required to have an accuracy of $\sim 1 \mu\text{cycles}/\sqrt{\text{Hz}}$ [59].

The phasemeter developed at the University of Florida adapts an architecture of digital phase-locking similar to the LISA phasemeter. As shown in Figure 3-2, the phasemeter is implemented on the Model 6256 A/D daughterboard. The clock frequency

to operate the 14-bit ADC is $f_{\text{clock}} = 62.5$ MHz. The digitized heterodyne signal, which carries a frequency $\nu_0 + \delta\nu(t)$ is demodulated by a 48-bit numerical control oscillator (NCO) that is phase-locked to the measured signal. The NCO frequency ν_m tracks the frequency of the measured signal, and it is given by the sum of a 16-bit preset offset frequency ν_{off} and a 48-bit time-varying frequency correction ν_{corr} . The frequency difference between the NCO and the measured signal gives the PLL error ν_e . Based on the phasemeter model shown in Figure 3-2, we have

$$\begin{aligned}\nu_{\text{corr}} &= \nu_e \cdot G, \\ \nu_m &= \nu_{\text{off}} + \nu_{\text{corr}}, \\ \nu_e &= \nu_0 + \delta\nu(t) - \nu_m,\end{aligned}\tag{3-1}$$

where G is the transfer function of the PLL controller satisfying the condition $G \gg 1$. We solve ν_{corr} given by

$$\nu_{\text{corr}} = \frac{G}{1+G}[\delta\nu(t) + (\nu_0 - \nu_{\text{off}})] \approx \delta\nu(t) + (\nu_0 - \nu_{\text{off}}).\tag{3-2}$$

Therefore, the frequency fluctuations of the measured signal is faithfully reproduced by ν_{corr} if $\nu_0 = \nu_{\text{off}}$ within the phasemeter bandwidth. If the preset offset frequency is not exactly equal to ν_0 , a constant offset will be added into ν_{corr} . This frequency offset can be easily removed in post-processing of phase measurements, but might cause a frequency pulling issue in arm locking.

The phasemeter is essentially a “frequency meter” that detects the frequency fluctuations of the beat signal. Integrating the frequency fluctuations will generate the phase information: $\delta\varphi(t) = \int_0^t \delta\nu(t) dt$. This integration can be done in post-processing. Note that the phase measurement can also be achieved by integrating the NCO frequency ν_m . As the NCO frequency contains the constant frequency offset, a linear drift in phase will show up in the result.

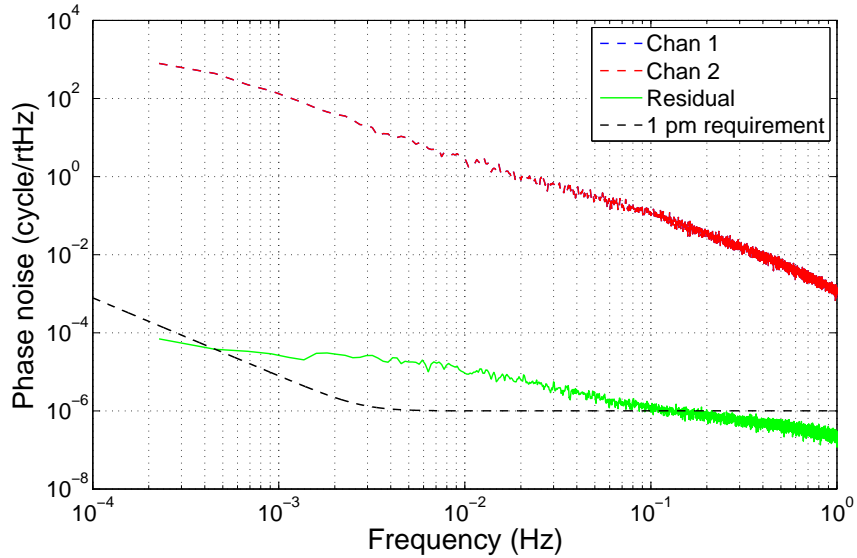


Figure 3-3. The phasemeter performance measured with split-and-subtracted VCO signals. The noise limitation of the phasemeter is the ADC noise, which is contributed by the temperature fluctuations for low RF frequencies and timing jitter for high RF frequencies. Although the ADC noise floor prevents the phasemeter from meeting the 1 pm requirement, it does not cause a significant problem in our arm locking experiments. However, the noise suppression performance in our tests may be limited by the ADC noise, which will be seen in Chapter 5.

The main loop of the digital PLL is running at $f_{\text{clock}}/128 \approx 488$ kHz as downsampled by a cascaded integrating comb (CIC) filter with a factor of 128. The data rate of the frequency fluctuations can be further downsampled to 61.0 kHz or 14.9 Hz, depending on whether the function of the phasemeter data is high-bandwidth tracking or science measurements. However, in our arm locking setup we directly use the 488 kHz frequency data stream without any additional downsampling stage to minimize the system processing delay (see the next chapter).

3.2.2.2 Performance

The phasemeter is characterized by taking measurements of a voltage controlled oscillator (VCO) signal, as shown in Figure 3-3. In this simple setup, the 4 MHz VCO signal is split by an electronic splitter and measured by two phasemeters. The two phasemeters are programmed on the same FPGA but connected to different ADCs;

therefore, they have a common clock noise but uncorrelated ADC noises. Figure 3-3 shows that the noise spectrum of their difference is limited by a $1/\sqrt{f}$ ADC noise floor, which is empirically given by

$$\varphi_{\text{ADC}}(f) = \frac{3 \times 10^{-7}}{\sqrt{f}} \cdot \frac{\nu_0}{4 \text{ MHz}} \text{ cycle Hz}^{-1/2}, \quad (3-3)$$

where ν_0 is the nominal frequency of the input signal.

In addition, the finite precision of the fixed integers in the phasemeter causes the digitization noise as frequency noise given by

$$\nu_{\text{Dig}}(f) = \frac{f_{\text{clock}} \cdot 2^{-N}}{\sqrt{6 \cdot f_s}}, \quad (3-4)$$

which is a limited-bandwidth white noise in terms of frequency fluctuations. For the high sampling frequency of 61.0 kHz, the digitization noise of the 48-bit phasemeter is about $3.67 \times 10^{-10} \text{ Hz Hz}^{-1/2}$. For the low sampling frequency of 14.9 Hz, the digitization noise is about $2.35 \times 10^{-8} \text{ Hz Hz}^{-1/2}$. When converted into phase fluctuations, the digitization noise floor is marginally below the 1 pm requirement curve.

Latest progress on the phasemeter development indicates that the ADC noise source is primarily attributed to the temperature-dependent phase dispersion in the RF transformer for low RF frequencies ($< 8 \text{ MHz}$) and timing jitter for high RF frequencies ($> 8 \text{ MHz}$). The phasemeter sensitivity performance has been substantially improved by replacing the RF transformers and has already met the $1 \text{ pm Hz}^{-1/2}$ requirement. Nevertheless, it should be noted that the phasemeters used in current EPD units (see the next section) and arm locking setup described in this dissertation have not adapted this enhancement.

3.2.3 Electronic Phase Delay

A challenging issue in benchtop experiments of LISA interferometry is the simulation of the round-trip propagation between spacecraft. The difficulty of reproducing a LISA-like 33 s delay line compromises the validity of LISA interferometry experiments

of TDI or arm locking. Compared with unrealistic short delay lines via very long cables or fibers used in most laboratories [89, 90], one distinctive feature of UFLIS is the emulation of realistic LISA-like delay times and MHz-range Doppler shifts via electronic delay. Such an electronic delay system built with high-bandwidth phasemeters is called an Electronic Phase Delay (EPD) unit.

The EPD system is also implemented on a Pentek board [91, 92] clocked at 62.5 MHz. An EPD unit consists of three main components, which are implemented on three parts of the Pentek board respectively. The Model 6256 A/D daughtercard is programmed with a 48-bit phasemeter.¹ The phasemeter measures the frequency fluctuation of the digitized laser beat note with a data rate of 61 kHz and then send the data stream to the memory of the Model 4205 motherboard. The motherboard stores the frequency information in a memory buffer for a certain amount of time. The high data rate in the phasemeter ensures the frequency information within the arm locking bandwidth (\sim kHz) can be properly delayed by the EPD system. After the delay in the memory buffer, the frequency information is sent to the Model 6228 D/A daughtercard, where an NCO integrates the sum of the frequency fluctuation and the frequency offset to regenerate the delayed copy of the input laser phase. After the NCO output, the digitized signal is converted back to an analog signal by the 500 MHz sampling frequency D/A converter. During this routine, a MHz-range Doppler frequency can be added dynamically to the nominal frequency of the delayed signal on the motherboard.

The EPD unit is capable of delaying a MHz-range signal by as long as 280 s. The performance of the EPD unit is measured using a simple setup where the VCO signal is electronically split and one channel is delayed by 1 s through the EPD unit. We measure

¹ Actually, the FPGA is programmed with four identical phasemeters that are connected to four different ADCs in order to operate four-channel delays simultaneously. Here we just consider a one-channel case for the purpose of simplicity.

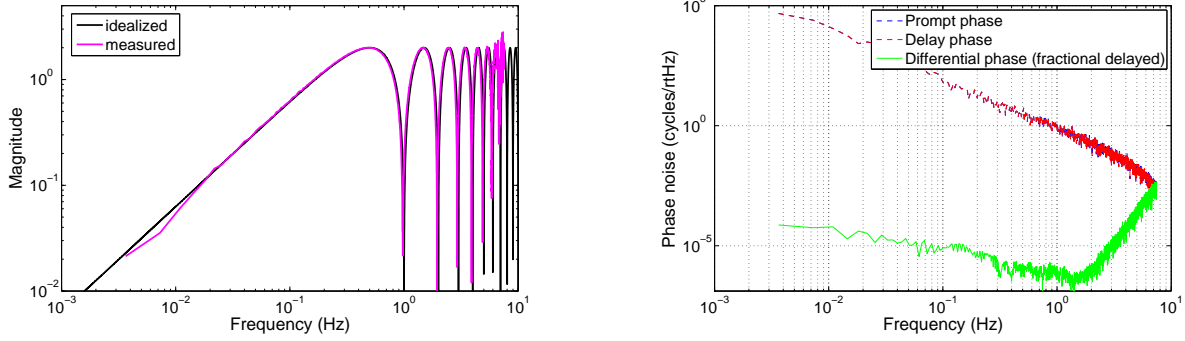


Figure 3-4. (Left) The magnitude response of an interferometer response with 1 s delay. (Right) The phase noise spectrum of the EPD unit.

the frequency/phase noise of the delayed signal and the prompt signal individually. The interferometer response of a LISA arm, which also yields a single arm locking sensor, is given by

$$P_{12}(s) = 1 - e^{-s\tau} = \frac{\phi_{12}(s)}{\phi_0(s)}, \quad (3-5)$$

where $\phi_{12}(s)$ is the difference $\phi_0(t) - \phi_0(t - \tau)$ between channel 1 and 2 represented in the Laplace domain.

The measurement results are shown in Figure 3-4. The left figure shows the magnitude response of $P_{12}(s)$, which exhibits interferometer nulls at n/τ and an s slope for frequencies far below $1/\tau$. The right figure shows the noise floor of the EPD unit. To evaluate the additional noise induced by the EPD unit, we time shift and fractional delay filter the delayed phase such that its time series could be maximally synchronized to the prompt phase in post-processing. Thus the EPD noise is given by differential phase noise between the two signals. The measured EPD noise is essentially on an equivalent level as the ADC noise in the phasemeter, since the primary contribution to the EPD noise is from the phasemeter ADCs. Note that the apparent increment of the EPD noise at frequencies above 1 Hz shown in the figure is an artifact from fractional delay filtering, while in reality the EPD noise continues to decrease with the same trend.

CHAPTER 4 EXPERIMENTAL VERIFICATION OF SINGLE ARM LOCKING

4.1 Motivation

Currently, UFLIS is the only existing hardware system that can simulate arm locking experimentally under realistic conditions, which is mainly ascribed to the long light travel time provided by the EPD unit. Compared with previous single arm locking experiments which were limited to μs delay times produced by long cables [89] or fibers, the first generation of EPD-based arm locking hardware simulations by Ira Thorpe has achieved significant progress [93]. Nevertheless, the first generation arm locking on UFLIS is still an extremely simplified model as it exploited only one single arm to build the sensor and did not add the Doppler shift as well as the noise limitations into the setup. By summarizing the discussions in Section 2.3, we list the following conditions that need to be reflected in a realistic arm locking hardware simulation.

- Due to the significant advantages of dual/modified dual arm locking, the error signal of arm locking has to be a combination of two interferometry signals, which means we need to have two delay lines, two phasemeters and a mapping vector implemented on the hardware system.
- The round-trip time on each arm should be around 33 seconds and, if possible, time-dependent. The arm length mismatch should be generated in a realistic range (no more than $\sim 1\%$, but also not equal to zero).
- The phase noise introduced by the phase-locked controller on the far spacecraft will couple into the sensor such that it cannot be suppressed by the arm locking controller. Therefore, the PLL on the far-end should be implemented realistically rather than be assumed to have an infinite gain given by an ideal optical transponder.
- A Doppler shift frequency applied to the heterodyne frequency of the beat signal needs to be taken into account. Also, a time-dependent Doppler shift frequency is desirable.
- Because it is impractical to measure and update the Doppler frequency on every data cycle, a Doppler frequency error within an acceptable range should be introduced.
- Finally there are other important noise sources we need to consider, including the clock noise in the phase measurement, the spacecraft jitter and the shot noise at

photodiodes. These noise sources will limit the noise suppression performance. And the effect of gravitational waves on arm locking should also be considered in order to investigate the impact of arm locking on gravitational wave detections.

The ultimate goal of arm locking simulations on UFLIS is to reproduce the above conditions, suppress the laser frequency noise and incorporate it into a TDI experiment to demonstrate the primary functions of IMS. A methodical procedure to build such an ultimate arm locking hardware system is to start with the basic single arm locking loop and take the realistic conditions into account stepwise. Thus in this chapter we will describe a series of enhanced single arm locking experiments which feature Doppler shifts [14] and incorporation with a tunable reference.

In our experimental verification of single arm locking, we use a MHz beat signal between two cavity stabilized lasers as the input noise source. This provides a frequency noise of approximately $100 - 200 \text{ Hz Hz}^{-1/2}$ at frequencies above $\sim 1 \text{ mHz}$. The single arm locking sensor, which is essentially the interferometer response of a single arm, is an electronic model same as the transfer function in Figure 3-4. The realistic round-trip travel time on the LISA arm is simulated via the EPD unit, where variable Doppler frequency shifts can be added to the nominal frequency of the delay signal. The arm locking controller is implemented on a second Pentek board, where a phasemeter will first measure the error signal with a high data rate ($\sim 488 \text{ kHz}$) and then send the data to a feedback filter (Section 4.2.2). The feedback signal from the controller output will be used to drive the actuator (a tunable frequency reference) to control the laser frequency. The actuator can be either a PZT actuator to tune the resonant frequency of the reference cavity (Section 4.3.2), or a local oscillator of a heterodyne phase-locked loop (Section 4.3.1).

Among these components, the sensor transfer function determines the controller design, because the slope of the controller filter will need to preserve some extra phase for frequencies above the first null in the sensor. To simplify our experiment setup, we set the delay time to be approximately 1 s at the EPD unit, which is still much longer

than the delay times used in previous arm locking experiments. The benefit is that in this case we only need to be concerned with the filter design in the frequency range above 1 Hz. Also, the 1 s delay time is comparable to the typical differential delay time when the second LISA arm is used to test the dual/modified dual arm locking configurations, where the sensor nulls are located at or above a few Hz.

4.2 Preliminary Test With Numerical Control Oscillator (NCO) Tracking

Before we actually start to build a complete realistic arm locking system incorporated with pre-stabilized lasers, it is reasonable to preliminarily verify the noise suppression capability and closed-loop stability of a basic single arm locking loop. Such a basic single arm locking loop does not need to be incorporated with a tunable reference, but simply reflects the closed-loop dynamics of the feedback control system. Also, the realistic noise limitations as well as Doppler frequency errors should be insignificant enough such that they should only cause negligible effects on the measurement results. A straightforward model to test a basic single arm locking loop is an electronic model with a VCO signal or a laser beat signal between two cavity stabilized lasers as the input noise.

4.2.1 Experimental Setup

The preliminary experimental setup is essentially a single arm locking loop featuring the EPD unit to stabilize the frequency of a numerical control oscillator (NCO) to a noisy laser beat signal. As shown in Figure 4-1, the NCO signal driven by the controller demodulates the beat signal from the photodiode such that it will try to track the input frequency noise when the loop is closed. The output of the mixer, which gives the residual frequency noise, is then sent to the single arm locking sensor and split into two parts. The first part is delayed at the EPD unit, which is implemented on a Pentek board with a 62.5 MHz clock frequency, by approximately 1 second as the round-trip travel time. During the delay process, a Doppler shift with a constant frequency is added onto the nominal frequency of the delayed signal. This frequency-shifted and delayed signal

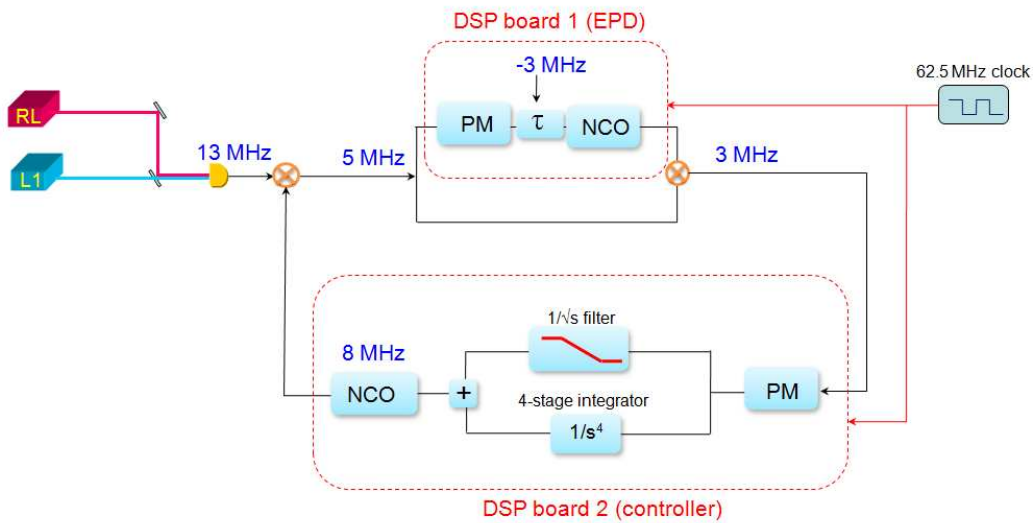


Figure 4-1. The preliminary experimental setup where the NCO tracks the input laser beat signal by means of single arm locking. This purely electronic routine simulates the control system of single arm locking. The single arm locking sensor (EPD) and controller are implemented on two different Pentek boards synchronized to a common clock. Note that the Doppler frequency of 3 MHz is perfectly demodulated in the phase measurement of the controller.

is then mixed together with the non-delayed second part to generate the error signal of single arm locking. Compared with the heterodyne interferometry in realistic LISA, this purely electronic routine precisely simulates the generation of the error signal coupled with the Doppler shift frequency. Due to the absence of the far-end PLL, the nominal frequency of the mixed signal does not include the offset frequency of the PLL. However, this simplification will not affect the purpose of this preliminary test.

Subsequently, the mixed signal is sent to the controller implemented on a second Pentek board with the same clock generator. The controller consists of a fast data rate phasemeter with a sampling frequency of $62.5 \text{ MHz}/128 \approx 448 \text{ kHz}$, a digital filter and an NCO. The phasemeter extracts the frequency fluctuations of the error signal by comparing a preset offset frequency with the nominal frequency of the error signal. If the preset offset frequency perfectly matches up the Doppler frequency, no Doppler frequency error will enter the frequency fluctuations of the error signal. After the digital

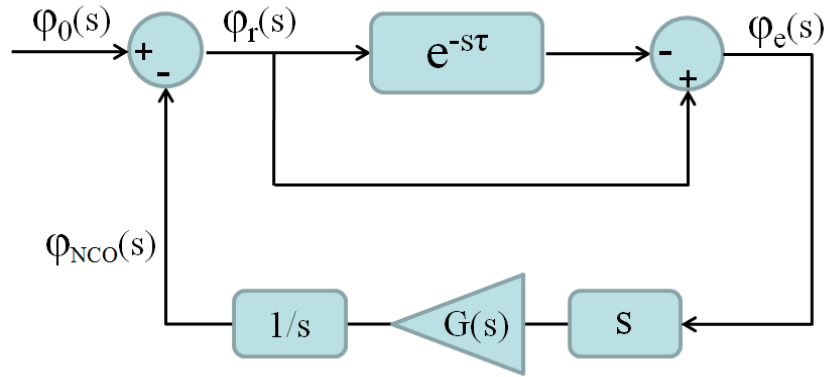


Figure 4-2. The closed-loop dynamics of single arm locking with NCO tracking in the Laplace domain. Note that we analyze most variables in the phase except in the arm locking controller, as the arm locking filter manipulates the frequency fluctuations rather than the phase, which is sent from the phasemeter. Therefore, the transfer function of the phasemeter is given by s , representing a conversion from phase to frequency. Oppositely, the transfer function of the NCO is $1/s$, which integrates the frequency fluctuations into phase fluctuations to track the input phase noise.

filter, the filtered frequency fluctuations will be integrated by the NCO, which generates the driving signal to track the input noise.

To describe the principle of this experimental setup, we draw Figure 4-2 that illustrates the closed-loop dynamics in the Laplace domain. The phase noises of the input signal, the tracking NCO signal, the residual signal and the error signal are represented by $\phi_o(s)$, $\phi_{NCO}(s)$, $\phi_r(s)$ and $\phi_e(s)$, respectively. The transfer function of the digital filter is given by $G(s)$. The phasemeter yields a conversion from phase to frequency such that it has a transfer function of s . On the other side, the NCO yields an inverse conversion from frequency back to phase such that it has a transfer function of $1/s$. Therefore, the relations between these phase noises are simply given by

$$\begin{aligned}
 \phi_r(s) &= \phi_o(s) - \phi_{NCO}(s), \\
 \phi_e(s) &= \phi_r(s)(1 - e^{-s\tau}), \\
 \phi_{NCO}(s) &= \phi_e(s)G(s).
 \end{aligned}
 \tag{4-1}$$

Thus we obtain the familiar definition of the closed-loop transfer function

$$\frac{\phi_r(s)}{\phi_o(s)} = \frac{1}{1 + (1 - e^{-s\tau})G(s)}, \quad (4-2)$$

which agrees with Eq. 2-32. The transfer function indicates that our preliminary experimental setup is sufficient to demonstrate the noise suppression and closed-loop stability of the single arm locking configuration.

4.2.2 Digital Filter Design

As previously mentioned in Section 2.3.2.1, the transfer function of the single arm locking controller will need to provide a slope steeper than $1/s$ at frequencies below $1/\tau$ and a lead compensator less steeper than $1/s$ at frequencies above $1/\tau$. This characteristic allows us to design a PI controller that consists of a compensator filter with a slope of $1/\sqrt{s}$ for frequencies above $1/\tau$ and 4-stage integrators for frequencies below $1/\tau$ in parallel. The combination of the compensator filter and integrators yields the magnitude response of the controller shown in Figure 4-3. The arm locking controller is also implemented on the 6256 ADC board, receiving the error signal via the direct connection to the phasemeter output.

Now we consider the design and realization of the digital compensator filter. The advantage of an infinite impulse response (IIR) filter is that it has higher efficiency and shorter latency during the calculation process, which is ideal for the feedback control. Also, digital IIR filters can be fast and accurately converted from their analog counterparts in the s-domain by means of discretization techniques such as the bilinear transform. On the other hand, all the poles of an IIR filter must be well inside the unit circle in the z-domain otherwise the open-loop stability would be compromised.

The $1/\sqrt{s}$ slope of an IIR filter in the s-domain can be approximately achieved by placing zeros and poles alternatively with a frequency spacing ratio of 10, i.e., poles at 1 Hz, 10 Hz, 100 Hz, 1 kHz and zeros at 3 Hz, 30 Hz, 300 Hz, 3 kHz. To convert the coefficients into the z-domain, we perform the bilinear transform with a sampling

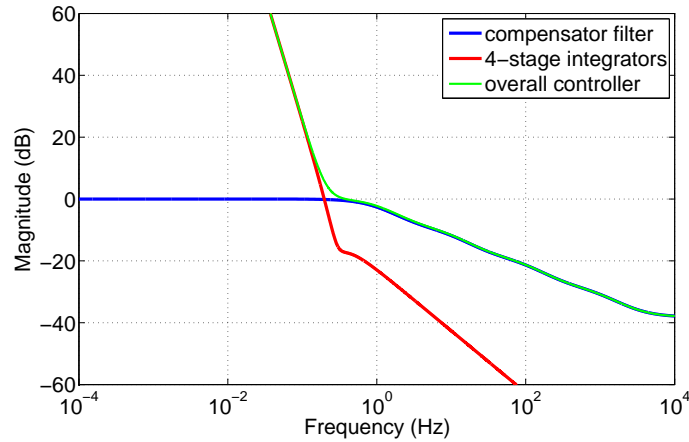


Figure 4-3. The magnitude responses of the PI controller: The 4-stage integrators (red) dominate the frequencies below $1/\tau \approx 1$ Hz to provide more suppression and the compensator filter with a slope of $1/\sqrt{s}$ (blue) dominates the frequency band from 1 Hz to 10 kHz to reduce phase loss. For frequencies beyond the bandwidth (> 10 kHz) the compensator filter flattens out to maintain the closed-loop stability.

frequency of 448 kHz, which is inherited from the data rate of the phasemeter output.

The IIR filter is implemented as a two-stage second-order-section (SOS) direct II form filter. Since the filter is implemented on the FPGA which yields the fixed-point arithmetic, the coefficients of the filter in the z-domain as well as the input and output values need to be further quantized into fixed-point numbers, where the issues related to the limited precision and the dynamic range arise. In practice, these issues are normally resolvable and a balance between them can be obtained through empirical attempts. In this design, the phasemeter sends 32-bit frequency data to the filter and during the entire data transfer it is kept to be a 32-bit fixed-point value down to the NCO.

The magnitude response of the implemented IIR filter shown in Figure 4-4 is measured by dividing the linear spectral densities of the input noise and the output noise. It is worth noting that unlike the EPD unit, the output of the controller filter will not be stored in the memory and then read out by the DAC board. In contrast, the output signal will bypass the 4205 motherboard and directly received by the DAC board via VIM

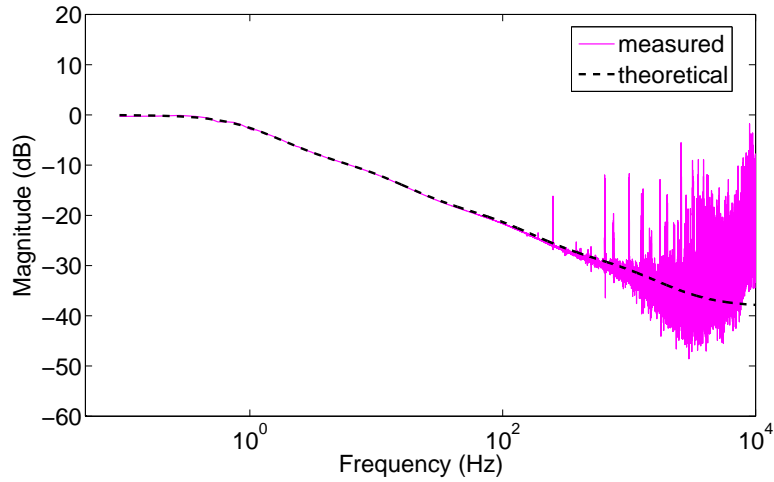


Figure 4-4. The magnitude response of the $1/\sqrt{s}$ filter, where the measured transfer function is very consistent with the theoretical design for frequencies below ~ 200 Hz. The high frequency noise (> 1 kHz) observed in the measurement is beyond the arm locking bandwidth.

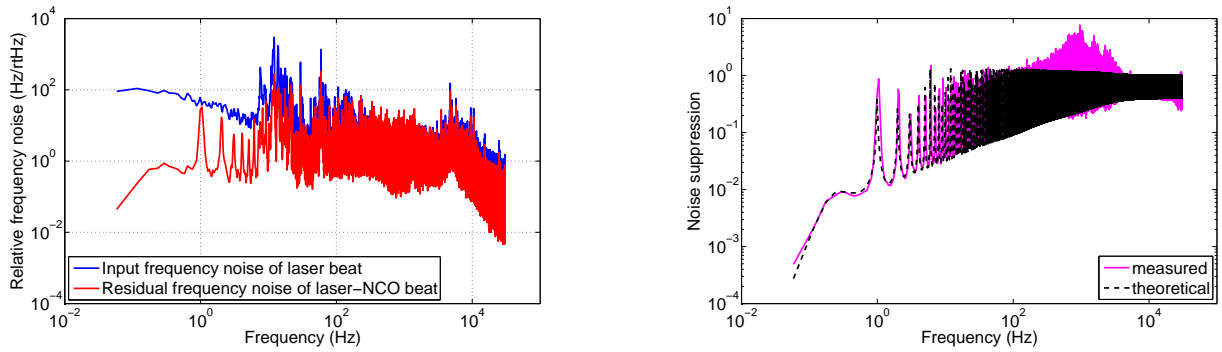


Figure 4-5. (Left) The measurement result of noise suppression performance at high frequencies shows that compared with the initial frequency noise spectrum of the beat signal between two cavity stabilized lasers (blue), the residual frequency noise spectrum of the laser-NCO beat (red) is suppressed by the compensator filter. (Right) The closed-loop transfer function is given by the ratio between the initial frequency noise spectrum and the residual frequency noise spectrum.

transfer. This feature is enabled when the motherboard is set to the VIM-to-VIM data transfer mode in order to minimize the data processing delay.

4.2.3 Measurement Results

After the arm locking starts and enters the steady state, we measure the phase fluctuations of the initial beat signal $\phi_o(s)$ and the residual signal $\phi_r(s)$ using two

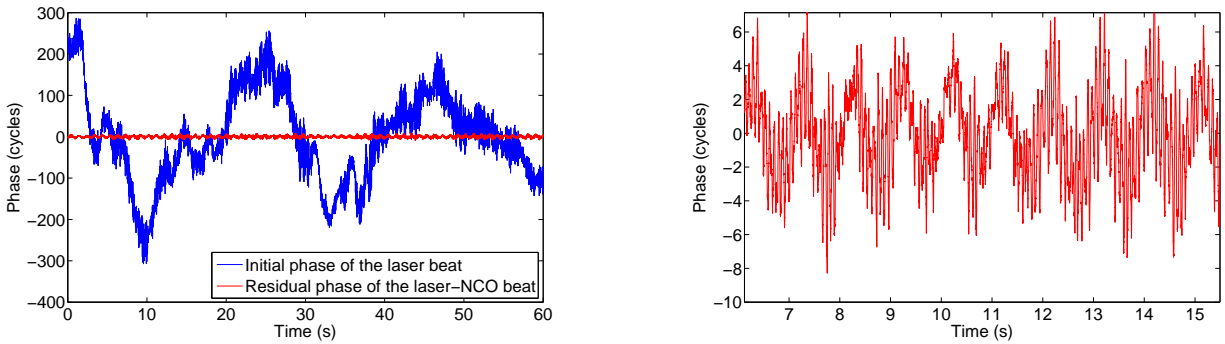


Figure 4-6. (Left) A 1 min time series of phase fluctuations of the initial beat signal (blue) and the residual laser-NCO beat (red) with a fast sampling frequency of 61 kHz. (Right) A close-up of the residual laser-NCO beat. The time series have a distinct oscillation at about 1 Hz, as well as higher harmonics on the top of it.

phasemeters individually. Here we have taken two kinds of phase measurements with two different phasemeter data rates. The phasemeter first sends data at the high rate of 61.0 kHz for 60 s in order to investigate the noise suppression and the system bandwidth at high frequencies. The linear spectral densities of the frequency noises are plotted in Figure 4-5 (left), which shows a moderate noise suppression due to the compensator filter for frequencies above 1 Hz. The ratio between them yields the magnitude of the closed-loop transfer function, which displays multiple peaks at frequencies very close to 1 Hz, 2 Hz, 3 Hz, etc. The deviation from the theoretical transfer function mainly lies at frequencies above 500 Hz, where a servo bump shows up at approximately 1 kHz. The servo dump is ascribed to the excessive phase shift due to the propagation delay in data transfer. Figure 4-6 plots the time series of the phase fluctuations within this time span. Note that in this plot the linear drift due to a constant frequency value is already removed from the phase data. Figure 4-6 (right) is the close-up of the residual phase fluctuations, which distinctly exhibits an oscillation with a frequency very close to 1 Hz, as well as other higher harmonics applied on it.

In the second set of phase measurements, the phasemeter runs at the low data rate of 14.9 Hz for 15 hours to investigate the noise suppression performance in the LISA

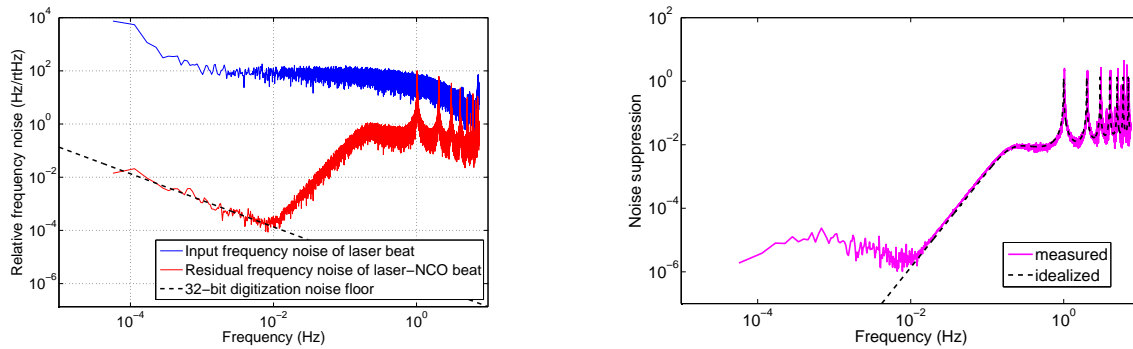


Figure 4-7. (Left) The measurement result of noise suppression performance at low frequencies shows that compared with the initial frequency noise spectrum of the beat signal between two cavity stabilized lasers (blue), the residual frequency noise spectrum of the laser-NCO beat (red) is suppressed by the 4-stage integrators by 5 to 6 orders of magnitude from 0.1 mHz to 10 mHz. (Right) The closed-loop transfer function is given by the ratio between the initial frequency noise spectrum and the residual frequency noise spectrum. The measurement has shown that the control system of this single arm locking loop is consistent with the theoretical design.

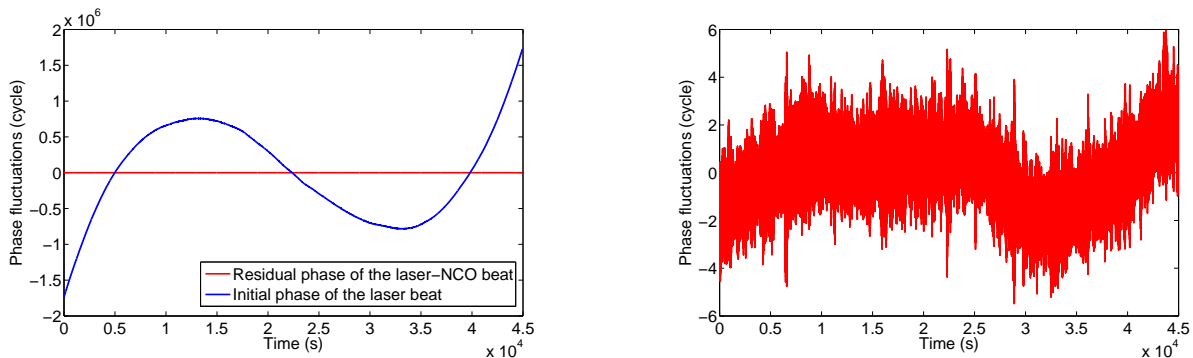


Figure 4-8. (Left) A 12.5 h time series of phase fluctuations of the initial beat signal (blue) and the residual laser-NCO beat (red) with a slow sampling frequency of 14.9 Hz. In this time span the initial phase fluctuates by more than 3.5×10^6 cycles. (Right) A close-up of the residual laser-NCO beat. The residual phase fluctuates by about 10 cycles and the general profile resembles the initial phase fluctuations, indicating that the noise suppression at low frequencies is limited.

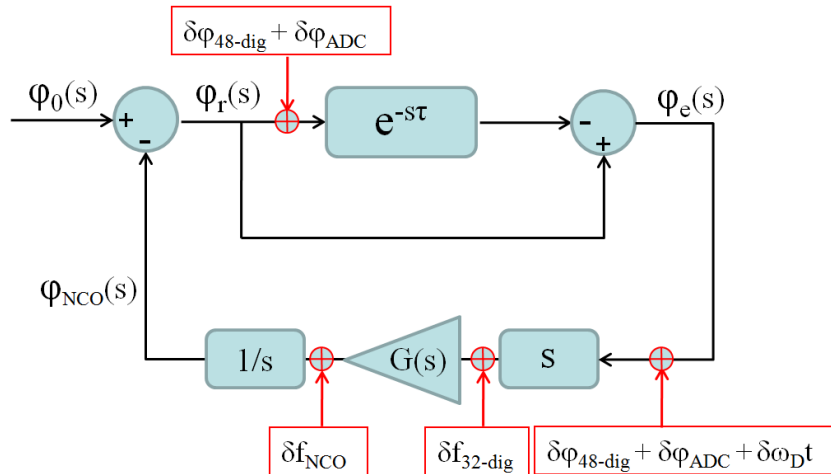


Figure 4-9. Single arm locking with NCO tracking - Laplace domain with noise sources. This single arm locking loop has four primary error input points. Note that the noise sources introduced outside the arm locking controller are treated as the phase noise and otherwise the frequency noise, in accordance with the convention used in Figure 4-2.

band. The linear spectral densities of the initial frequency noise and residual frequency noise, and the time series of the phase fluctuations are shown in Figure 4-7 (left) and Figure 4-8, respectively. The ratio between the two spectra yields the magnitude of the closed-loop transfer function, which indicates 5 to 6 orders of magnitude noise suppression from 0.1 MHz to 10 MHz as shown in Figure 4-7 (Right).

The closed-loop transfer function shown in Figure 4-7 (Right) yields a s^3 slope from 10 MHz to 0.1 Hz due to the 4-stage integrators in the controller. The measurement result agrees well with the theoretical design, which indicates that the noise suppression performance is gain limited in this frequency region. However, for frequencies below 10 MHz the result shows an obvious deviation as the closed-loop transfer function flattens out rather than continue decreasing with a s^3 slope. This behavior indicates that in this frequency region the suppression performance is limited by a different noise source. As shown in Figure 4-7 (Left), the deviation in the closed-loop transfer function is caused by the $1/s$ slope in the residual frequency noise spectrum.

4.2.4 Noise Analysis

To analyze the noise limits and determine the dominating noise floor in the setup, we consider possible noise sources in Figure 4-2 and then draw Figure 4-9. These noise sources include the 48-bit digitization noise $\delta\varphi_{48\text{-dig}}$ and the ADC jitter φ_{ADC} introduced at the EPD unit as well as the arm locking phasemeter, which are represented as phase noises in the figure; any Doppler frequency mismatch introduced at the arm locking phasemeter, which is also represented as a phase noise $\delta\omega_{\text{D}} \cdot t$; the 32-bit digitization noise $\delta f_{32\text{-dig}}$ at the feedback filter, which is represented as a frequency noise; as well as frequency noise δf_{NCO} introduced by the NCO.

Among these noise sources, it is obvious that any NCO noise δf_{NCO} will be suppressed by the open-loop gain. Since the Doppler shift frequency is designed to be perfectly accounted for by the phasemeter preset frequency, the phase noise representing the Doppler frequency error also vanishes. The 48-bit digitization noise and the ADC jitter added at the EPD unit will be tracked by the residual signal; however, they are at a fairly low level compared with the $1/s$ slope. Actually, the calculation indicates that the $1/s$ slope is an effect of the 32-bit digitization noise added in the feedback filter, where the 32-bit frequency fluctuation is sampled at 488 kHz. Thus we determine the digitization noise

$$N_{\text{Dig}} = \frac{f_{\text{clock}} \cdot 2^{-N}}{\sqrt{6} \cdot f_s} = 8.50 \times 10^{-6} \text{ Hz Hz}^{-1/2}. \quad (4-3)$$

In terms of frequency noise the digitization noise is white through the entire band. As this frequency noise becomes an additional term in the error signal transferred from the phasemeter to the filter, it has an equivalent effect as the Doppler frequency error entering and being accumulated by the closed-loop. Therefore in the presence of a DC-coupled controller, the digitization noise multiplied by $1/s$ will appear in the spectrum of the residual frequency noise and the level of the noise floor scales with $1/\tau$:

$$\delta\nu_{\text{Dig}}(f) = \frac{N_{\text{dig}}}{\tau s} = \frac{1.35 \times 10^{-6}}{f} \text{ Hz Hz}^{-1/2}. \quad (4-4)$$

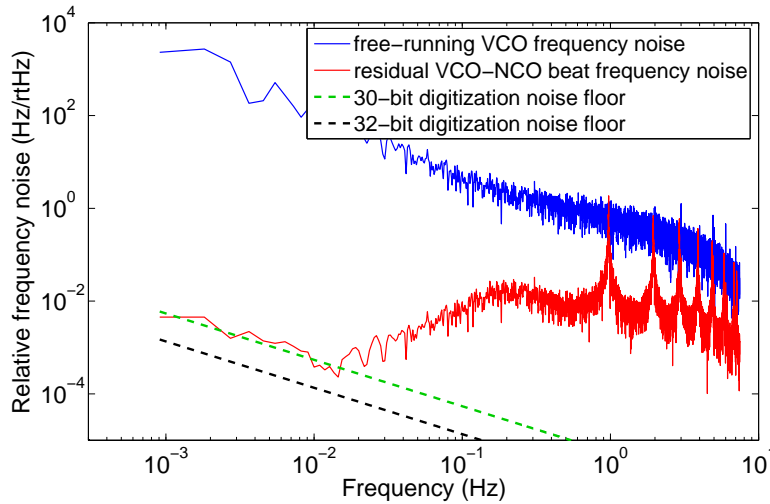


Figure 4-10. The dashed green noise floor is given by the 30-bit digitization noise coupled into the single arm locking loop. Compared with the 32-bit digitization noise floor (dashed black), the dashed green floor is higher by a factor of 4 since the precision given by the lowest two bits is lost in the frequency information. The measurement has shown that the noise suppression is limited by the new noise floor when the 30-bit arm locking controller is used.

As shown in Figure 4-7, this noise floor accurately matches up the $1/s$ slope in the residual frequency spectrum. This noise floor can further be verified by changing the delay time or changing the fixed-point precision of the frequency fluctuations. To demonstrate the influence of the precision to the level of the noise floor, we truncate the 32-bit frequency fluctuation in the filter to 30-bit by hard coding the values of the lowest two bits to zero. We take the measurement using a free-running VCO as the input noise and the result of the 30-bit filter is shown in Figure 4-10. The result explicitly demonstrates that the measured 30-bit digitization noise floor agrees with the theoretical prediction that the new noise floor increases by a factor of 4 due to the 2-bit precision loss in the filter.

Since the digitization noise in the feedback filter is equivalent to a Doppler frequency error at the phasemeter, the direct consequence of this $1/s$ noise floor in the time domain is a linear drift in the output frequency. Here a higher digitization noise

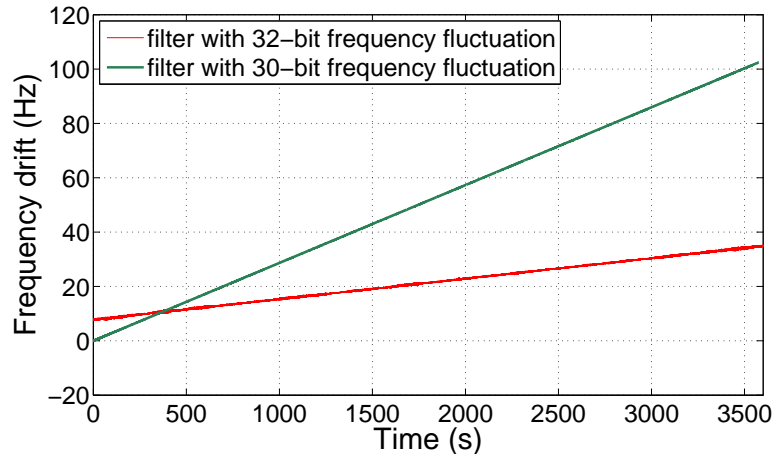


Figure 4-11. Comparison of frequency drift rate between a 30-bit filter (28.6 mHz/s) and a 32-bit filter (7.5 mHz/s). The frequency drift rate of a 30-bit filter is larger by a factor of about 4, scaling with the rms amplitude of the digitization noise.

floor corresponds to a faster frequency drift, as illustrated in Figure 4-11. The frequency data in this figure has been low-pass filtered by averaging out the high frequency noise (e.g., using a boxcar filter) such that the linear drift can be explicitly revealed. The linear regression approach shows that for the 32-bit filter the frequency drift rate is approximately 7.5 mHz/s and for the 30-bit filter it is approximately 28.6 mHz/s, which is again roughly four times the drift rate of the 32-bit case. Given that in realistic LISA the light travel time on one arm is approximately 33 times larger than the 1 s delay time in our experiment, the 32-bit digitization noise should not have significant effects on the noise suppression performance or frequency pulling if single arm locking is used.

4.3 Single Arm Locking Integrated with a Tunable Reference

In this section we move forward to the authentic electro-optical models where single arm locking is used to stabilize the laser frequency. The incorporation of arm locking and pre-stabilization subsystem requires an additional actuator to tune the pre-stabilization reference. The specific approaches have been already introduced in Section 2.3.4 and so far, all proposed methods to integrate single arm locking with Pound-Drever-Hall technique have been experimentally demonstrated on UFLIS. Instead of the preliminary

verification of the noise suppression performance and closed-loop stability in the previous electronic model, we will focus on the characterization of the tunable references and additional noise sources introduced by them in these more realistic single arm locking demonstrations.

4.3.1 Heterodyne Phase-locked Loop

The actuation method of heterodyne phase-locking requires an auxiliary laser to faithfully reproduce the laser frequency noise of the cavity stabilized laser. For this reason it is not a concise option for realistic LISA, yet it is a simple approach to demonstrate in benchtop experiments.

4.3.1.1 Experimental setup

As described in Figure 2-27, the concept of PLL-based single arm locking is to stabilize an auxiliary laser which is phase-locked to the cavity stabilized laser such that the local oscillator of the PLL can be tuned by the arm locking controller. The bench-top experimental setup of the PLL-based single arm locking resembles the setup in Figure 2-27 except that we use another cavity stabilized laser RL to generate a beat signal against the phase-locked laser. Figure 4-12 illustrates the experimental setup in which the reference laser RL and the master laser L_1 are cavity stabilized via Pound-Drever-Hall technique. The slave laser L_2 is phase-locked to L_1 with a frequency offset, which is driven by the NCO in the arm locking controller. Therefore, the stability of the cavity stabilized laser L_1 is transferred into L_2 through phase-locking and the frequency noise in the $RL - L_2$ beat signal is approximately equal to the frequency noise in the beat signal $RL - L_1$. Also, due to the heterodyne PLL the stability of the beat signal $RL - L_2$ is tunable, which means it can be further stabilized by a more stable reference: the arm length (i.e., the fixed delay time in our experiment). Compared with the preliminary test with NCO tracking the input noise, the frequency of the laser beat signal $RL - L_2$ is directly suppressed by the arm locking open-loop gain.

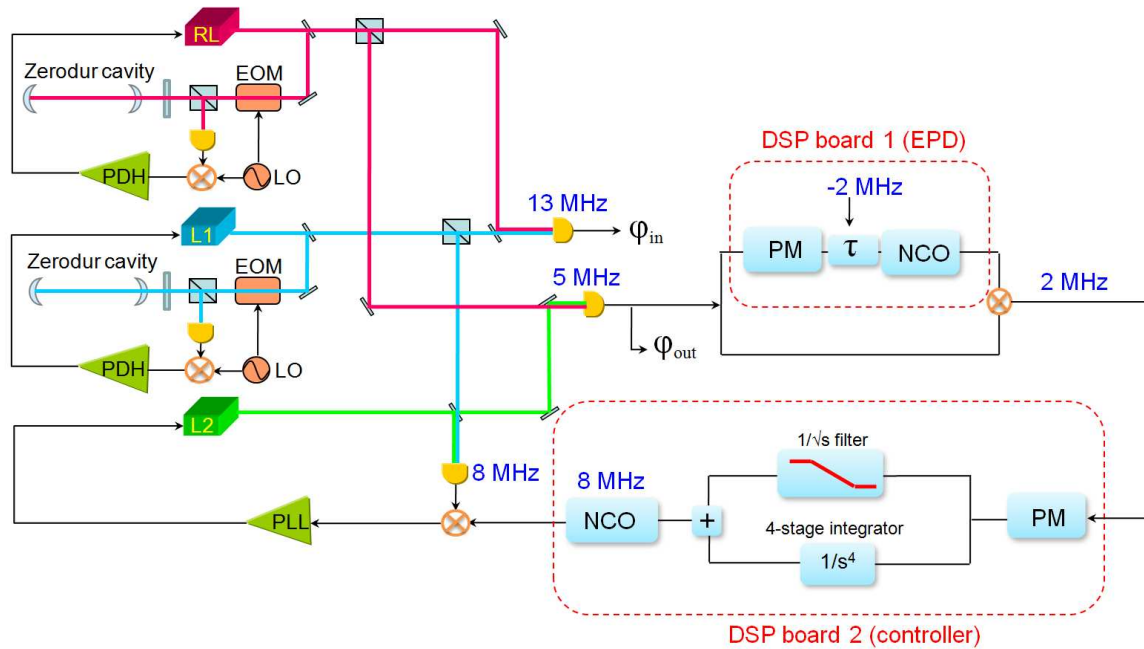


Figure 4-12. The experimental setup of single arm locking experiment using an additional heterodyne phase-locked laser. In this setup the reference laser RL and the master laser L_1 are cavity stabilized via Pound-Drever-Hall technique. The slave laser L_2 is phase-locked to L_1 with a frequency offset, which is driven by the NCO in the arm locking controller. Therefore, within the PLL bandwidth L_2 faithfully reproduces the laser frequency noise of L_1 , both referenced to the “optical clock” RL . Note that the PLL bandwidth is about 20 kHz, which is well larger than the arm locking bandwidth (~ 1 kHz); therefore it will not limit our arm locking performance and a direct feedback of the arm locking control signal to the laser is not necessary. The arm locking controller is used to adjust the NCO that drives the PLL and the frequency noise of L_2 can be further suppressed by the arm locking controller gain.

In our experiment the nominal frequency of the $RL - L_1$ beat signal is approximately 13 MHz. If we set the nominal frequency of the NCO signal to be 8 MHz and phase-lock L_2 to L_1 , there will be two possibilities for the nominal frequency of the the $RL - L_2$ beat signal: 5 MHz and 21 MHz, depending on which value is larger between the nominal frequencies of L_1 and L_2 . Only one of the two beat frequency values is working for the setup as the other configuration would yield a wrong sign. In our setup the right configuration is a 5 MHz $RL - L_2$ beat signal. The EPD unit is configured in the same way as for the NCO tracking setup, providing a 1 s delay time and -2 MHz Doppler shift.

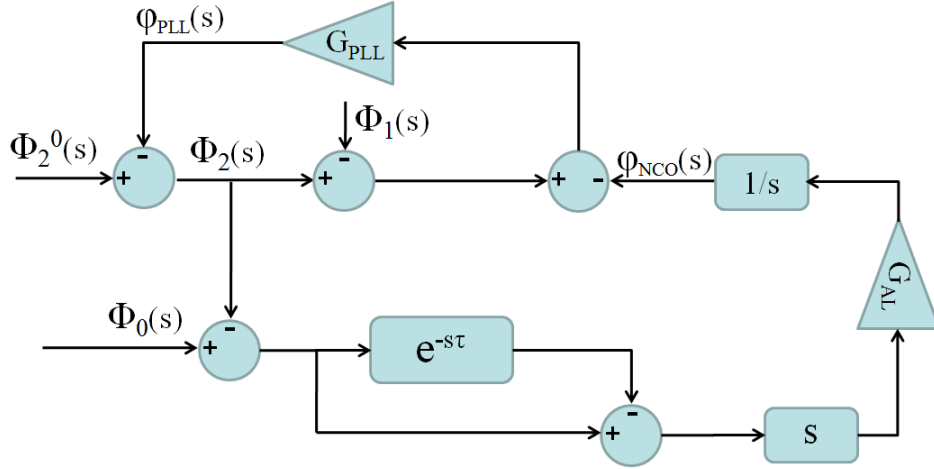


Figure 4-13. The closed-loop dynamics of single arm locking tuned by a heterodyne PLL in the Laplace domain. The control system is based on two loops: PLL and single arm locking. The stability of the arm locking reference is transferred into the error signal of the PLL via the driving NCO.

4.3.1.2 Closed-loop dynamics

Figure 4-13 illustrates the experimental setup represented in the Laplace domain. In this diagram we use Φ_i to represent the phase of the laser L_i (The laser phase of a free-running L_2 is given by Φ_2^0 and the in-loop phase of the phase-locked (and then arm locked) L_2 is given by Φ_2 .) and φ to represent the phase of the PLL feedback, the phase of the NCO signal, etc. Note that in this diagram the configuration of the plus and minus signs assumes the nominal frequencies of the three lasers yield $\Omega_{RL} > \Omega_{L_2} > \Omega_{L_1}$. Not all permutations of the three frequencies are allowed for the system stability and different permutations will result in different configuration of the plus and minus signs.

If we consider the phase-locked loop, the relations are given by

$$\begin{aligned}\Phi_2 &= \Phi_2^0 - \varphi_{PLL} \\ \varphi_{PLL} &= (\Phi_2 - \Phi_1 - \varphi_{NCO})G_{PLL}.\end{aligned}\tag{4-5}$$

Hence we solve the in-loop phase of L_2 given by

$$\Phi_2 = \frac{1}{1 + G_{PLL}}\Phi_2^0 + \frac{G_{PLL}}{1 + G_{PLL}}(\Phi_1 + \varphi_{NCO}).\tag{4-6}$$

The first term represents the initial noise suppressed by the open-loop gain and the second term represents the reference noise that this PLL tracks, i.e., the slave laser L_2 tracks the master laser L_1 . A phase modulation φ_{NCO} from the NCO signal is also coupled into the PLL reference. The tunability of φ_{NCO} allows the phase of L_2 can be further stabilized.

In the arm locking loop, the NCO noise is given by

$$\varphi_{\text{NCO}} = (\Phi_0 - \Phi_2)(1 - e^{-s\tau})G_{\text{AL}}. \quad (4-7)$$

Substitute Eq. 4-7 into Eq. 4-6 and we have

$$\begin{aligned} \Phi_2 &= \frac{1}{1 + G_{\text{PLL}}}\Phi_2^0 + \frac{G_{\text{PLL}}}{1 + G_{\text{PLL}}}(\Phi_1 + (\Phi_0 - \Phi_2)(1 - e^{-s\tau})G_{\text{AL}}) \\ &= \frac{1}{1 + G_{\text{PLL}}}\Phi_2^0 + \frac{G_{\text{PLL}}}{1 + G_{\text{PLL}}}\Phi_1 + \frac{(\Phi_0 - \Phi_2)(1 - e^{-s\tau})}{1 + G_{\text{PLL}}}G_{\text{PLL}}G_{\text{AL}}. \end{aligned} \quad (4-8)$$

We combine the terms involving Φ_2 to the left and add terms $\Phi_0 - \frac{1}{1+G_{\text{PLL}}}\Phi_0 - \frac{G_{\text{PLL}}}{1+G_{\text{PLL}}}\Phi_0 (= 0)$ to the right:

$$\begin{aligned} \left[1 + \frac{G_{\text{PLL}}}{1 + G_{\text{PLL}}}(1 - e^{-s\tau})G_{\text{AL}}\right] \Phi_2 &= \quad (4-9) \\ \frac{1}{1 + G_{\text{PLL}}}\Phi_2^0 + \frac{G_{\text{PLL}}}{1 + G_{\text{PLL}}}\Phi_1 + \frac{\Phi_0(1 - e^{-s\tau})}{1 + G_{\text{PLL}}}G_{\text{PLL}}G_{\text{AL}} + \Phi_0 - \frac{1}{1 + G_{\text{PLL}}}\Phi_0 - \frac{G_{\text{PLL}}}{1 + G_{\text{PLL}}}\Phi_0. \end{aligned} \quad (4-10)$$

The purpose of these additional terms is such that the above equation can be simplified into

$$\left[1 + \frac{G_{\text{PLL}}}{1 + G_{\text{PLL}}}(1 - e^{-s\tau})G_{\text{AL}}\right] (\Phi_2 - \Phi_0) = \frac{1}{1 + G_{\text{PLL}}}(\Phi_2^0 - \Phi_0) + \frac{G_{\text{PLL}}}{1 + G_{\text{PLL}}}(\Phi_1 - \Phi_0), \quad (4-11)$$

where $\Phi_i - \Phi_0$, $i = 1, 2$ is the phase of the beat signal, i.e., the phase of $L_{1,2}$ relative to the reference laser RL . From this equation we obtain the equivalent open-loop transfer function

$$TF_{\text{OL}} = \frac{G_{\text{PLL}}}{1 + G_{\text{PLL}}}(1 - e^{-s\tau})G_{\text{AL}}. \quad (4-12)$$

The first term on the right indicates that the phase noise of a free-running L_2 relative to the reference laser is double suppressed by the open-loop gain of phase locking as well as that of arm locking. The second term on the right, which was tracked in phase locking, is now suppressed by the open-loop gain of arm locking. In the high gain limit ($G_{\text{PLL}} \gg 1$) of the PLL, $\frac{1}{1+G_{\text{PLL}}} \approx 0$ and $\frac{G_{\text{PLL}}}{1+G_{\text{PLL}}} \approx 1$, then Eq. 4-12 approximates to the open-loop transfer function in Eq. 4-2 and Eq. 4-11 is further reduced into

$$[1 + (1 - e^{-s\tau})G_{\text{AL}}] (\Phi_2 - \Phi_0) = \Phi_1 - \Phi_0. \quad (4-13)$$

Finally, the closed-loop transfer function is given by

$$TF_{\text{CL}} = \frac{1}{1 + (1 - e^{-s\tau})G_{\text{AL}}} = \frac{\Phi_2 - \Phi_0}{\Phi_1 - \Phi_0}. \quad (4-14)$$

This relation indicates the phase noise of $RL - L_2$ beat signal is suppressed from the noise level of $RL - L_1$ by the arm locking open-loop gain and the closed-loop transfer function of the entire system can be approximately given by the ratio between them. In other words, the PLL-based single arm locking setup is mathematically equivalent to the preliminary experiment of NCO tracking in the presence of an ideal PLL.

4.3.1.3 Results and analysis

We measure the frequency noises of the $RL - L_1$ beat signal and the $RL - L_2$ beat signal as the input noise and the output noise, respectively. Their noise spectra in the low frequency region are shown in Figure 4-14. As seen in the figure, the noise spectrum of the $RL - L_2$ is almost identical to the residual frequency noise shown in Figure 4-7 (left), except for some difference in the overall loop gain. The measured closed-loop transfer function, which is given by the ratio between the two spectra, indicates that the $RL - L_2$ beat signal has been stabilized with 5 to 6 orders of magnitude. In the low frequency region the noise suppression is again limited by the same 32-bit digitization noise floor described in Section 4.2.4.

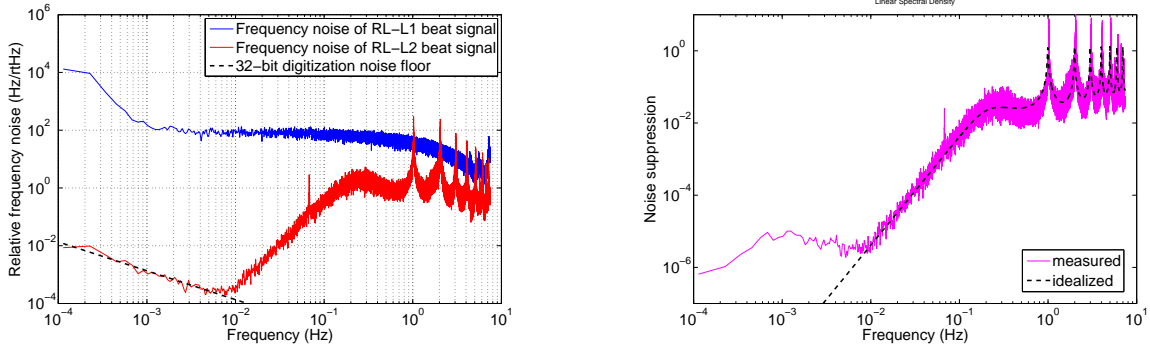


Figure 4-14. (Left) The noise spectra of the initial $RL - L_1$ beat signal (blue) and the stabilized $RL - L_2$ beat signal (red). The noise suppression performance is almost identical to the result given by Figure 4-7. (Right) The closed-loop transfer function given by the ratio between the two LSDs is also the same as the previous experiment. The deviation from the theoretical design again comes from the 32-bit digitization noise floor.

In addition to the 32-bit digitization noise and ADC noise already mentioned in Section 4.2.4, the phase-locked loop in this setup also introduces spurious phase variations $\delta\varphi_{\text{PLL}}$ into the error signal. Also, the uncertainty in the lightpath length from the laser to the photodiode results in the uncertainty in the laser phase; therefore, the $L_1 - L_2$ beat signal and the $RL - L_2$ beat signal will have uncorrelated lightpath noises $\delta\varphi_{\text{LP12}}$ and $\delta\varphi_{\text{LP02}}$ attributed to the difference in the lightpath of each laser. We need to investigate the influence of these noise sources to the measurement result as well. The noise model in the Laplace domain is drawn as Figure 4-15.

It is straightforward to show that the phase of L_2 also tracks the PLL noise $\delta\varphi_{\text{PLL}}$ in the PLL:

$$\Phi_2 = \frac{1}{1 + G_{\text{PLL}}} \Phi_2^0 + \frac{G_{\text{PLL}}}{1 + G_{\text{PLL}}} (\Phi_1 + \varphi_{\text{NCO}} + \delta\varphi_{\text{PLL}}), \quad (4-15)$$

which indicates that the PLL noise is simply coupled into the phase noise of L_1 .

Although it increases the noise level of L_2 from the point of view of the phase-locked loop, the phase noise of the $RL - L_1$ beat signal, including this PLL noise, is well suppressed by the arm locking open-loop gain. This demonstrates that any noise

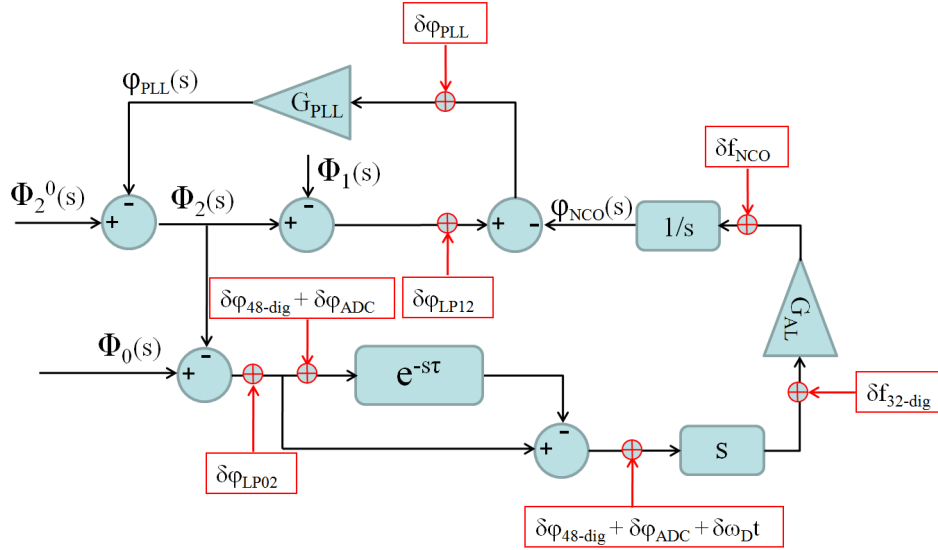


Figure 4-15. Single arm locking with heterodyne PLL - Laplace domain with noise sources. In addition to the noise sources analyzed in Figure 4-9, the heterodyne PLL actuator also introduces the PLL noise $\delta\varphi_{PLL}$, as well as the lightpath noise $\delta\varphi_{LP12}$ and $\delta\varphi_{LP02}$.

introduced by the PLL will be adequately suppressed and unlikely cause a limitation in the arm locking performance.

The same situation is for the lightpath noise $\delta\varphi_{LP12}$ and $\delta\varphi_{LP02}$, which is coupled into the $L_1 - L_2$ beat signal and $RL - L_2$ beat signal individually. The existence of the light noise $\delta\varphi_{LP12}$ and $\delta\varphi_{LP02}$ is nothing more than an additional term added in φ_{PLL} and φ_{NCO} , i.e.,

$$\begin{aligned}\varphi_{PLL} &= (\Phi_2 - \Phi_1 + \delta\varphi_{LP12} - \varphi_{NCO})G_{PLL} \\ \varphi_{NCO} &= (\Phi_0 - \Phi_2 + \delta\varphi_{LP02})(1 - e^{-s\tau})G_{AL}.\end{aligned}\tag{4-16}$$

In other words, they can be considered as being coupled into the phase noise Φ_1 and Φ_0 , respectively. $\delta\varphi_{LP12}$, as a small portion of Φ_1 , will again be suppressed by the arm locking open-loop gain. However, $\delta\varphi_{LP02}$ coupled in the reference laser will show up in all the beat signals and then increases the stabilized noise of $RL - L_2$ beat signal by an insignificant amount.

4.3.2 Piezoelectric Transducer (PZT) Actuated Cavity

The PZT actuated cavity is a straightforward concept to continuously tune the frequency of a cavity stabilized laser by actively modulating the cavity length. The advantage of a PZT cavity is that the modification to the optical cavity does not significantly complicate the implementation while still could achieve considerable tuning range. Although the PZT actuator will inevitably compromise the reference stability of pre-stabilization by probably one order of magnitude, the incorporation with arm locking is capable of suppressing the noise significantly well below the requirement.

4.3.2.1 Characterization of the PZT cavity

In a PZT actuated cavity, a PZT actuator is used to change the distance between the two mirrors forming the reference cavity. In our experiment the PZT actuator is placed between the fused silica mirror and the Zerodur spacer of the cavity using hydroxide bonding. This additional PZT actuator compromises the stability of the cavity length: Measurements have shown that the frequency noise of the beat signal between two lasers, which are locked to a standard Zerodur cavity and a PZT cavity individually, is approximately on the level of $\sim \text{kHz Hz}^{-1/2}$ at 1 mHz, with an applied voltage from 0 V to 100 V. With the voltage increased from 100 V to 200 V, the frequency noise will also increase slightly. The typical frequency drift rate of the beat signal has been observed to be within the range of $50 \sim 350 \text{ Hz/s}$.¹

The feedback signal arriving at the PZT actuator has to be a DC signal. Since the NCO in the controller is AC-coupled, we program another NCO generating a free-running signal with the same nominal frequency and then use an analog mixer to generate a DC output by means of demodulation. The DC-coupled error signal is used to drive the PZT actuated cavity. When the arm locking loop is closed, the frequency of

¹ The hydroxide bonding of the PZT cavity as well as the characterization measurements described in this paragraph are done by Alix Preston.

the error signal is close to DC. In this region a small change in phase can be considered linearly proportional to a small change in the voltage applied on the PZT actuator, i.e., $dV = Kd\varphi$, where K is the conversion coefficient determined by the analog mixer. Using the full range of the DAC, the conversion coefficient was found to be approximately 3.2 mV/degree.

Consequently, the PZT actuator converts the change in voltage into a change in the cavity length. This conversion is also almost linear at frequencies below 20 kHz. The cavity length change then results in the change of the resonant frequency. As we know, the relation between the resonant frequency Ω_L of a reference cavity and its optical path length L is given by

$$\Omega_L = \frac{2\pi nc}{L}. \quad (4-17)$$

By taking the first-order derivative on both sides, we obtain the relation between the change in the resonant frequency and the change in the optical length:

$$d\Omega_L = -\frac{2\pi nc}{L^2}dL. \quad (4-18)$$

The linear conversion from the applied voltage to the change in the resonant frequency can be described using a tuning coefficient, which is measured to be ~ 1.5 MHz/V. As previously mentioned in Section 2.3.4, the tuning range for the tunable reference is required to be at least tens of MHz. If the desired tuning capability is designed to be 100 MHz, the applied voltage is then required to have a range of 0 \sim 70 V, which generally requires a low-noise DC amplifier to amplify the feedback signal.

If we take the conversions starting from the NCO output to the resonant frequency change as a whole, it is essentially a conversion from the phase change to the frequency change. This conversion resembles the frequency actuator in laser controllers, which actuate the phase change from the controller signal into the laser frequency change. Since a frequency actuator is equivalent to a phase actuator with a $1/s$ factor,

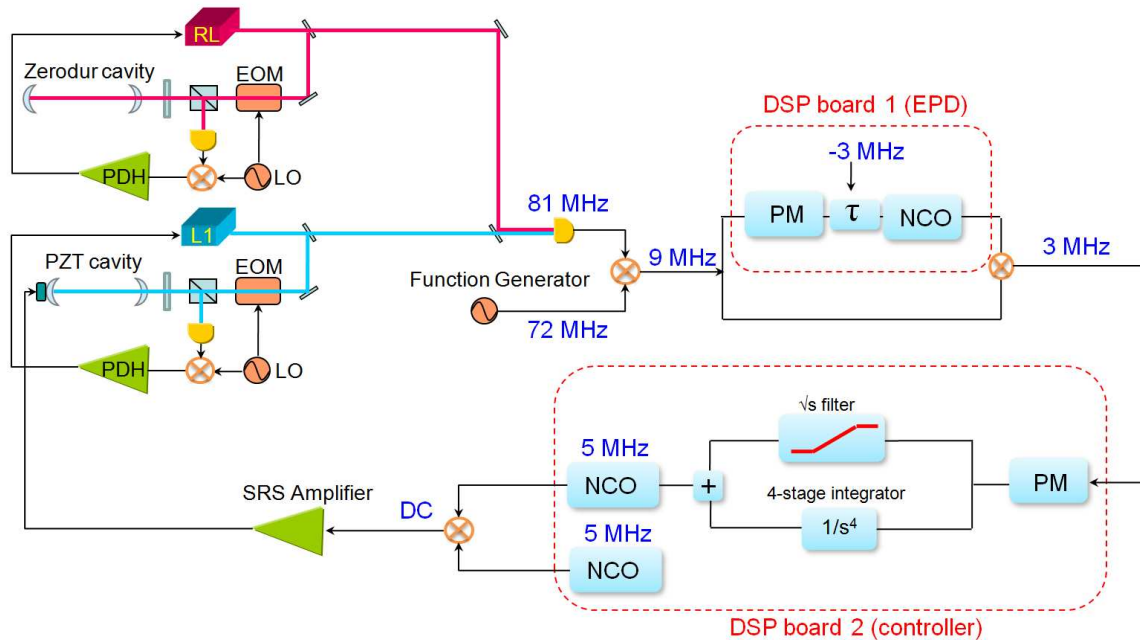


Figure 4-16. The experimental setup of single arm locking experiment using a PZT actuated cavity. In this setup the reference laser RL is locked to a standard cavity and the main laser L_1 is locked to the PZT cavity. Their beat signal is first demodulated by a function generator signal to the desired frequency range and then sent into the control system of single arm locking. As the PZT actuator needs the feedback signal at DC, a second free-running NCO is used to demodulate the NCO signal that is adjusted by the arm locking controller. Note that the controller filter is multiplied with s in the transfer function to compensate the phase-to-frequency conversion in the PZT actuator.

the PZT actuated cavity contains an intrinsic $1/s$ integrator that must be taken into account in closed-loop dynamics.

4.3.2.2 Experimental setup

The experimental verification of PZT-actuated single arm locking is illustrated by Figure 4-16. In this setup the main laser L_1 is stabilized to a PZT actuated cavity via Pound-Drever-Hall technique. Another pre-stabilized reference laser RL , which is locked to a standard Zerodur cavity with a fixed length, is used to generate a 81 MHz heterodyne beat signal with L_1 at the photodiode. This beat signal is demodulated by a 72 MHz function generator signal to 9 MHz, which is sent into the arm locking sensor with 1 s delay and then appropriately filtered by the controller. As mentioned in the

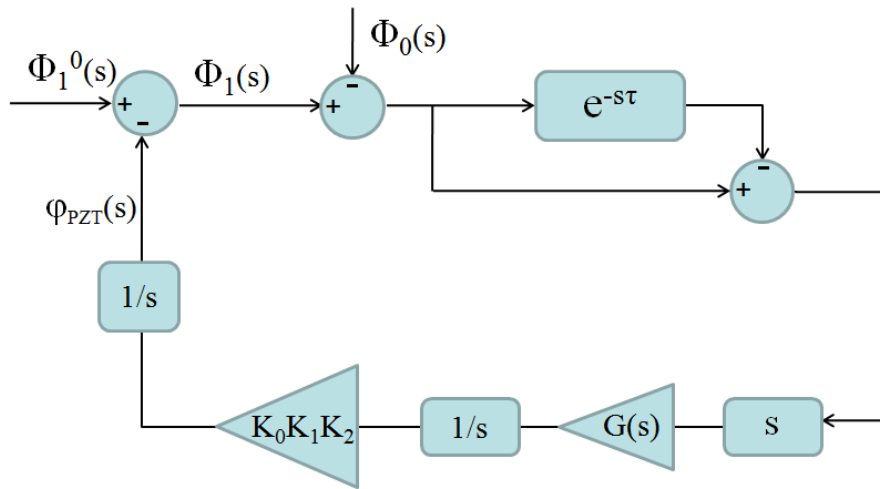


Figure 4-17. The closed-loop dynamics of single arm locking tuned by a PZT actuated cavity in the Laplace domain. The closed-loop dynamics of this experimental setup is simple as the arm locking feedback signal is directly sent back to the laser via the PZT actuator. Compared with Figure 4-2, the main difference is the additional gain stages and the intrinsic integrator in the PZT actuation.

previous section, the controller is configured to have two parallel NCOs running at the same 5 MHz nominal frequency. The difference between them is that one NCO receives the filtered frequency fluctuations from the arm locking error signal, while the other NCO is free-running to demodulate the first NCO signal. The output of the analog mixer carries the information of the phase fluctuations, which is already converted into a DC voltage. After appropriately amplified to ~ 70 V, the voltage is applied onto the PZT actuator to modulate the optical length of the cavity. The modulation on the cavity length is then used to correct the resonant frequency that L_1 is locked to.

Due to the intrinsic $1/s$ integrator in the PZT actuator, the controller filter needs to be modified by multiplying an s slope to maintain the closed-loop stability. The controller filter in this setup is designed to have a \sqrt{s} slope to provide 45° phase advance, which can be realized by switching the frequencies of zeros and poles in the $1/\sqrt{s}$ filter. The experiment model in the Laplace domain is shown in Figure 4-17. In this model the controller output is followed by a series of gain stages, where K_0 represents the

amplifier gain, K_1 represents the conversion from the phase to the voltage at the analog mixer, K_2 represents the conversion from the voltage to the resonant frequency at the PZT actuator. To properly close the loop, another $1/s$ stage is required to convert the frequency back to the phase. Therefore, the relations to describe this model are given by

$$\begin{aligned}\Phi_1 &= \Phi_1^0 - \varphi_{\text{PZT}} \\ \varphi_{\text{PZT}} &= (\Phi_1 - \Phi_0)(1 - e^{-s\tau}) \frac{K_0 K_1 K_2 G}{s}.\end{aligned}\quad (4-19)$$

If we define the open-loop transfer function

$$TF_{\text{OL}} = (1 - e^{-s\tau}) \frac{K_0 K_1 K_2 G}{s}, \quad (4-20)$$

The stabilized phase noise of L_1 is then given by

$$\Phi_1 = \frac{1}{1 + TF_{\text{OL}}} \Phi_1^0 + \frac{TF_{\text{OL}}}{1 + TF_{\text{OL}}} \Phi_0. \quad (4-21)$$

Since we are more concerned with the phase noise of the $RL - L1$ beat signal, Eq.4-21 is equivalent to

$$TF_{\text{CL}} = \frac{\Phi_1 - \Phi_0}{\Phi_1^0 - \Phi_0} = \frac{1}{1 + TF_{\text{OL}}}. \quad (4-22)$$

4.3.2.3 Results and analysis

The measurement results of the frequency noise are shown in Figure 4-18. According to the noise spectra, although the frequency noise of the beat signal stabilized by a free-running PZT cavity does not meet the stringent $30 \text{ Hz Hz}^{-1/2}$ pre-stabilization requirement, single arm locking is capable of appropriately tuning the PZT cavity such that the noise spectrum is significantly reduced by 6 or 7 orders of magnitude. Note that even in the gain limited region, the initial frequency noise and the stabilized frequency noise are not correlated since they were not measured simultaneously. Nevertheless, we modeled the open-loop transfer function of the setup given by Eq. 4-20 and the idealized stabilized noise spectrum, represented by the green

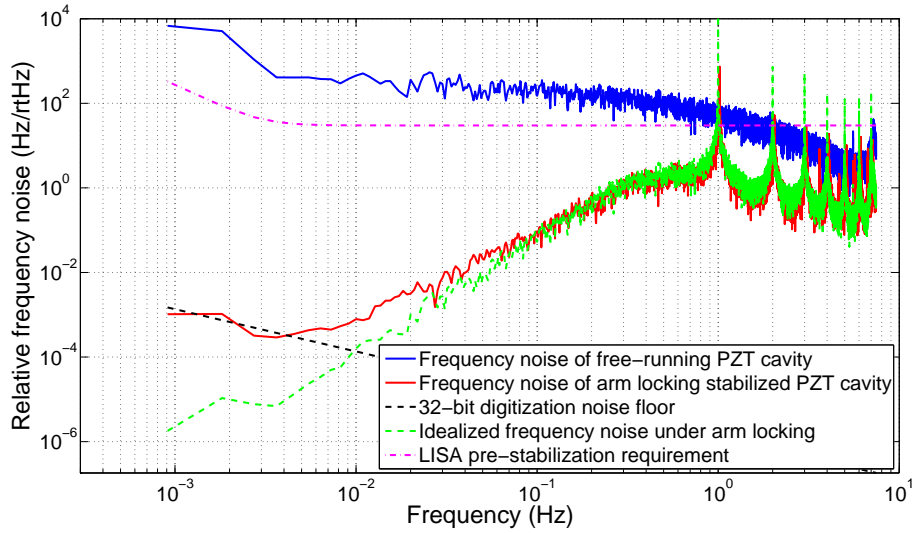


Figure 4-18. Noise spectra of single arm locking experiment using a PZT actuated cavity. The initial noise spectrum (blue) is approximately $200 \text{ Hz Hz}^{-1/2}$ and it was not measured simultaneously with the stabilized noise spectrum (red), which is again limited by the 32-bit digitization noise floor. The green curve yields the idealized frequency noise in the presence of the closed-loop gain, ignoring the noise limitations. The red and green curves are consistent at high frequencies (gain limited region) and the deviation comes in below 0.1 Hz.

curve, is evaluated by the initial frequency noise multiplied by the magnitude of the modeled closed-loop transfer function. The frequency region where the idealized noise spectrum agrees with the measured one is obviously gain limited, while the deviation indicates the noise limited region which is dominated by the digitization noise floor.

Figure 4-19 illustrates the noise sources generated in the setup. The noise sources that are introduced after the NCO output can be various and complicated, including the electronic noise in the amplifier, thermal noise in the PZT actuator and in the optical cavity, etc. However, we can roughly generalize these various noises as a phase fluctuation $\delta\varphi_{\text{PZT}}$ introduced into the NCO output. Then the closed-loop transfer function from this error point to the output noise Φ_1 is given by

$$TF_{\text{PZT}}(s) = \frac{K_0 K_1 K_2 / s}{1 + K_0 K_1 K_2 (1 - e^{-s\tau}) G(s) / s}. \quad (4-23)$$

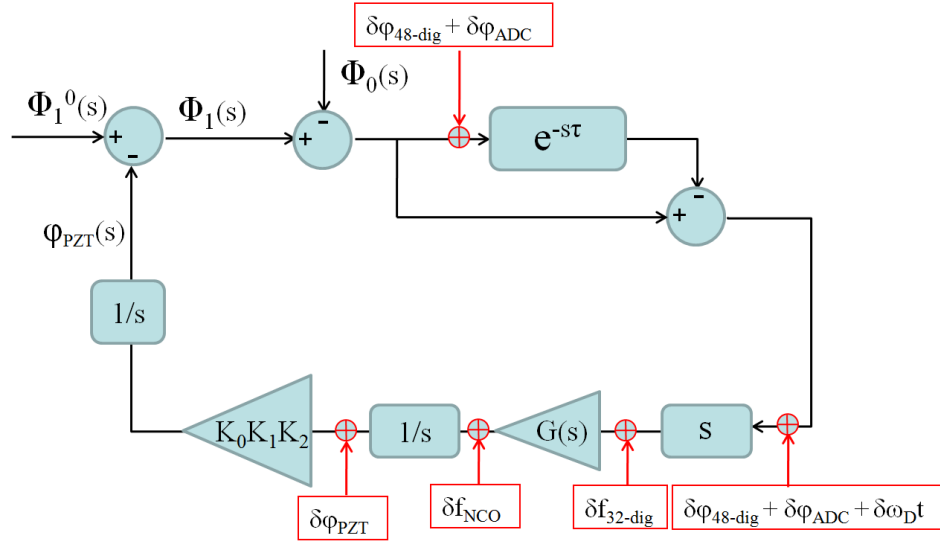


Figure 4-19. Single arm locking with a PZT actuated cavity - Laplace domain with noise sources. Compared with Figure 4-9, the PZT actuation introduces additional noise sources such as the electronic noise, thermal noise, etc. These noise sources can be generalized as the phase noise $\delta\varphi_{\text{PZT}}$ introduced after the NCO output, and are consequently suppressed by the closed-loop gain.

At low frequencies, it is easy to show that this transfer function approximates to $\frac{1}{(1-e^{-s\tau})G(s)}$ such that any phase noise introduced after the NCO output is still well suppressed by the integrator gain.

4.3.3 Electro-optic Modulator (EOM) Sideband Locking

In addition to the two tunable references described above, the experimental verification of single arm locking with EOM sideband locking has also been demonstrated on UFLIS. The experiment was performed by Jeffery Livas *et al.* at Goddard Space Flight Center (GSFC) [94], incorporating the arm locking components on UFLIS and the pre-stabilization system including the broadband EOM provided by GSFC. In the setup a sideband generated at the EOM is locked to the fixed length cavity using the standard PDH technique. Tunability is achieved by changing the frequency of the phase modulation signal applied on the EOM and the local oscillator, which both need to be

broadband. In the experiment, the tunable range of the entire control system is limited by the tunability of the local oscillator to a few tens of MHz.

This experiment has demonstrated additional noise suppression can be achieved by the incorporation of single arm locking and sideband locking as the tunable pre-stabilization reference, which only requires minimal modifications to the PDH cavity stabilization and does not explicitly degrade the noise suppression performance of it.

CHAPTER 5 EXPERIMENTAL VERIFICATION OF DUAL/MODIFIED DUAL ARM LOCKING

5.1 Common Arm Locking

In this chapter we discuss the experimental verification of advanced arm locking configurations that utilize the interferometer outputs on both two LISA long arms, including common arm locking, dual arm locking and modified dual arm locking [15]. Among these configurations, although common arm locking takes a linear combination of the phasemeter measurements on both arms, it still resembles single arm locking in a variety of ways such that it has never been considered promising. Nevertheless, we will still first demonstrate the validity of common arm locking with relatively short time delays on UFLIS. The reason is that as the simplest two-arm configuration, the common arm locking experiment can be considered as a preliminary test for the follow-on arm locking experiments with more elaborated linear combinations.

5.1.1 Common Arm Locking Sensor

Based on the discussion in Section 2.3.2.2, the common arm sensor is essentially given by the sum of two long arm interferometry outputs on two different arms. In the realistic architecture, the phase noise of the long arm interferometry on each arm is fast sampled and then measured by the controller phasemeter individually. A mapping vector, which is an adder for the case of common arm locking, will be implemented right behind the phasemeters to generate an sensor/error signal. For our simulation on UFLIS, the long arm interferometry is represented by electronic mixing of the prompt and EPD-delayed phase. To generate differential light travel time between two LISA arms, the EPD unit will need to exploit the bottom VIM on the Pentek board where the delay buffer can be specified with a different array length.

As shown in Figure 5-1 (left), the common arm sensor of UFLIS is implemented on two Pentek boards which function respectively as front end and back end. The front end includes two EPD units that simulate the round-trip travel time on two different

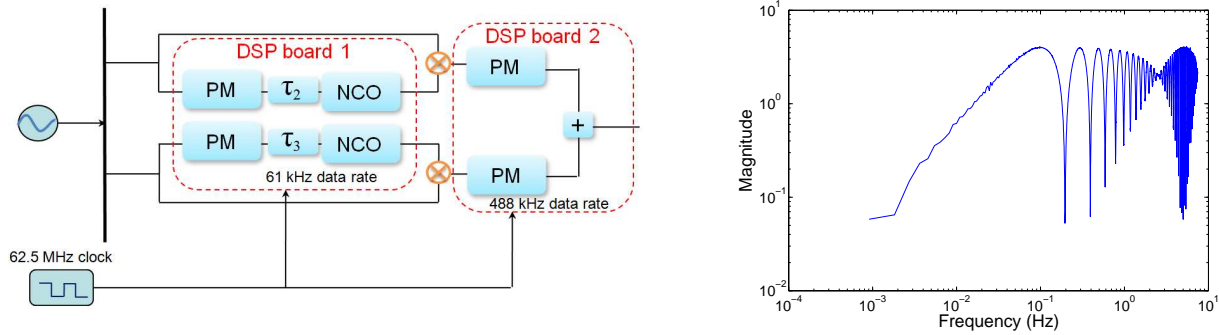


Figure 5-1. (Left) The design of the common arm locking sensor on the FPGA. The common arm sensor is implemented on two Pentek boards. DSP board 1 functions as the round-trip delay lines on two arms and DSP board 2 functions as the phase measurements and the mapping vector on the local spacecraft. The phasemeters send the frequency data with a fast rate of 488 kHz. (Right) The measured common arm sensor transfer function. The averaged delay time is 5 s and the differential delay time is 0.1 s. Note that the first sensor null is at $1/\Delta\tau = 10$ Hz, which is higher than the Nyquist frequency of this measurement. The measured transfer function only have local minima at $n/\bar{\tau}$.

arms individually. We use an voltage controlled oscillator as a noisy oscillator for initial experiments. The VCO signal is electronically split into two arms and the signal on each arm is split again to generate a prompt signal and a delayed and Doppler shifted signal via the EPD unit. On the other Pentek board the back end starts with two phasemeters that measures the phase difference on each arm individually. Identical to the single arm locking case, the phasemeter design is optimized in a way that they send data with a fast rate of 488 kHz to minimize the data transfer delay. The mapping vector calculates the sum of the two phase measurements and then send the 32-bit error signal into the following controller filter.¹

For the purpose of demonstration, the delay provided by the EPD units are set to be relatively short times such as 2 s or 5 s. The reason is simply that the design of the

¹ The phasemeter measures the frequency fluctuations and send out the data with a precision of 48-bit. Then the 48-bit data is truncated in the VHDL code and only high 32-bit has been kept before they are received by the mapping vector.

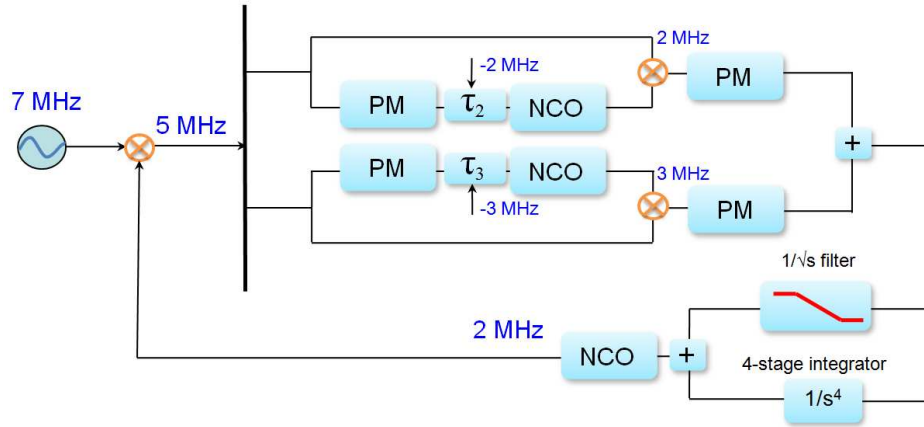


Figure 5-2. The experimental setup of common arm locking using an NCO to track the input noise. The basic configuration resembles the setup in Figure 4-1. The delay times are 2.1 s and 1.9 s.

controller filter for single arm locking experiments can be directly adapted for common arm locking with similar delay times, while a common arm locking demonstration with realistic 33 s delay would only be compatible with a totally different set of zeros and poles to be designed in the controller filter. Figure 5-1 (right) shows the measurement of the magnitude response of a common arm locking sensor with delay times 5.1 s and 4.9 s ($\bar{\tau} = 5$ s and $\Delta\tau = 0.1$ s). The magnitude response has nulls starting from $1/(\Delta\tau) = 10$ Hz, which is already beyond the LISA band; however, there are also local minima at multiples of $1/\bar{\tau} = 0.2$ Hz where each phase shift is still close to $\pi/2$ with various degrees.

5.1.2 Preliminary Test with Numerical Control Oscillator (NCO) Tracking

The experimental setup to demonstrate the control system of common arm locking is shown in Figure 5-2, which is identical to the setup described in Figure 4-1 except for the replacement with the common arm sensor. In this experiment the delay times are set to be 2.1 s and 1.9 s. By following similar procedures discussed in Section 4.2.1, the residual phase noise $\varphi_r(s)$ is given by

$$\varphi_r(s) = \varphi_o(s) - \frac{G(s)}{1 + H_C(s)G(s)} \mathbf{S}_k \cdot \Phi_1(s), \quad (5-1)$$

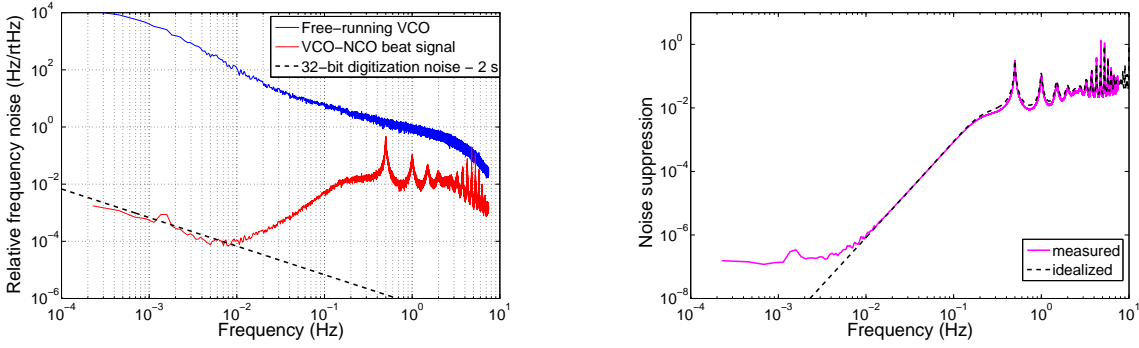


Figure 5-3. (Left) The noise spectra of the free-running VCO signal (blue) and the VCO-NCO beat signal (red). The noise spectrum of the residual frequency noise is limited by the 32-bit digitization noise floor, which is given by the integrated quadrature sum of the 32-bit digitization noise from the two independent phasemeter. (Right) The closed-loop transfer function is given by the ratio between the two noise spectra.

Then the closed-loop transfer function is given by

$$\frac{\varphi_r(s)}{\varphi_o(s)} = \frac{1}{1 + (2 - e^{-s\tau_2} - e^{-s\tau_3})G(s)}. \quad (5-2)$$

The measurement results of the original noise and residual noise, as well as the closed-loop transfer function given by the ratio between them, are shown in Figure 5-3. Due to the local minima at $n/\bar{\tau}$ in the sensor magnitude response, the residual frequency spectrum still exhibits periodic peaks, although not noise enhancements, at these frequencies and at $1/\bar{\tau} = 0.5$ Hz the peak reaches the highest.

In the low frequency region, the noise suppression is again limited by the 32-bit digitization noise floor. The experiment model in the Laplace domain is shown in Figure 5-4, which depicts a generic arm locking configuration with NCO tracking. In this diagram the block labeled with “mapping vector” represents an adder for common arm locking. Note that the ADC noise and the digitization noise introduced on different arms is uncorrelated to each other. Based on the discussion in Section 2.3.5.2, the arm locking sensor will detect the common noise between two arms, which is given by the quadrature sum of them. Since the digitization noises in two arms are uncorrelated but have the same amplitude in our setup, the quadrature sum is given by $\sqrt{2}N_{\text{dig}}$. The

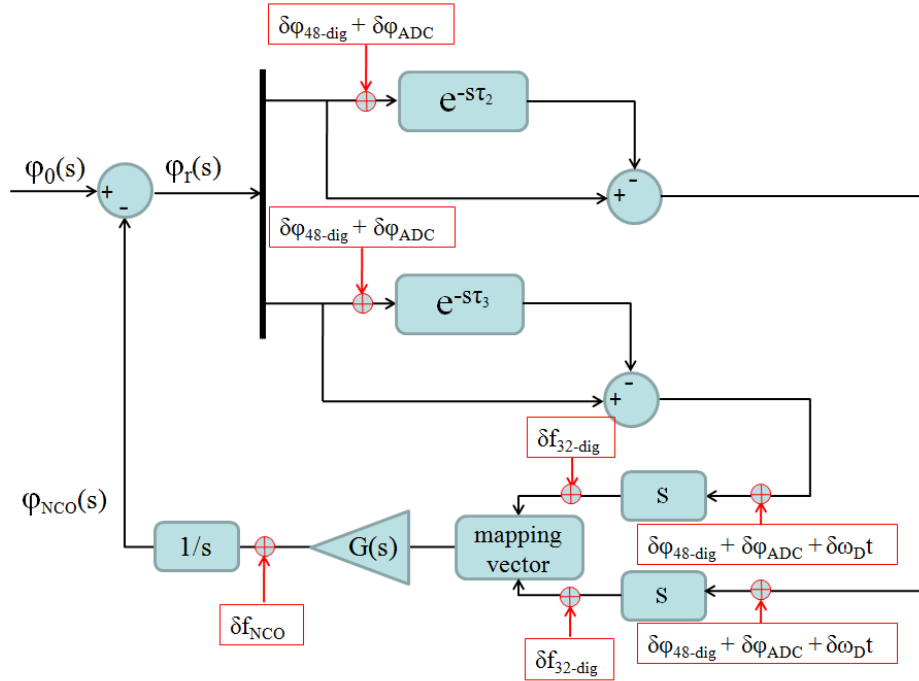


Figure 5-4. The closed-loop dynamics of common arm locking with NCO tracking in the Laplace domain. This diagram can represent the control system of any two-arm-based arm locking configuration, where the block labeled with mapping vector determines the specific arm locking type. Note that the same kind noise sources (digitization noise, ADC noise) between the two channels are uncorrelated and their common noise is given by the quadrature sum of them.

magnitude response of the common arm locking loop to the common digitization noise scales with $1/\bar{\tau}$, therefore we have

$$\delta\nu_{\text{Dig}}(f) = \frac{\sqrt{2}N_{\text{dig}}}{\bar{\tau}S} = \frac{9.53 \times 10^{-7}}{f} \text{ Hz Hz}^{-1/2}. \quad (5-3)$$

Compared with the single arm locking experiments, the digitization noise floor has been decreased by a factor of $\sqrt{2}$ due to the longer averaged delay time. For realistic 33 s light travel time, the digitization noise floor can be further decreased for single or common arm locking and hence should not cause significant impact on the noise suppression performance.

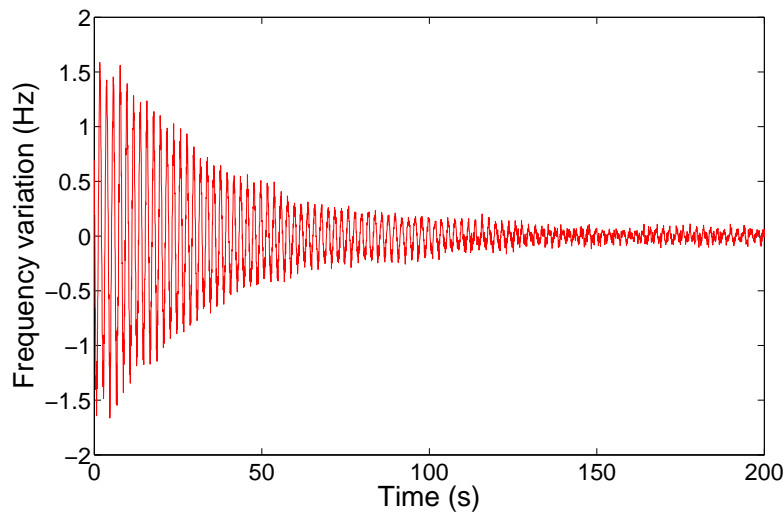


Figure 5-5. The lock acquisition process observed in the common arm locking experiment. The start-up transients caused by a non-zero initial error signal appear in the time series with a period of 2 s. The transients decay with a time constant less than 50 s; however, this observed time constant is based on an averaged light travel time of 2 s. For a 33 s round-trip travel time, the time constant would increase proportionally and become comparable to the single arm locking case.

Analogous to single arm locking, the periodic impulse peaks are also visible in the time series and the most distinguishable oscillation yields a period of 2 s. Figure 5-5 illustrates the measurements in the first couple of minutes, where the start-up transients with a period of 2 s appear in the lock acquisition process and decay with a time constant less than 50 s. Note that the time scale used in our experiment is shorter than the realistic LISA situation by a factor of about 16. Therefore, the expected time constant for a realistic 33 s delay is on the level of more than 500 s, which is comparable to the single arm locking model described in Figure 2-13.

5.2 Dual Arm Locking

5.2.1 Dual Arm Locking Sensor

As an enhanced version of common arm locking, dual arm locking recovers the instantaneous phase noise by combing the common phase noise and the integrated differential phase noise on two interferometer outputs. To realize such a linear

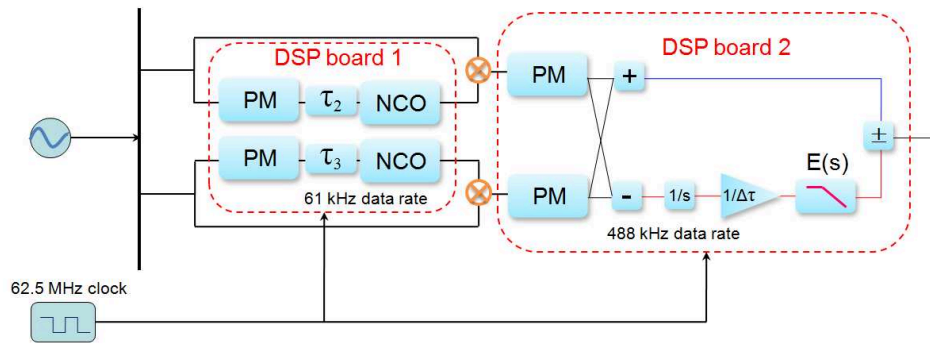


Figure 5-6. The implementation diagram of the dual arm locking sensor. In comparison to Figure 5-1, the mapping vector provides the differential path where the differential frequency noise between two channels is integrated and scaled by $1/\Delta\tau$. The low-pass filter $E(s)$ is also implemented to attenuate the excessive phase loss in the differential path.

combination, we modify the mapping vector on the basis of common arm sensor. As shown in Figure 5-6, the updated mapping vector calculates the common and difference between the two phase measurements. In the differential path, the differential frequency noise is integrated and scaled by $1/\Delta\tau$. A low-pass filter with a single pole at 1 Hz is placed in the differential path to attenuate the excessive phase loss in the open-loop transfer function of the dual arm locking sensor. Depending on which arm is longer, an adder or subtractor subsequently combines the two paths to generate the dual arm locking sensor signal. In all the following experiments we always assume $\tau_2 > \tau_3$ such that the differential arm is kept to be added to the common arm.

To make sure each component in the dual arm locking sensor works appropriately, we first measured the magnitude responses of the common arm, differential arm and integrated differential arm independently. The delay times are set to be 5.1 s and 4.9 s ($\bar{\tau} = 5$ s and $\Delta\tau = 0.1$ s) and the measurement results are shown in Figure 5-7 (left). The entire transfer function of dual arm locking sensor, given by the combination of common arm and integrated differential arm, is measured and displayed in Figure 5-7 (right). The measured transfer function agrees very well with the theoretical transfer function, which retains a flat magnitude response at low frequencies. The measurement

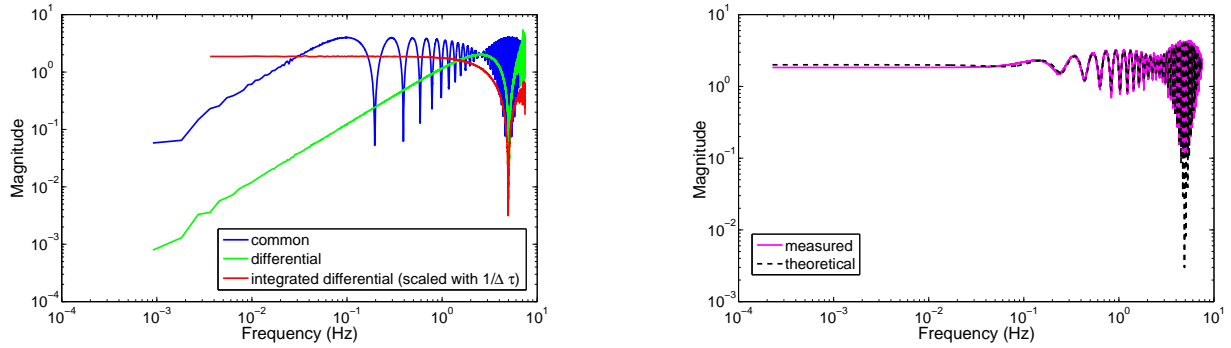


Figure 5-7. (Left) The measurement results on UFLIS display the transfer functions of common arm, differential arm and integrated differential arm using two EPD units with delay time 5.1 s and 4.9 s. The integrated differential arm is already scaled with $1/\Delta\tau$. (Right) The measurement result of the dual arm locking sensor transfer function, which is a linear combination of the three transfer functions on the left. The low-pass filter $E(s)$ is also included in the measured transfer function. The first null is located at ~ 5 Hz.

results also explicitly show the first null at $1/2\Delta\tau = 5$ Hz, which is well beyond the LISA band.² Since the sensor nulls of dual arm locking only depend on the differential light travel time, the sensor transfer function will essentially remain the same if the averaged delay time is changed to 33 s.

5.2.2 Preliminary Test with NCO Tracking

To validate the feasibility of the dual arm locking sensor, we performed hardware simulations featuring this sensor to study its noise suppression performance. In our preliminary experiment we configured a dual arm locking loop with the same NCO tracking scheme. Figure 5-8 illustrates the experimental setup in which the frequency of a 2 MHz NCO signal is stabilized to a free-running 7 MHz VCO signal. The two EPD units provide 33.25 s and 32.75 s delay times (arm length mismatch $\sim 1.5\%$) as well as -2 MHz and -3 MHz Doppler shifts, respectively. This sensor signal is filtered by the feedback controller to drive the NCO signal tracking the input phase noise. Since the

² Strictly speaking, this is a non-zero local minimum and it is not exactly located at 5 Hz.

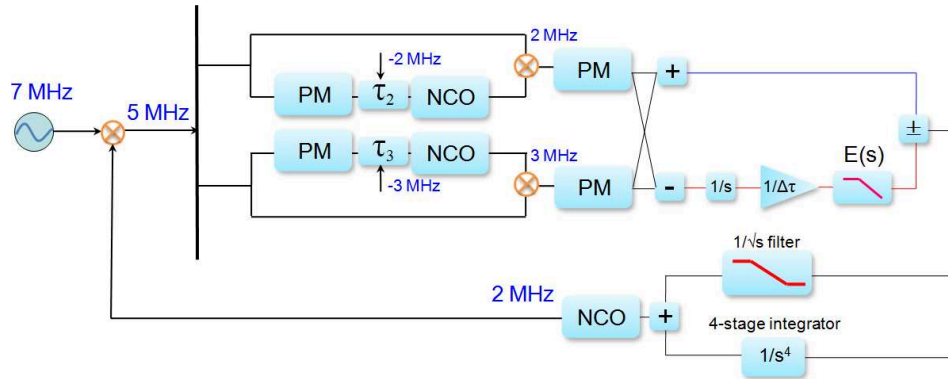


Figure 5-8. The preliminary experimental validation of the dual arm locking sensor on UFLIS is to stabilize the frequency of an NCO signal to track the input frequency noise of a VCO signal. The two EPD units provide 33.25 s and 32.75 s delay times as well as -2 MHz and -3 MHz Doppler shifts, respectively. The analog mixers mix the prompt and delayed signals. The mixer outputs are then sent to the phasemeters and the mapping vector on the second DSP board to generate the sensor signal of dual arm locking.

differential delay time $\Delta\tau = 0.25$ s, the compensator filter designed in Section 4.2.2 still satisfies the requirement of closed-loop stability.

The linear spectral densities of the free-running VCO signal and the VCO-NCO beat signal are shown in Figure 5-9 (Left). The ratio between the two spectrum yields the closed-loop transfer function, which indicates 6 orders of magnitude noise suppression below 1 mHz as shown in Figure 5-9 (Right). Figure 5-9 (Right) also demonstrates some deviation from the idealized closed-loop transfer function for frequencies below ~ 30 mHz. Theoretical calculation indicates that the $1/f$ 32-bit digitization noise floor, which now scales with $1/\Delta\tau$, still dominates this frequency range. Therefore, the 32-bit controller filter in the presence of a 0.25 s arm length mismatch results in a noise floor given by

$$\delta\nu_{\text{Dig}}(f) = \frac{N_{\text{dig}}}{\Delta\tau S} = \frac{5.41 \times 10^{-6}}{f} \text{ Hz}/\sqrt{\text{Hz}}. \quad (5-4)$$

This result indicates that a smaller arm length mismatch will cause a higher $1/f$ digitization noise floor. In realistic LISA this kind of digitization noise within the dual arm locking sensor/controller may limit the noise suppression performance under certain

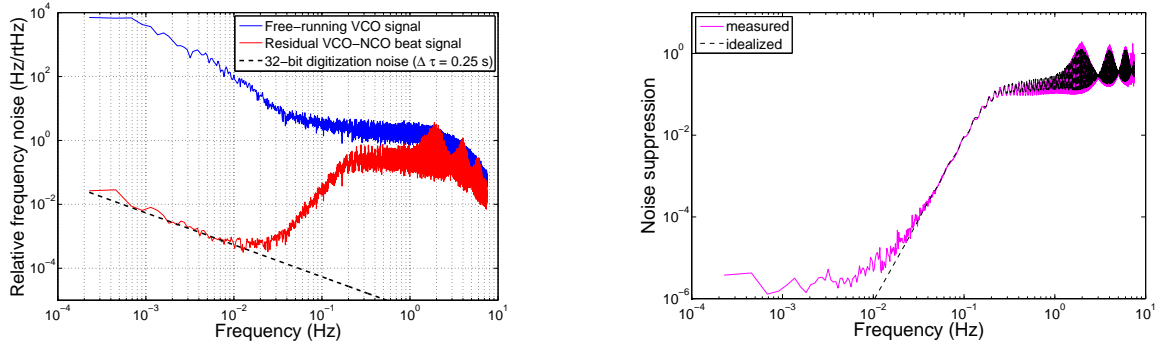


Figure 5-9. (Left) The measurement result of noise suppression performance shows a noise suppression of ~ 6 orders of magnitude below 1 mHz. In the residual frequency noise curve the $1/s$ slope starting from around 10 mHz toward DC is due to the 32-bit digitization noise integrated by the differential arm. For this reason, this noise limitation is proportional to the factor of $1/\Delta\tau$. (Right) The closed-loop transfer function is given by the ratio between the initial frequency noise spectrum and the residual frequency noise spectrum. The deviation from the idealized closed-loop transfer function in the low frequency range is mainly due to the digitization noise floor.

circumstances of very short arm length mismatch. For a differential light travel time less than 1 ms (~ 300 km), the residual noise would fail to meet the $0.3 \text{ Hz}/\sqrt{\text{Hz}}$ requirement, as well as exhibit relatively fast frequency drift. This potential issue indicates that the controller with a 32-bit fixed-point precision is somewhat inadequate especially for the dual arm locking configuration. If we enhance the precision of the sensor/controller up to 48-bit, the corresponding digitization noise is

$$N_{\text{Dig-48}} = \frac{f_{\text{clock}} \cdot 2^{-48}}{\sqrt{6} \cdot f_s} = 1.30 \times 10^{-10} \text{ Hz}/\sqrt{\text{Hz}}. \quad (5-5)$$

Although we are able to increase the integer precision of the arm locking sensor/controller, the precision in the VIM transfer from the controller output to the NCO is still limited to 32-bit due to the hardware specification. However, as long as we maintain the 48-bit data until it is sent to the VIM transfer at the controller output, the additional 32-bit digitization noise introduced by the VIM transfer will be suppressed by the open-loop gain and will not cause an issue. The results using the same experimental setup are shown in Figure 5-10. The delay times generated at the EPD units are 33.025 s and

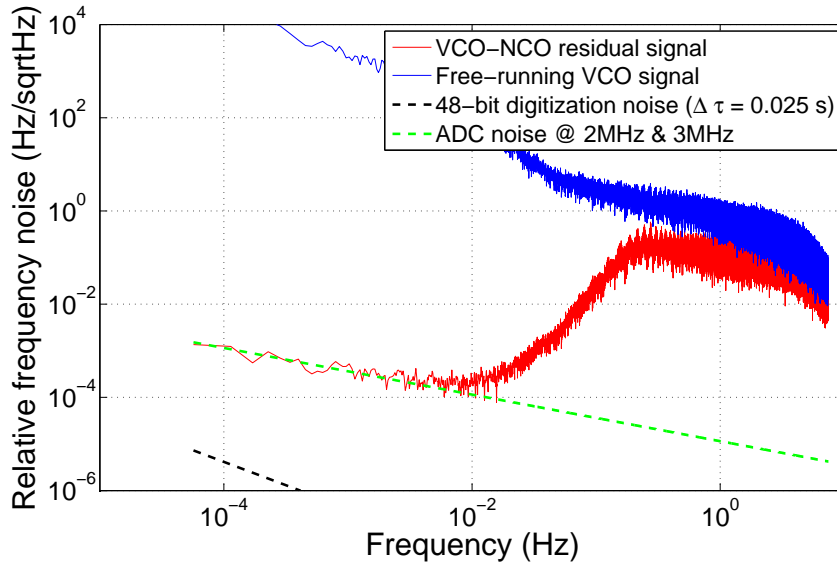


Figure 5-10. In this measurement we use the same experimental setup except that the fixed-point precision in the controller filter has been improved to 48-bit. Compared to Figure 5-9, the digitization noise floor has been decreased by a factor of 2^{16} and thereby the noise suppression performance has been enhanced. However, it does not hit the 48-bit digitization noise floor but is limited by the ADC noise in the phase measurements. The ADC noise in the phasemeter is a \sqrt{f} slope and is integrated by the arm locking loop in the same manner as the digitization noise.

32.975 s, respectively. Compared with the 32-bit case, the digitization noise floor has been decreased by a factor of 2^{16} due to the higher precision. However, the result indicates that the residual noise spectrum is well above the 48-bit digitization noise and limited by a different noise floor featuring a $1/f^{1/2}$ slope.

The closed-loop response to the technical noise (48-bit digitization noise, ADC noise) introduced at the EPD units is $H(s)G(s)/(1 + H(s)G(s)) \approx 1$. As a result, these noises will only increase the residual frequency noise by an insignificant amount. In contrast, the ADC noise at the controller phasemeters will be integrated by the transfer function of the differential arm. Based on the introduction in Section 3.2.2.3, the ADC frequency noise at the phasemeter, when digitizing a 3 MHz and 2 MHz RF signal, is

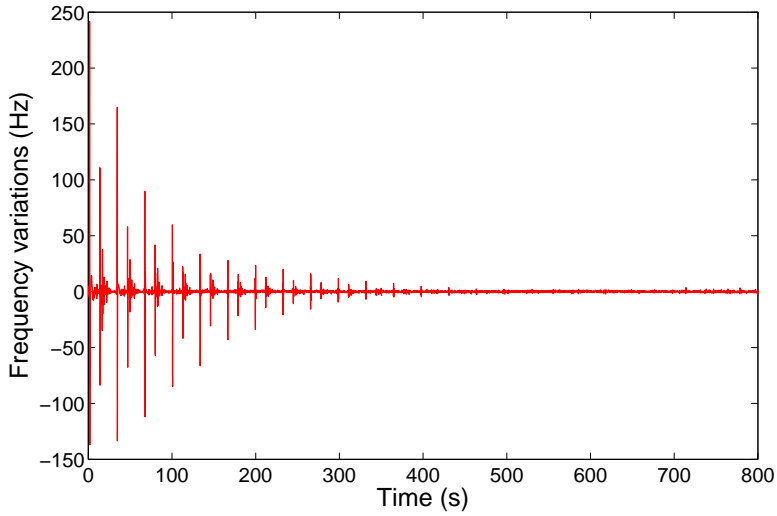


Figure 5-11. The lock acquisition process observed in dual arm locking. In the time series the initial transients oscillate with a period of 33 s and decay much faster than the single or common arm locking case. The time constant in this model is less than 100 s.

approximately given by

$$\begin{aligned}
 N_{\text{ADC}@3\text{MHz}}(f) &= 10^{-6} \sqrt{f} \text{ Hz}/\sqrt{\text{Hz}}, \\
 N_{\text{ADC}@2\text{MHz}}(f) &= 1.5 \times 10^{-6} \sqrt{f} \text{ Hz}/\sqrt{\text{Hz}}.
 \end{aligned}
 \tag{5-6}$$

Since the two ADCs on different channels are uncorrelated, the above two noises are combined in quadrature when enter the arm locking controller. The closed-loop response to the combined ADC noise is dominated by the differential arm, which causes a $1/f$ slope scaled with $1/\Delta\tau$:

$$\delta\nu_{\text{ADC}}(f) = \frac{\sqrt{N_{\text{ADC}@3\text{MHz}}(f)^2 + N_{\text{ADC}@2\text{MHz}}(f)^2}}{\Delta\tau S} = \frac{1.15 \times 10^{-5}}{\sqrt{f}} \text{ Hz}/\sqrt{\text{Hz}}.
 \tag{5-7}$$

As shown in Figure 5-10, this $1/\sqrt{f}$ noise floor agrees with the residual noise spectrum.

Another distinctive feature of dual arm locking is that the initial transients decay with a relatively short time constant. As shown in Figure 5-11, the initial transients exhibit a damped oscillation with a period of 33 s. After about 400 s the 33 s oscillation becomes

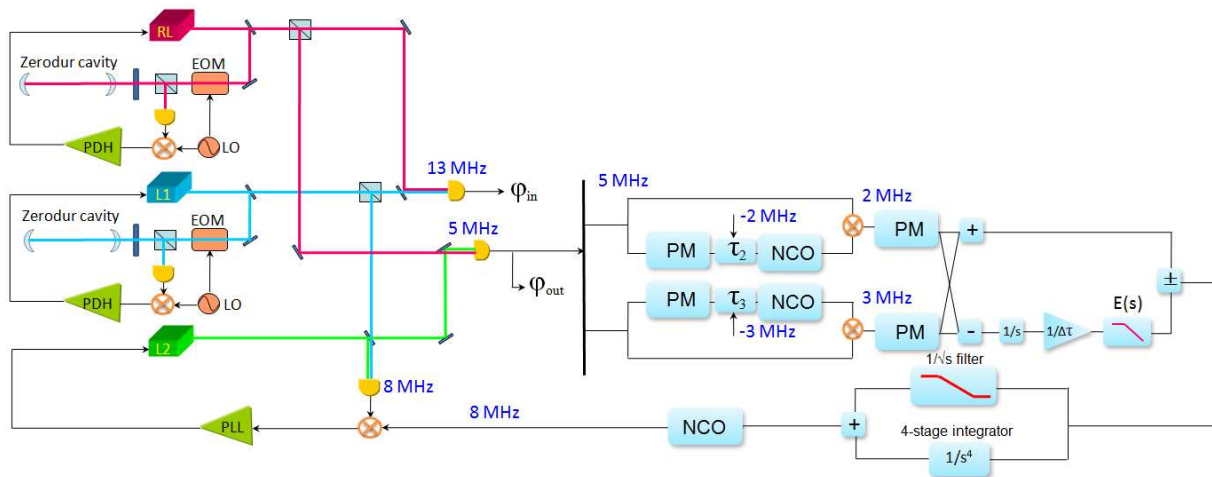


Figure 5-12. The experimental setup of frequency noise mitigation of the cavity stabilized laser using dual arm locking. The experimental principle is the same as described in Figure 4-12, where the single arm locking sensor is replaced with the dual arm locking sensor designed in the previous section. The averaged delay time between the two EPD units is realistic 33 s. We measured the stabilized frequency noise of the $RL - L_2$ beat signal with multiple differential delay times.

invisible in the time series of the stabilized frequency, which is much shorter than the required duration of more than ~ 2000 s in single or common arm locking.

5.2.3 Integration with Pre-stabilized Laser

The application of dual arm locking on the frequency noise mitigation of pre-stabilized lasers has been performed by means of an auxiliary phase-locked laser. This experiment for the first time demonstrates that arm locking is capable of sufficiently reducing the frequency noise of a cavity stabilized laser in the presence of realistic 33 s light travel times. The experimental setup resembles the setup illustrated by Figure 4-12, while the arm locking configuration has been expanded into two arms. As shown in Figure 5-12, the frequency noise of L_2 tracks the L_1 as a phase-locking reference. The phase-locking reference, which is driven by a NCO, is further phase-modulated via the dual arm locking setup.

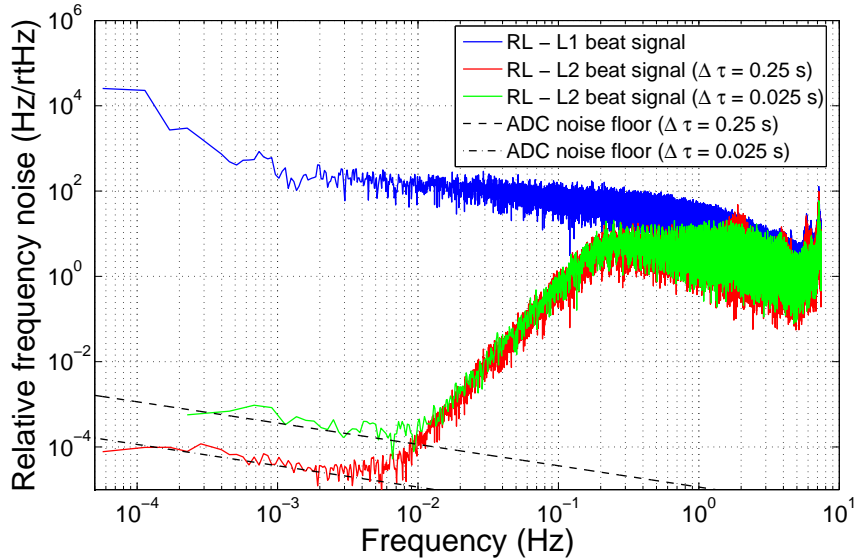


Figure 5-13. The noise spectra of the cavity stabilized beat signal $RL - L_1$ (blue) and the beat signal $RL - L_2$ further stabilized by dual arm locking. Compared to the $RL - L_1$ beat signal, the frequency noise of $RL - L_2$ is suppressed by 7 to 8 orders of magnitudes in the noise limited region, where the dominant noise floor comes from the phasemeter ADCs. Also we investigate the frequency noise spectra of $RL - L_2$ in the presence of various differential delay times. These measurements simulate the inversely proportional change of the limiting noise floor in accordance with the change of the arm length mismatch in dual arm locking.

The measurement results are shown in Figure 5-13, which includes the frequency noise spectra under the cases with two different differential delay times. Starting from the frequencies around about 10 mHz, the arm locking performance gradually changes from gain limited to noise limited. For the differential delay time that equals 0.25 s, the frequency noise of the $RL - L_2$ beat signal in the noise limited region is suppressed below $10^{-4} \text{ Hz Hz}^{-1/2}$. In comparison to the cavity stabilized $RL - L_1$ frequency noise, the closed-loop gain of dual arm locking provides a noise suppression with 7 to 8 orders of magnitudes in the noise limited region. Like the NCO tracking measurement, the limiting noise floor exhibits a slope of $1/f^{1/2}$, which matches up the expected ADC noise floor given by Eq. 5-7. When the differential delay time decreases by a factor of 10, the ADC noise floor also increases by a factor of 10 accordingly.

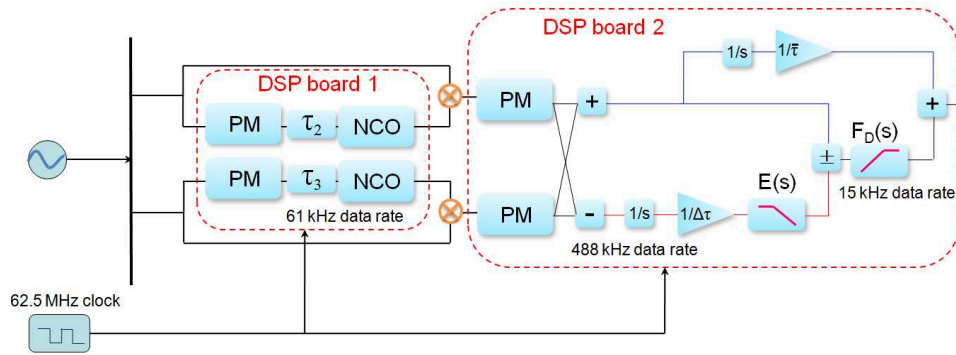


Figure 5-14. The implementation of the modified dual arm locking sensor on UFLIS expands the original dual arm locking design by linearly combining the common arm and dual arm sensor signals. The low-pass filter $F_C(s)$ to be multiplied with the common arm sensor is simplified into an integrator with a scaling factor of $1/\bar{\tau}$. The high-pass filter $F_D(s)$ has a zero at DC and a pole at around $1/\bar{\tau} \approx 30$ mHz to smooth the crossover between the two transfer function. Note that the sampling frequency of $F_D(s)$ is downsampled by a factor of 32 to maintain the open-loop stability.

5.3 Modified Dual Arm Locking

5.3.1 Modified Dual Arm Locking Sensor

As introduced in Section 2.3.3.3, the mapping vector of a modified dual arm locking sensor consists of a low-pass filter $F_C(s)$ to amplify the common arm and a high-pass filter $F_D(s)$ to suppress the differential arm at low frequencies. In spite of the two additional filters, Figure 5-14 shows that the modified dual arm locking sensor is designed in a similar way to the dual arm locking sensor. Our design follows the simplified design described in Section 2.3.5, where the low-pass filter $F_C(s)$ is reduced into an integrator with a scaling factor of $1/\bar{\tau}$ for the purpose of simplicity and efficiency.

The high-pass filter $F_D(s)$ has a zero at DC and a pole around $1/\bar{\tau} \approx 30$ mHz to decrease the low frequency gain as well as to smooth the crossover between the common arm and the dual arm.³ Compared with the data transfer rate of 488 kHz, the

³ In the specific design, the pole of $F_D(s)$ is actually at approximately 10 mHz to smooth the crossover. Compared with Eq. 2–60, this will increase the noise limitations in

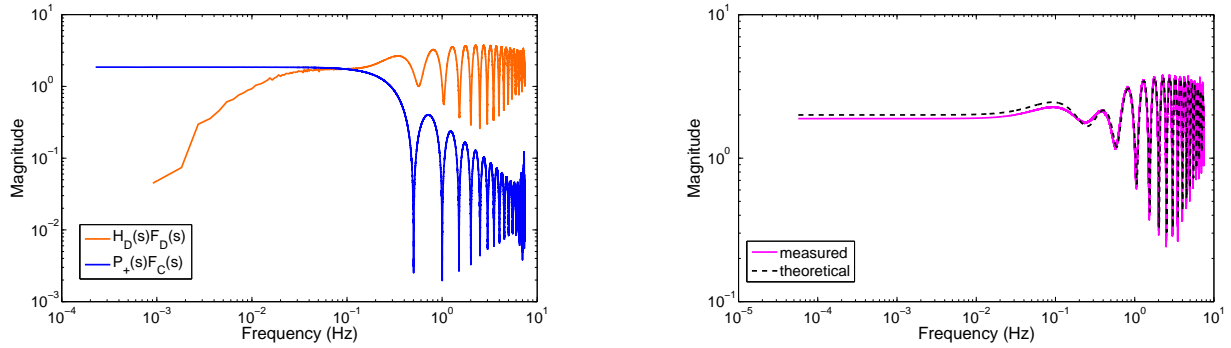


Figure 5-15. An example of a modified dual arm locking sensor with time delays of 2.025 s and 1.975 s. (Left) The transfer function measurements of the dual arm and common arm components in the modified dual arm locking sensor. The originally flat magnitude response in the dual arm component is filtered by the high-pass filter $F_D(s)$ such that it starts to roll down with a s slope to zero at DC. The common arm component is multiplied by $1/s$ and scaled by the factor of $1/\bar{\tau}$. (Right) The combination of those two components yields the overall transfer function of the modified dual arm locking sensor, where the overall magnitude response still retains flatness yet the common arm now dominates at low frequencies.

pole is at a significantly lower frequency such that the high-pass filter would be fairly unstable with such a high sampling rate.⁴ For this reason, the sampling frequency of the high-pass filter is downsampled by a factor of 32 to maintain the open-loop stability.

The overall transfer function of the modified dual arm locking sensor is given by

$$H_{MD}(s) = \frac{1}{\bar{\tau}s} P_+(s) + F_D(s) H_D(s). \quad (5-8)$$

We measured the transfer function of the modified dual arm locking sensor and an example with time delays of 2.025 s and 1.975 s is shown in Figure 5-15. The left figure shows that the common arm dominates the frequencies below $1/\bar{\tau}$ and the dual arm

modified dual arm locking by a factor of about 3 and in the following analysis we need to keep this factor in mind.

⁴ If we perform a z-transform to convert the filter with a 30 mHz corner frequency into the z-domain using a sampling frequency of 488 kHz, the pole would be very close to the edge of the unit circle on the z-plane.

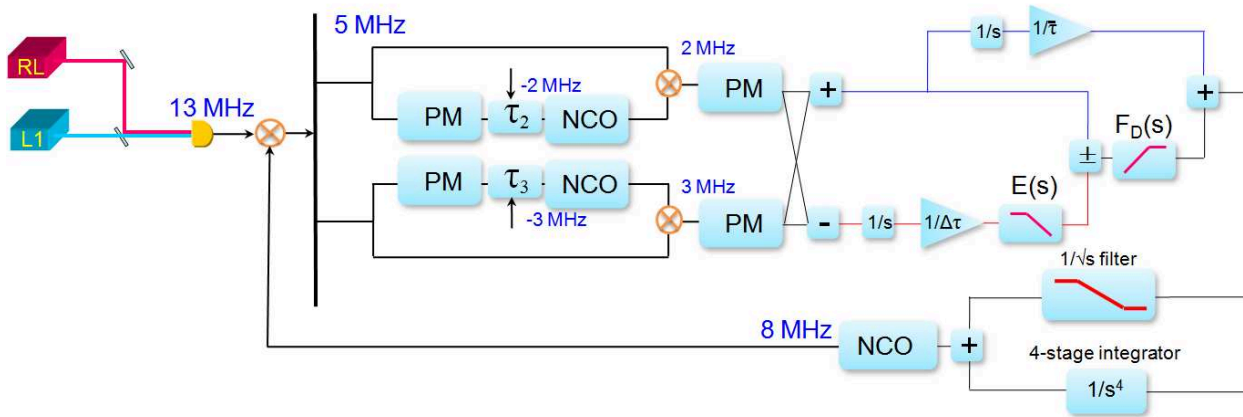


Figure 5-16. The preliminary experimental validation of the modified dual arm locking sensor on UFLIS resembles the previous dual arm locking experiment. The modified dual arm locking sensor extracts the instantaneous phase information of the input laser noise and send it to the arm locking controller, which drives an 8 MHz NCO signal to track the 13 MHz laser beat note. The delay time on each arm is 33.025 s and 32.975 s, respectively.

dominates the frequencies above it. Their smooth crossover allows the shape of the combined transfer function to be maintained flat in the LISA band.

5.3.2 Preliminary Test with NCO Tracking

The noise suppression performance of this modified dual arm locking sensor is validated in a similar experiment setup with delay time 33.025 s and 32.975 s, as shown in Figure 5-16. The input noise source is a 13 MHz beat signal between two Zerodur cavity stabilized lasers RL and L_1 . The measurement results are shown in Figure 5-17. Compared with the residual frequency noise spectrum obtained via dual arm locking under the same arm length mismatch condition, the noise suppression performance has been substantially improved to approximately $10^{-4} \text{ Hz Hz}^{-1/2}$ at 3 mHz.

The enhancement in the noise suppression performance is attributed to the mitigation of the noise limitations. Same as the experiment in the previous section, the primary noise sources in this control system include the 48-bit digitization noise inside the arm locking sensor/controller and the ADC noise at the phasemeters. The noise amplitude is specified by Eq. 5-5 and Eq. 5-6, respectively. The frequency

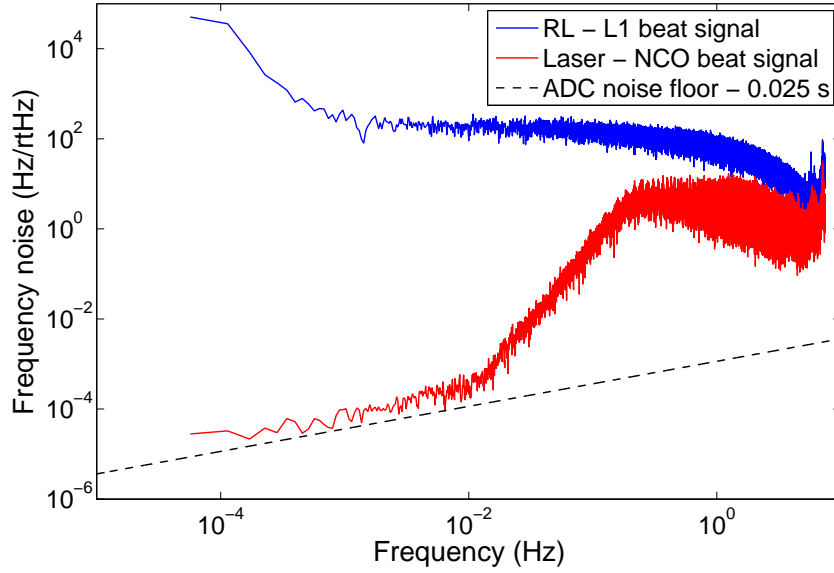


Figure 5-17. The measurement result shows the modified dual arm locking significantly improved the noise suppression performance compared with the original dual arm locking experiment. The $1/\sqrt{f}$ slope ADC noise floor observed in dual arm locking experiments has been surpassed. The final noise limitation in a modified dual arm locking configuration, as described in Eq. 5–9, is a combined effect of the digitization/ADC noise coupled in the common arm and in the differential arm.

response of the modified dual arm locking system to the input noise is described by Eq. 2–80, i.e.,

$$\delta\nu_{\text{Dig/ADC}}(f) = \frac{H_+}{H_{\text{MD}}} N_{\text{Dig/ADC}}(f) + \frac{H_-}{H_{\text{MD}}} N_{\text{Dig/ADC}}(f). \quad (5-9)$$

Whether the common arm component or the differential arm component dominates depends on the filter design and the arm length mismatch. In our setup the transfer function of $H_+(s)$ and $H_-(s)$ is specified by Eq. 2–60. Under the condition of a 0.025 s differential delay time, the magnitude responses are plotted in Figure 5-18. Due to the simplified design of the filter $F_D(s)$ and the relatively short $\Delta\tau$, the differential arm component dominates across the entire LISA band. Thus for frequencies below 10 mHz (also the noise limited region), the ADC noise and the 48-bit digitization noise will be amplified by the differential arm with a factor of $3 \cdot \bar{\tau}/(2\pi\Delta\tau H_{\text{MD}}(s)) \approx 318$, where the factor of 3 comes from the pole frequency of $F_D(s)$ at 10 mHz. For frequencies well

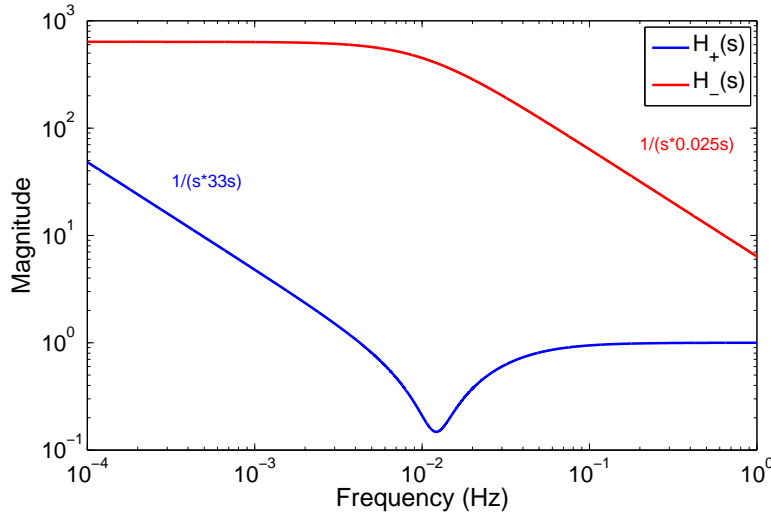


Figure 5-18. The magnitude responses of $H_+(s)$ and $H_-(s)$ for the modified dual arm locking experiment. The expressions of $H_+(s)$ and $H_-(s)$ are specified by Eq. 2–60, except that the pole of $F_D(s)$ is at 10 mHz rather than 30 mHz, causing the magnitude of $H_-(s)$ increases by a factor of 3 in the flat region. Due to the relatively short differential delay, the differential arm dominates across the entire LISA band.

below $1/\bar{\tau}$, the dominant noise source is the proportionally scaled ADC noise floor, which is given by

$$\delta\nu_{\text{ADC}}(f) = N_{\text{ADC}}(f) \cdot \frac{\bar{\tau}}{2\pi\Delta\tau H_{\text{MD}}} = 5.73 \times 10^{-4} \sqrt{f} \text{ Hz Hz}^{-1/2}. \quad (5-10)$$

In the noise limited region, the noise spectrum of the Laser-NCO beat signal is consistent with the ADC noise floor given by Eq. 5–10. In this measurement we have demonstrated that under the same condition of arm length mismatch, modified dual arm locking has a better noise suppression performance than dual arm locking. Now that the noise floor in the control system of our modified dual arm locking experiments has been identified and verified quantitatively, we would expect the same noise floor when this control system is applied onto the frequency noise mitigation of cavity stabilized lasers.

5.3.3 Integration with Pre-stabilized Laser

The incorporation of modified dual arm locking and a cavity stabilized laser was experimentally demonstrated using the setup illustrated by Figure 5-19. The

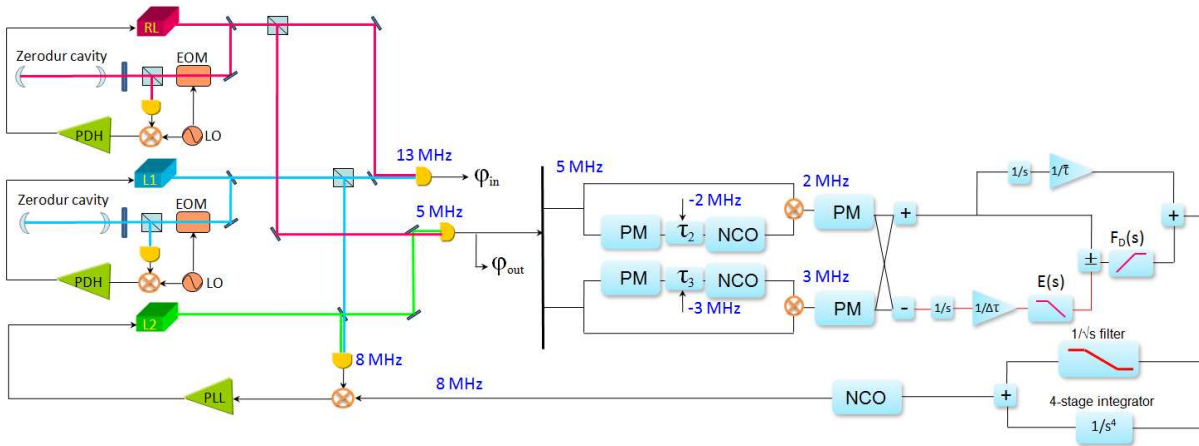


Figure 5-19. Experimental setup of modified dual arm locking using an auxiliary phase-locked laser. The experimental principle is the same as described in Figure 5-12, where the dual arm locking sensor is replaced with the modified dual arm locking sensor designed in the previous section. The averaged delay time between the two EPD units is 33 s and the differential delay time is 0.025 s (arm length mismatch $\sim 0.15\%$). We measured the stabilized frequency noise of the $RL - L_2$ beat signal.

experimental setup is essentially the same as in Figure 5-12, where the frequency noise of the $RL - L_1$ beat signal is faithfully reproduced by the heterodyne phase-locked $RL - L_2$ beat signal. The frequency noise of $RL - L_2$ can be therefore further suppressed via the phase modulation from the arm locking feedback signal. The delay time on each arm is 33.025 s and 32.975 s, respectively. The measurement results are shown in Figure 5-20. In this measurement the frequency noise of the $RL - L_1$ beat signal has been suppressed by about 7 orders of magnitude at 3 mHz. The noise limited region starts from ~ 20 mHz, where the same ADC noise floor with a $f^{1/2}$ slope dominates the frequency noise of the $RL - L_2$ beat signal. The measured closed-loop transfer function is consistent with the idealized model down to 20 mHz.

5.4 Arm locking Integrated With Far-end Phase-locking

Up to now we have characterized various arm locking configurations with LISA-like delay time and Doppler shifts. We have also demonstrated the incorporation of arm locking with cavity stabilization systems on our EPD-based electro-optical model and

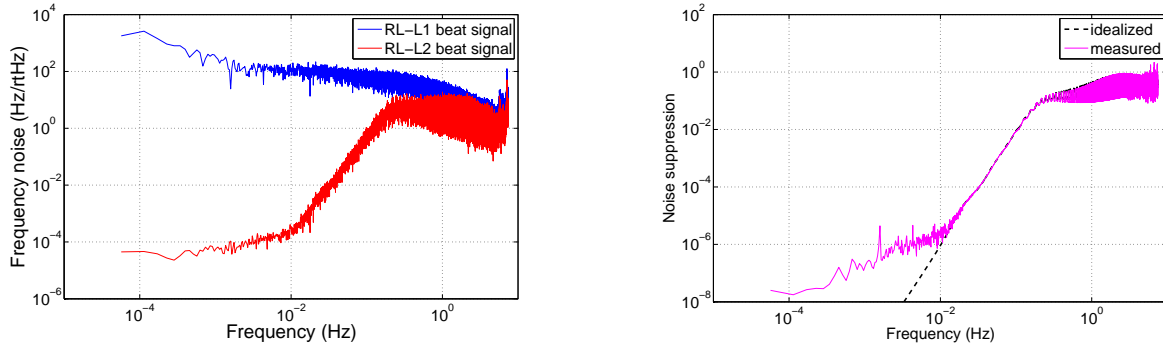


Figure 5-20. (Left) The noise spectra of the $RL - L_1$ beat signal (blue) and the $RL - L_2$ beat signal (red). In this measurement we have achieved about 7 orders of magnitude noise suppression at 3 mHz. The noise limitation starting from ~ 10 mHz is the same ADC noise floor with a $f^{1/2}$ slope as seen in Figure 5-17. The frequency noise from 0.1 Hz to 1 Hz is slightly above the $0.3 \text{ Hz Hz}^{-1/2}$ requirement, which can be alleviated by increasing the integrator gain in that region. (Right) The measured transfer function agrees with the idealized model very well down to about 10 mHz. Below 10 mHz the control system becomes noise limited, which causes the deviation from the idealized model.

achieved substantial noise suppression performance. In this section we take one step forward to the aim of realistic arm locking hardware simulation by introducing the transponder noise at far spacecraft. We will implement the phase-locked loop at the far-end realistically rather than assume that the optical transponder functions perfectly with an infinite feedback gain.

Moreover, in Section 2.3.5 we have derived that other realistic noise sources (clock noise, spacecraft jitter, etc.) would couple into the stabilized laser noise in accordance with the same transfer function as the transponder noise. Therefore, the transponder noise limitation observed in the stabilized laser noise can be equivalently considered as a manifestation of any additional noise source presented in arm locking. Our experiment has for the first time demonstrated the arm locking performance in the presence of the realistic transponder noise.

Table 5-1. Parameters in time-domain arm locking simulations with transponder noise

Parameter	Symbol	Value	Units
Sampling frequency	f_s	10	Hz
Pre-stabilized frequency noise	$\delta\nu_1^0$	$30 \times \sqrt{1 + (2.8 \text{ mHz}/f)^4}$	Hz Hz ^{-1/2}
Free-running frequency noise	$\delta\nu_2^0$	10 kHz/ f	Hz Hz ^{-1/2}
Averaged delay time	$\bar{\tau}$	33	s
Differential delay time	$\Delta\tau$	0.025	s
Doppler frequency error on arm 1-2	$\Delta\omega_{D2}$	0	Hz
Doppler frequency error on arm 1-3	$\Delta\omega_{D3}$	0	Hz
Transponder noise on arm 1-2	$\delta\nu_{PLL}^2$	$\sim 10^{-2} \cdot f$	Hz Hz ^{-1/2}

5.4.1 Transponder Noise Floor - Time Domain Simulation

The additional far-end PLL is nothing more than introducing an additional noise source between the two delay lines, which can be either the transponder noise or any other kind of realistic noise sources. The noise limitation derived from the transponder noise is given by

$$\delta\nu_{\text{trans}} = \frac{H_+}{H}(\delta\nu_{\text{trans2}} + \delta\nu_{\text{trans3}}) + \frac{H_-}{H}(\delta\nu_{\text{trans2}} - \delta\nu_{\text{trans3}}), \quad (5-11)$$

where the independent transponder noises on each arm, $\delta\nu_{\text{trans2}}$ and $\delta\nu_{\text{trans3}}$, are uncorrelated. The common and difference noise between them yield the quadrature sum, which is comparable to the transponder noise on a single arm. Therefore, we could apply the additional transponder noise on only one arm without loss of quantitative validity. For dual arm locking we have $H_+ = 1$ and $H_- = 1/\Delta\tau S$ and for modified dual arm locking we have $H_+ = F_C + F_D$ and $H_- = EF_D/\Delta\tau S$.

The verification of the transponder noise limitations was initially performed by time-domain simulations using MATLAB SIMULINK packages. The software simulations replicate LISA-like conditions as well as the sensor/controller design that have been built in our benchtop experiments. The filters used in the time-domain simulation are designed in the Laplace domain. Therefore, some deviation in the frequency response between the software filters and the hardware filters should be expected. Tabel 5-1 lists the parameters that are used in our simulations.

In the simulation the outgoing travel time and the return travel time are equal on both arms, i.e., for $\Delta\tau = 0.025$ s we have $\tau_{12} = \tau_{21} = 16.5125$ s and $\tau_{13} = \tau_{31} = 16.4875$ s. The Laplace domain filters, including $E(s)$, $F_C(s)$, $F_D(s)$ and the $f^{-1/2}$ controller filter, have the same zeros and poles as their quantized z-domain counterparts in the hardware implementation. Here we assume the transponder noise is a band-limited blue noise (an f slope) in terms of frequency fluctuations. Note that this is just an over-simplified model for the purpose of quick demonstration, while the realistic noise of an analog PLL exhibits a $f^{1/5}$ slope in our measurement (see next section).

The simulation results are shown in Figure 5-21 using modified dual arm locking. In this figure, the arm locking stabilized frequency noise is determined by three different limitations: For frequencies above 0.1 Hz, the control system is gain limited and the stabilized frequency noise agrees with the gain limited case without the transponder noise. For frequencies below 0.1 Hz the noise suppression performance is limited by the transponder noise floor, which is given by two segments: In the region from 30 mHz to 0.1 Hz, the transponder noise floor is dominated by the differential arm, which yields a noise floor

$$\delta\nu_{\text{Trans}}(f) = \frac{10^{-2} \cdot f}{2\Delta\tau S} = 3.2 \times 10^{-2} \text{ Hz Hz}^{-1/2}. \quad (5-12)$$

In a dual arm locking configuration this noise floor would dominate down through lower frequencies. However for modified dual arm locking, for frequencies below 30 mHz the high-pass filter F_D effectively suppresses the magnitude of the differential arm, which yields a noise floor with a lower magnitude:

$$\delta\nu_{\text{Trans}}(f) = 10^{-2} f \cdot \frac{\bar{\tau}}{2 \cdot 2\pi\Delta\tau} = 1.05 \cdot f \text{ Hz Hz}^{-1/2}. \quad (5-13)$$

The simulated frequency noise spectrum of the stabilized laser signal (the red curve) agrees with the analytical limitations in all frequency regions. This simulation numerically demonstrates that the transponder noise floor in a modified dual arm locking configuration is less sensitive to the arm length mismatch.

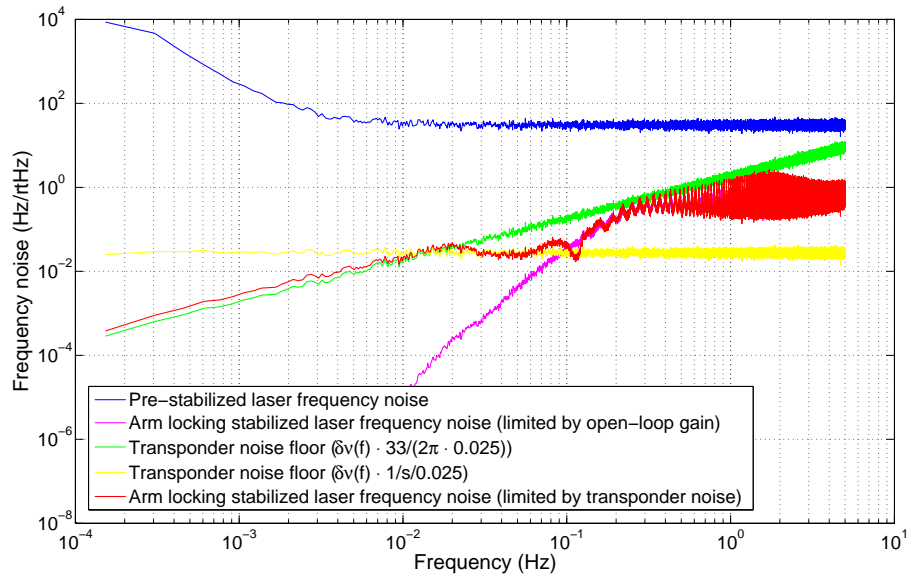


Figure 5-21. Time domain simulation of modified dual arm locking limited by the transponder noise floor. The frequency noise of the stabilized laser (red) is determined by different mechanism in different frequency regions. For frequencies above 0.1 Hz the control system is gain limited and the red curve follows the purple curve (the gain limited case). For frequencies between 0.1 Hz and 30 mHz, the frequency noise of stabilized laser is limited by the transponder noise floor determined in dual arm locking (the yellow curve) with a transfer function of $1/s\Delta\tau$. For frequencies below 0.1 Hz, the high-pass filter starts to suppress the magnitude of the differential arm sensor, which although still dominates through the rest of the measurement band. In this region the red curve follows the green curve, which is given by the introduced transponder noise multiplied with the differential arm gain of $\bar{\tau}/(2\pi\Delta\tau \cdot H_{MD})$.

5.4.2 Experimental Verification - Simple Model

To simulate an additional noise source from far spacecraft on our hardware system, we need to divide the delay time at the EPD units equally and delay the input electronic signal using two split delay lines in cascade. Analogously, the arm length change due to the LISA spacecraft motion is insignificant over a short time interval of 33 s, which makes the outgoing time and the return time are almost the same. At the output of the first delay line, the delayed signal can be used to phase-lock another laser that functions

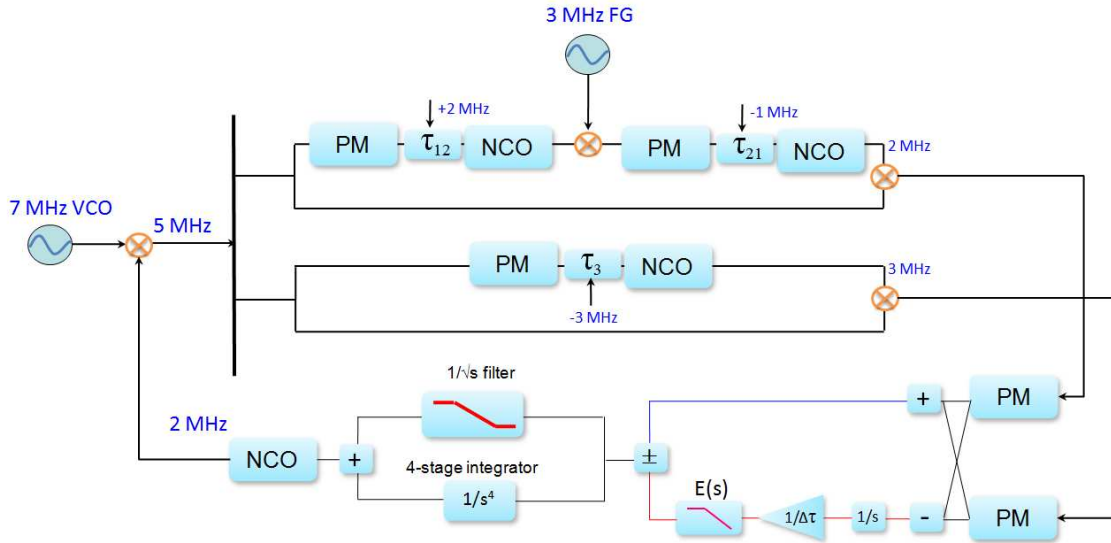


Figure 5-22. Experimental setup of dual arm locking with function generator signal as the transponder noise. In this setup the delay line on the arm 1-2 is equally divided into two, representing the outgoing travel time τ_{12} and the return travel time τ_{21} . A function generator signal is used to demodulate the signal delayed by τ_{12} such that the noise of the function generator signal enters the entire round-trip delay line. It should be noted that in the phase measurement the frequency of the function generator signal has to be exactly accounted for to avoid the frequency pulling.

as a far spacecraft laser. Then the output signal of the phase-locked laser is sent to the second delay line to generate the returning beam.

A simplified experimental verification of dual arm locking with the transponder noise was performed using the NCO tracking configuration. Since the transponder noise can be simplified into an arbitrary noise source entering between the outgoing delay and the return delay, we use a function generator signal to simulate this additional noise source. As shown in Figure 5-22, the delay line on the arm 1-2 is equally divided into two delay times, representing the outgoing travel time τ_{12} and the return travel time τ_{21} . The Doppler shift frequency added to the nominal frequency of the “outgoing beam” is +2 MHz, generating a 7 MHz Doppler-shifted signal. We place a function generator producing a 3 MHz signal to demodulate the 7 MHz signal such that the noise of the function generator signal enters the entire round-trip delay line via the analog mixer. It is

worth noting that like the local oscillator that drives the far-end phase-locking in realistic LISA, the offset frequency of the function generator signal has to be taken into account in the phase measurement of the long arm interferometry. That is, the function generator has to be synchronized to the master clock and its nominal frequency has to match up the corresponding 16-bit integer value (e.g., 3 MHz corresponds to 2.999305725 MHz) to avoid generating an unwarranted Doppler frequency error. The demodulated 4 MHz signal is then sent to the second delay line, which simulates the return beam being transferred back to the local spacecraft.

The function generator noise is measured to be approximately $10^{-4} \cdot f^{3/4}$ Hz Hz^{1/2} via fractional delay filtering. With a differential delay time of 0.25 s and 0.025 s, the expected transponder noise floor is given by $3.18 \times 10^{-5} f^{-1/4}$ Hz Hz^{-1/2} and $3.18 \times 10^{-4} f^{-1/4}$ Hz Hz^{-1/2}, respectively. We plot the measured residual frequency noise spectrum in Figure 5-23. The measurements sufficiently demonstrate that in dual arm locking the performance limitation due to the transponder noise inversely scales with the arm length mismatch and the noise amplitude is consistent with our analytical expectations.

5.4.3 Experimental Verification - Full Model

The complete experimental setup to verify the transponder noise floor in a modified dual arm locking configuration is illustrated by Figure 5-24. In this setup we still use an auxiliary phase-locked laser L_2 to obtain the tunability of the pre-stabilization reference. As the outgoing beam from the “local spacecraft”, the beat signal $RL - L_2$ is electronically split. Then the split signals travel to corresponding “far spacecraft” individually, which is simulated by the EPD units. Similar to the simple model in the previous section, we allocate the 33.025 s round-trip time equally into two delay lines, representing the outgoing travel time τ_{12} and the return travel time τ_{21} . Once the $RL - L_2$ beat signal is delayed by τ_{12} and arrives at the “far spacecraft”, its delayed and Doppler-shifted version (a 3 MHz NCO signal) is used to heterodyne phase-lock a “far laser” represented by

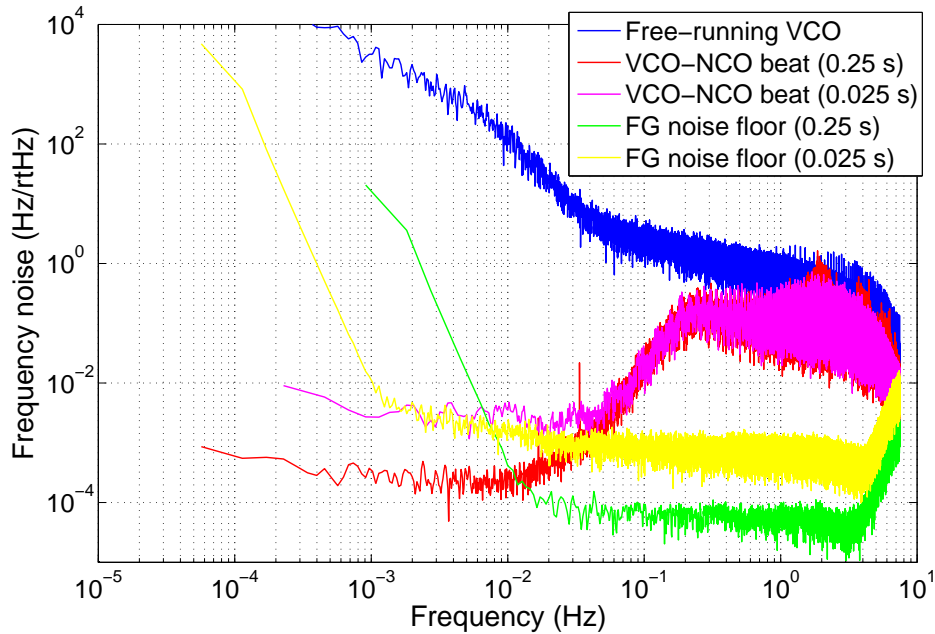


Figure 5-23. Noise spectra of dual arm locking with FG signal as the transponder noise. In this figure the red and purple curves are the residual frequency noise in the presence of the differential delay time 0.25 s and 0.025 s, respectively. The green and yellow curves are obtained from the measured function generator noise multiplied with the transfer function $1/s\Delta\tau$. Our measurements have verified that the limitation of the residual frequency noise is consistent with the transponder noise floor.

the $RL - L_3$ beat signal. The 5 MHz $RL - L_3$ beat signal tracks the frequency noise of $RL - L_2$ and also carries an uncorrelated residual noise due to the finite gain of the PLL controller. The 2 MHz offset frequency of the PLL, which is driven by a function generator, is synchronized to the master clock and rounded to its corresponding 16-bit value. Also, the frequency noise of the function generator signal enters the PLL and becomes a part of the transponder noise. This process resembles the clock noise that enters the far-end PLL during the phase measurement at far spacecraft. Then we delay the phase-locked $RL - L_3$ beat signal by the return travel time τ_{21} and form the long arm interferometry with the “local beam” $RL - L_2$ beat signal.

Figure 5-25 illustrates the experimental setup represented in the Laplace domain. Following the notation used in Figure 4-13, we use Φ_i to represent the phase of the laser

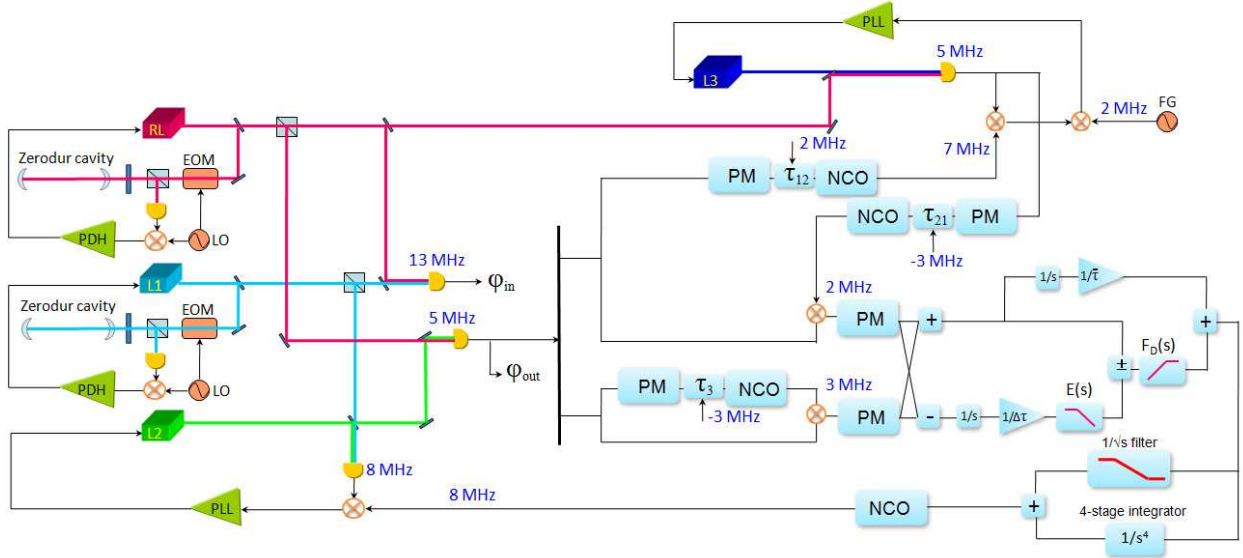


Figure 5-24. Experimental setup of modified dual arm locking with far-end PLL. This setup exploits an auxiliary phase-locked laser L_2 to obtain the tunability of the pre-stabilization reference. The delay line to simulate the LISA arm 1-2 is divided equally into two, representing the outgoing and return travel time individually. Another beat signal $RL - L_3$ is phase-locked to the $RL - L_2$ delayed by the outgoing travel time with an offset frequency of 2 MHz and then delayed by the return travel time to have the heterodyne interference with the prompt beam. In this setup the function generator demodulating the heterodyne frequency of the PLL has an equivalent function as the clock on far spacecraft, where the clock noise enters the phase measurement of the far-end PLL in a similar way.

L_i and an upper index of 0 to indicate the out-of-loop phase. In this diagram G_0 is the PLL gain for the phase-locking L_2 to L_1 , while G_1 and G_2 follow the notation convention to represent the arm locking gain and the PLL gain on the local spacecraft and the far spacecraft, respectively. In the analysis we only consider the transponder noise as it is the only dominant primary noise source in this setup and neglect any other secondary noise including the digitization noise, the ADC noise, the lightpath noise, etc.

Identical to Eq. 4-6, the phase of the slave laser L_2 is given by

$$\Phi_2 = \frac{1}{1 + G_0} \Phi_2^0 + \frac{G_0}{1 + G_0} (\Phi_1 + \varphi_{NCO}). \quad (5-14)$$

Since the $RL - L_3$ beat signal is phase-locked to the delayed $RL - L_2$ beat signal, we have

$$\Phi_0 - \Phi_3 = \frac{1}{1 + G_2}(\Phi_0 - \Phi_3^0) + \frac{G_2}{1 + G_2} [(\Phi_0 - \Phi_2)e^{-s\tau_{12}} + \varphi_{CL}], \quad (5-17)$$

where φ_{CL} is the phase noise of the function generator that drives the PLL. Once the function generator is synchronized to the master clock, it has an equivalent effect as the clock noise from the far spacecraft SC_2 .

Substitute Eq. 5-17 into Eq. 5-16, we obtain the phase measurement on arm 1-2:

$$\begin{aligned} \phi_{12} &= (\Phi_0 - \Phi_2) - \frac{1}{1 + G_2}(\Phi_0 - \Phi_3^0) - \frac{G_2}{1 + G_2} [(\Phi_0 - \Phi_2)e^{-s\tau_{12}} + \varphi_{CL}] e^{-s\tau_{21}} \\ &= \left(1 - \frac{G_2}{1 + G_2} e^{-s\tau_2}\right) (\Phi_0 - \Phi_2) - \frac{1}{1 + G_2}(\Phi_0 - \Phi_3^0)e^{-s\tau_{21}} - \frac{G_2}{1 + G_2}\varphi_{CL}e^{-s\tau_{21}}. \end{aligned} \quad (5-18)$$

The first term of Eq. 5-18 is the phase of the local beam multiplied by the transfer function of the round-trip on arm 1-2. We define the transponder noise on arm 1-2:

$$\delta\varphi_{Trans} = \frac{1}{1 + G_2}(\Phi_0 - \Phi_3^0)e^{-s\tau_{21}} + \frac{G_2}{1 + G_2}\varphi_{CL}e^{-s\tau_{21}}. \quad (5-19)$$

Eq. 5-19 indicates that the transponder noise involves the intrinsic noise of the far-end PLL due to the limited gain as well as the clock noise from far spacecraft.

For the purpose of symmetrical formalism, we also write the phase measurement on arm 1-3 in the following form:

$$\phi_{13} = \left(1 - \frac{G_3}{1 + G_3} e^{-s\tau_3}\right) (\Phi_0 - \Phi_2), \quad (5-20)$$

where the PLL gain G_3 is assumed to be infinite.

If we consider a generic arm locking configuration with a mapping vector $\mathbf{S}_k = [H_+ + H_-, H_+ - H_-]$, the phase of the NCO signal is then given by

$$\begin{aligned}
\varphi_{\text{NCO}} &= [(H_+ + H_-)\phi_{12} + (H_+ - H_-)\phi_{13}] G_1 \\
&= [H_+(\phi_{12} + \phi_{13}) + H_-(\phi_{12} - \phi_{13})] G_1 \\
&= [(H_+P_+ + H_-P_-)(\Phi_0 - \Phi_2) + (H_+ + H_-)\delta\varphi_{\text{Trans}}] G_1 \\
&= [H(\Phi_0 - \Phi_2) + (H_+ + H_-)\delta\varphi_{\text{Trans}}] G_1,
\end{aligned} \tag{5-21}$$

where $H = H_+P_+ + H_-P_-$ is the sensor of an arbitrary arm locking configuration.

Substitute Eq. 5-21 into Eq. 5-14 and Φ_2 becomes

$$\Phi_2 = \frac{1}{1 + G_0}\Phi_2^0 + \frac{G_0}{1 + G_0}\Phi_1 + [H(\Phi_0 - \Phi_2) + (H_+ + H_-)\delta\varphi_{\text{Trans}}] G_1. \tag{5-22}$$

Following the same procedure in Eq. 4-9, we combine the terms involving Φ_2 to the left and add terms $\Phi_0 - \frac{1}{1+G_0}\Phi_0 - \frac{G_0}{1+G_0}\Phi_0 (= 0)$ to the right:

$$\begin{aligned}
\left(1 + \frac{G_0}{1 + G_0}HG_1\right) \Phi_2 &= \frac{1}{1 + G_0}\Phi_2^0 + \frac{G_0}{1 + G_0}\Phi_1 + \frac{G_0}{1 + G_0}HG_1\Phi_0 + \frac{G_0}{1 + G_0}(H_+ + H_-)G_1\delta\varphi_{\text{Trans}} \\
&\quad + \Phi_0 - \frac{1}{1 + G_0}\Phi_0 - \frac{G_0}{1 + G_0}\Phi_0,
\end{aligned} \tag{5-23}$$

which can be simplified into

$$\left(1 + \frac{G_0}{1 + G_0}HG_1\right) (\Phi_2 - \Phi_0) = \frac{1}{1 + G_0}(\Phi_2^0 - \Phi_0) + \frac{G_0}{1 + G_0}(\Phi_1 - \Phi_0) + \frac{G_0}{1 + G_0}(H_+ + H_-)G_1\delta\varphi_{\text{Trans}}. \tag{5-24}$$

The first two terms on the right side of Eq. 5-24 represent the noise suppression, while the third term determines the noise limitation. The transponder noise floor is given by

$$\begin{aligned}
\Delta_{\text{Trans}} &= \frac{1}{1 + G_0} \frac{(H_+ + H_-)G_1}{1 + \frac{G_0}{1 + G_0}HG_1} \delta\varphi_{\text{Trans}} \\
&\approx \frac{H_+ + H_-}{H} \delta\varphi_{\text{Trans}} \quad (G_0, G_1 \gg 1).
\end{aligned} \tag{5-25}$$

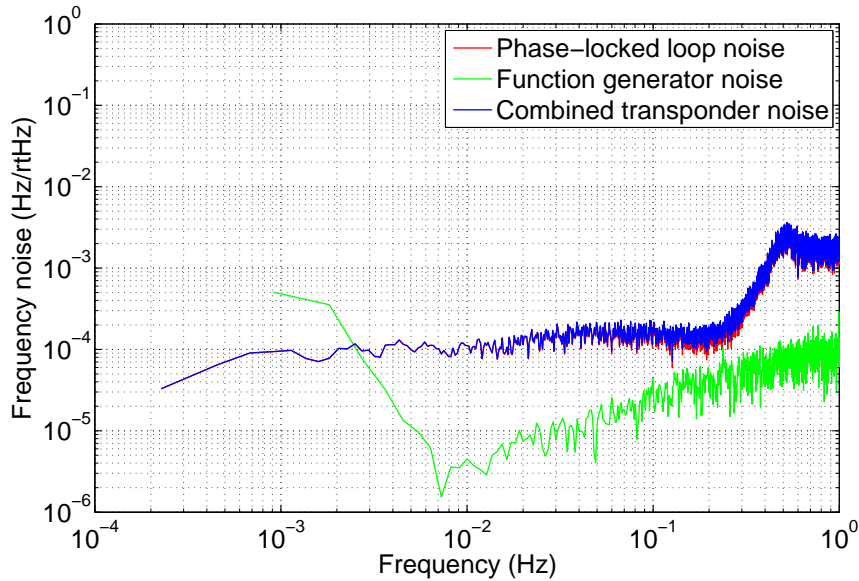


Figure 5-26. Noise spectra of the transponder noise observed in modified dual arm locking. The measurement has identified that the primary contribution to the transponder noise comes from the gain limited PLL and the function generator noise is well below it.

The result of Eq. 5-25 is consistent with Eq. 5-11, proving the validity of this experimental setup to demonstrate the transponder noise floor.

With a certain controller gain, the transponder noise is measured to be approximately a $3 \times 10^{-4} f^{1/5} \text{ Hz Hz}^{-1/2}$ slope, as shown in Figure 5-26. The primary contribution in the transponder noise comes from the phase-locked loop, while the function generator noise is much lower. As the PLL gain decreases, the transponder noise amplitude will proportionally increase.

The measurement results are illustrated in Figure 5-27. As the differential delay time equals 0.025 s, the expected transponder noise floor below 30 mHz is approximately given by $0.20 f^{1/5} \text{ Hz Hz}^{-1/2}$, which limits the noise suppression performance in that region. Our measurement has originally demonstrated that the arm locking stabilized frequency noise agrees with this expected noise floor and still sufficiently meet the LISA requirement in the presence of transponder noise. For frequencies around 30 mHz the arm locking performance is still gain limited and the transponder noise floor given

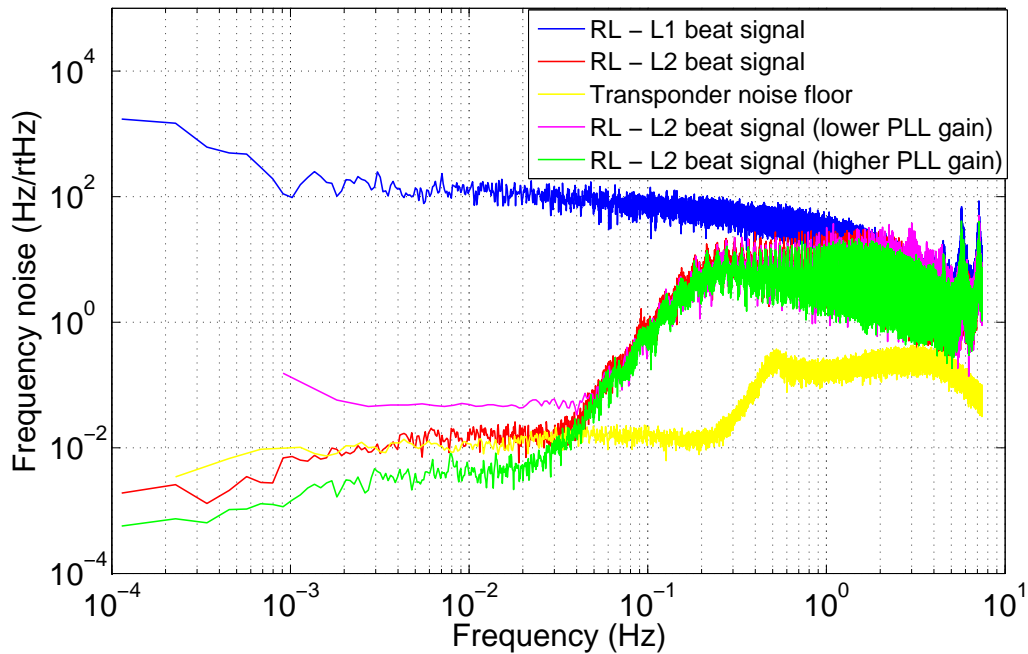


Figure 5-27. Noise spectra of the stabilized laser frequency and the transponder noise floor. In this figure the stabilized frequency noise is represented by the red curve, which is limited by the transponder noise floor. The yellow curve represent the transponder noise floor given by the combined noise in Figure 5-26 multiplied with the differential arm gain of $\bar{\tau}/(2\pi\Delta\tau \cdot H_{MD})$. The red and yellow curves agree with each other in the noise limited region. Note that the far-end PLL was set to gain limited such that the amplitude of the PLL noise can be continuously manipulated by adjusting the loop gain. As the PLL noise increases or decreases, the transponder noise floor in the stabilized laser frequency also tracks this change, which is shown by the green (a higher PLL gain) and purple (a lower PLL gain) curves.

by $1/\Delta\tau S$ is still below the $RL - L_2$ frequency noise. We also have demonstrated that as the PLL gain changes, the corresponding transponder noise will track the change accordingly within a certain range. The measurements indicate that the transponder noise floor inversely scales with the PLL gain as expected.

CHAPTER 6 DOPPLER FREQUENCY ERROR IN ARM LOCKING

In this chapter we will investigate the impact of Doppler frequency errors on arm locking. The research of Doppler frequency errors can be divided into two categories: The on-board estimation of Doppler frequency errors and the techniques to restrict the induced frequency pulling. In realistic LISA, the Doppler shift frequency is a time-variable quantity due to the changing relative velocity between spacecraft. Therefore, the initial Doppler frequency, as well as its first time derivative will be estimated. The error in this estimation will cause a Doppler frequency error in the phase measurements on the local spacecraft. Since the estimated Doppler frequency will not be updated while arm locking is in operation, the consequent Doppler frequency error is also a function of time. In this chapter we will focus more on the frequency pulling and associated remedy schemes, rather than the simulation of Doppler frequency errors. Note that the Doppler-induced frequency pulling also includes the situations in lock acquisition and in the steady state, and here we primarily investigate the latter situation as it has a long-term effect on the laser frequency.

6.1 Doppler Frequency Error in LISA

The LISA orbits are designed to have a 1-year period oscillations of the arm lengths, interior angles and relative velocities, which means the Doppler frequency variation also oscillates with a 1-year period. Therefore, the Doppler frequency corresponds to an oscillation at 3.17×10^{-8} Hz. Since the relative velocity between spacecraft can reach up to $v_{SC} = 18$ m/s, the corresponding round-trip Doppler shift frequency ν_D to the laser frequency ν_0 yields the relation

$$\frac{\nu_D}{\nu_0} = \frac{v_{SC}}{c}. \quad (6-1)$$

Thus the Doppler frequency can be up to approximately 17 MHz. As this frequency is estimated and then subtracted in the phase measurements, a Doppler frequency error

will show up in the phase data and eventually drive the frequency of the master laser. In realistic LISA, the Doppler frequency as well as its time derivatives (the Doppler change rate) will be initially measured and then subtracted before arm locking is engaged. The estimation of the Doppler frequency ν_D can be realized by various techniques: For example, the on-board ranging can measure the relative velocity between the spacecraft or the averaged laser beat frequency allows to estimate the Doppler frequency directly by comparing the incoming beat frequency and the outgoing beat frequency.

However, how large the Doppler frequency error $\Delta\nu_D$ will be is still uncertain. If we expand the time-varying Doppler frequency error to the second order of time derivative in the time domain and assume that the Doppler change rate (the first and second derivatives) are constant as the variation is very small, the Doppler frequency error $\Delta\nu_D$ as a function of time is given by

$$\Delta\nu_D(t) \approx \Delta\nu_{D0} + \Delta\nu_D t + \frac{1}{2}\Delta\ddot{\nu}_D t^2. \quad (6-2)$$

The performance of Doppler estimations depends on the initial laser frequency noise $\tilde{\nu}_0(f)$ before arm locking and the estimation duration time T , yet is independent of arm locking configurations, provided that the round-trip travel time τ is constantly 33 s. In the initial phase measurement, the contribution to the variance of the measured frequency, σ^2 , primarily comes from the Doppler frequency error. Thus they can be considered as equivalent to each other. According to Ref [13], the variance is given by

$$\sigma^2 = 4 \int_0^\infty df \tilde{\nu}_0(f)^2 \text{sinc}^2(fT) \sin^2(\pi f\tau), \quad (6-3)$$

where the sinc function comes from the Laplace transform of the averaging time T and the sin function comes from the interferometer response on one arm.

For an averaging estimation time of 100 s, the initial Doppler frequency error would be approximately 400 Hz with a Mach-Zehnder pre-stabilized laser; while for a free-running laser the error could be as high as $\sim 10^5$ Hz.

Once the arm locking is engaged, the Doppler frequency error will enter the controller which causes the laser frequency to ramp. During this lock acquisition process, the Doppler frequency error could generate a relatively large initial transient (several hundred MHz) imposed onto the laser frequency, which is given by the product of the error and the step response of the control system. When arm locking enters its steady state, the Doppler frequency estimations will not be updated until the next time the arm locking loop is needed to be unlocked (e.g., when changing the heterodyne frequency or switching the arm locking configuration). After days or months, the Doppler frequency estimations will be made very accurate due to the long averaging time and thereby the initial transients occurring in lock acquisition will be significantly smaller than the first time.

Thus in the steady state, the residual Doppler frequency error primarily comes from the time-varying Doppler frequency that tracks the orbital motion of LISA spacecraft. Depending on different arm locking configurations, the frequency pulling rate is derived in Section 2.3.3. The expected frequency pulling in the steady state is limited within 10 MHz peak to peak, which is even less significant than the intrinsic drift of the laser frequency, provided that the arm locking configuration can be exploited appropriately based on the arm length mismatch.

6.2 Investigation of Frequency Pulling on UFLIS

In this section we will study the Doppler-induced frequency pulling rate in the steady state, in the presence of various arm locking configurations. So far, all of the arm locking benchtop experiments simulated an ideal situation without any Doppler shift or when the Doppler frequency was perfectly accounted for in the phase measurements. In the following time-domain simulations and benchtop experiments [95], we will generate constant and step Doppler frequency errors in phase measurements, which is adequate to observe the frequency pulling in the steady state. We will also use the modified dual

arm locking sensor to experimentally demonstrate its capability to concisely reduce the frequency pulling rate.

In addition to the modified dual arm locking sensor, an AC-coupled controller with its magnitude suppressed below the LISA band is also capable of reducing the frequency pulling rate. Such a low frequency filtering mechanism can still be included in the arm locking controller design as an additional constraint, even if a modified dual arm locking sensor is used. The advantage is that it can further reduce the residual frequency pulling rate and ensure the frequency pulling rate will never reach too high in case the system is switched to other arm locking configurations. However, an AC-coupled controller may bring a limitation to the achievable gain, which makes the control system of arm locking gain limited when the arm length mismatch is large. Also, the phase margin at the zero-crossing below the LISA band needs to be carefully retained for the purpose of the closed-loop stability. Both of the two issues require a deliberate controller design.

6.2.1 Generation of Doppler Frequency Errors

Since the Doppler shift frequency generated by current EPD units is a constant value and cannot be continuously tuned, the Doppler frequency error can only be generated as a constant. In Chapter 3 we already mentioned that the phasemeter offset frequency is a 16-bit fixed-point integer number while the Doppler frequency specified on the motherboard is a floating-point number. And to perfectly account for the Doppler frequency, we rounded the floating-point Doppler frequency to the corresponding 16-bit integer value. Therefore, if we generate the Doppler frequency error by changing the phasemeter offset frequency, it can only be discretely introduced with a frequency resolution $62.5 \text{ MHz}/2^{16} \approx 954 \text{ Hz}$. With such a large Doppler error, the arm locking filters would be required to have a much larger dynamic range to track the fast frequency pulling. To generate a smaller Doppler frequency error, we have to decrease the frequency resolution by increasing the precision of the phasemeter offset frequency.

In comparison, the EPD delay line is more flexible to change for the generation of a Doppler frequency error with essentially an arbitrary value. Currently, a constant Doppler frequency error can be simulated in three simple ways on UFLIS:

1. Directly modify the Doppler frequency value in the C program by adding an additional constant to the original 16-bit number such that the Doppler frequency error is given by the constant. The advantage of this method is that a LISA-like time-varying Doppler frequency can also be simulated based on this method, where the additional value becomes a frequency modulation with a 1-year period.
2. Change the clock frequency for the EPD unit. Since in the EPD unit the Doppler frequency scales with the clock frequency of 62.5 MHz, the Doppler frequency error $\delta\nu_D$ is given by $(\Delta f_{\text{clock}}/f_{\text{clock}}) \cdot \nu_D$. This method is straightforward as neither software or hardware is needed to be modified. Also if we apply a frequency modulation on the clock frequency, a time-varying Doppler frequency is essentially achievable. However, the frequency of the frequency modulation cannot be made as low as 10^{-8} Hz due to the hardware limit. Another issue of this method is that the Doppler frequency error generated on two arms become correlated.
3. Use the setup illustrated by Figure 5-22, where the Doppler shift frequency is applied in the middle of two delay lines. The signal source to provide the Doppler frequency, such as a function generator, is suggested to be synchronized to the master clock (though not required in this situation). Similar to the second method, a time-varying Doppler frequency can also be realized by frequency-modulating the signal frequency, although the period of the frequency modulation is limited by the parameter of the function generator.

In the following experiments we mainly employ Method 2 and 3.

6.2.2 Frequency Pulling in Single Arm Locking

In this section we will first discuss a pioneering experiment in which a constant Doppler error is introduced into our single arm locking loop and a designed AC-coupled controller is dedicated to eliminate the frequency pulling. Figure 6-1 illustrates the experimental configuration, in which a 6 MHz free running VCO signal is demodulated with a 9 MHz NCO signal. The beat signal of 3 MHz is then split into a prompt signal and a signal which is delayed by 1 s as well as shifted by 4 MHz. The phasemeter will demodulate the error signal with an 16-bit offset frequency.

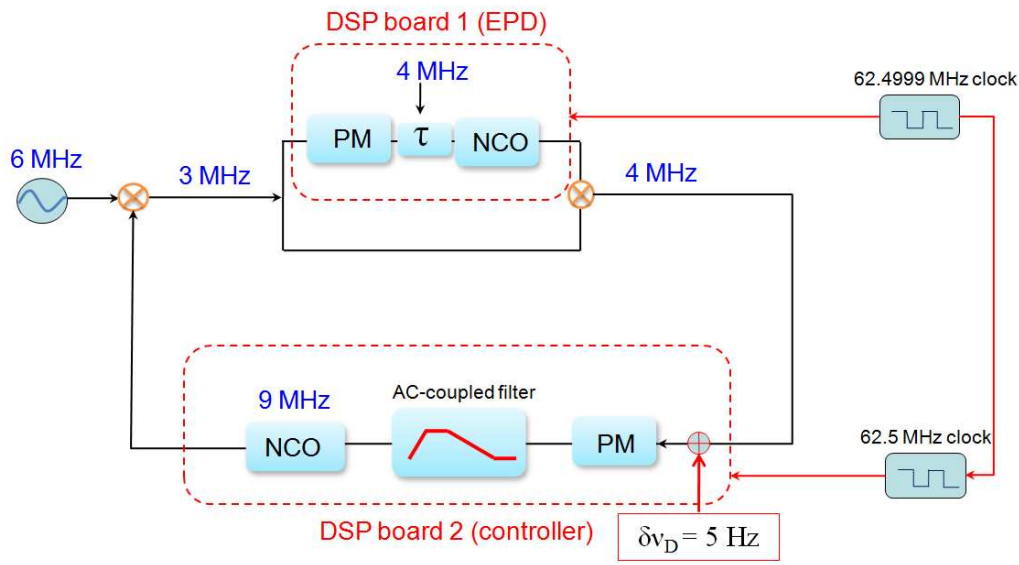


Figure 6-1. The preliminary experimental setup of AC-coupled single arm locking with Doppler error. A 5 Hz constant Doppler frequency error is generated by shifting the clock frequency of the EPD unit by 80 Hz. The clocks that drive the EPD unit and the arm locking controller are synchronized to accurately control the Doppler frequency. An AC-coupled controller with a flat magnitude response at DC is used to eliminate the frequency pulling.

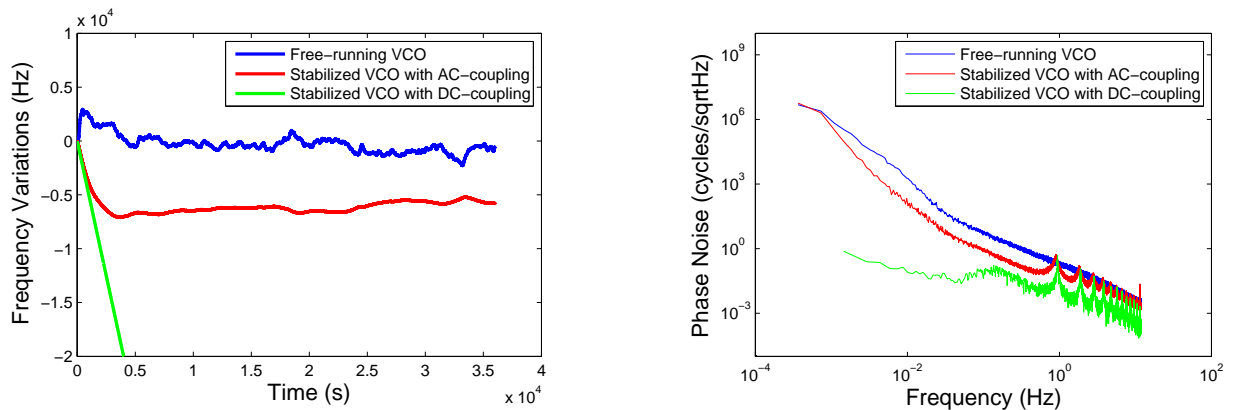


Figure 6-2. (Left) Time series of a free-running VCO signal, a stabilized VCO signal with the AC-coupled controller and a stabilized VCO signal with a standard DC-coupled controller. The AC-coupled controller is capable of removing the frequency pulling that shows up in the situation with the DC-coupled controller. (Right) Linear spectral densities of the phase noise of the three time series. Although the Doppler error does not cause frequency pulling with the AC-coupled controller, the controller gain is significantly limited and the noise suppression performance is compromised.

In the basic experiment described in Section 4.2, this offset frequency matches the Doppler frequency perfectly, while here we introduce a constant Doppler frequency error of 5 Hz by changing the clock frequency of the EPD unit. In the presence of a standard DC-coupled controller, the frequency pulling rate is then given by $\nu_D/\tau = 5 \text{ Hz/s}$, which is demonstrated by the stabilized time series (the green curve in Figure 6-2 (left)). In contrast, the red curve represents the time series stabilized by an AC-coupled controller. The time series of frequency fluctuations exhibit the frequency pulling in lock acquisition, which is given by the convolution between the Doppler error and the AC-coupled controller transfer function at low frequencies. Since the AC-coupled controller is designed to have a constant low gain at DC, a constant frequency offset ($\sim 9 \text{ kHz}$) is added to the output frequency through the lock acquisition process. After the initial frequency pulling is relaxed and the system enters the steady state, the stabilized frequency stays flat and the residual frequency pulling rate is strictly zero. Figure 6-2 (right) shows the linear spectral densities of the phase fluctuations of the three beat signals. The DC-coupled controller has the best in-band performance but the frequency is ramping down with the expected rate. Note that this AC-coupled controller is just for the purpose of demonstration: We use a fairly high low unity gain frequency compared to LISA to perform the measurement in a reasonable time. This limits the noise suppression in our experiments compared to the noise suppression expected in LISA.

6.2.3 Frequency Pulling in Dual and Modified Dual Arm Locking

6.2.3.1 Time-domain simulations with AC-coupled controller

The Doppler impact becomes critical in a dual arm locking configuration when the arm length mismatch is small. Here we represent a time-domain simulation of an AC-coupled dual arm locking configuration with Doppler errors. This time-domain simulation is running on a Matlab Simulink model with floating point arithmetic. In dual arm locking the critical parameter is the differential Doppler frequency error between

Table 6-1. Parameters in AC-coupled dual arm locking simulations with Doppler errors

Parameter	Symbol	Value	Units
Sampling frequency	f_s	10	Hz
Free-running frequency noise	$\delta\nu_1^0$	10 kHz/f	Hz Hz ^{-1/2}
Average delay time	$\bar{\tau}$	33	s
Differential delay time	$\Delta\tau$	0.255	s
Doppler frequency error on arm 1-2	$\Delta\nu_{D2}$	150	kHz
Doppler frequency error on arm 1-3	$\Delta\nu_{D3}$	149	kHz
Loop gain	G_0	100	

Table 6-2. Parameters of the AC-coupled filter used in simulations

zeros (Hz)	poles (Hz)
10^{-7}	5×10^{-6}
10^{-7}	5×10^{-6}
10^{-6}	3×10^{-3}
5×10^{-5}	3×10^{-3}
5×10^{-5}	3×10^{-3}
0.1	3×10^{-3}
0.3	3×10^{-3}

two arms, where a smaller arm length mismatch results in a smaller differential Doppler error. In our simulation we assume a free-running laser with a large Doppler frequency error on each arm, while the difference between them is 1 kHz. The parameters used are list in Table 6-1 and the AC-coupled controller is designed with the zeros and poles listed in Table 6-2.

The black curve in Figure 6-3 (right) is the open-loop transfer function which is given by the dual arm locking sensor (the blue curve) multiplied by the AC-coupled controller (the red curve) with a loop gain factor G_0 . The AC-coupled controller consists of a $f^{-1/2}$ slope low-pass filter for the high frequency suppression and a high pass filter to reduce the frequency pulling. The open-loop transfer function provides a bandwidth of around 42 kHz and a unity gain frequency of 15 μ Hz at low frequencies. The maximum of the open-loop gain is approximately 100 dB at 3 mHz; then the gain starts to decrease with a slope of f^2 due to the AC-coupling. Note that the slope of the AC-coupled filter at the zero-crossing yields an s slope to avoid excessive phase shift.

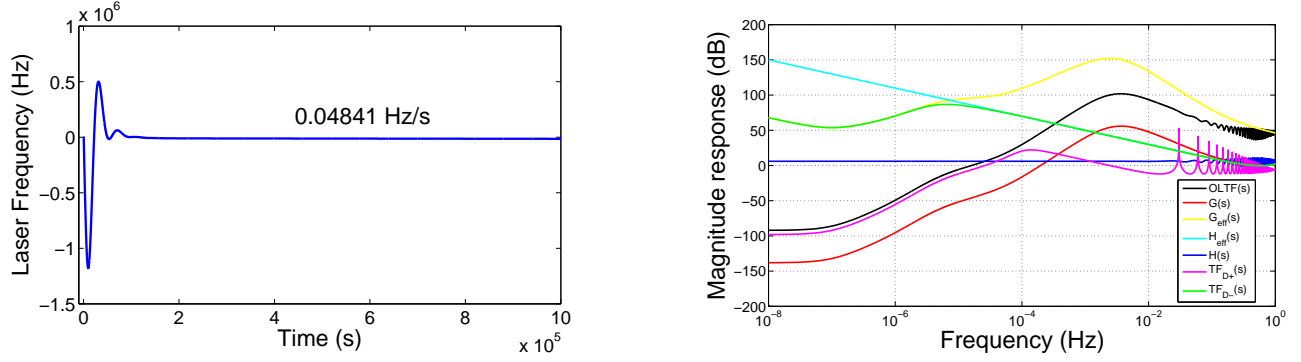


Figure 6-3. (Left) Simulated time series of the output frequency change due to a 1 kHz Doppler error with an AC-coupled controller. (Right) Modeled frequency responses of a generic dual arm locking loop to common and differential Doppler errors in the presence of an AC-coupled controller.

The frequency response to Doppler errors can be more easily explained by defining an effective sensor $H_{\text{eff}}(s) = P_-(s)$ and effective controller $G_{\text{eff}}(s) = G_0 G(s)/(\Delta\tau s)$ in the differential path. In Figure 6-3 (right) the yellow curve and the cyan curve demonstrate the effective controller G_{eff} and the effective sensor H_{eff} in the differential arm respectively. The closed-loop frequency response to the differential Doppler error is illustrated by the green curve in the figure. Depending on the gain level of the open-loop transfer function $H_{\text{eff}}(s)G_{\text{eff}}(s)$, the closed-loop frequency response consists of three segments in different frequency regions:

$$TF_{D-}(s) = \begin{cases} \frac{1}{H_{\text{eff}}(s)} \approx \frac{1}{2\Delta\tau s}, & \text{when } f \gg f_{UG} \\ \frac{G_{\text{eff}}(s)}{1+H_{\text{eff}}(s)G_{\text{eff}}(s)}, & \text{when } f \sim f_{UG} \\ G_{\text{eff}}(s), & \text{when } f \ll f_{UG} \end{cases} \quad (6-4)$$

where f_{UG} is the lower UGF of the high pass filter.

We are more interested in the region where the closed-loop frequency response is approximately equal to the effective controller, i.e., $TF_{D-}(s) = G_{\text{eff}}(s) = G_0 G(s)/(\Delta\tau s)$. The $1/s$ slope in the frequency response indicates a Doppler error induced pulling still occurs in the output frequency. However, compared with the large gain factor of $1/(2\Delta\tau)$ in the DC-coupling situation, the gain factor now is significantly reduced due to the

low gain of the AC-coupled controller. If we recall that the gain factor of $1/s$ is directly proportional to the drift rate of the frequency pulling, it is straightforward to derive the reduced drift rate given by

$$\left(\frac{d\nu_L}{dt}\right)_{\text{AC-coupled}} = 2G_0 G(s) \left(\frac{d\nu_L}{dt}\right)_{\text{DC-coupled}} \quad (6-5)$$

This relation indicates that the reduced drift rate is also directly proportional to the loop gain. Our time-domain simulation is based on a long arm length mismatch of $2\Delta\tau = 0.51$ s and an inaccurate differential Doppler estimation of $\Delta\nu_{D-} = 1$ kHz. Without the AC-coupling scheme the drift rate would be $1 \text{ kHz}/0.51 \text{ s} \approx 1961 \text{ Hz/s}$ for a high gain DC-coupled controller. Figure 6-3 (left) shows the time series of the variation of the laser frequency using our AC-coupled controller. The frequency pulling in lock acquisition yields a maximal frequency offset of approximately 1.2 MHz. In the steady state the drift rate has been reduced to 0.04841 Hz/s, which is exactly what we expect based on the frequency domain analysis presented above. Note that we reduced the laser frequency noise in this simulation to zero to be able to determine the drift rate with this accuracy.

6.2.3.2 Experiments with modified dual arm locking sensor

In the following experiments we will verify the frequency pulling rate of dual/modified dual arm locking in the steady state. The experimental setup is illustrated by Figure 6-4, where the Doppler frequency errors are generated by shifting the clock frequency. The block labeled with mapping vector represents the dual or modified dual arm locking mapping vector designed in Chapter 5. The Doppler frequency errors generated in the phase measurements are 6.4 Hz and 9.6 Hz, respectively. Therefore, with $\bar{\tau} = 33$ s and $\Delta\tau = 0.025$ s, the expected frequency pulling rates are

$$\begin{aligned} \left(\frac{d\nu_L}{dt}\right)_{\text{Dual}} &= \frac{\Delta\nu_{D-}}{2\Delta\tau} = 64 \text{ Hz/s}, \\ \left(\frac{d\nu_L}{dt}\right)_{\text{ModifiedDual}} &= \frac{\Delta\nu_{D+}}{2\bar{\tau}} = 0.24 \text{ Hz/s}. \end{aligned} \quad (6-6)$$

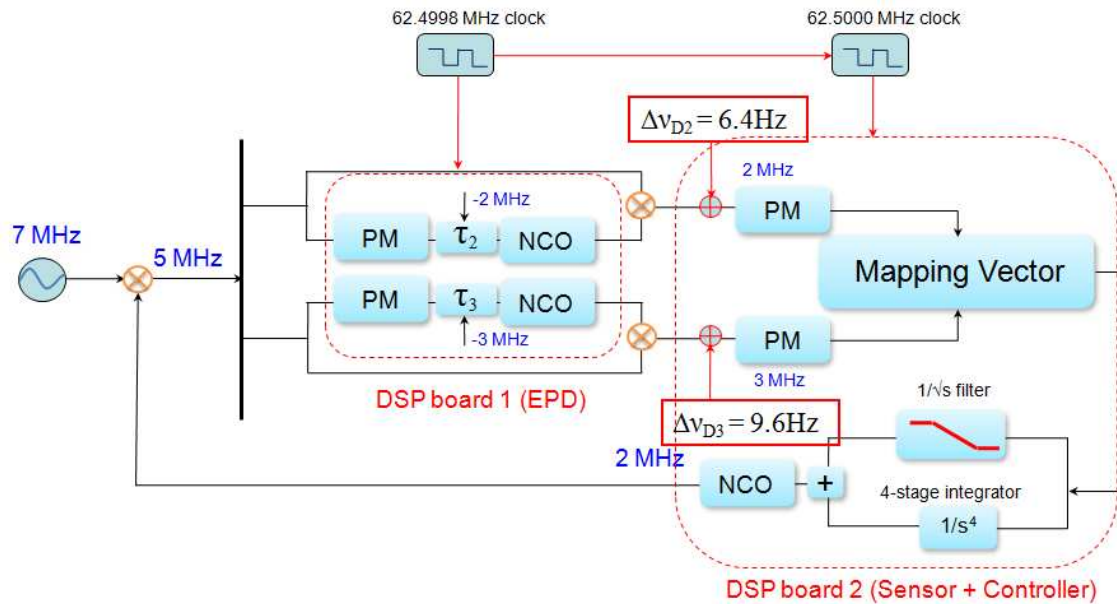


Figure 6-4. Experimental setup of dual/modified dual arm locking with Doppler frequency errors, which are generated from the clock frequency offset of 200 Hz. The Doppler frequency errors in the phase measurements are 6.4 Hz and 9.6 Hz, respectively. The controller in this setup is still high-gain DC-coupled to observe the frequency pulling rate.

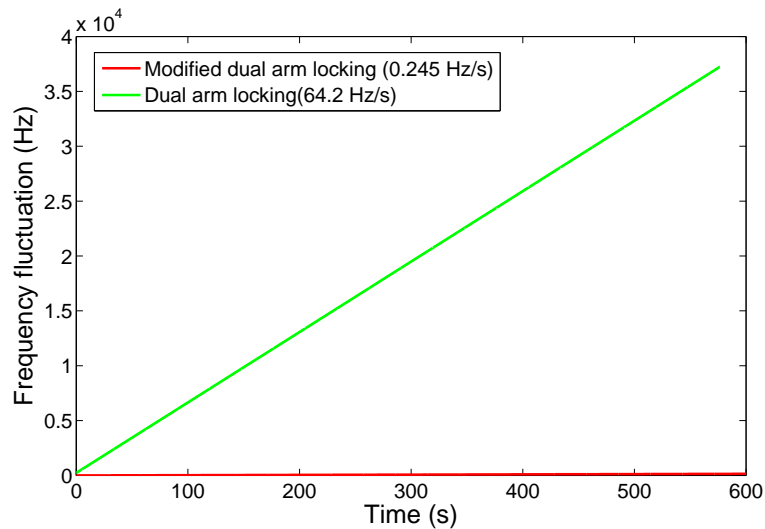


Figure 6-5. Observed frequency pulling of dual/modified dual arm locking with Doppler frequency errors. For a dual arm locking and a modified dual arm locking configuration, the observed frequency pulling rate is 64.2 Hz/s and 0.245 Hz/s, respectively. These measurement results are consistent with the theoretical predictions and demonstrate that the modified dual arm locking sensor is capable of alleviating the Doppler issue substantially when the arm length mismatch is not very large.

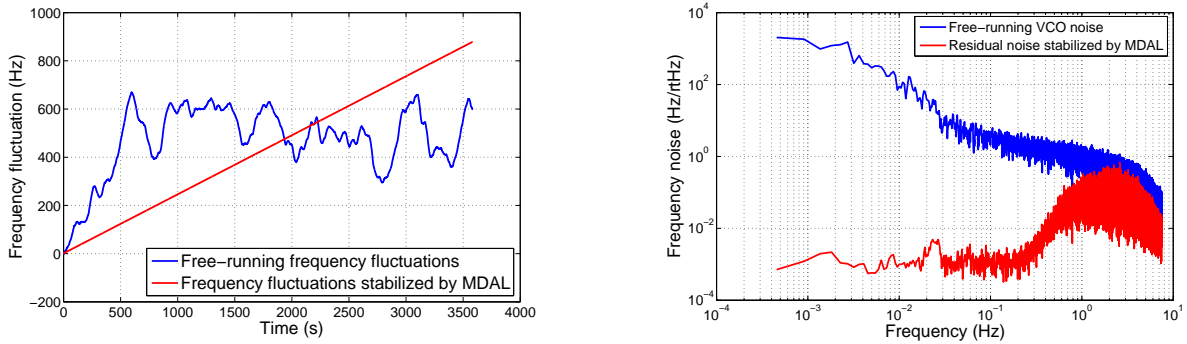


Figure 6-6. (Left) The frequency fluctuations of the free-running VCO signal and the residual signal stabilized by modified dual arm locking. Compared to the frequency pulling of dual arm locking in Figure 6-5, where the stabilized frequency has been pulled by more than 35 kHz in 600 s, the modified dual arm locking sensor restricts the frequency pulling within a range of less than 900 Hz in one hour. (Right) The noise spectra of the two time series. Here we can see that the noise suppression performance is essentially not affected by the frequency pulling after the linear drift is removed in post-processing.

The observed frequency pulling for both two cases is shown in Figure 6-5. In a duration of 600 s, the output frequency has drifted by more than 35 kHz when dual arm locking is used. In contrast, the modified dual arm locking configuration limits the 1-hour frequency pulling within a range of less than 900 Hz, as shown in Figure 6-6 (left). Note that this frequency pulling rate is even smaller than a typical drift rate of cavity stabilized lasers. From the frequency data we have obtained the frequency pulling rates are 64.2 Hz/s and 0.245 Hz/s. The measured frequency pulling rates match up the expected values and has demonstrated that the modified dual arm locking sensor is capable of alleviating the Doppler issue substantially when the arm length mismatch is not very large. Figure 6-6 (right) shows the linear spectral density of the residual frequency noise, which is essentially not affected by the linear frequency drift.¹

¹ The LSD of the residual frequency noise is limited by precision loss in the $E(s)$ filter, which is an old design, and is in any case independent of the frequency pulling rate.

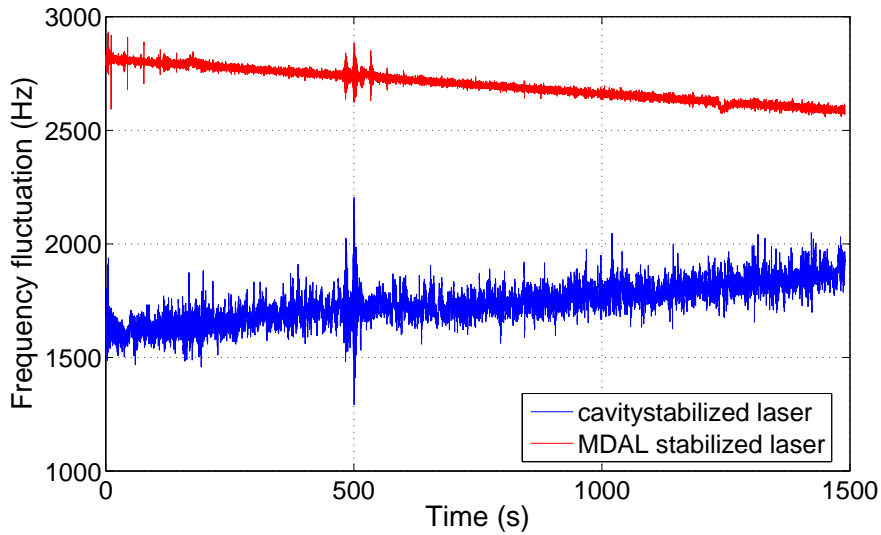


Figure 6-7. Observed frequency pulling of modified dual arm locking with Doppler errors in the cavity stabilized laser. The Doppler frequency error on one arm is set to be -10 Hz while zero on the other arm. The measured frequency pulling rate is comparable to to the spontaneous drift rate of cavity stabilized lasers.

Similar linear frequency drifts have also been observed on stabilized lasers. The experimental setup is essentially a hybrid of the setups in Figure 5-19 and Figure 5-22: The master laser is stabilized via a modified dual arm locking loop that is actuated by a heterodyne PLL. We place a synchronized function generator in the middle of the two delay lines on one arm to simulate the Doppler shift. The convenience of this setup is that the Doppler shift frequency can be precisely tuned to generate a continuously varying Doppler error on one arm, while simultaneously the Doppler frequency on the other arm will not be affected.

Figure 6-7 illustrates the linear drift in the laser frequency stabilized by a modified dual arm locking loop with $\bar{\tau} = 33$ s and $\Delta\tau = 0.025$ s. In this setup we set the Doppler frequency error on one arm to be -10 Hz, while the Doppler frequency is perfectly accounted for on the other arm. Therefore, the frequency pulling rate should be given by $\Delta\nu_{D+}/2\bar{\tau} = -0.15$ Hz/s and the observed frequency pulling rate is consistent with the theoretical value. For comparisons, the intrinsic frequency drift rate in this cavity stabilized laser is measured to be approximately 0.18 Hz/s and if dual arm locking is

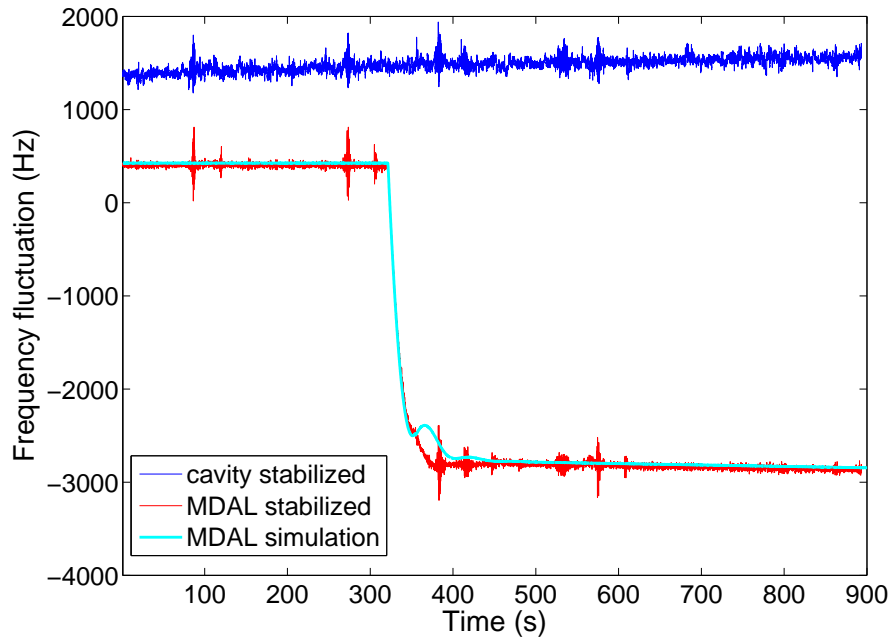


Figure 6-8. Observed frequency pulling in lock acquisition due to a step function in Doppler errors. After the step Doppler error enters the loop, the laser frequency has been pulled by ~ 3 kHz in lock acquisition and then drifts with a constant rate in the steady state. A time-domain simulation with the same conditions was performed and the time series (the cyan curve) have shown consistency with our measurements.

used, the frequency pulling rate would become -200 Hz/s. Our measurement has demonstrated that modified dual arm locking is capable of reducing the frequency pulling rate to a negligible level that is comparable to the spontaneous drift of cavity stabilized lasers, provided that a reasonable Doppler estimation could be given.

In addition, we have also studied the responsive behavior of the stabilized laser frequency to a step function in the Doppler error. Using the same experimental setup, we start the arm locking loop without any Doppler error. After the laser frequency is settled down, we initiate a step function in the Doppler frequency by 10 Hz and observe the frequency pulling in the relock duration. The time series of the laser frequency is shown in Figure 6-8, where we can see the laser frequency has been pulled by ~ 3 kHz and re-entered the steady state with a constant drift rate of -0.152 Hz/s in about 2 min.

To verify this lock acquisition process, we have run a time-domain simulation with the same conditions and the result is given by the cyan curve in the figure. We can see that in most regions the numerical simulation agrees with the measurement very well.² The deviation that happens during 350 s – 400 s is mainly ascribed to the difference in the filter design between the simulation and hardware models, such as the error caused by bilinear transform in the time-domain.

Still, to realistically simulate the time-variable Doppler frequency error, a simulator to generate time-variable Doppler shift frequencies that track the spacecraft orbital motions must be implemented on the EPD unit. However, an oscillation frequency of $\sim 10^{-8}$ Hz is too low for laboratory experiments to effectively simulate. To circumvent this problem, the plan is to rescale the orbital frequency of LISA and consequently the delay times, as well as zeros and poles in arm locking filters, to a relatively short “lab-reasonable” time scale, which requires the redesign of the entire arm locking system. Currently, a new version of the EPD unit featuring such time-varying Doppler frequencies is in development. Consequently, an adapted arm locking system will be built to study the arm locking performance with realistic time-variable Doppler errors.

² The time series of the stabilized laser frequency shows spurious peaks, which are highly correlated to the unwarranted jumps in the input laser frequency. Our arm locking loop is capable of attenuating frequency jumps within a range of ~ 1 kHz.

CHAPTER 7 CONCLUSION AND OUTLOOK

We tested different arm locking schemes for LISA using our LISA interferometer testbed. The EPD-based electro-optical arm locking hardware simulations can effectively and faithfully reproduce realistic LISA-like conditions such as 16 s light travel time and variable MHz Doppler shifts, which are vital for the validity of arm locking experiments. In particular, the dual and modified dual arm locking configurations are linear combinations of LISA inter-spacecraft phase measurements optimized for the noise performance and minimization of the Doppler-induced frequency pulling issue. In this dissertation experimental verifications to examine them under realistic LISA-like conditions are presented for the first time.

7.1 Control System of Arm Locking

On UFLIS we have implemented four basic arm locking configurations and demonstrated their control system in a series of verification measurements. In our experiments a laser beat signal with a heterodyne frequency in the range of 2 – 20 MHz is received and converted into an electronic signal at the photodiode. The long arm interferometer output is simulated via the analog mixing of the electronic signal and its delayed replica. By demodulating the interferometer outputs, the phasemeters extract the frequency fluctuations from each heterodyne beat signal. A dedicated mapping vector is used to synthesize and manipulate the frequency fluctuations to form an adequate linear combination, known as the error signal of arm locking. The measurements have shown that the open-loop transfer functions of these arm locking sensors agree very well with the theoretical design.

The arm locking controller on UFLIS was designed and built in parallel paths: A compensator filter yields a $1/\sqrt{f}$ slope at frequencies above 1 Hz to alleviate the large phase shift due to the round-trip delays. Four-stage cascaded integrators provide sufficient noise suppressions in the LISA band. Through the combination of these two

control paths, a robust control system of arm locking have been achieved with both a high bandwidth and a satisfactory noise suppression performance. Consequently, we present the first ever experimental proof of these arm locking schemes in the presence of realistic LISA-like long time delays and Doppler shifts, with unprecedented noise suppression performances. In our experiments we achieved up to 6 orders of magnitude noise suppression via single arm locking and up to 8 orders of magnitude via dual/modified dual arm locking in the LISA band.

We also have studied the incorporation of arm locking with cavity stabilized lasers. The combination of arm locking and the PDH stabilization technique will provide more noise suppressions; however, it requires the reference of the PDH stabilization to be frequency tunable. Therefore, we present a modification to the standard PDH setup known as the PZT actuator, by which the resonant frequency of the cavity can be adjusted in accordance with the arm locking feedback signal. We also present a second method to introduce an auxiliary laser offset phase-locked to the master laser. The slave laser reproduces the noise property of the master laser as well as obtains the frequency tunability through the offset frequency of the local oscillator. These measurements have demonstrated that arm locking can be easily reconciled with the cavity stabilization without explicitly degrading the noise suppression performance of either of them.

7.2 Noise Limitations

Depending on scheme used and actual light travel times, arm locking can be gain limited or limited by several external noise sources. The primary noise sources in arm locking include clock noise, spacecraft motion, shot noise, technical noise and possibly far-end PLL noise. In our experiments we analyzed the impact of various noise sources on the noise suppression performance under different circumstances.

We also studied the influence of digitalization noise in the digital arm locking sensors and controllers on the performance of arm locking. These results can be used to design the digital arm locking system for LISA. The ADC noise in phase

measurements is another primary noise source that limits the arm locking performance in our experiments. In realistic LISA the ADC noise performance in the phasemeter will be optimized to meet the $1 \text{ pm Hz}^{-1/2}$ requirement and should not cause a problem. Nevertheless, our measurements have verified that the limiting ADC noise floor is consistent with the theoretical predictions in the context of UFLIS. Moreover, by investigating the ADC noise limitation we present the experimental proof that with the same arm length mismatch, the noise performance of modified dual arm locking is substantially superior to that of dual arm locking.

A more realistic demonstration of modified dual arm locking with the far-end transponder noise is also presented in this dissertation. In the experiment we implemented an analog phase-locked loop at the far-end to phase lock the local beat signal to the incoming delayed signal. The transponder noise limitation observed in the stabilized laser noise can be equivalently considered as a manifestation of any noise source presented on the far spacecraft as they all couple into the arm locking control system in the same fashion, i.e.,

$$\delta\nu = \frac{H_+}{H}(\delta\nu_2 + \delta\nu_3) + \frac{H_-}{H}(\delta\nu_2 - \delta\nu_3), \quad (7-1)$$

where $\delta\nu_i$, $i = 2, 3$ is any transponder noise introduced on the far spacecraft $SC_{2,3}$. We measured the transponder noise limit in the stabilized laser and the PLL noise at the far-end independently and found them in accordance with Eq. 7-1. The experiment also reveals that in the presence of a non-negligible transponder noise and a relatively short arm length mismatch ($\Delta\tau = 0.025 \text{ s}$), our modified dual arm locking configuration with cavity stabilization still sufficiently meets the TDI capability with a margin of more than 25,000 at 3 mHz.

7.3 Doppler-induced Frequency Pulling

The impact of Doppler shifts on arm locking was firstly identified from the arm locking experiments on UFLIS and is a very critical issue that would ultimately affect

the feasibility of arm locking. More in-depth research on the Doppler impact gave a better understanding of the Doppler frequency error, frequency pulling and helped to identify solutions to overcome it. The arm locking control system implemented on UFLIS provides an ideal environment to test the effects of frequency pulling and relevant remedies.

By introducing a Doppler frequency error in the phase measurement, we have demonstrated how the frequency pulling depends on different arm locking sensors. These experiments are the first ever experimental proofs of arm locking in a realistic and non-static LISA constellation. In particular, an AC-coupled controller for single arm locking and dual arm locking has been developed in hardware and software respectively, confirming that the frequency pulling can be substantially reduced or even eliminated. We also compared the distinct frequency pulling rates of dual arm locking and modified dual arm locking in response to same Doppler frequency errors. Our experiment indicates that the modified dual arm locking sensor is capable of alleviating the frequency pulling rate in the steady state to a negligible level, which is comparable to the typical drift rate of a cavity stabilized laser.

We also have started the investigation of time-variable Doppler frequency errors in hardware simulations. The observed frequency pulling in lock acquisition due to a step function in the Doppler error agrees very well with the time domain simulation under the same conditions.

7.4 Outlook

With the everlasting endeavor on gravitational wave detections in the past 50 years, gravitational wave astronomy is expected to open a new window to the universe in this decade, with the help of the next generation ground-based detectors, such as advanced LIGO, VIRGO and LCGT, and the space-based project LISA. From gravitational wave detections on compact binaries, black holes and Big Bang relics, entirely new

information on astrophysics and cosmology will be revealed and consequently extend our understanding of the universe.

The low-frequency region that LISA will probe is full of interesting gravitational wave sources, many of which still have never been seen. For coalescences of massive black holes, as well as primordial gravitational waves generated in the extremely short time after Big Bang, a space gravitational wave observatory such as LISA might be the only accessible method to study them. LISA will precisely measure thousands of binary systems in our Galaxy and yield new insights into the astrophysics of binary stars; LISA will also provide a very first test of general relativity in extremely strong gravitational fields on the vicinity of black holes by listening to the inspiral signals.

From the point of view of instrumentation, LISA is also a technically challenging mission due to the required high sensitivity. The noise requirements for laser interferometry and drag-free control are unprecedentedly stringent for current technology. The laser frequency stabilization was once considered a difficult issue that may cause Time Delay Interferometry to fail. Now multiple frequency control options have been proposed to solve this problem and the selection is more based on the consideration of complexity, cost, etc. Arm locking as one of the proposed laser frequency stabilization techniques, entirely exploits LISA's long arm interferometry to generate an error signal. This simple architecture substantially saves on implementation resources. In addition, the integration of arm locking and other pre-stabilization subsystems can suppress the laser frequency noise below the pre-TDI requirement of 1 m ranging capability with an abundant margin, which will further relax the dependence on ranging. The issue of Doppler-induced frequency pulling slightly complicates the design of the control system of arm locking and additional on-board data processing to estimate the Doppler frequency is needed. Nevertheless, both analysis and experiments have shown that modified dual arm locking solves this Doppler problem. We look forward a better understanding of LISA technology, as well as a gravitational wave universe that LISA will ultimately discover.

REFERENCES

- [1] A. Einstein. Gravitationswellen. *Preussische Akademie der Wissenschaften, Sitzungsberichte*, 1918:154–167, 1918.
- [2] J. Weber. Detection and generation of gravitational waves. *Phys. Rev.*, 117:306, 1960.
- [3] J. H. Taylor and J. M. Weisberg. A new test of general relativity - Gravitational radiation and the binary pulsar PSR 1913+16. *Astrophys. J.*, 253:908–920, 1982.
- [4] J. M. Weisberg and J. H. Taylor. Observations of post-newtonian timing effects in the binary pulsar psr 1913+16. *Phys. Rev. Lett.*, 52:1348, 1984.
- [5] B. F. Schutz. Gravitational wave astronomy. *Class. Quantum Grav.*, 16:A131, 1999.
- [6] D. Sigg *et al.* Status of the LIGO detectors. *Class. Quantum Grav.*, 23:S51, 2006.
- [7] P. Bender *et al.* LISA - Laser Interferometer Space Antenna for the detection and observation of gravitational waves. MPQ-208, 1996.
- [8] K. Danzmann *et al.* LISA - an ESA cornerstone mission for the detection and observation of gravitational waves. *Advances in Space Research*, 32:1233, 2003.
- [9] R. N. Lang and S. A. Hughes. Measuring coalescing massive binary black holes with gravitational waves: the impact of spin-induced precession. *Phys. Rev. D*, 74:122001, 2006.
- [10] R. N. Lang and S. A. Hughes. Localizing coalescing massive black hole binaries with gravitational waves. *Astrophys. J.*, 677:1184, 2008.
- [11] M. Tinto and J. W. Armstrong. Cancellation of laser noise in an unequal-arm interferometer detector of gravitational radiation. *Phys. Rev. D*, 59:102003, 1999.
- [12] M. Tinto and S.L. Larson. The LISA zero-signal solution. *Class. Quantum Grav.*, 22:S531, 2005.
- [13] K. McKenzie, R. E. Spero, and D. A. Shaddock. Performance of arm locking in LISA. *Phys. Rev. D*, 80:102003, 2009.
- [14] V. Wand *et al.* Implementation of arm locking with a delay of 1 second in the presence of Doppler shifts. *J. Phys.: Conf. Series*, 154:012024, 2009.
- [15] Y. Yu, S. Mitryk, and G Mueller. Experimental verification of dual/modified dual arm locking. *Class. Quantum Grav.*, 28, 2011.
- [16] C. Misner, K. Thorne, and J. Wheeler. *Gravitation*. W.H. Freeman and Company, San Francisco, CA, 1973.

- [17] M. Maggiore. *Gravitational Waves: Volume 1: Theory and Experiments*. Oxford University Press, 2007.
- [18] K. Thorne. Gravitational waves. *arXiv:gr-qc/9506086v1*, 1995.
- [19] J. W. T. Hessels, S. M. Ransom, I. H. Stairs, P. C. C. Freire, V. M. Kaspi, and F. Camilo. A radio pulsar spinning at 716 hz. *science*, 311:1901, 2006.
- [20] L. Wang *et al.* The axisymmetric ejecta of supernova 1987a. *Astrophys. J.*, 579:671, 2002.
- [21] S. A. Hughes. Listening to the universe with gravitational-wave astronomy. *Annals Phys.*, 303:142, 2003.
- [22] R. F. Webbink. Watch this space: Observing merging white dwarfs. *arXiv:1011.6317v1 [astro-ph.SR]*, 2010.
- [23] A. Stroeer and A. Vecchio. The LISA verification binaries. *Class. Quantum Grav.*, 23:S809, 2006.
- [24] K. Belczynski, M. Benacquista, and T. Bulik. Double compact objects as low-frequency gravitational wave sources. *Astrophys. J.*, 725:816, 2010.
- [25] G. Nelemans, S. F. P. Zwart, F. Verbunt, and L. R. Yungelson. Population synthesis for double white dwarfs. *A & A*, 363:939, 2001.
- [26] A. J. Ruiter, K. Belczynski, M. Benacquista, and K. Holley-Bockelmann. The contribution of halo white dwarf binaries to the Laser Interferometer Space Antenna signal. *Astrophys. J.*, 693:383, 2009.
- [27] Y. B. Zeldovich and I. D. Novikov. *Soviet Physics Doklady*, 9:246, 1964.
- [28] E. F. Belland S. Phleps, R. S. Somerville, C. Wolf, A. Borch, and K. Meisenheimer. The merger rate of massive galaxies. *Astrophys. J.*, 652:270, 2006.
- [29] Flanagan and S. A. Hughes. Measuring gravitational waves from binary black hole coalescences. i. signal to noise for inspiral, merger, and ringdown. *Phys. Rev. D*, 57:4535, 1998.
- [30] Flanagan and S. A. Hughes. Measuring gravitational waves from binary black hole coalescences. i. signal to noise for inspiral, merger, and ringdown. *Phys. Rev. D*, 57:4566, 1998.
- [31] F. Pretorius. Evolution of binary black-hole spacetimes. *Phys. Rev. Lett.*, 95:121101, 2005.
- [32] M. Campanelli, C. O. Lousto, and Y. Zlochower. Last orbit of binary black holes. *Phys. Rev. D*, 73:061501, 2006.

- [33] S. Chandrasekhar and S. Detweiler. The quasi-normal modes of the schwarzschild black hole. *Proc. R. Soc. Lond. A*, 344:441, 1975.
- [34] P. Amaro-Seoane, J. R. Gair, M. Freitag, M. C. Miller, I. Mandel, C. J. Cutler, and S. Babak. Intermediate and extreme mass-ratio inspirals - astrophysics, science applications and detection using LISA. *Class. Quantum Grav.*, 24:R113, 2007.
- [35] J. R. Gair, L. Barack, T. Creighton, C. Cutler, S. L. Larson, E. S. Phinney, and M. Vallisneri. Event rate estimates for LISA extreme mass ratio capture sources. *Class. Quantum Grav.*, 21:S1595, 2004.
- [36] Stanislav Babak, Hua Fang, Jonathan R. Gair, Kostas Glampedakis, and Scott A. Hughes. “kludge” gravitational waveforms for a test-body orbiting a kerr black hole. *Phys. Rev. D*, 75:024005, 2007.
- [37] C. Hopman and T. Alexander. The effect of mass segregation on gravitational wave sources near massive black holes. *Astrophys. J. Lett.*, 645:L133, 2006.
- [38] J. R. Gair and E. K. Porter. Cosmic swarms: a search for supermassive black holes in theLISA data stream with a hybrid evolutionary algorithm. *Class. Quantum Grav.*, 26:225004, 2009.
- [39] L. Barack and C. Cutler. LISA capture sources: Approximate waveforms, signal-to-noise ratios, and parameter estimation accuracy. *Phys. Rev. D*, 69:082005, 2004.
- [40] M. Hueller, M. Armano, L. Carbone, A. Cavalleri, R. Dolesi, C. D. Hoyle, S. Vitale, and W. J. Weber. Measuring the LISA test mass magnetic properties with a torsion pendulum. *Class. Quantum Grav.*, 22:S521, 2005.
- [41] S. A. Teukolsky. Perturbations of a rotating black hole. i. fundamental equations for gravitational, electromagnetic, and neutrino-field perturbations. *Astrophys. J.*, 185:635, 1973.
- [42] L. M. Krauss and M. White. Grand unification, gravitational waves, and the cosmic microwave background anisotropy. *Phys. Rev. Lett.*, 69:869, 1992.
- [43] R. Brustein, M. Gasperinib, M. Giovanninib, and G. Veneziano. Relic gravitational waves from string cosmology. *Phys. Lett. B*, 361:45, 1995.
- [44] A. Buonanno, M. Maggiore, and C. Ungarelli. Spectrum of relic gravitational waves in string cosmology. *Phys. Rev. D*, 55:3330, 1997.
- [45] E. Witten. Cosmic separation of phases. *Phys. Rev. D*, 30:272, 1984.
- [46] M. Kamionkowski, A. Kosowsky, and M. S. Turner. Gravitational radiation from first-order phase transitions. *Phys. Rev. D*, 49:2837, 1994.

- [47] T. Vachaspati and A. Vilenkin. Gravitational radiation from cosmic strings. *Phys. Rev. D*, 31:3052, 1985.
- [48] D. Blair. *The Detection of Gravitational Waves*. Cambridge University Press, 2005.
- [49] M. Tinto. Spacecraft doppler tracking as a xylophone detector of gravitational radiation. *Phys. Rev. D*, 53:5354, 1996.
- [50] F. Jenet, A. Lommen, S. Larson, and L. Wen. Constraining the properties of supermassive black hole systems using pulsar timing: an application to 3c 66b. *Astrophys. J.*, 606:799, 2004.
- [51] F. Jenet, G. Hobbs, K. Lee, and R. Manchester. Detecting the stochastic gravitational wave background using pulsar timing. *Astrophys. J.*, 625:L123, 2005.
- [52] F. Acernese *et al.* The status of VIRGO. *Class. Quantum Grav.*, 23:S63, 2006.
- [53] B. Willke *et al.* GEO600: status and plans. *Class. Quantum Grav.*, 24:S389, 2007.
- [54] M. Ando *et al.* Current status of TAMA. *Class. Quantum Grav.*, 19:1409, 2002.
- [55] K. Kuroda and the LCGT Collaboration. The status of LCGT. *Class. Quantum Grav.*, 23:S215, 2006.
- [56] D. Shoemaker *et al.* Ground-based interferometric gravitational-wave detectors in the LISA epoch. *Class. Quantum Grav.*, 20:S11, 2003.
- [57] S. Kawamura *et al.* The Japanese space gravitational wave antenna - DECIGO. *J. Phys.: Conf. Ser.*, 122:012006, 2008.
- [58] T. Prince and K. Danzmann. LISA science requirement document version 4.1. *LISA International Science Team documentation*, 2007.
- [59] D. Shaddock, B. Ware, P. Halverson, R.E. Spero, and B. Klipstein. Overview of the LISA phasemeter. *JPL Technical Report*, 2006.
- [60] T. Prince *et al.* LISA: Unveiling a hidden universe: Assessment study report. *European Space Agency documentation*, 2011.
- [61] S. L. Larson, W. A. Hiscock, and R. W. Hellings. Sensitivity curves for spaceborne gravitational wave interferometers. *Phys. Rev. D*, 62:062001, 2000.
- [62] R. Dolesi *et al.* Gravitational sensor for LISA and its technology demonstration mission. *Class. Quantum Grav.*, 20:S99–108, 2003.
- [63] W. J. Weber *et al.* Position sensors for LISA drag-free control. *Class. Quantum Grav.*, 19:1751–6, 2002.

- [64] L. Carbone *et al.* Achieving geodetic motion for LISA test masses: ground testing results. *Phys. Rev. Lett.*, 91:151101, 2003.
- [65] D. W. Budworth, F. E. Hoare, and J. Preston. The thermal and magnetic properties of some transition element alloys. *Proc. R. Soc. A*, 257:250–62, 1960.
- [66] Z. Silvestri *et al.* Volume magnetic susceptibility of gold-platinum alloys: possible materials to make mass standards for the watt balance experiment. *Metrologia*, 40:172–6, 2003.
- [67] P. McNamara *et al.* LISA Pathfinder. *Class. Quantum Grav.*, 25:114034, 2008.
- [68] G. Heinzel, C. Braxmaier, R. Schilling, A. Rüdiger, D. Robertson, M. Plate, V. Wand, K. Arai, U. Johann, and K. Danzmann. Interferometry for the LISA technology package (LTP) aboard SMART-2. *Class. Quantum Grav.*, 20:S153, 2008.
- [69] O. Jennrich. LISA technology and instrumentation. *Class. Quantum Grav.*, 26:153001, 2009.
- [70] M. Tinto, F. B. Estabrook, and J. W. Armstrong. Time-delay interferometry for LISA. *Phys. Rev. D*, 65:082003, 2002.
- [71] D. A. Shaddock, B. Ware, R. E. Spero, and M. Vallisneri. Post-process time delay interferometry for LISA. *Phys. Rev. D*, 70:081101, 2004.
- [72] D. A. Shaddock *et al.* LISA frequency control white paper. *LISA Project technical note LISA-JPL-TN-823*, 2009.
- [73] J. W. Armstrong, F. B. Estabrook, and M. Tinto. Time-delay interferometry for space-based gravitational wave searches. *Astrophys. J.*, 527:814–26, 1999.
- [74] D. A. Shaddock *et al.* Data combinations accounting for LISA spacecraft motions. *Phys. Rev. D*, 68:061303, 1999.
- [75] D. A. Shaddock. Operating LISA as a Sagnac interferometer. *Phys. Rev. D*, 69:022001, 2004.
- [76] V. Leonhardt and J. B. Camp. Space interferometry application of laser frequency stabilization with molecular iodine. *Appl. Optics*, 45:4142, 2006.
- [77] R. W. P. Drever, J. L. Hall, F. V. Kowalski, J. Hough, G. M. Ford, and A. J. Munley. Laser phase and frequency stabilization using an optical resonator. *Appl. Phys. B*, 31:97–105, 1983.
- [78] G. Mueller G, P. McNamara P, J. I. Thorpe, and J. Camp. Laser frequency stabilization for LISA. *Technical Report NASA/TM-2005-212794*, 2005.
- [79] F. Steier, F. C. Guzman, A. F. M. Garcia, D. Gerardi, G. Heinzel, and K. Danzmann. The end-to-end testbed of the optical metrology system on-board LISA pathfinder. *Class. Quantum Grav.*, 26:094010, 2009.

- [80] E. D. Black. An introduction to pound-drever-hall laser frequency stabilization. *Am. J. Phys.*, 69:79–87, 2001.
- [81] G. Heinzel *et al.* The LTP interferometer and phasemeter. *Class. Quantum Grav.*, 21:S581–7, 2004.
- [82] V. Wand *et al.* Noise sources in the LTP heterodyne interferometer. *Class. Quantum Grav.*, 23:S159, 2006.
- [83] J. Eichholz *et al.* Heterodyne laser frequency stabilization for the Laser Interferometer Space Antenna. *accepted by J. Phys.: Conf. Series*, 2011.
- [84] B. S. Sheard, M. B. Gray, D. E. McClelland, and D. A. Shaddock. Laser frequency stabilization by locking to a LISA arm. *Phys. Lett. A*, 320:9, 2003.
- [85] A. Sutton and D. A. Shaddock. Laser frequency stabilization by dual arm locking for LISA. *Phys. Rev. D*, 78:082001, 2008.
- [86] M. Tinto and M. Rakhmanov. On the laser frequency stabilization by locking to a LISA arm. *gr-qc/0408076*, 2004.
- [87] J. Sylvestre. Simulations of laser locking to a LISA arm. *Phys. Rev. D*, 70:102002, 2004.
- [88] M. Herz. Active laser frequency stabilization and resolution enhancement of interferometers for the measurement of gravitational waves in space. *Opt. Eng.*, 44:090505, 2005.
- [89] A. Marín *et al.* Phase locking to a LISA arm: first results on a hardware model. *Class. Quantum Grav.*, 22:S235, 2005.
- [90] Glenn de Vine *et al.* Experimental demonstration of Time-delay Interferometry for the Laser Interferometer Space Antenna. *Phys. Rev. Lett.*, 104:211103, 2010.
- [91] J. I. Thorpe, R. J. Cruz, S. Sankar, and G. Mueller. Electronic phase delay - a first step towards a bench-top model of LISA. *Class. Quantum Grav.*, 22:S227–34, 2005.
- [92] S. Mityrk, V. Wand, and G. Mueller. Verification of time-delay interferometry techniques using the University of Florida LISA interferometry simulator. *Class. Quantum Grav.*, 27:084012, 2010.
- [93] J. I. Thorpe and G. Mueller. Experimental verification of arm-locking for LISA using electronic phase delay. *Phys. Lett. A*, 342:199–204, 2005.
- [94] J. C. Livas, J. I. Thorpe, K. Numata, S. Mityrk, G. Mueller, and V. Wand. Frequency-tunable pre-stabilized lasers for LISA via sideband locking. *Class. Quantum Grav.*, 26:094016, 2009.

- [95] Y. Yu, V. Wand, S. Mitryk, and G Mueller. Arm locking with doppler estimation errors. *J. Phys.: Conf. Series*, 228:012044, 2010.

BIOGRAPHICAL SKETCH

Yinan Yu was born in Tianjin in the east of China. He spent most of his childhood and adolescence in Tianjin and graduate from Nankai University with a bachelor's degree in science in 2005. In his senior year he decided to apply for graduate school to pursue his PhD degree as well as to expand his career of scientific research. He was accepted by the Department of Physics at the University of Florida with teaching assistantship in 2005. In the summer of 2006 he joined Dr. Mueller's research group and began working with him on the benchtop experiments of Laser Interferometer Space Antenna (LISA) instrumentations for gravitational wave detections. Their work has demonstrated the validity and feasibility of laser frequency stabilization by means of arm locking. After five years of research, he graduated from the University of Florida with a Doctorate of Philosophy in physics.